Conception of organic capsules by self-organization of functionalized heterocycles

Serhii Krykun

▶ **To cite this version:**

Serhii Krykun. Conception of organic capsules by self-organization of functionalized heterocycles. Organic chemistry. Université d'Angers; Kiïvs kij nacìonal nij unìversitet imeni Tarasa Ševčenka (Ukraine), 2019. English. NNT : 2019ANGE0007 . tel-02307126

HAL Id: tel-02307126

https://theses.hal.science/tel-02307126

Submitted on 7 Oct 2019

Thèse de doctorat de

L'UNIVERSITE D'ANGERS
COMUE UNIVERSITE BRETAGNE LOIRE

ECOLE DOCTORALE N° 596
Matière, Molécules, Matériaux
Spécialité : *Chimie Organique*

Par

Serhii KRYKUN

Conception de capsules organiques par auto-organisation d'hétérocycles fonctionnalisés

Thèse présentée et soutenue à Kyiv (Ukraine), le 15 Mai 2019
Unité de recherche : Laboratoire MOLTECH-Anjou, UMR CNRS 6200
Thèse N° :

Rapporteurs avant soutenance :		Composition du Jury :	
		Rapporteurs	
Pr. Rémi CHAUVIN	Professeur, Université de Toulouse III Paul Sabatier	Pr Rémi CHAUVIN	Professeur, Université de Toulouse III Paul Sabatier
Pr. Oleksandr ROSHAL	Professeur, Research Institute of Chemistry V.N. Karazin Kharkiv National University	Pr Oleksandr ROSHAL	Professeur, Research Institute of Chemistry V.N. Karazin Kharkiv National University
		Examinateurs	
		Pr Yuriy SHERMOLOVICH	Professeur, Institute of Organic Chemistry NAS of Ukraine d'exercice
		Directeur de thèse	
		Pr Marc SALLE	Professeur, Laboratoire MOLTECH-Anjou
		Co-directeur de thèse	
		Pr Zoia VOITENKO	Professeur, Taras Shevchenko National University of Kyiv
		Co-encadrant de thèse	
		Dr Sébastien GOEB	Chargé de recherche CNRS, Laboratoire MOLTECH- Anjou

Titre : Conception de capsules organiques par auto-organisation d'hétérocycles fonctionnalisés

Mots clés : chimie supramoléculaire, chimie organique, auto-assemblage, cages de coordination, tétrathiafulvalène, redox

Résumé : Ce travail traite de la synthèse et de la caractérisation de nouvelles cages moléculaires discrètes riches en électrons préparées via la méthodologie d'auto-assemblage dirigée par les métaux, ainsi que de leurs propriétés redox et d'encapsulation. Les concepts généraux guidant la méthodologie d'auto-assemblage pilotée par les métaux sont présentés. Trois types de ligands tétratopiques rédox-actifs (L) constitués de tétrathiafulvalène (TTF), de dithiol-fluorène (DTF) ou de tétrathiafulvalène π étendu (exTTF) ont été conçus. Leur capacité à générer des cages auto-assemblées avec divers complexes (M) a été étudiée. Dans le premier cas, des métallacages M_8L_2 dont la géométrie offre une opportunité unique de favoriser des interactions inter-TTF étroites au cours du processus d'oxydation ont été décrites. Ces interactions ont été confirmées par des études électrochimiques ainsi que par DRX à partir d'un sel oxydé électrocristallisé. Dans le second cas,

plusieurs auto-assemblages discrets MxLy (cages, clips) ont été obtenus à partir de nouveaux ligands électroactifs basés sur l'unité 9- (1,3-dithiol-2-ylidène) fluorène (DTF). Leurs propriétés rédox ainsi que leur capacité à complexer des unités électro-déficientes sont fortement dépendantes de la géométrie de l'auto-assemblage. Concernant le ligand exTTF, de grandes métallacages électroactives $M_{12}L_6$ (environ 4 000 Å^3) ont été obtenues par combinaison avec des complexes *trans* de palladium ou d'argent. Ces dernières se désassemblent lors de l'oxydation, donnant lieu à une transformation sans précédent d'une cage métallique discrète en un polymère de coordination. Enfin, un nouveau squelette aromatique benzo[1,2-b:4,5-b'] dithiophène est décrit en tant qu'alternative aux dérivés riches en électrons π étendus. Le rôle critique des interactions non-covalentes 1,5 S ⋯S est démontré par une approche combinée expérimentale et théorique.

Title : Conception of organic capsules by self-organization of functionalized heterocycles

Keywords: supramolecular chemistry, organic chemistry, self-assembly, coordination cages, tetrathiafulvalene, redox.

Abstract: This work deals with the synthesis and characterization of new electron-rich discrete molecular cages, prepared via the coordination-driven self-assembly methodology, as well as on evaluating their redox and host-guest properties. The general concepts guiding the metal-driven self-assembly methodology are presented. Three types of redox-active tetratopic ligands (L) featuring either a tetrathiafulvalene (TTF), a dithiol-fluorene (DTF) or a π-extended tetrathiafulvalene (exTTF) have been designed. Their ability to generate self-assembled cages upon combination with various metal complexes (M) has been studied. In the first case, M_8L_2 metallacages were obtained, whose geometry offers a unique opportunity to promote close inter-TTF interactions upon oxidation, as confirmed through electrochemical studies as well as from single-crystal DRX from an electrocrystallized oxidized salt. In the

second case, several discrete self-assemblies M_xL_y (cages, clips) were obtained and characterized from new electro-active ligands based on the 9-(1,3-dithiol-2-ylidene)fluorene (DTF) unit. Their redox properties as well as their binding ability towards electro-deficient planar species show a strong dependence to the self-assembly geometry. Considering the exTTF ligand, large (*ca.* 4000 Å^3) electroactive $M_{12}L_6$ metallacages were obtained from combining with *trans* palladium or silver complexes. Le latter exhibits a disassembling process upon oxidation, giving rise to an unprecedented redox-triggered transformation of discrete metalla-cage into a coordination polymer. Finally, a new benzo[1,2-b:4,5-b'] dithiophene aromatic scaffold is investigated as an alternative π-extended electron-rich derivative. The critical role of non-covalent 1,5 S⋯S interactions is demonstrated by a combined experimental and theoretical approach.

Table of Contents

Abbreviations

2D	two-dimensional
3D	three-dimensional
CV	cyclic voltammetry
D	diffusion coefficient
DCTNF	9-dicyanomethylen-2,4,7-trinitrofluoren
DFT	density functional theory
DMF	dimethylformamide
DMSO	dimethyl sulfoxide
DOSY	diffusion-ordered spectroscopy
dppf	[1,1'-bis(diphenylphosphino)ferrocene]
DTF	dithiafulvalene
Equiv.	equivalent
ESI	electrospray ionization
exTTF	π-extended tetrathiafulvalene
GC	glassy carbon
HRMS	high resolution mass spectrometry
HWE	horner wadsworth reaction reaction
IR	infra-red
M	mol.l^{-1}
MALDI	matrix-assisted laser desorption/ionisation
MS	mass spectrometry
NMR	nuclear magnetic resonance
PC$_{61}$BM	phenyl-c61-butyric acid methyl ester
Pddppf	[1,1'-bis(diphenylphosphino)ferrocenepaladium (ii) triflate
Ph	phenyl
Ppm	parts per million
Py	pyridine
r_H	hydrodynamique radius
rt	room temperature
Ru1	bis(triflate (p-cymene)rhuthenium(ii))oxalato-1,4-bis(olate)
Ru2	bis(triflate(p-cymene)ruthenium(ii)) 5,8-dioxo-5,8-dihydronaphthalene-1,4-bis(olate)
Ru3	bis(chloro(p-cymene)ruthenium(ii)) 6,11-dihydroxy-6,11-dihydrotetracene-5,12-bis(olate)
Ru4	bis(triflate(p-cymene)ruthenium(ii))6,11-dihydroxy-6,11-dihydrotetracene-5,12-bis(olate)
SEC	spectroelectrochemistry
TDAE	tetrakis(dimethylamino)ethylene
Tf	triflate
TFA	trifluoroacetic acid
THF	tetrahydrofuran
TLC	thin layer chromatography
TLCV	thin layer cyclic voltammetry
TTF	tetrathiafulvalene
UV	ultraviolet
XRD	x-ray diffraction
δ	chemical shift, ppm

Introduction

The synthesis of macrocyclic structures has always focused a strong interest from the chemistry community. This fascination probably results from a combination of several reasons, among which *i)* the wide range of applications which can be envisaged from such compounds, *ii)* the synthetic challenge and *iii)* for some of them, the quest for a certain degree of aesthetic value.

Although a myriad of examples have been obtained for the last few decades, the synthesis of synthetic macrocycles using traditional covalent chemistry often constitutes a challenge and generally results in many-step procedures and low yields. The birth of the metal-driven self-assembly strategy in the early 90's led to a breakthrough in this area. First applied for obtaining macrocyclic compounds, this concept was further used to reach molecular metallocages (3D structures) in a single step and in high yields, starting from organic ligands and metal ions or complexes. Today, this approach has allowed creating a wide variety of functional molecular polygons and polyhedra.

These metallocages possess an intrinsic cavity which in principle, is able to accept a guest species (ion or molecule), giving rise to a host-guest complex. The latter complex can be designed to target various types of applications, such as catalysis and drug transport. In order to control the encapsulation and the subsequent release of the guest, different types of stimulus can be applied to monitor the host-guest binding interaction. The most commonly used are pH variation, irradiation or introduction of a competitive guest. Another approach, recently developed, consists in using a redox stimulus. Indeed, the latter (oxidation or reduction) is prone to modify the electrostatic charges of either the guest, the host, or both subunits.

We propose in this work to design, characterize and study the binding properties of new redox-active metalloreceptors, issued from the combining of specific metal complexes to electron-rich organic ligands enriched in sulfur atoms.

Chapter One is dedicated to the general principles guiding the metal-driven self-assembly processes, through specific examples of the literature. A special focus is made on redox-active self-assemblies and notably on tetrathiafulvalene-based cages.

Chapter Two is focused on a new generation of self-assembled M_8L_2 type metallacages, featuring ligands based on the tetrathiafulvalene core and *bis*-Ruthenium complexes.

Chapter Three depicts the use of a new dithiafulvalene scaffold in the preparation of redox-active self-assemblies. Two types of ligands are described and compared upon combining with different metal complexes.

Chapter Four describes the use of a π-extended tetrathiafulvalene ligand in creating new metallocages. Self-assemblies of the $M_{12}L_6$ type are depicted, as well as the first example of a redox-triggered transformation of a discrete cage into a supramolecular 3D polymer.

Chapter Five explores a new aromatic scaffold (benzo[1,2-b:4,5-b'] dithiophene) in designing an alternative π-extended electron-rich derivative. A combined experimental and theoretical study is proposed to characterize the specific structural and electronic properties of this new compound, in comparison with the previous π-extended tetrathiafulvalene.

Chapter I. Metal-directed self-assembly (literature review)

1.1. Main approaches to self-assembly

The general concept supporting the self-assembly methodology consists of combining several components, which spontaneously organize into a more complex structure, possibly under the influence of different factors. One of the main advantages of such approach lies on its ability to self-correct in the course of the process. Due to the relatively low energy of the intermolecular interactions which are involved (Table 1), the formation of the supramolecular bonds remains reversible within the reaction conditions, favoring the thermodynamic product in front of the kinetic one.

Interaction	Energy (kJ/mol)	Example
Ion-ion	100-350	Sodium chloride
Ion-dipole	50-200	Crown ether – Na^+
Dipole-dipole	5-50	Acetone
Hydrogen bond	4-120	DNA
Cation-π	5-80	K^+ in benzene
π-π	0-50	Benzene and graphite
Van der Waals	≤ 5	Alkyl chains
Hydrophobic	Depending on the solvent	Inclusion compounds in cyclodextrines, self-organization of proteins

Table 1. Non-covalent interactions in supramolecular chemistry.

Main approaches to achieve self-assembly can be divided into:

➢ non-covalent self-assembly, mostly supported by hydrogen bonds;
➢ covalent self-assembly, using reversible organic reactions;
➢ metal-driven self-assembly, using organic ligands and metal ions or complexes.

1.1.1. Non-covalent self-assembly

The first example of non-covalent self-assembly which comes to mind corresponds to the double DNA helix, based on a combination of hydrogen bonds and alternative non-covalent interactions. (figure **1.1.1**).
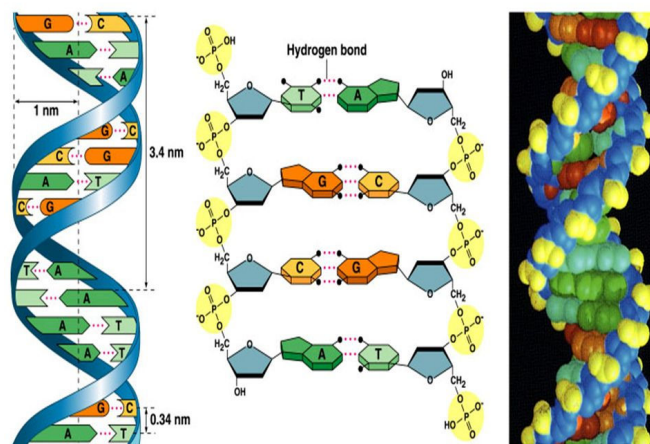
Figure 1.1.1. Self-organization of the DNA spiral using hydrogen bonds

By mimicking natural processes, a wide variety of synthetic supramolecular helicates, foldamers and other structures have been obtained.

When considering the specific case of macrocyclic receptors, three illustrative examples (among many existing in the literature) are proposed: *i)* a self-assembled capsule **1.1,**[2] based on the calixarene platform and which is capable of encapsulating small planar guests (figure **1.1.2**, a), *ii)* a capsule **1.2**[3] based on the cyclotriveratrylene core and featuring DDAA ureidopyrimidinone groups, which is able to bind large neutral guests such as fullerenes (figure **1.1.2**, b), and *iii)* a hybrid cage **1.3**[4] featuring a *bis*-Ruthenium complex which preorganizes an organic ligand involving the DDAA ureidopyrimidinone group (figure **1.1.3**).
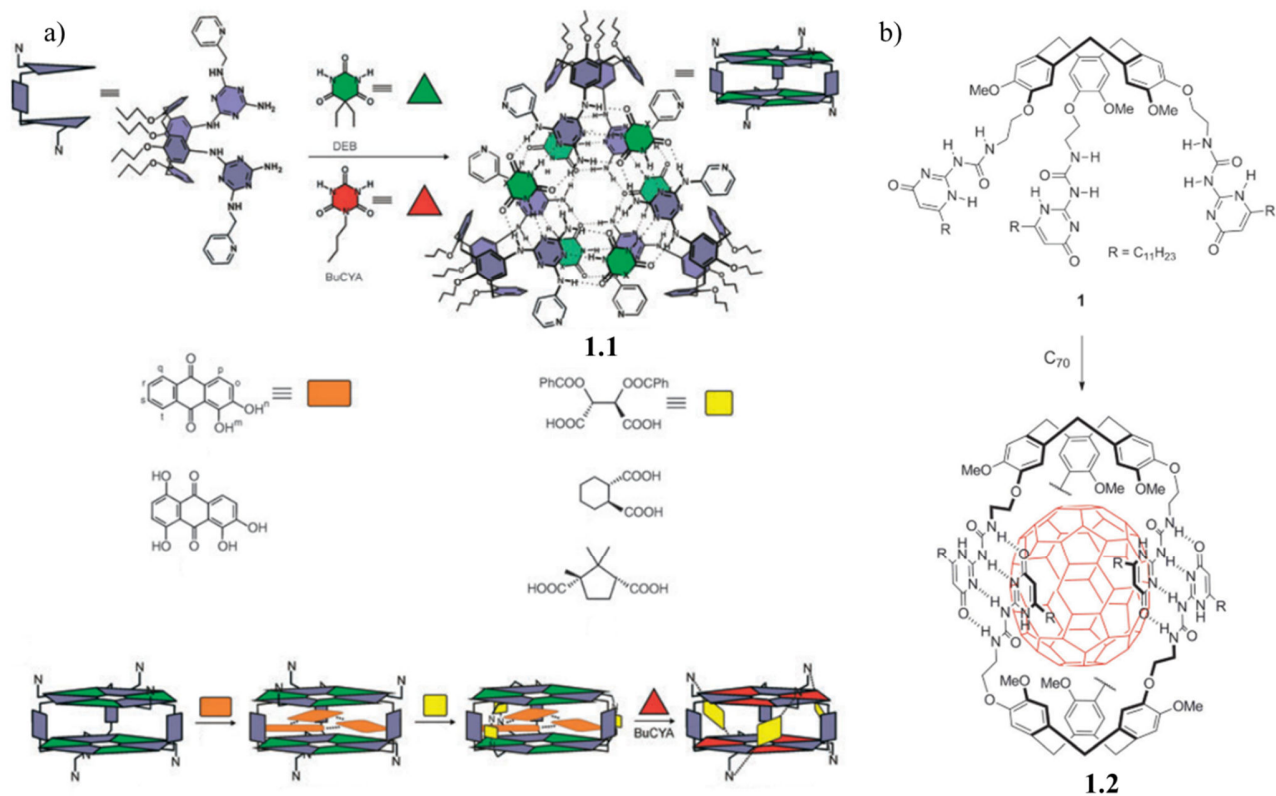
Figure 1.1.2. Self-assembled cages based on the hydrogen-bond.[2-3]

1.3
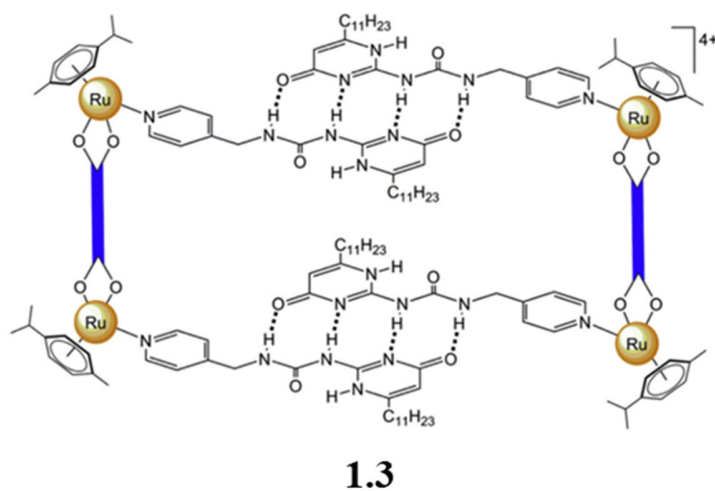
Figure 1.1.3. Self-assembly using a combination of coordination and hydrogen bonds.[4]

1.1.2. Covalent self-assembly

Another possibility to circumvent the low yields limitations often reencountered with conventional organic synthesis when synthesizing macrocyclic structures, lies on the use the dynamic covalent reactions approach[5] (figure **1.1.4**). This approach is focused on reversible covalent reactions creating a rapid equilibrium. This consecutively allows to move from kinetic to thermodynamic products.
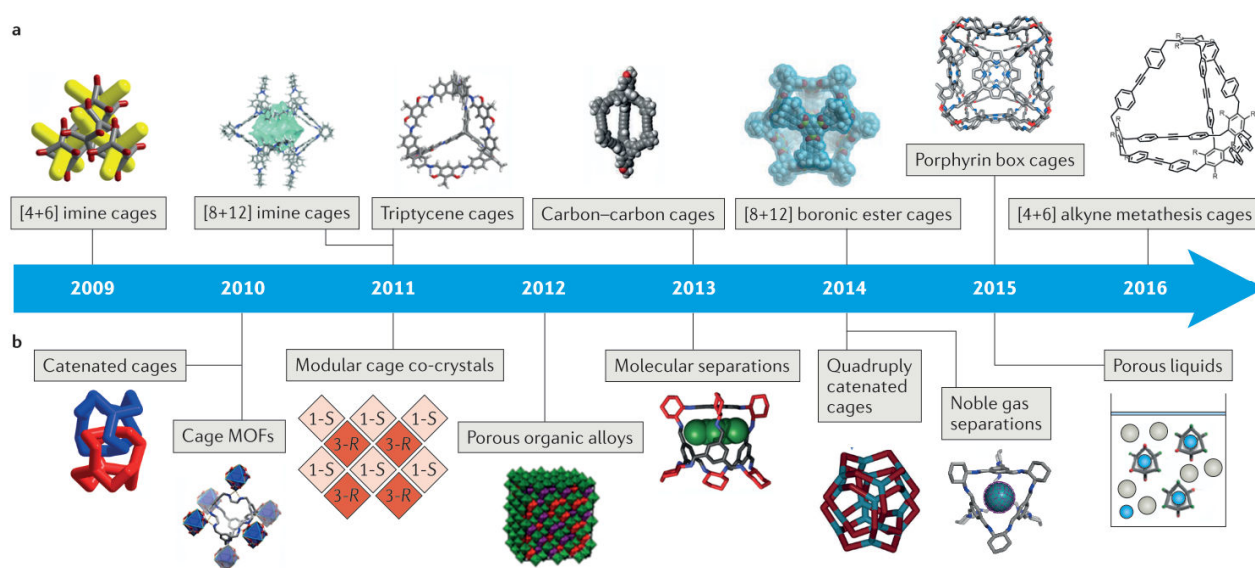
Figure 1.1.4. Timeline of different organic cages (a) and some examples of application (b).[5]

These methodology was first introduced using imine chemistry in 2009[6]. Later, other types of reactions were shown to be effective in covalent self-assembly, such as boronic esters[7], disulfide bonds[8], alkyne metathesis[5] and others[10] (figure **1.1.4**).

The reversible nature of such reactions allows dynamic error corrections, similar to hydrogen bonds methodology. Another advantage lies on the relatively high stability of the resulting structures due to the nature of the covalent bonds, especially for more recent carbon-carbon cages. Nevertheless, one limitation lies on the difficulty to design on purpose the cage structure from the starting building blocks formula.

1.2. Metal-directed self-assembly

Despite being first introduced nearly three decades ago, the metal-driven self-assembly remains a hot topic and has been the subject of many recent reviews.[9-15] It is based on the formation of a coordination bond between a metal and suitably designed organic ligands.

Starting reagents   Mixture of kinetic intermediates   Final self-assembly
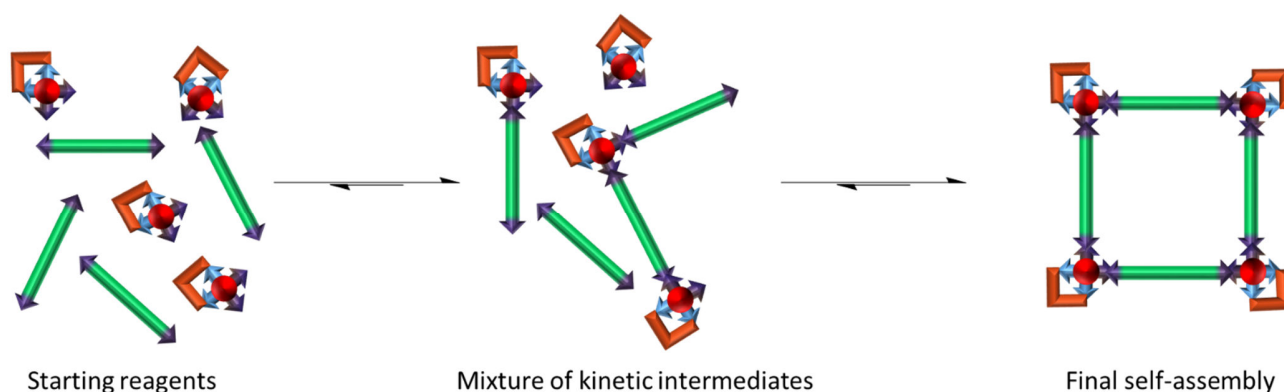
Scheme 1.2.1. Schematic representation of the self-assembly process.

One of the main advantages of this methodology in comparison to above-mentioned ones lies on the predictable nature of the coordination bond. Combining this with the appropriate geometry of organic

10

ligand allows efficient designing of the resulting metallocages. At the same time, reversibility of the coordination bond between main components allows transition from the kinetic intermediates to the thermodynamically more favorable macrocyclic 2D and 3D structures (scheme **1.2.1**). In this process entropy favors formation of the closed systems with a minimum number of components over long polymeric chains. All these factors allow obtaining metallocycles with high yields in just one step.

For the sake of prediction, the metallocycles structure is often described as high-symmetry polygons/polyhedra[16] with metal atoms in the vertices (V) and organic ligands as edges (E, edge-directed self-assembly) or faces (F, face-directed self-assembly) (figure **1.2.1**).
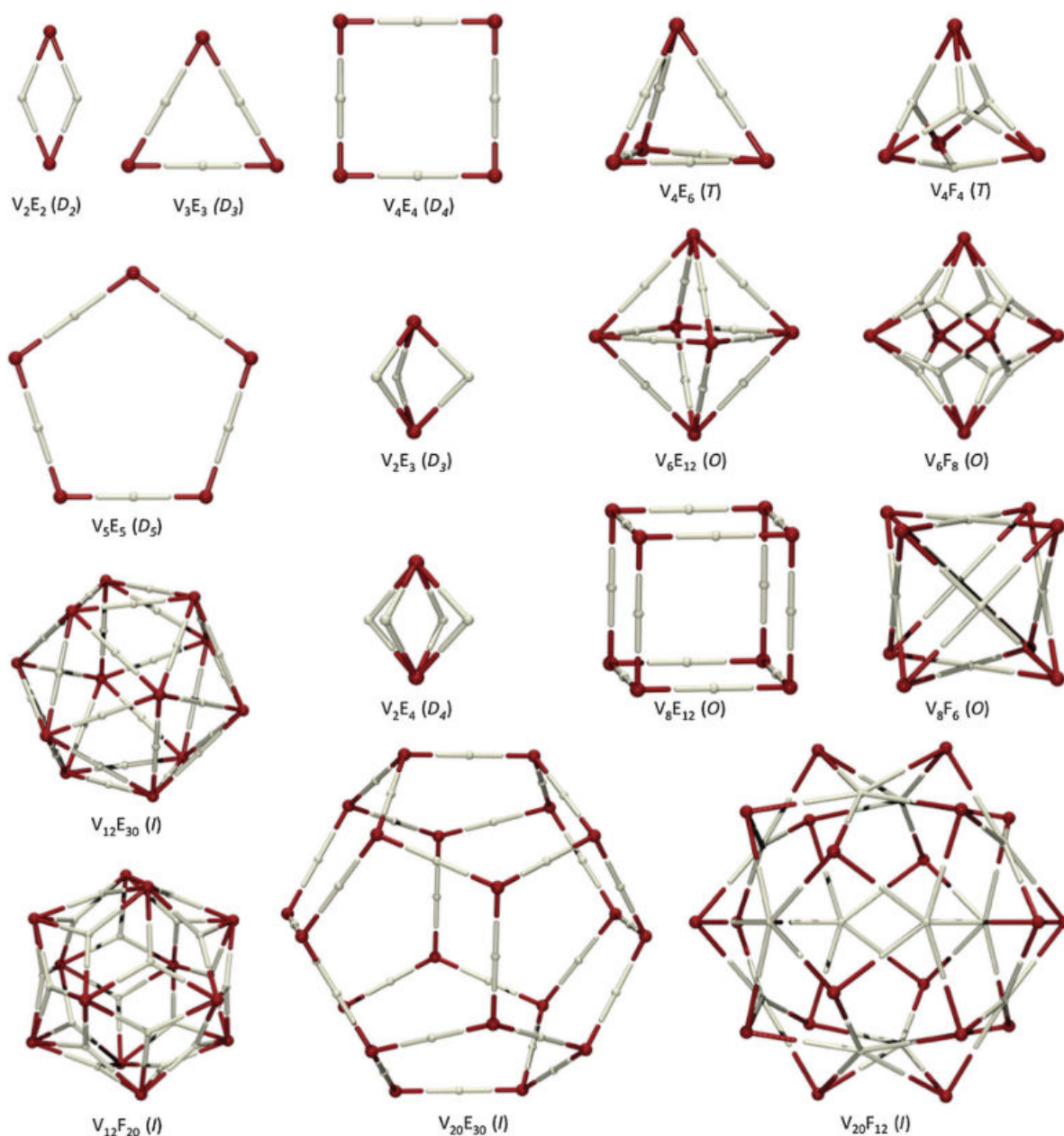

Figure 1.2.1. High-symmetry polygons and polyhedra and their projections on the self-assembly structures.[16]

11

The *directional bond approach* is well-supported by combinatory libraries for using in metal-directed self-assembly. It was first shown by the groups of Fujita[17] and Stang[18] for 2D metallocycles. There are two main requirements for this method to be used:

  ➢ Organic ligands should have a rigid geometry and appropriate bite angle,
  ➢ Starting components must be mixed in exact stoichiometric proportions.
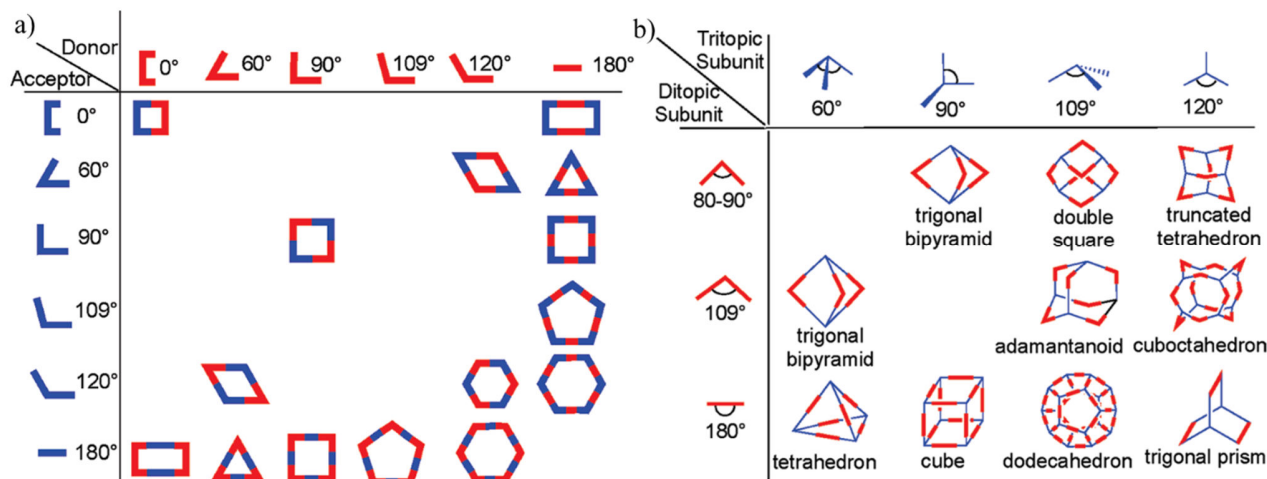

Figure 1.2.2. Combination of structural blocks for 2D (a) and 3D (b) architectures.[1]

Result of the self-assembly process is defined by the combination of geometry and stoichiometric proportions[1] (figure **1.2.2**). Creation of the 2D monocyclic assemblies requires subunits having symmetry axes no higher than a 2-fold axis, resulting in the corresponding polygons (figure **1.2.2**, a). So, for instance, molecular rectangles can be created using combination of two 0° donor units with 180° acceptor units or vice versa. Molecular triangles can be designed by combining three 180° acceptors with three 60° donors.

3D self-assembly (*i.e.* polyhedra (figure **1.2.2**, b)) requires symmetry axes higher than a 2-fold axis and more than 2 binding sites. For instance, a trigonal bipyramid can be designed in few ways: either by combining two tritopic units with orthogonal binding sites, by using three 80-90° ditopic components or by mixing two tridentate 60° units with three ditopic 90° units.

One of the main limitations for this methodology is the assumption that angular components keep their geometry along the self-assembly process. Actually, these angles do change, but due to relatively low energy of coordination bond, the shape of the resulting self-assembled structure usually remains close to prediction. Notably, in the case of long and/or flexible ligands, a mixture of several self-assembled products can be observed, limiting the use of this approach to the case of rigid molecules.

1.2.2. Design using the *symmetry interaction approach*

The *symmetry interaction approach* is mostly used for construction based on "naked" metal ions (devoid of any coligand). The outcome of the assembly is determined by the inherent symmetry of the coordination sites on the metal ion, in combination with the chelating mode of the ligand. Similarly to the directional bonding approach, this methodology requires ligands with relatively rigid structures in order to avoid formation of several products or oligomers.

The main terms, such as *coordinate vector* and *chelate plate*, and first application of the symmetry interaction approach were demonstrated by the group of Raymond.[19-20] The *coordinate vector* describes the bond between the metal and the ligand. For the ligands, *the chelating plane* is placed orthogonal to the main symmetry axis of the metal complex and holds chelate vectors of the ligand (figure **1.2.3**, a). Further combination of orientation of chelating planes with corresponding coordinate vectors allows prediction of the resulting high-symmetry coordinate structures.

For example, a triple M_2L_3 helicate has a D_{3h} symmetry and can be designed by combining orthogonal components with C_2 and C_3 axes. The C_3 component is in this case a metal center with parallel chelate planes (figure **1.3.3**, b). In similar fashion M_4L_6 tetrahedron can be obtained from four metal ions in the vertices and six corresponding ligands. Therefore, C_2 axes of the tetrahedron lie inside chelate planes of the metals, while coordinate vectors must maintain $70.6°$. Another way to get tetrahedron is to use a M_4L_4 stoichiometry, which requires that both ligand and metal have a C_3 symmetry.
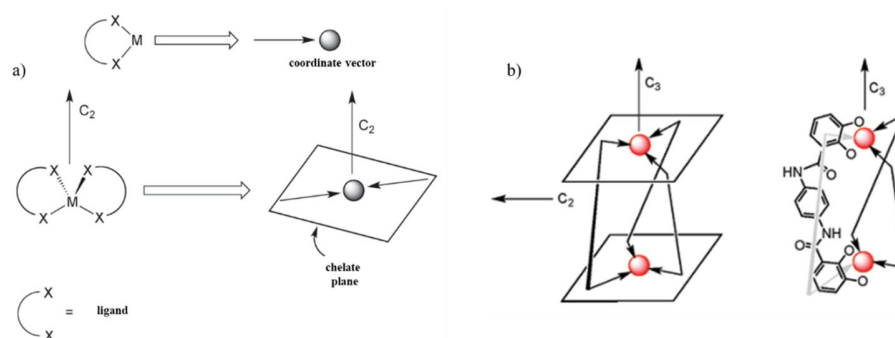
Figure 1.2.3. Main elements of the symmetry interaction approach (a) and chosen examples (b).[1]

Another example of this methodology in application to the heterometallic self-assembly was demonstrated using a stepwise process[21]. First was obtained precursor **1.4**, containing Fe, which upon further reaction with either cis-blocked C_2 Pd complex or naked C_4 Pd ion, results in formation of a trigonal bipyramide **1.5** or a cube **1.6** respectively (figure **1.2.4**)
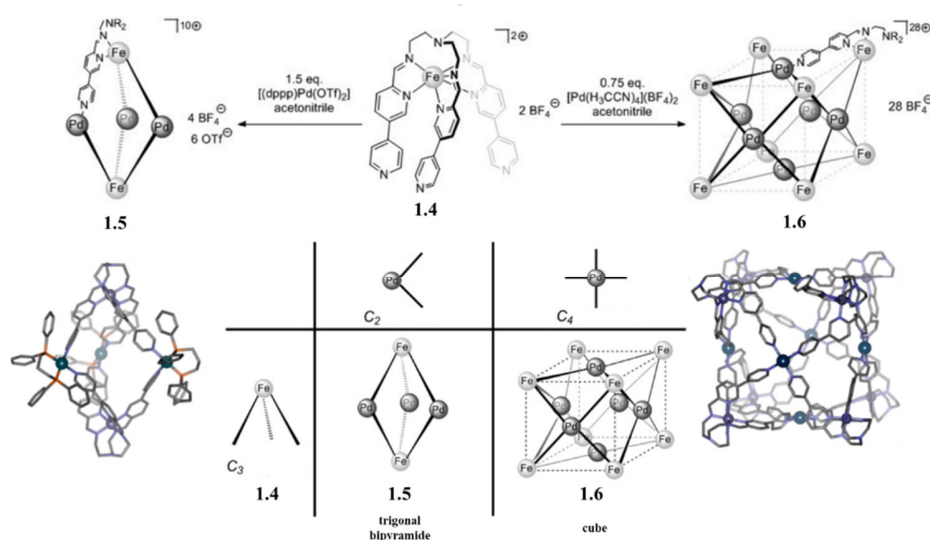
Figure 1.2.4. Heterometallic self-assembly based on the symmetry interaction approach.[21]

13

1.2.3. Design using the *paneling approach*

The *paneling approach* can be illustrated by the pioneering works of the group of Fujita, while creating a variety of coordination polyhedra[22-23]. This is an example of a face-directed self-assembly process (contrary to the above-mentioned directional bond and symmetry interaction which are edge-directed methodologies). This means that ligands do not constitute the edges, but the faces of the polyhedra with metal atoms in the vertices. For instance, combination of triangular panels can result in a tetrahedron or an octahedron (figure **1.2.5**). In a similar way, square panels may lead to a cube or a prism.
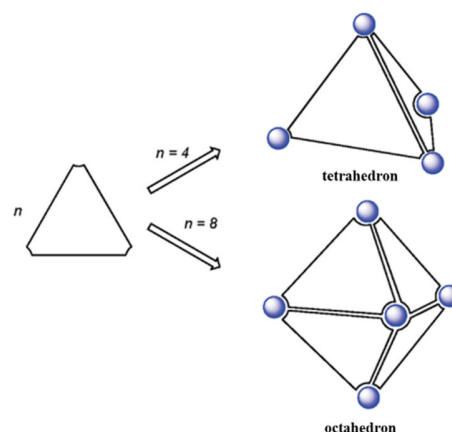
Figure 1.2.5. Tetrahedron and octahedron using the paneling approach.[1]

Therefore, this approach requires ligand that gets a rigid planar geometry with coordination sites located on its edges and within the plane of the ligand. As vertices mostly *cis*-blocked metal complexes are used for the sake of geometry. This allows efficient self-assembly process without oligomeric by-products.

For example, using a triangular ligand with a D_{3h} symmetry leads to the truncated tetrahedron M_6L_4 (figure **1.2.6**, a), while changing the direction of the bonding groups leads to a square pyramidal cone. Square panels with D_{4h} symmetry can lead to either trigonal[24] or hexagonal[25] prisms depending on the orientation of binding groups (figure **1.2.6**, b).
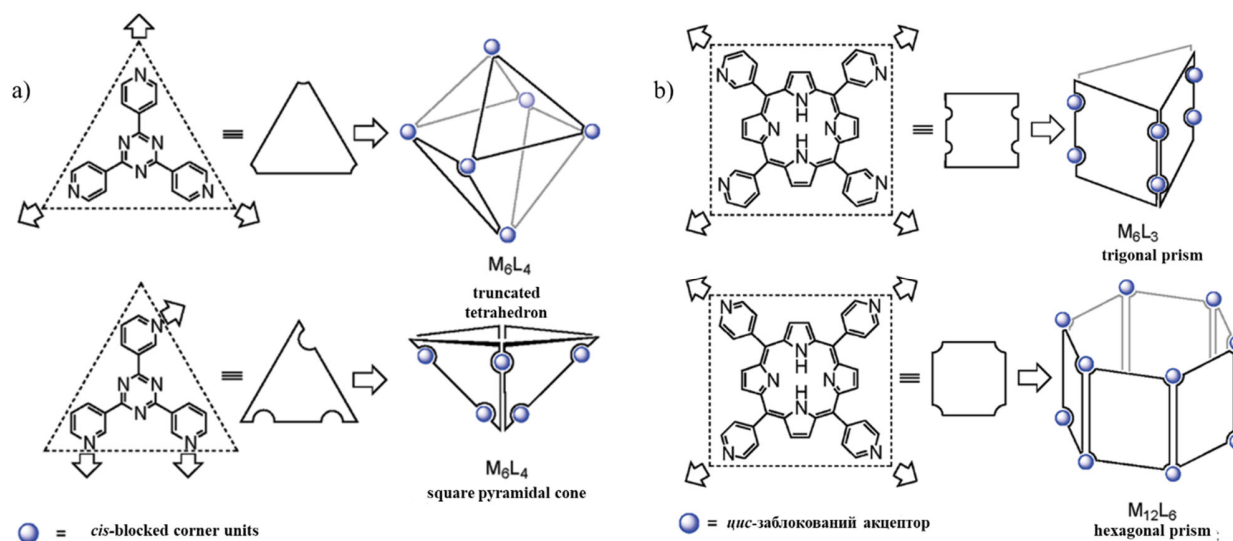
Figure 1.2.6. Design of coordination cages using triangle (a) and square (b) panels.[1]

One of the main advantages of this approach lies on the formation of cages with large internal cavities. This process often requires the use of a template molecule during the assembly process.

1.2.4. *Weak ligand approach*

The *weak ligand approach* was first described by the group of Mirkin[26-28] and relies on flexible hemilabile ligands. Such ligands require a coordination with the metal atom in a bidentate mode with one binding site weaker than the other. After the initial formation of the kinetic product ("closed form" (figure

1.3.7, a)), addition of the stronger ligand L leads to the final metallocycles in its "open form". Therefore, in this methodology the ligand must possess a conformational flexibility allowing to switch from the closed to the open form. This is opposite to the demand for rigid ligands in most approaches and allows to widen the potential range of suitable ligands. Another advantage comes from the ancillary ligand L, which can be switched later without impacting the structure, which can be useful both for application in catalysis or for accessing to more complex structures.
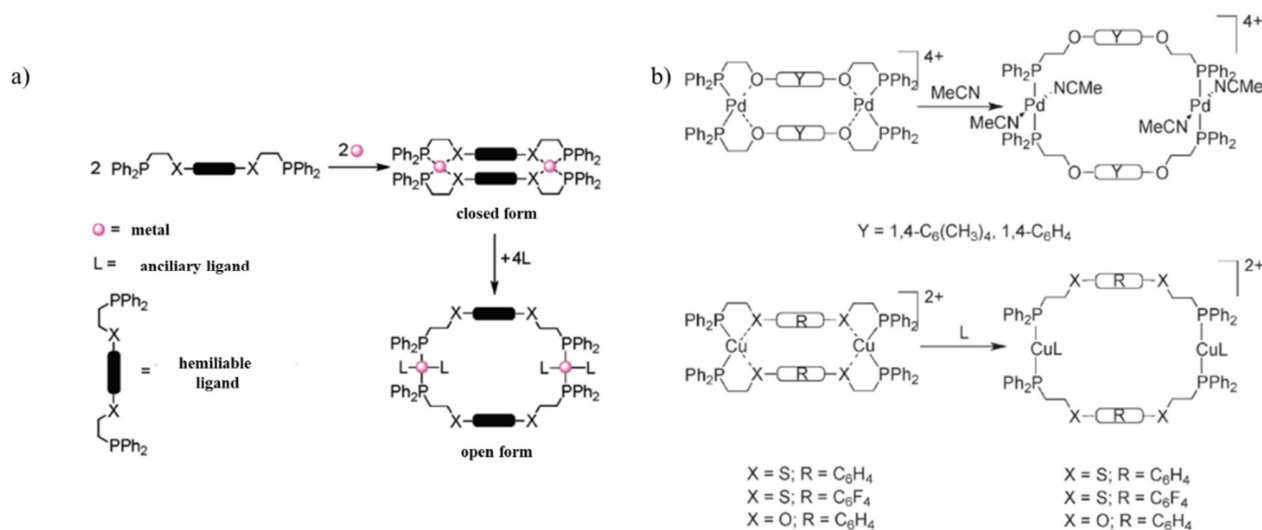
Figure 1.2.7. Mechanism of the weak ligand approach (a) and examples of 2D metallocycles (b).[1]

1.3. Main types of coordination-driven assemblies depending on the metal part

Coordination-driven self-assembly methodology can afford a wide variety of metals. Within this PhD work, we have focused our attention onto square-planar Palladium and Platinum acceptors (both used either as "naked ions" or as *cis-* / *trans*-blocked complexes), as well as on *bis*-Ruthenium acceptors. Besides having compatible geometry, these metals allow using the NMR techniques, which greatly facilitates both the monitoring of the self-assembly process as well as further characterization related to the resulting cages.

1.3.1. Using *cis*-blocked metal complexes

In general, *cis*-blocked acceptors are constituted of square-planar complexes (either charged or neutral) with two over four coordination sites in the *cis* orientation occupied with strong organic ligands (usually with bidentate ligands, but not necessary). The remaining two sites are occupied by good leaving groups, such as nitrate or triflate in the case of charged complexes, and by 1,5-cyclooctadien in the case of neutral ones. As a result, these complexes constitute very useful 90° building blocks, which can be efficiently used to reach 2D or 3D self-assemblies. Figure **1.3.1** summarizes some of the most common cis-blocked acceptor units, while some more exotic ones can also be found in literature.[29]

Figure 1.3.1. Structures of common cis-blocked acceptor units.

According to figure **1.3.2**, the appropriate donor units (ligands) for the formation of metallocycles should be ditopic and have $90°$ or $180°$ angles. As a result, the most common motives consist of molecular triangles[30] and squares[31-32] (figure **1.3.2**).

Figure 1.3.2. Self-assembled molecular triangles (a) and squares (b, c).[30-32]

As mentioned before, less rigid ligands may sometimes cause the deformation of the binding angles. As a result, an equilibrium between formation of triangles and squares can be observed[33-35] (figure **1.3.3**).

Figure 1.3.3. Triangle-square equilibrium.[35]

Using tritopic ligands leads to 3D metallocages. For example, Fujita and coworkers obtained a face-directed assembly starting from a planar tritopic ligand with 60^0 angle in combination with a *cis*-blocked Palladium (figure **1.3.4**, a). This cage was efficiently used for instance for catalyzing

cycloaddition reactions between two confined partners[36]. A similar cage can be obtained by combining linear ditopic and angular tritopic ligands[37] (figure **1.3.4**, b). This cage was shown to be able to encapsulate two TTF molecules and to allow their further oxidation into mixed valence species.
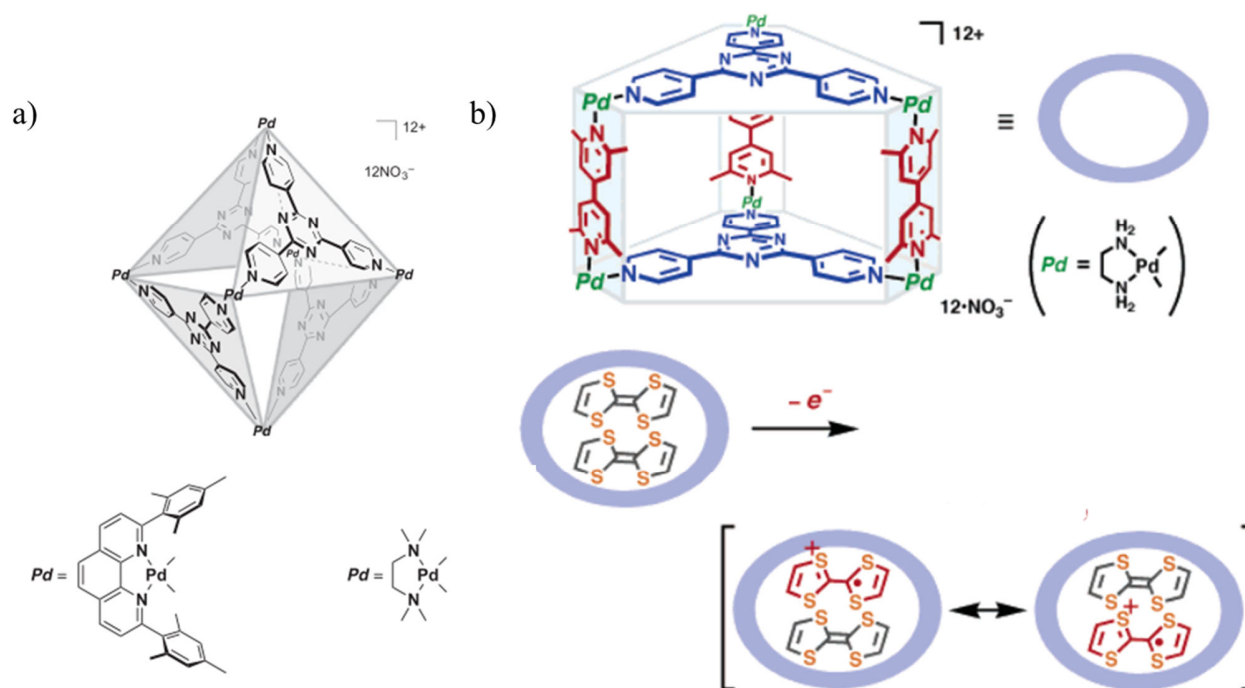

Figure 1.3.4. Examples of self-assembled metallocages using cis-blocked acceptors.[36-37]

1.3.2. Using *trans*-blocked metal complexes

Trans-blocked acceptors are isomeric to the above-mentioned cis-blocked units (figure **1.3.5**, a). As such they are used as $180°$ linear building block. Most commonly used blocking ligands consist of phosphine ligands with either alkyl or aryl substituents. Aliphatic ligands are often preferable, as they don`t have corresponding ^{1}H NMR signals in the aromatic region, where signals of the ligand are usually located.

According to figure **1.2.2**, linear *trans*-blocked acceptors can be combined with a large variety of ligands, but the most used are linear $0°$ ligands, resulting in 2D squares[38-39] (figure **1.3.5**, b, c), and tritopic ligands, resulting in 3D cages[40] (figure **1.3.5**, d). Another cage using the chiral ligand based on the oxocalix[3]arene with *trans*-blocked Palladium allows for the recognition of chiral molecules[41] (figure **1.3.5**, e).
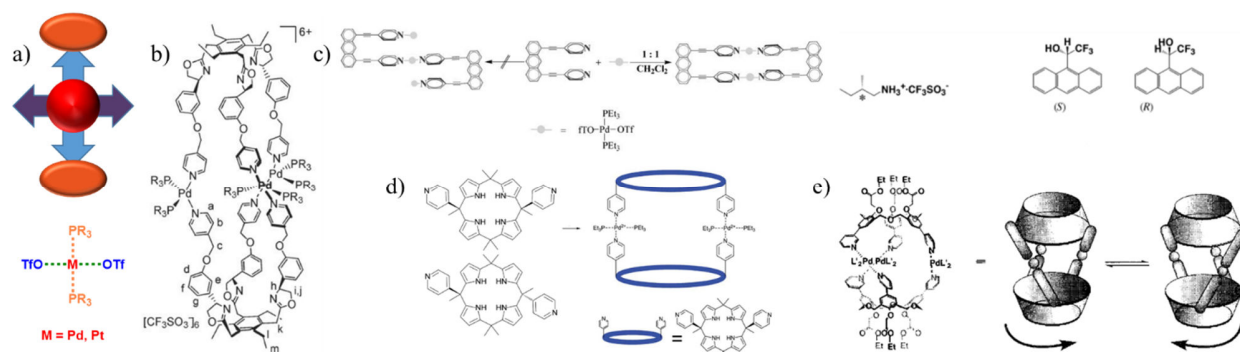
Figure 1.3.5. General structure (a) and examples of application (b, c, d, e) of the trans-blocked acceptor units. [38-41]

1.3.3. Using *"naked"* metal ions

Square-planar metals with the four coordination sites free or with good leaving groups can in principle be used as tetracoordinated building blocks for coordination-driven self-assembly. They are usually used in a form of metal salts, such as triflates, nitrates or tetrafluoroborates. Further possible structure depending on the ligand is summarized in figure **1.3.6**[9].
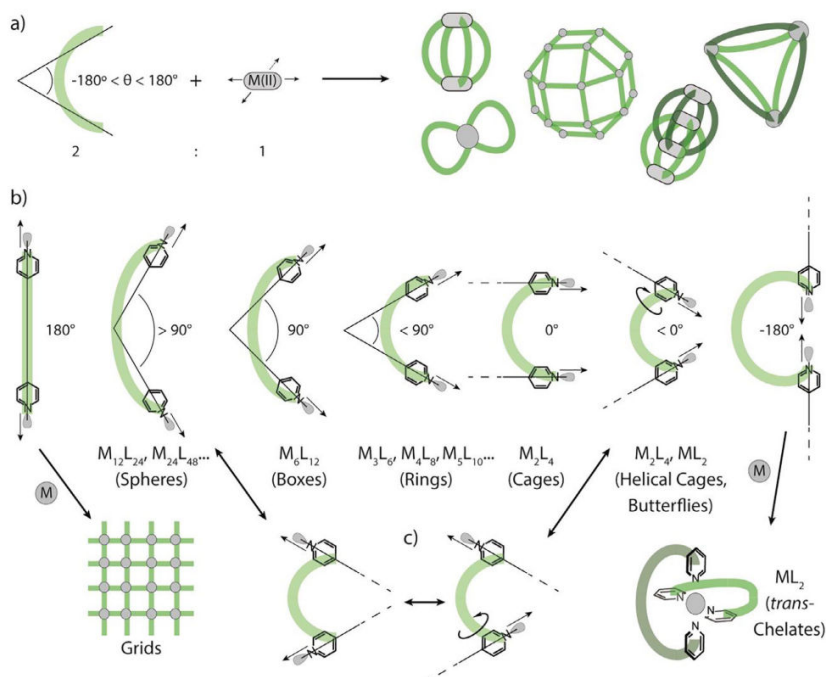
Figure 1.3.6. Possible structures using "naked ions" in combination with various types of ligands. [9]

One of the most common self-assembly architecture based on naked ions corresponds to a M_2L_4 stoichiometry. Clever and co-workers have shown the flexibility of related cages by introducing different additional groups pointing inside the cavity[42] (figure **1.3.7**, a). This allows to tailor guest molecules, which fit inside the cavity. Cages can also be modified on the outer part, for example by introducing carboxyl group with subsequent reactions[43] (figure **1.3.7**, b).

Figure 1.3.7. Examples of inner (a) and outer (b) modification of M_2L_4 cages.[42-43]

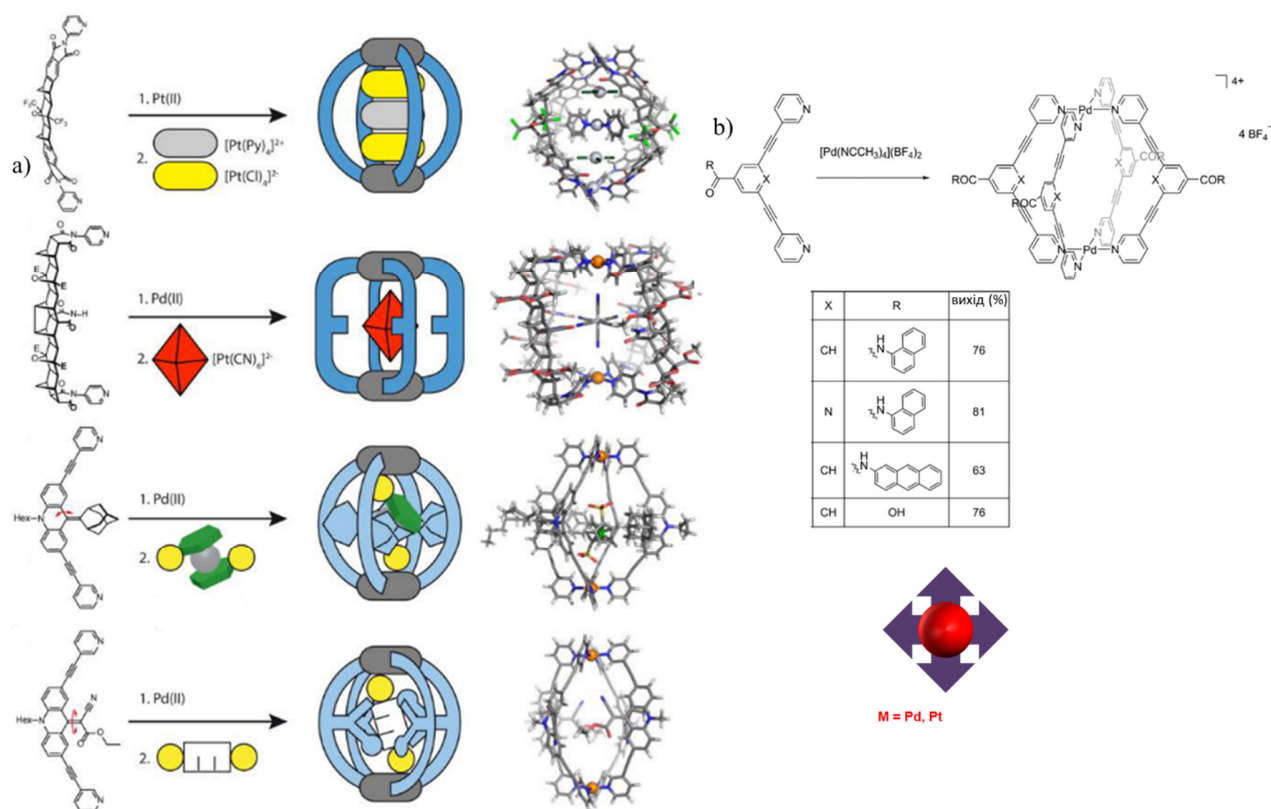As seen from figure **1.3.6**, though common, the M_2L_4 stoichiometry is not the only option. In some cases, one can observe formation of the bigger cages, such as M_4L_8[44], within the same stoichiometry of the starting components (figure **1.3.8**). Also one can trigger rearrangement of the smaller cage M_3L_6 into the bigger (up to M_7L_{14}) using template molecule or ion [45] (figure **1.3.8**, b). Another possibility to fit larger molecule that the cage would not normally allow is to lose some of its components[46]. In this example the cage loses one of its three metal centers (yellow sphere) in order to create additional space between the ligands (green) inside the self-assembly for two guest molecules (pink sphere) (figure **1.3.8**, c).
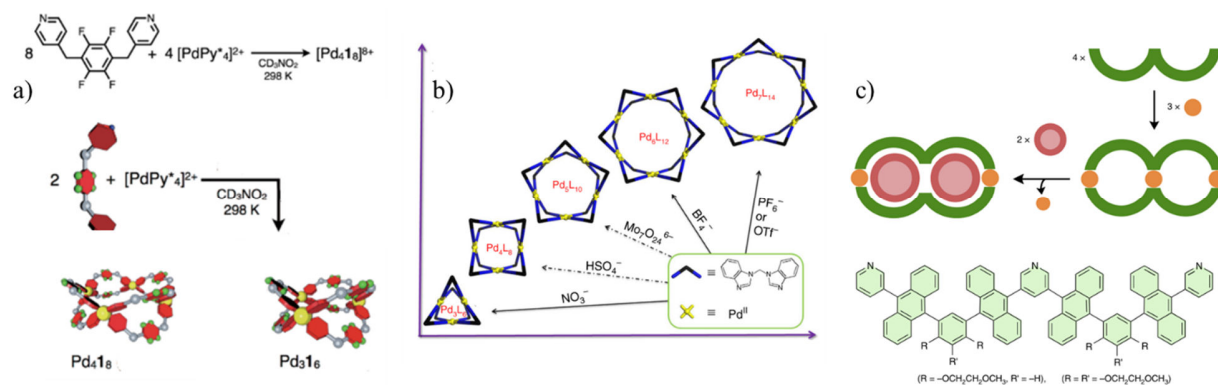
Figure 1.3.8. Adaptive self-assembled cages based on the "naked" square-planar ions.[44-46]

Fujita and coworkers have used this strategy to reach remarkably large size cages, from M_6L_{12} to $M_{30}L_{60}$, depending on the angle in the ditopic ligand[47] (figure **1.3.9**)
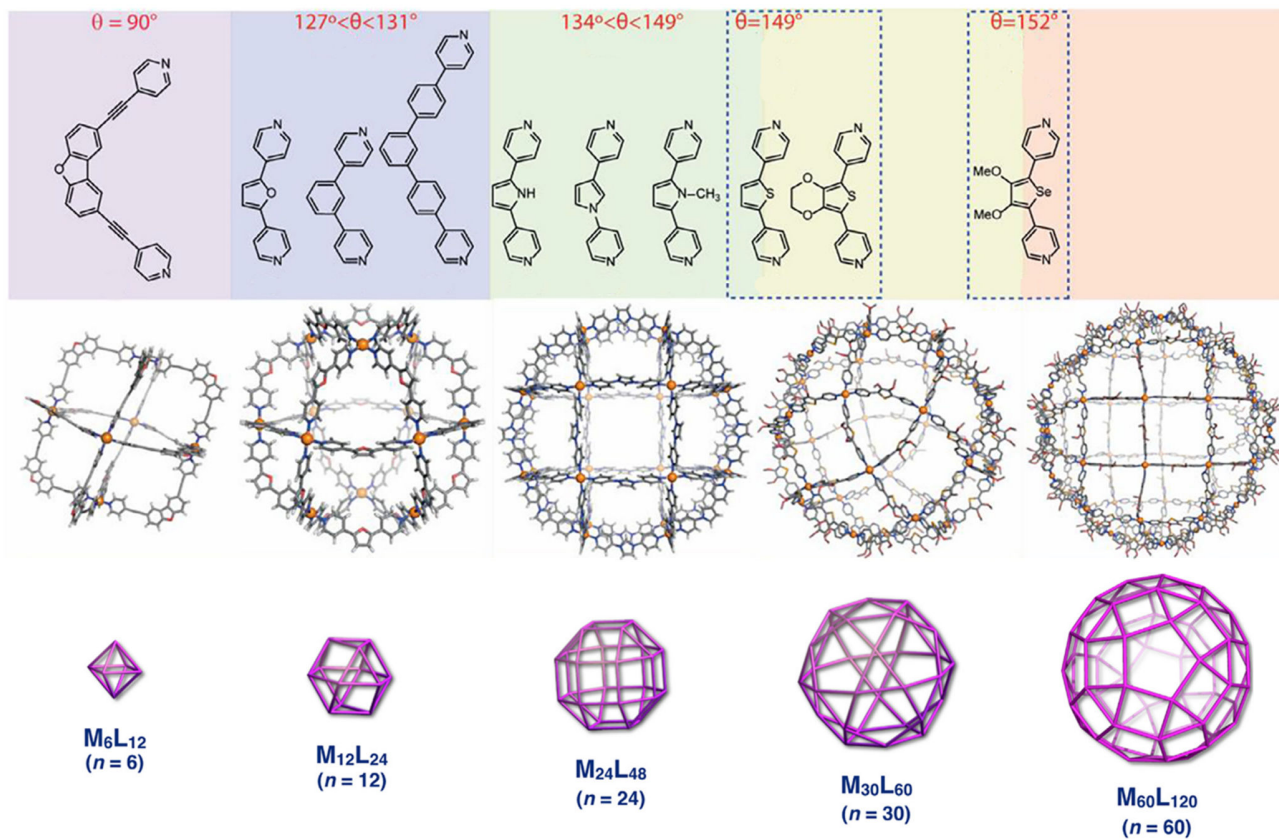
Figure 1.3.9. Large cages of the M_nL_{2n} type.[48]

A series of such $M_{12}L_{24}$ cages were also modified by using functionalized related ditopic ligands allowing chemical modification of the corresponding cavity space [49] (figure **1.3.10**).
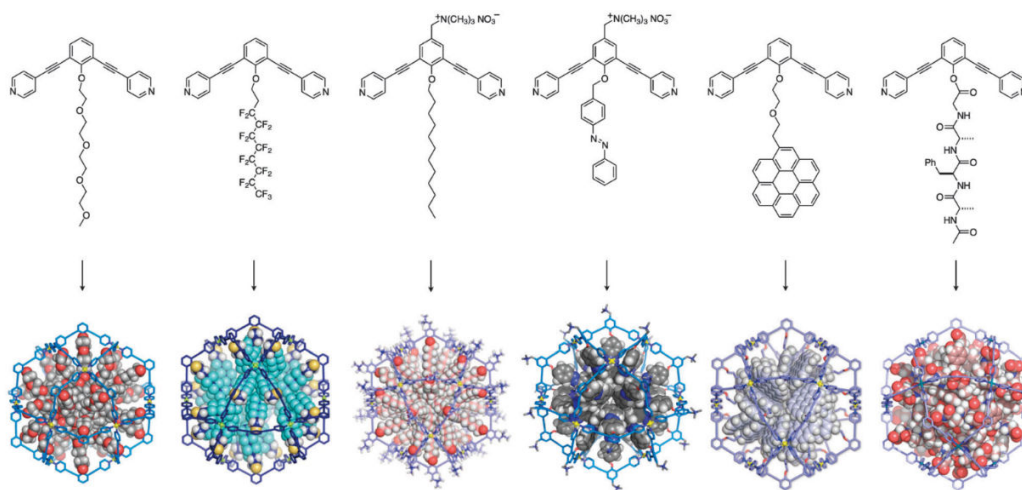
Figure 1.3.10. Functionalized $M_{12}L_{24}$ cages.[49]

1.3.4. Using *bis*-metal complexes

Another possibility consists in using two bridged metal centers. This can be reached either by direct metal-metal bond[50] (figure **1.3.11**) or, more commonly, by introducing a bridging organic ligand between both metal atoms.
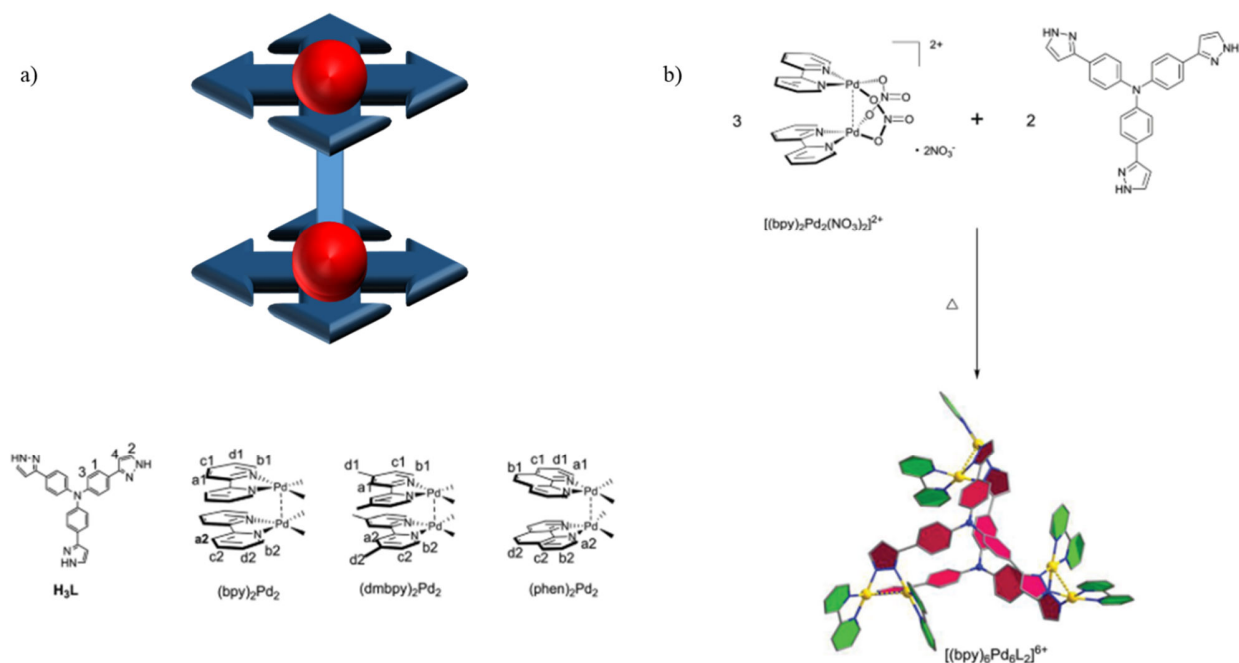

Figure 1.3.11. Some bis-Palladium acceptors (a) and example of self-assembly (b).[51]

The second category is much more common and is usually based on Platinum or Ruthenium (also sometimes Iridium or Rhodium[52]). *Bis*-Ruthenium acceptors consist of two Ru metal atoms associated to a bridging dihydroxy-dione conjugated fragment whose size can be varied (figure **1.3.12**). They are best used with linear ligands to create both 2D and 3D sandwich architectures.[53-54]
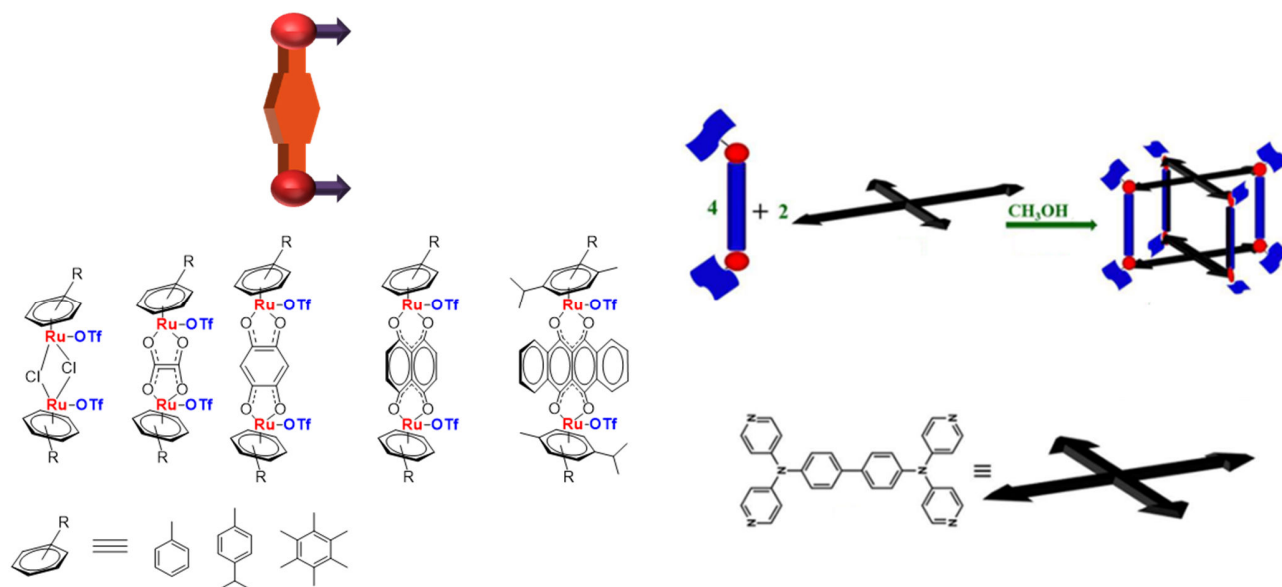
Figure 1.3.12. Common bis-Ruthenium acceptors and examples of self-assembly.[54]

Another type of bimetallic can be obtained by connecting several atoms of Platinum to organic ligand. In this acceptor units, platinum atoms are covalently bonded to an organic block, leaving free the second bonding site. Depending on the organic unit both 2D[55] and 3D[56-57] architectures can be obtained (figure **1.3.13**)
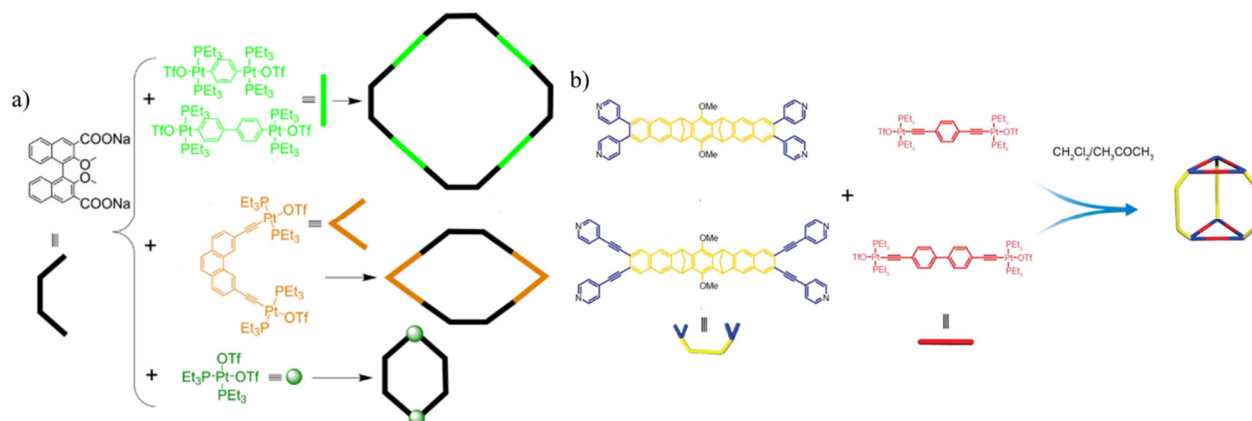
Figure 1.3.13. Examples of self-assembly using bis-Platinum complexes.[55-56]

1.3.5. Heteroleptic self-assembly

Interestingly, the self-assembled cages can be formed using several organic ligands. Two situations can be encountered: a narcissistic self-sorting or a social self-sorting (figure **1.3.14**). In the first case, two ligands separately bind with metals, resulting in several cages. In contrast, social self-sorting allows incorporating of several ligands into one cage. These processes can be illustrated in both covalent[58] and coordination-driven[59] self-assembly cages.
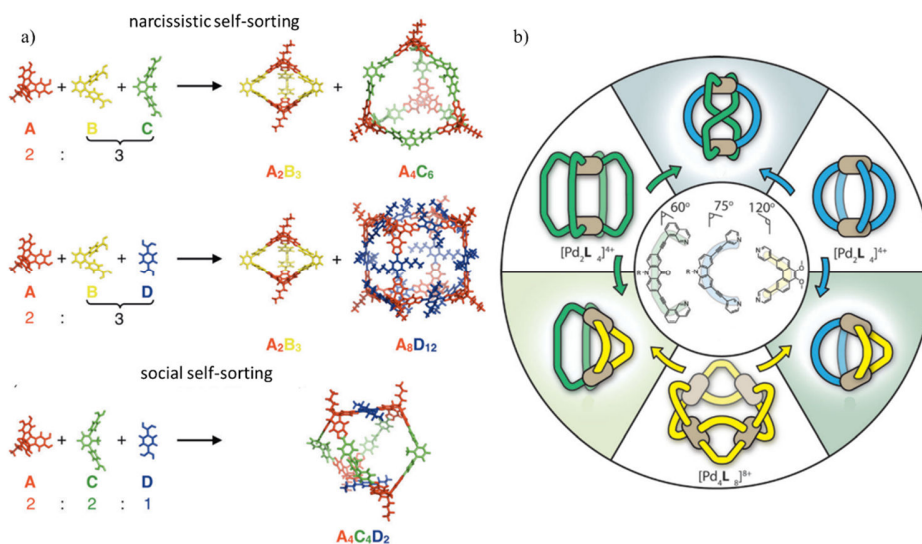
Figure 1.3.14. Examples of different self-sorting for covalent (a) and coordination (b) self-assembly.[58-59]

An interesting example of rational design for social self-assembly was demonstrated by Clever and co-workers[60] through the design of a *cis*-[PdL$_1^2$L$_2^2$] cage. Using ligands with different steric constraints (pointing toward and outside the cage cavity, respectively), results in formation of homoleptic

metallocycles in the case of a narcissistic self-assembly, and to a heteroleptic cage involving both ligands in the case of a social self-assembly (figure **1.3.15**).

Figure 1.3.15. Rational design of a social cage leads to the formation of either mixture of homoleptic cages (left) or heteroleptic cis-*[PdL₁²L₂²] cage (right).*[60]
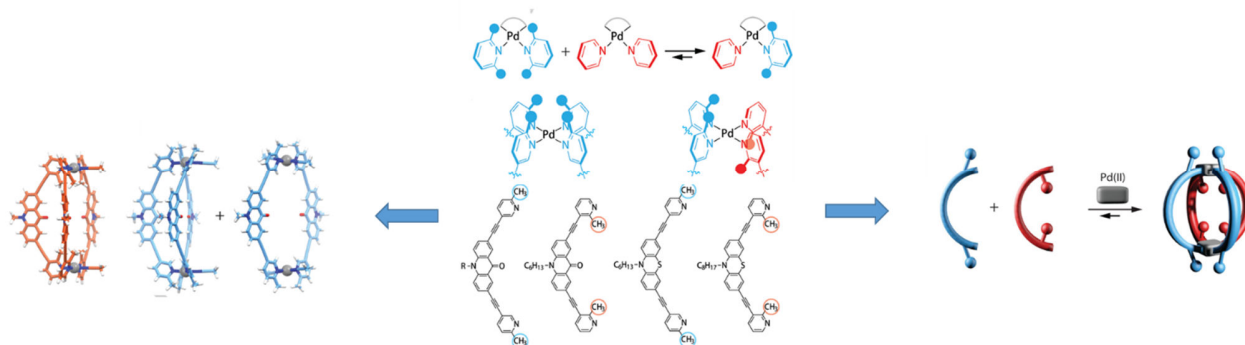
1.3.6. Interlocked self-assembly

Further progress in the coordination-driven self-assembled cages results in obtaining interlocked architectures. These motifs are interesting both for fundamental research[61] and for application in molecular machines and catalysis.[62-64] The formation of such interlocked self-assemblies is always competitive with preparation of linear products. To favor closed structures, metals can be added both as a template[65-68] (which can be removed later) or as a part of the structure (which is discussed here).

For example, Kuroda and coworkers[69-70] showed formation of a catenane using a nitrate anion from the Palladium salt as a template. It should be noted, that changing the anion triggers reversion to the simple cage (figure **1.3.16**, a). Similar work was showed by Clever and coworkers[71] with formation of a catenane from a simple cage upon addition of the halide anion. Interestingly, further addition of halide anion leads to an infinite catenane (figure **1.3.16**, b).
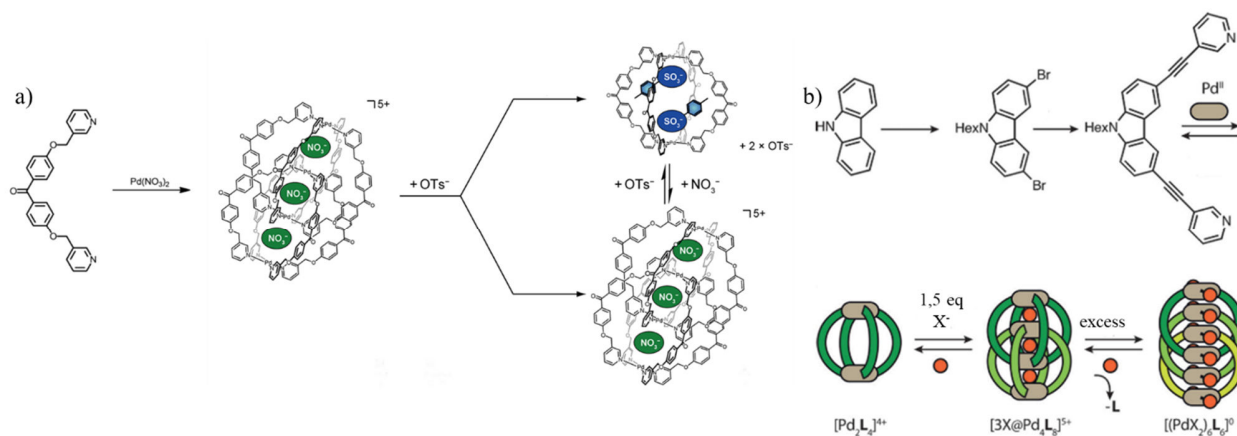
Figure 1.3.16. Interlocked self-assemblies using Palladium complexes.[70-71].

Bis-ruthenium (more rarely Iridium and Rhodium) complexes are also widely employed in preparation of interlocked self-assemblies. The possibility of adjusting their size by changing the linker fragment helps to tailor them for the self-assembly process (see § 1.3.4). For example, Chi and coworkers[72] demonstrated the formation of [2]catenanes using complexes of various size (figure **1.3.17**, a). Solvent and concentration also play a substantial role in such systems. Dilution causes formation of a

monomer, as well as changing the solvent from methanol to nitromethane. The same group also showed formation of a Solomon knot using more rigid bent ligand[73] (figure **1.3.17**, b).
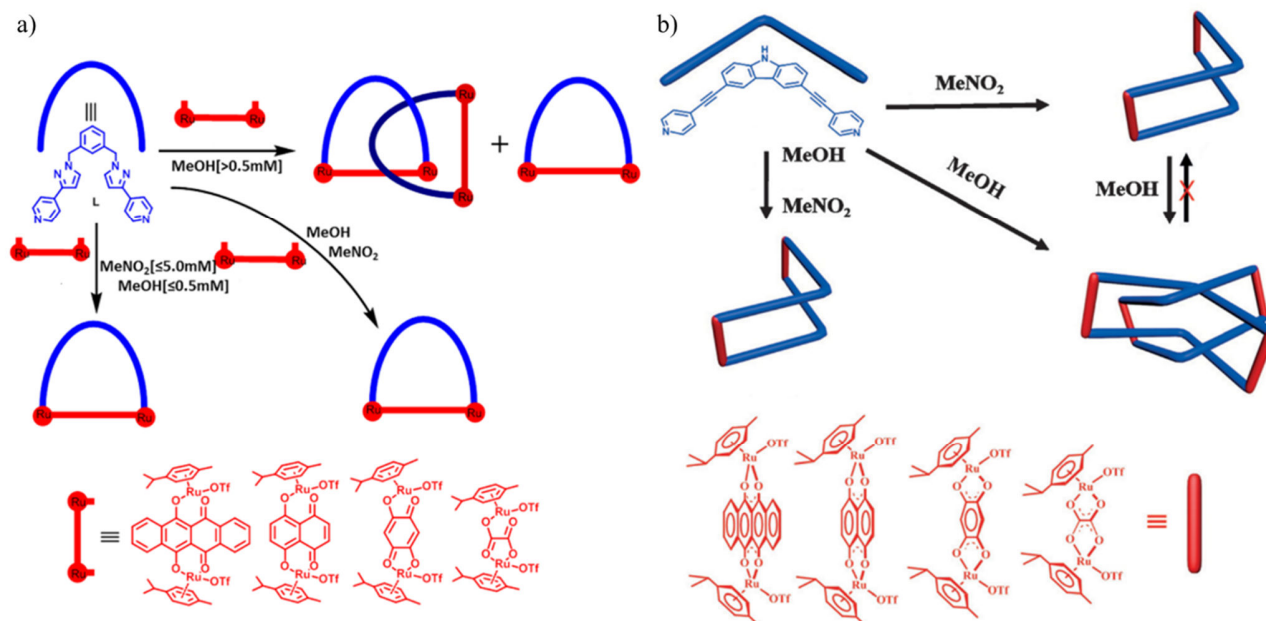
Figure 1.3.17. Interlocked self-assemblies using bis-Ruthenium complexes. [72-73]

1.4. Properties and examples of applications of self-assembled cages

Main areas of application for the self-assembled cages are determined by their intrinsic cavity. Thus, 3D cages are mostly used for the recognition and encapsulation of anions[74], organic[75] and inorganic[76] molecules and gases[77]. It should be noted that a well-defined cavity isn`t always necessary, as shown by some 2D architectures[32]. Considering host-guest properties, a special interest concerns the control over the encapsulation process[10, 78-79] (figure **1.4.1**). This can be achieved either by changing the properties of the cage (upon changing its structure or through its partial or complete dissociation) or of the guest. The most commonly used stimuli to promote those changes are controlled pH[80] or irradiation.[81] It should be noted, that optical properties of the cage (beside releasing the host[82-83]) could be also used to either stabilize photosensitive molecules[84] or for photosensibilisation[85].

Figure 1.4.1. Different ways to control host-guest chemistry. a) general principle; b) pH c) irradiation d) redox stimuli.[10]

Coordination cages can also be used for drug delivery.[86] Encapsulated biologically active molecules could be protected from the physiological conditions without changing its structure. For example, the anti-cancer *cis*-Platine d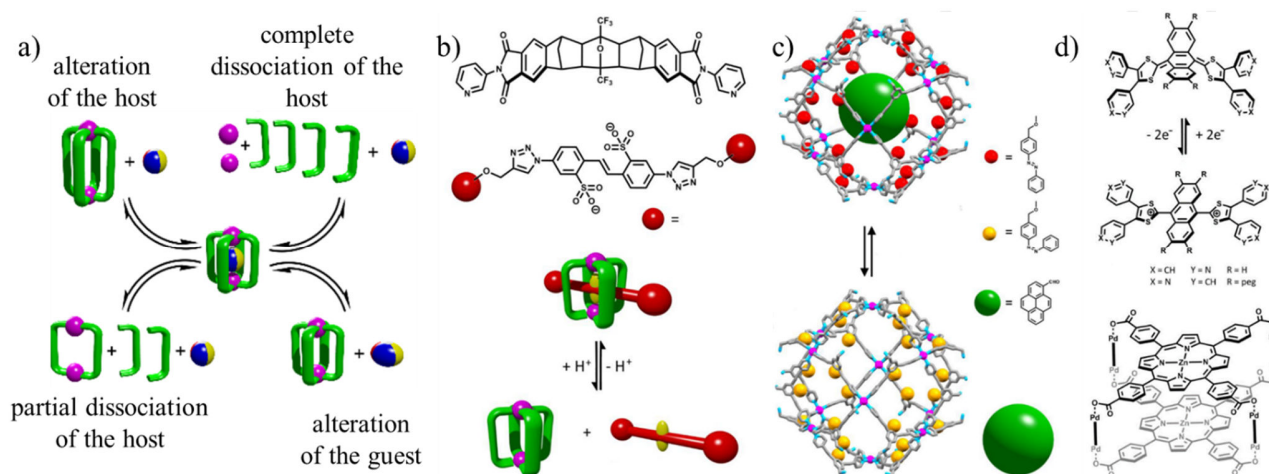rug was encapsulate by a Palladium M_2L_4 cage.[87-88] At the same time, the cage could be modified by specific proteins to increase selectivity of the delivery[89]. Moreover, some self-assembled structures can be used as a biologically active compounds. For example, *bis*-Ruthenium complexes,[90] their corresponding metallocycles[91-93] and metallocages[94] have anti-cancer activity. Similar results were shown for cages based on Palladium[95-96] and Platinum.[95, 97]

Finally, another application of self-assembled cages concerns catalysis. Depending on the structure, the catalyst can be part of the cage or an encapsulated molecule[98-99]. This allows to increase the selectivity towards both the substrate[100-102] and the product[103-104]. In some cases, self-assembly cages could be used to perform tandem reactions in one-pot synthesizes using several catalysts[105-106].

1.5. Electro-active metal-driven self-assemblies

As previously mentioned, a redox stimulus can be used to tune the host-guest properties of electroactive self-assembled cages[107]. Various situations can be encountered depending on the location of the electroactive unit. The latter can be the organic ligand (naked or appended with a redox-active unit), the metal or even a co-ligand on the metal. Moreover, through-space or through-bond interactions between the different components can potentially occur. Several selected illustrative examples are provided below.

1.5.1. Using electron-deficient ligands

Most coordination-driven self-assembled architectures feature electron-poor systems, which is partially caused by the nature of coordination bond. One of the first examples, described by Fujita and colleagues, used triazine panels (2,4,6-tris(4pyridyl)-1,3,5-triazine) and square-planar Pd(II) or Pt(II) as metal corners (figure **1.5.1**). The redox behavior of the cage was investigated by cyclic voltammetry (CV)[108], which showed a reversible redox wave corresponding to a one-electron reduction process at E = -1.02 V vs. Ag/Ag+, followed by pseudoreversible redox waves from E = -1.40 to -2.00 V, assigned to three electrons in total. It is worth noting that the four triazine panels are not simultaneously reduced. The ability of the cage to encapsulate adamantane was evidenced by J. T. Lippard and coworkers who introduced a prodrug made of adamantane modified with platinum[109](figure **1.5.1**).

The same triazine ligand was also used in combination with a *bis*-Ruthenium complex by B. Therrien and coworkers[110] (figure **1.5.2**). Cyclic voltametry showed irreversible oxidation at E = 0.27 V

Figure 1.5.1. Triazine-based electron-poor redox-active cages.[126]

vs. Ag/AgNO₃ and a quasi-reversible reduction at E = -2.33 V. Upon encapsulation of a coronene guest, the general behavior remains the same with a small positive shift of potential.
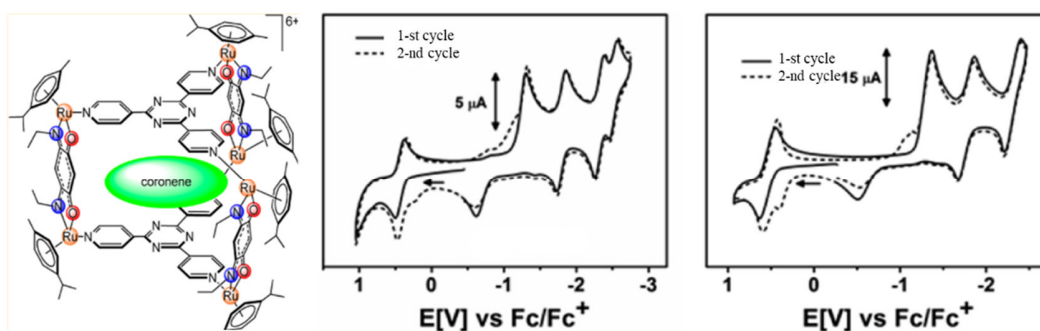
Figure 1.5.2. Ruthenium-based triazine redox-active cage and its cyclic voltammetry. [110]

The perylene bisimide (PBI) unit is interesting for both electronic and optical properties. F. Wurthner and colleagues have developed metalla-square constructed from a tetraarylsubstituted N,N`-4-pyridyl-substituted PBI ligand and a square planar Pt(II) complex[111] (figure **1.5.3**, a). The cyclic voltammetry reveals two successive reversible reduction waves at E = -1.01 and -1.14 V vs. *Fc/Fc+*, which are slightly shifted compared to the free ligand PBI-ligand precursor (E = -1.08 and -1.23 V respectively). They correspond to the successive radical anion and dianion formation for each perylene unit, which behave independently contrary to the above-presented triazine-based cages. Finally, a reversible oxidation process is observed at E = 0.93 V vs. *Fc/Fc+*. The PBI panels can also be additionally

decorated using ferrocene moiety.[112] Interestingly, in this case a splitting of the ferrocene oxidation wave is observed, resulting from intramolecular electronic interactions between the spatially confined ferrocene units.

Figure 1.5.3. Redox-active self-assemblies using perylene bisimide (PBI) unit. [113-114]

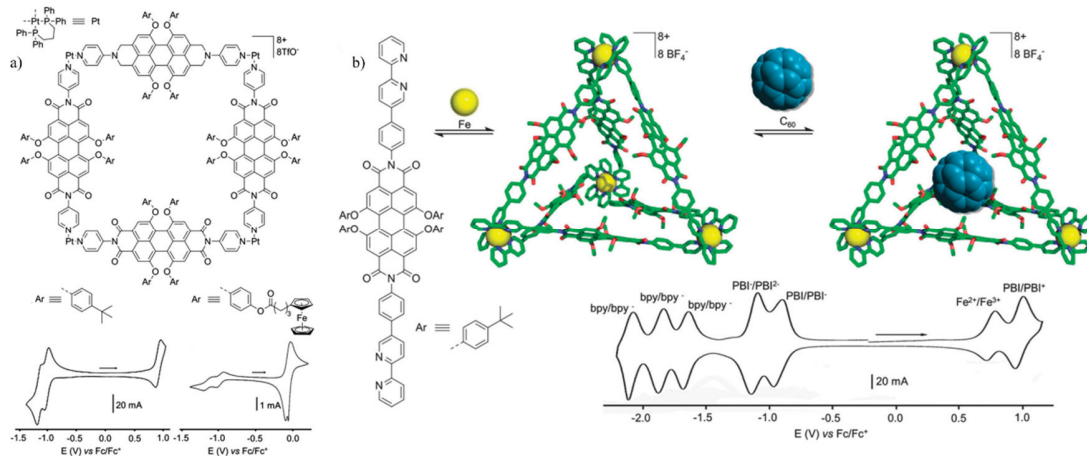The resulted square is able to modulate the ionic charge from 0 to +12, although authors failed to get guest encapsulation within the cavity. The same group recently designed a robust PBI-based metallacage presenting host–guest properties.[114] The very large M_4L_6 tetrahedron (figure **1.5.3**, b) is assembled from an octahedral Fe(II) ion and a PBI ligand bearing 2,2'-bipyridine units on the imide positions. The resulting $Fe_4(PBI)_6$ tetrahedron exhibits a particularly rich electrochemical activity manifested by multiple redox processes. Cyclic voltammetry shows reversible redox waves at E = -0.94 and -1.11 V vs. *Fc/Fc+*, which correspond to the successively reduced radical-anion and dianion species respectively. They are followed by the three successive reductions of the bpy fragments. In addition, two oxidation waves are observed at E = 0.73 and 0.95 V, assigned to the successive Fe^{2+} and PBI oxidation. This results in a broad range of charges surrounding the cavity (from -16 up to +18), which corresponds to a total of 34 electrons which can be switched, simply by controlling the electrochemical potential. A guest encapsulation was successfully demonstrated using a fullerene C_{60} molecule, as confirmed by ESI-TOF mass spectrometry.

1.5.2. Using electron-rich ligands

Ferrocene is widely used as an electron-rich unit, *e.g.* in catalysis, electrochemistry and functional materials.[115] In self-assembles structures, it has been incorporated as a substituent either on the ligand or on the metal complex.[116] The groups of Stang and Young have described a series of molecular hexagons and triangles using ferrocene in the *exo*-position[117-119] (exo refers to the respective location related to the cavity) (figure **1.5.4**). They were obtained using Platinum-based ligands with 120^0 (for hexagons) and 60^0 (for triangles) angle. All hexagons show one reversible oxidation (figure **1.5.4**, a) whereas the molecular triangles lead to a oxidation wave splitting, due to a closer distance between the ferrocene units. Cyclic voltammetry data could be used to calculate the hydrodynamic radius of the self-assemblies using the diffusion coefficient (*D*) from Randles–Sevcik equation. Using a tritopic ligand results in a 3D metallocage (figure **1.5.4**, b).[120] The size of the cage was estimated using cyclic voltammetry (6.7 nm) and is in good correlation with a theoretical estimation (6.9 nm).
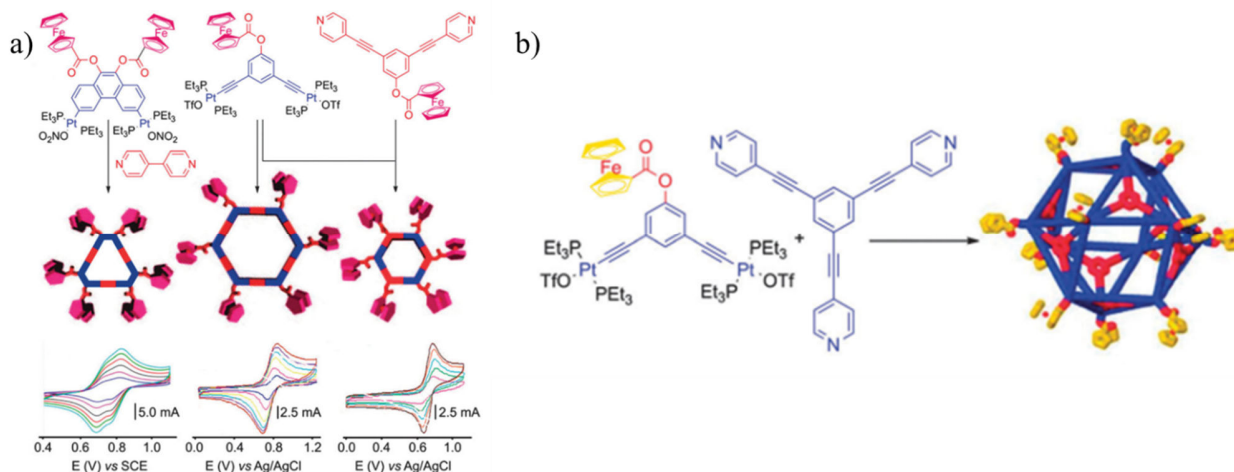
Figure 1.5.4. Redox-active self-assemblies using exo-located ferrocene. [116]

Similar metallocycles with ferrocene fragment in the *endo-* position were depicted by H.-B. Yang and coworkers.[121] Interestingly, despite the close location of the ferrocene units, no electronic interaction was observed in the cyclic voltametry experiment for both molecular triangles and hexagons (figure **1.5.5**). Also endo-position of the ferrocene makes it harder to approach and thus oxidate, which is confirmed by a higher oxidation potential and a lower current intensity.
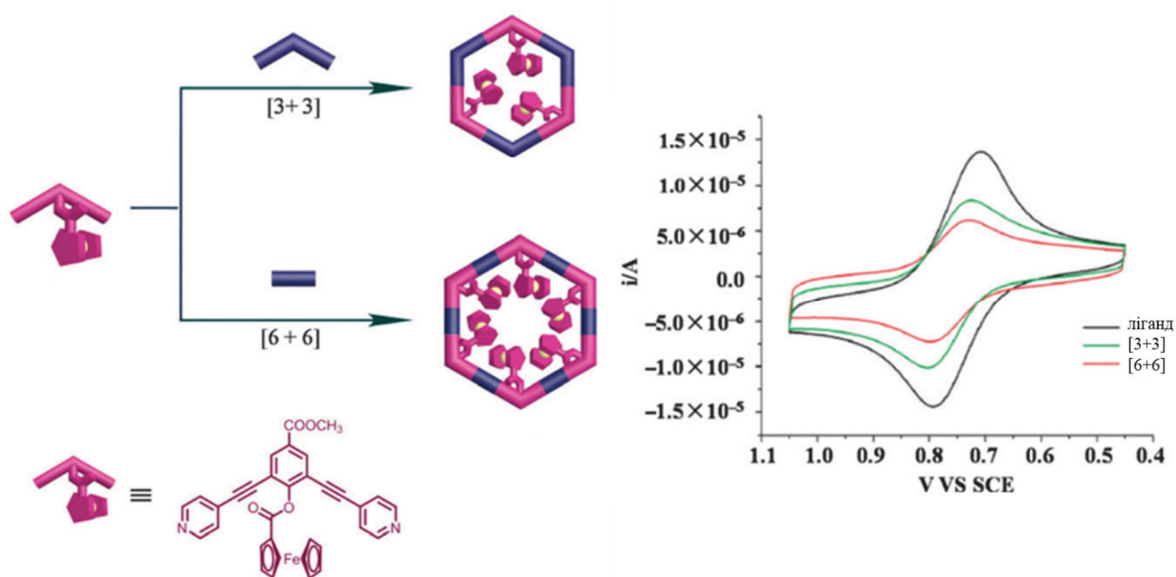
Figure 1.5.5. Redox-active self-assemblies using endo-located ferrocene. [116]

The ferrocene unit can also be directly engaged as a cavity constituent along the self-assembly. For instance, S.-Y. Yu and coworkers used *syn*-1,1'-disubstituted ferrocene complexe with di-Palladium corners to obtain metallocycles (figure **1.5.6**, a) capable of recognizing Br⁻ anions[122]. Stang and coworkers used *anti*-1,1'-disubstituted ferrocene unit with cis-blocked Pd and Pt acceptors to prepare molecular rhomboids and squares[123] (figure **1.5.6**, b). Similar metallocycles were reached by S.-Y. Yu and coworkers using another *anti*-1,1'-disubstituted ferrocene complexe which has shown an ability to

recognize different anion (with the best affinity towards HSO_4^-), as detected by square wave and cyclic voltametry[124] (figure **1.5.6**, c).

Figure 1.5.6. Redox-active self-assemblies using syn-*1,1'-(a) and* anti-*1,1'-disubstituted (b) ferrocene.* [116]

Finally, the ferrocene unit can also be located onto the corners of the self-assembled discrete structure, notably with cis-blocked Pd and Pt complexes. On thi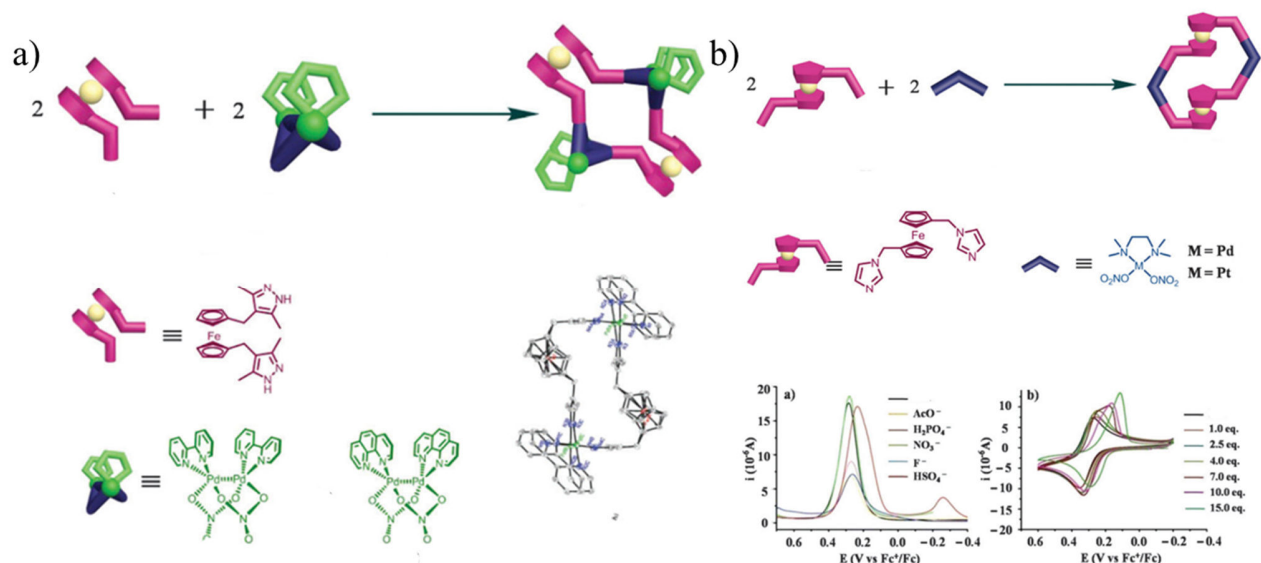s basis, Stang and coworkers described various molecular squares involving the *dppf* complex (diphénylphosphinoferrocene)[125-126] (figure **1.5.7**). Upon using tritopic ligands, various metallocages could be also obtained, as shown by R. Yang and coworkers[127].
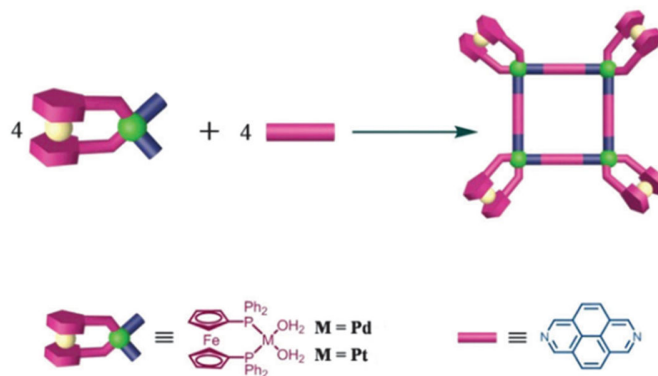
Figure 1.5.7. Redox-active self-assemblies using dppf cis-blocked Palladium and Platinum complexes. [116]

M. Yoshizawa and coworkers have recently shown the use of the dihydrophenazine fragments with "naked" Palladium ions in order to obtain electron-rich M_2L_4 cage (figure **1.5.8**, a).[128] Cyclic voltametry of the starting ligand shows two close reversible oxidation processes, corresponding to formation of mono- and di-radicalcation (figure **1.5.8**, b). Resulting cage can be reversibly oxidized (figure **1.5.8**, d) to the tetracationic state with alternating localisation of oxidized fragments (both electrochemically and chemically using silver nitrate). Increasing the potential leads to irreversible formation of an octacationic structure $M_2L_4^{8+}$ (figure **1.5.8**, c). The reversible formation of the tetraradical cage was confirmed by NMR, UV and EPR data.

29
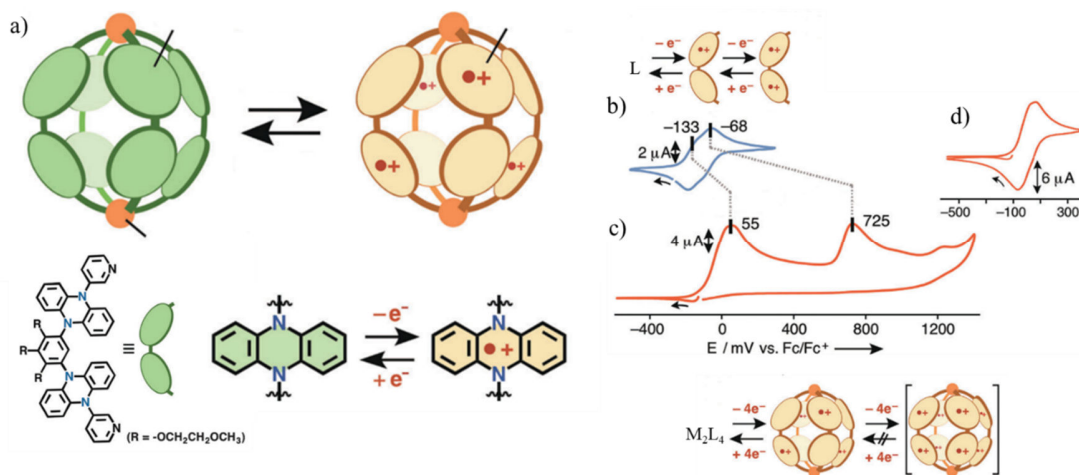
Figure 1.5.8. Redox-active self-assemblies using polyaromaric shell (a), CV of the starting ligand (b) and cage (c, d). [128]

A rare example of a host-guest redox study was recently proposed by J. R. Nitschke and coworkers[129] from a tetrahedral Fe(II)$_4$L$_6$ tetrahedral cage and a C$_{60}$ fullerene molecule (figure **1.5.9**). The metallacage is based on a porphyrin-based ligand and is capable of encapsulation from one (in nitromethane) to four (in nitrobenzene) C$_{60}$ molecules. The free cage shows two irreversible redox processes – broad oxidation at +0.17 V *vs* Fc/Fc$^+$ and reduction at -1.73 V *vs* Fc/Fc$^+$, both assigned to the porphyrin moieties and a reversible reduction at -2.09 V *vs* Fc/Fc$^+$ corresponding to the pyridyl-imines. The binding of several fullerenes is accompanied by significant changes of these potentials. Therefore, the electronic interaction between fullerene and porphyrin cavity walls strongly impacts the fullerene electronic behavior and lowers the HOMO-LUMO gap.

Figure 1.5.9 Modification of the redox behavior of encapsulated C$_{60}$ molecules. [129]

1.5.3. Using tetrathiafulvalene-based (TTF) ligands

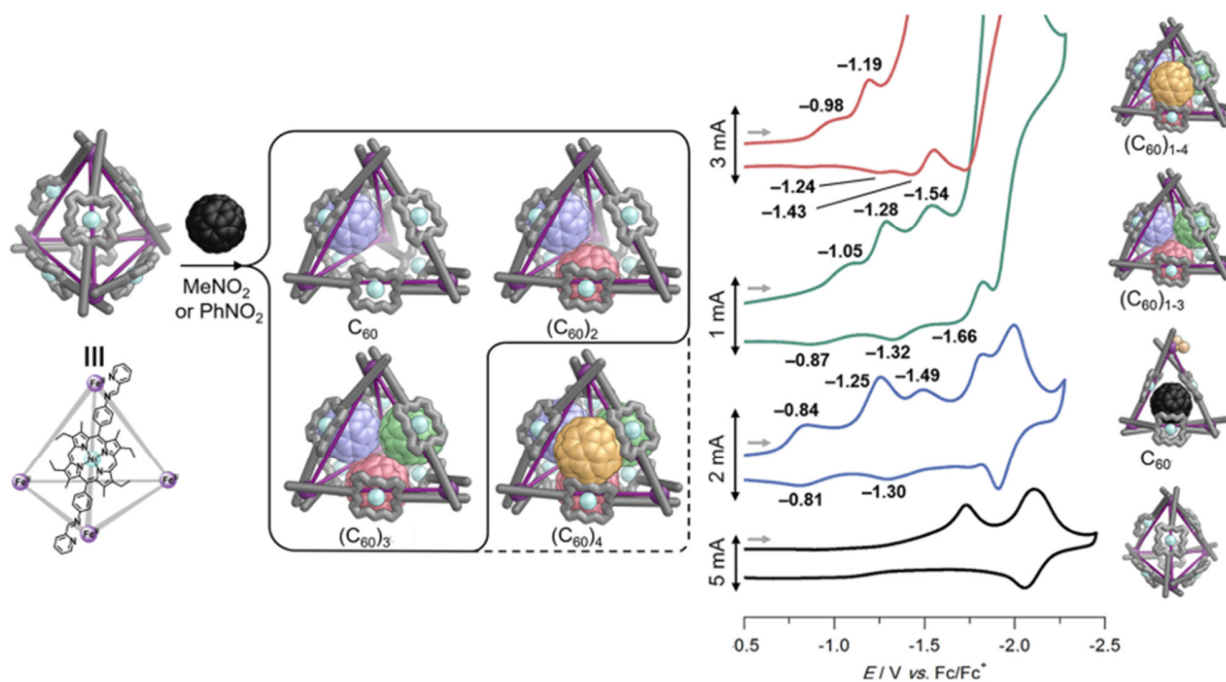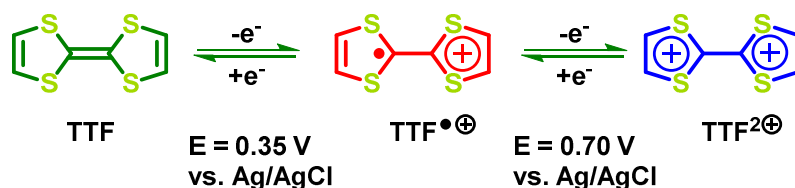Tetrathiafulvalene or TTF was simultaneously discovered in 1970 by Hünig[130], Coffen[131] and Wudl[132]. The interest to this molecule was further fueled by the discovery of high conductivity for its salt TTF^+Cl^- and first organic conductors in the form of its

Scheme 1.5.1. Redox behavior of the TTF molecule

complex with highly acceptor TCNQ molecule[133-134]. TTF[135] is a non-aromatic molecule with 14π electrons, which presents two fully reversible oxidations at low potential (scheme **1.6.1**), giving rise successively to a cation-radical ($TTF^{.+}$) and a dication (TTF^{2+}). Therefore, this unit can exist under three stable redox states, based on the successive formation of one ($TTF^{.+}$) and two (TTF^{2+}) heteroaromatic 1,3-dithiolium rings, upon oxidation of both 1,3-dithiol rings of neutral TTF (often abusively named dithiafulven (DTF)).

More than seven thousand publications covering a wide variety of applications, ranging from organic electronics to chemical sensors, have been produced from TTF and derivatives.[136-139] In particular, it has been shown to be an efficient redox unit in switchable molecular or supramolecular processes.[107, 140]

The TTF core can be synthetically modified, *e.g.* by changing Sulfur atoms for other chalcogens or by extending the conjugated system (figure **1.5.10**).[141-142] This results in new derivatives presenting specific structural and electronic properties. For example, truxeneTTF has a concave shape whereas exTTF presents a butterfly conformation. Such varieties are useful in supramolecular chemistry.[143-144]
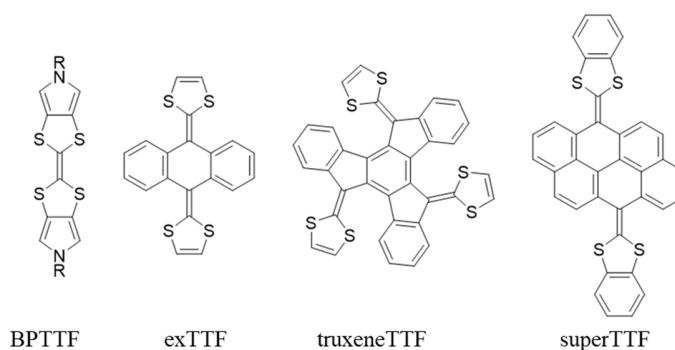
Figure 1.5.10. Examples of TTF derivatives presenting an extended π-extension.

1.5.4. Previous works of our group related to electro-active metal-driven self-assemblies

First metallocycles were obtained by our group with the bispyrroloTTF (BPTTF) bearing pyridine groups.[145-146] Upon its coordination with *cis*-blocked Pt complex, a mixture of a molecular square and a triangle was produced, which could be separated (figure **1.5.11**, a). Cyclic voltammetry shows the two classical reversible oxidation scheme at 0.3 V and 0.63 V *vs Fc/Fc⁺*. Ferrocene was used as an internal coulometric standard to confirm the independent oxidation of each BPTTF fragments (figure **1.5.11**, b). As a result, charge of the internal cavity can be modulated from 0 to +8 (square) and from 0 to +6

(triangle). The electron-rich cavity of the molecular triangle M_3L_3 was shown to bind electron-poor C_{60} and C_{70} molecules in a 1/1 ratio (figure **1.5.11**, c), whether no interaction was observed for the molecular square M_4L_4.
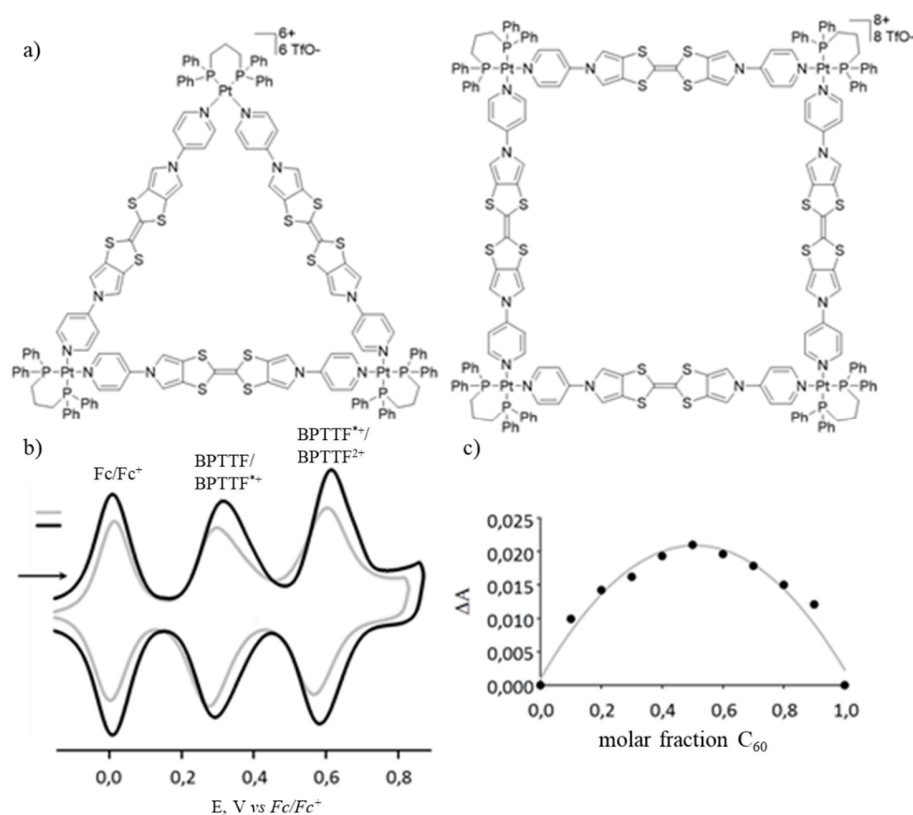
Figure 1.5.11. BPTTF-based metallocycles (a), their deconvoluted cyclic voltammetry (black, square; grey, triangle) (b) and Job's plot for the interaction between the electron-rich triangle cavity and C_{60}. [145]

A redox-active supramolecular cage using BPTTF was obtained by designing a tetratopic ligand (tetrapyridyl BPTTF) [147-148] followed by coordination with a *cis*-blocked Pt complex. A M_6L_3 molecular prism was obtained (figure **1.5.12**), whose X-ray structure could be solved. This cage exhibits two irreversible oxidations at fairly high potentials (0.43 V and 0.62 V *vs Fc/Fc+*) and it was shown by UV-vis titration that this cavity is able to encapsulate one electron-poor molecule (tetrafluorotetracyano-*p*-quinodimethane (TCNQ-F4)) in acetonitrile, in a 1/1 stoichiometry.

Figure 1.5.12. A BPTTF metallocage and XRD structure (a), cyclic voltammetry (b).[148]

As mentioned above, the so-called *π-extended tetrathiafulvalene* unit (9,10-di(1,3-dithiol-2-ylidene)-9,10-dihydroanthracene, abbreviated **exTTF**) features a dihydroanthracene fragment bridging two five-membered 1,3-dithiol rings. In contrast to the planar parent TTF system, exTTF exhibits a butterfly geometry, due to repulsive 1,6-inter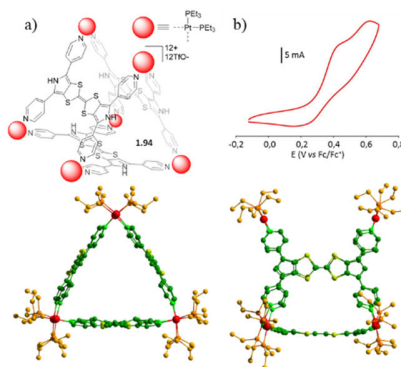actions between S atoms and periplanar anthracenyl H atoms. As a consequence, only one quasi-reversible two-electron oxidation process is observed while generating a dication, which structurally corresponds to an assembly of three independent aromatic entities (figure **1.5.13**).
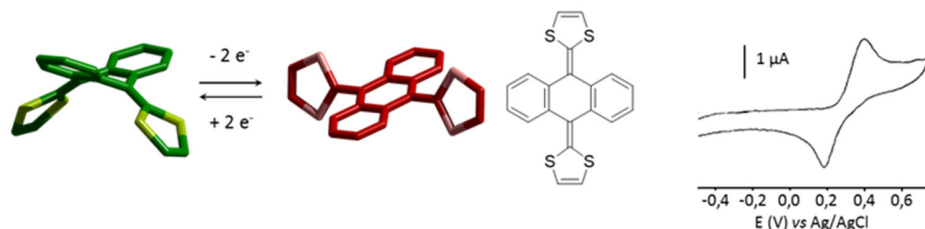
Figure 1.5.13. exTTF and its drastic conformational change upon a two-electron oxidation.

Four pyridine groups were introduced onto the exTTF core, generating a tetratopic ligand which was used in combination with *cis*-blocked Pd and Pt *dppf* complexes (figure **1.5.14**, a).[149] The resulting M_4L_2 cages both presents an irreversible oxidation at 0.57 V (Pd cage) and 0.65 V (Pt) *vs Fc/Fc$^+$* and a second reversible oxidation ($E_{ox}^2 = 0.80$ V) which corresponds to oxidation of ferrocene units from the *dppf* coligand (figure **1.5.14**, b).
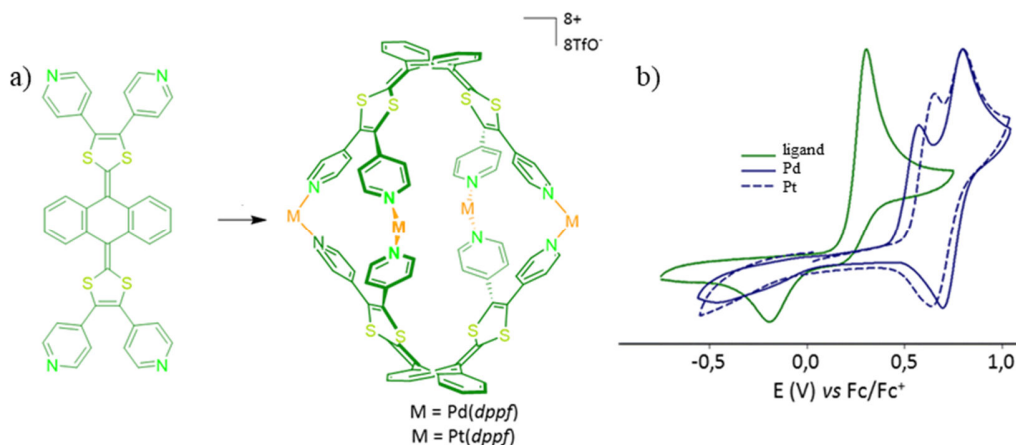
Figure 1.5.14. exTTF-based cages (a) and corresponding cyclic voltammograms (b). [149]

In order to improve the solubility, a modified version of the exTTF ligand was developed by introducing auxiliary triethylene glycol (TEG) chains (scheme **1.6.2**). This allowed to build octacationic cages ($M_4L_2^{8+}$, M = Pd, Pt) but also a neutral cage (M_4L_2). The former dissociates upon oxidation due to the geometry change in the ligand and reassemble upon reduction. This property was used to encapsulate an anionic guest cluster ($K_2B_{12}F_{12}$) and to control the guest release by a reversible cage disassembling.[150]
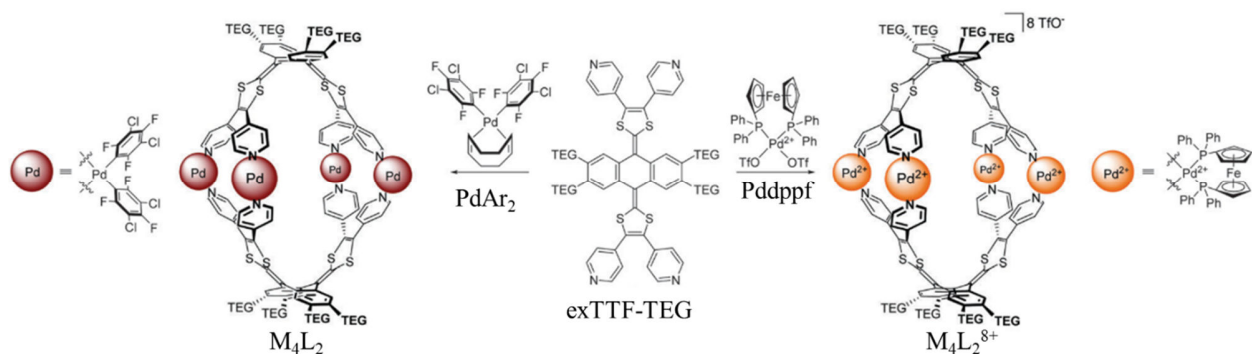
The neutral M_4L_2 cage shows a better affinity for neutral guests (*e.g.* coronene, bound in a 1/1 ratio).[151] Interestingly, this M_4L_2 cage with M = Pt, is remarkably more robust upon oxidation than is the Pd one, and therefore does not disassemble. This means that a sequence of oxidation-reduction leads in this case to a reversible generation of four positive charges on the cavity, without disassembling. This situation allows a controlled release of the coronene guest upon electrochemical oxidation, thanks to an exchange with anions of the supporting electrolyte.[152]

1.6. Objectives of the thesis

My thesis is part of the project dedicated to the design of new self-assembled coordination-driven redox active cages. Two main objectives are targeted:

➢ Developing new building blocks for constructing supramolecular redox-active cages endowed with specific properties, through:
- designing new electron-rich ligands inspired from the TTF core and its derivatives, including their full characterization and the study of their ability to generate discrete self-assemblies;
- exploring new metal complexes and studying their impact upon the self-assembly process;

➢ Studying the resulting metallocycles and metallocages: electrochemical, structural and guest binding properties.

2. Chapter II. Tetrathiafulvalene-based self-assemblies

2.1. Ligands based on the tetratiafulvalene moiety

Tetra-pyridyl TTF derivatives with 3-pyridyl units (**TTF(3Py)$_4$**) or 4-pyridyl units (**TTF(4Py)$_4$**) were first obtained in our group using a C-H activated arylation, as first developed on the TTF motif with alternative aryl groups by Mitamura and coworkers.[153] Further coordination of the tetratopic ligand **TTF(4Py)$_4$** with a short bis-Ruthenium complex (**Ru1**, oxalato linker) resulted in a M$_8$L$_2$ cage (figure **2.1.1**, a), while other combinations from **TTF(4Py)$_4$** or **TTF(3Py)$_4$** with **Ru1** or **Ru2** gave simple M$_4$L$_1$ metalloplates[154] (figure **2.1.1**, b-d). Interestingly, all metalloplates exhibit two reversible oxidations, while the cage displays only one reversible oxidation at 0.44 V *vs Fc/Fc$^+$*. This is assigned to the rigid geometry of the cage, which does not allow conformational changes upon oxidation.
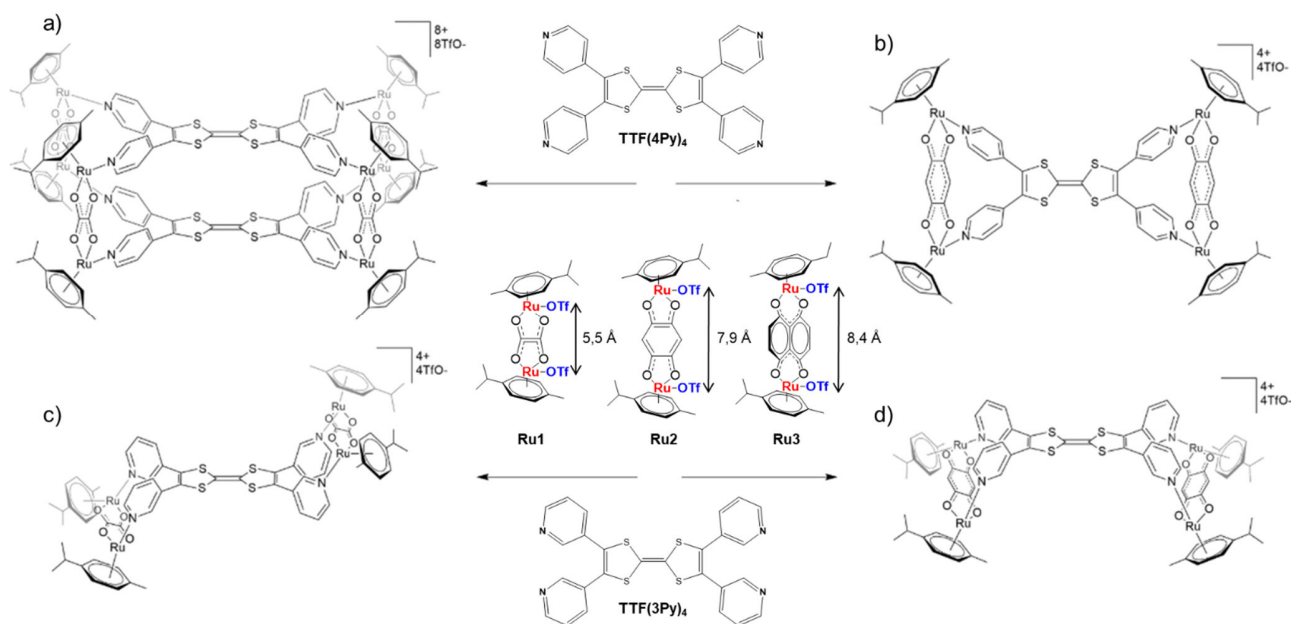
*Figure 2.1.1. A TTF-based cage from **TTF(4Py)$_4$** (a) and corresponding metalloplates from **TTF(4Py)$_4$** and **TTF(3Py)$_4$** (b-d).[154]*

Beside, ligand **TTF(4Py)$_4$** in combination with a *cis*-blocked Pd or a Pt complex results in M$_8$L$_4$ cage[116]. In contrast to the Ruthenium cage above, both cages show two reversible oxidations[149] (figure **2.1.2**). The ferrocene unit of the *dppf* coligand is used as an internal standard and confirms independent oxidation of the four TTF fragments.
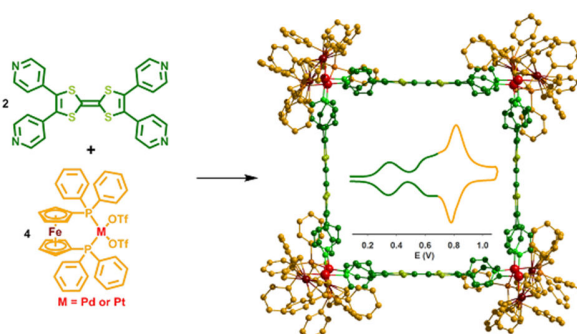
Figure 2.1.2. A TTF-based M$_8$L$_4$ cage and its cyclic voltammetry.[149]

2.1.1. Design and synthesis of ligand TTF(PhPy)$_4$

The above-mentioned M$_8$L$_2$ cage **TTF(4Py)$_4$** featuring *bis*-Ruthenium complexes is particularly interesting. Indeed such system allows to tune the distance between both facing TTF units depending on the length of the *bis*-Ruthenium complex, and to the best of our knowledge, only one example exists in

the literature where two TTF planes are forced to stand overlapped (figure **2.1.3**).[155] Nevertheless, the distance between both TTF units in the latter system is quite important and did not allow to characterize any interaction between the redox units.

Figure 2.1.3. Example of a tetrathiafulvalene "belt" involving to facing TTF planes.

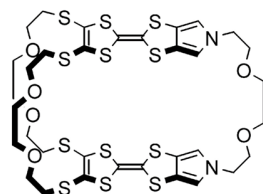The peculiar geometry of M_8L_2 cages (e.g. Figure 2.1.1) offers two promising opportunities:

1) if the Ru-Ru distance is large enough in the *bis*-Ruthenium complex, an electron-poor guest may be bound according to a sandwich mode between both electron-rich TTF units;

2) if the Ru-Ru distance is short enough in the *bis*-Ruthenium complex, one may assume that both TTF will interact upon oxidation.

The scheme **2.1.1** illustrates the interaction modes which can be anticipated when two TTF units are in close contact: i/ formation of a mixed-valence dimer $(TTF)_2^{·+}$, observed and characterized with covalent poly-TTFs systems;[156] ii/ formation of a π-dimer $(TTF^{·+})_2$ system, and iii/ a final oxidation step towards dicationic (TTF^{2+}) units, which dissociate due to electrostatic repulsion.

In addition to the well-established conducting properties of some of them in the solid state,[157] the mixed-valence dimer $(TTF)_2^{·+}$ have known a strong recent interest, as a new interaction mode of the supramolecular toolbox.[158-159] Indeed, such interactions allows to redox-govern the contacts between two units, offering promising perspectives, notably in terms of triggering molecular movement.
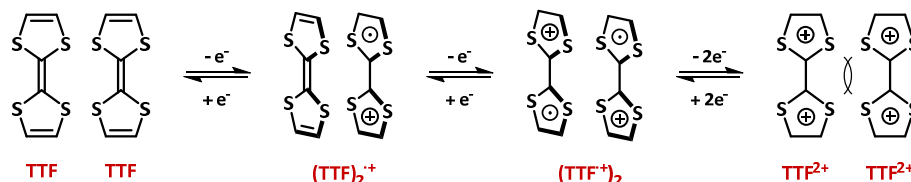
Scheme 2.1.1. Successive oxidation steps of a TTF dimer

Importantly, it has to be noted that till now, the radical-cation homodimerisation to produce $(TTF^{·+})_2$ has been observed only in the solid state or in highly concentrated solutions at low temperature (Figure **2.1.4**).[160-162]
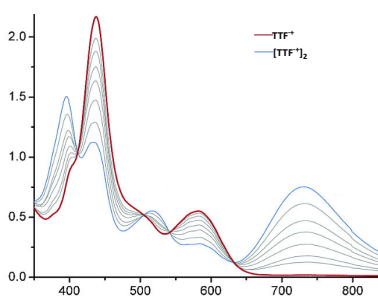
Moreover, the π-dimer $(TTF^{·+})_2$ could be observed at rt in very specific cases, either by: *i/* confinement of the dimer in a cavity (*i.e.* in cucurbituril[163] or in a coordination cage[37], *ii/* designing covalent species allowing preorganization of the cation-radical dimer[164-167] or by 3/ dimer stabilization in interlocked structures.[168]

On this basis, and in order to get a deeper insight over the occurring interactions, it appears timely to design a system allowing to control the distance between two TTF units.

As shown in figure **2.1.1**, long bisRuthenium complexes essentially afford metalloplates instead of the desired M_8L_2 cages, due to a good matching between the Ru-Ru distance and N-N distance from neighbored pyridine units. One solution to favor the M_8L_2 cage consists therefore in enlarging the distance between pyridine units compared to **TTF(4Py)₄**, which can be obtained through incorporation of a phenyl linker between the TTF core and pyridyl units and which corresponds to compound **TTF(PhPy)₄**.
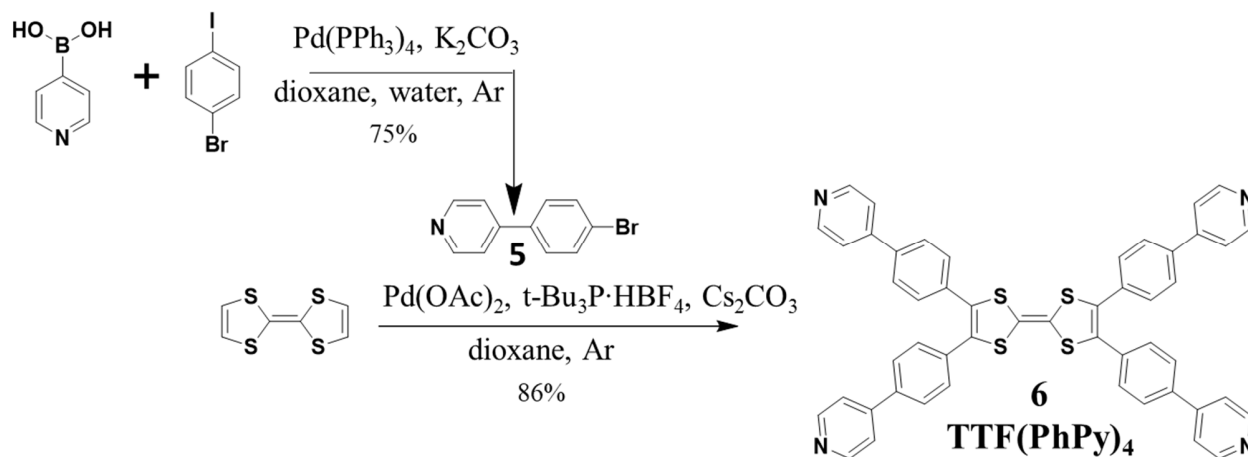
*Scheme 2.1.2. Synthesis of the **TTF(PhPy)₄***

The ligand **TTF(PhPy)₄** was synthesized with a 86% yield using a Palladium-catalyzed C-H activated tetraarylation, starting from the commercially available TTF and (4-bromophenyl)pyridine (scheme **2.1.2**). The latter was previously obtained through a Palladium-catalyzed Suzuki coupling[169].

2.1.2. Characterization

TTF(PhPy)$_4$ was characterized by ^{1}H, ^{13}C NMR spectroscopy, as well as mass-spectroscopy and elemental analysis. Single crystals, suitable for analysis, were obtained by slow evaporation of dichloromethane/methanol mixture and the x-ray analysis was carried out at T = 250 K. X-ray data (see annex **6.1**) show a significant disorder of the phenyl units, which confirms the structural flexibility (figure **2.1.5**).

The molecule has a rectangular shape with 12.8 x 19.3 Å dimensions between the four Nitrogen atoms, to be compared with the 6.7 x 13.1 Å in the case of the smaller **TTF(4Py)$_4$** ligand. This size should avoid formation of undesired metalloplates upon coordination with *bis*-Ruthenium complexes and remains fully suitable for the formation of M$_4$L$_2$ cages.
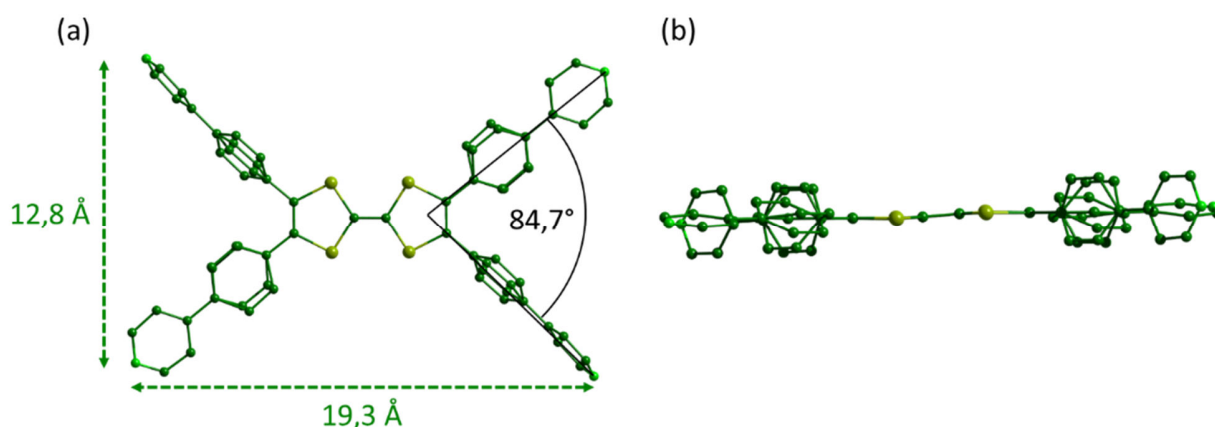
Figure 2.1.5. X-ray structure of TTF(PhPy)$_4$ ligand.

2.1.3. Electrochemical properties

The electrochemical properties of the **TTF(PhPy)$_4$** ligand were studied in a 1:1 acetonitrile/dichloromethane mixture. As in the case of **TTF(4Py)$_4$**, this ligand exhibits two reversible oxidation waves (E_{ox}^1 = 0.06 V; E_{ox}^2 = 0.46 V *vs. Fc/Fc$^+$*) corresponding to two successive one-electron oxidations to the radical-cation and dication states (Figure **2.1.6**). Nevertheless, these oxidations occur at significantly lower potentials comparing with **TTF(4Py)$_4$** (E_{ox}^1 = 0.20V and E_{ox}^2 = 0.55V *vs. Fc/Fc$^+$*). This difference is explained by the presence of the phenyl spacer which isolate the pyridyl groups from the TTF core, thereby attenuating the withdrawing inductive effect of nitrogen atoms. On this basis, the **TTF(PhPy)$_4$** unit appears as a remarkably strong π-donating ligand, suitable for generating discrete assemblies endowed with an electron-rich cavity.
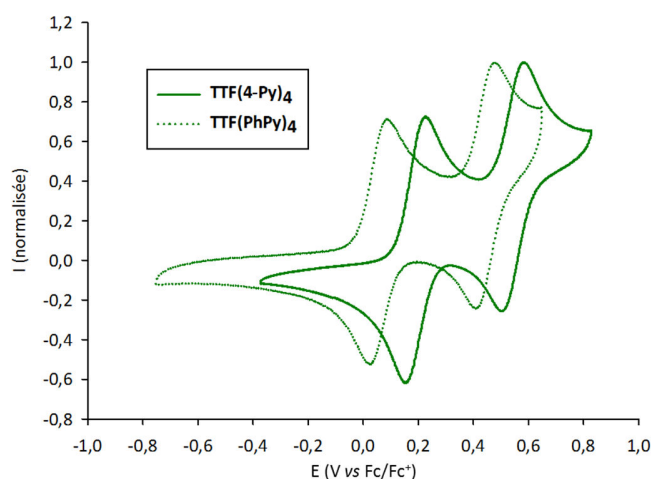
*Figure 2.1.6. Cyclic voltammetry of the **TTF(PhPy)₄** and **TTF(4Py)₄**: CH₃CN/CH₂Cl₂ (C = 1 mM, n-Bu₄NPF₆ (0,1 M)), 100 mV.s⁻¹, glassy carbon, vs Fc/Fc⁺.*

2.2. Self-assemblies based on the tetrathiafulvalene moiety

2.2.1. M₈L₂ self-assemblies with Ru complexes: AA1 and AA2

The previous M_8L_2 cage involving the **TTF(4Py)₄** ligand in combination with a short *bis*-Ruthenium acceptor (**Ru1**, d_{Ru-Ru} = 5.5 Å) failed to successfully encapsulate a guest molecule because of the small distance between TTF planes. Longer *bis*-Ruthenium complexes could not be used since they preferentially afford metalloplates rather than cages (see § **1.4.4**). In the case of the new **TTF(PhPy)₄** ligand, longer *bis*-Ruthenium complexes **Ru3** and **Ru4** can be used (d_{Ru-Ru} = 8.4 Å) to drive the self-assembly towards metallocages.
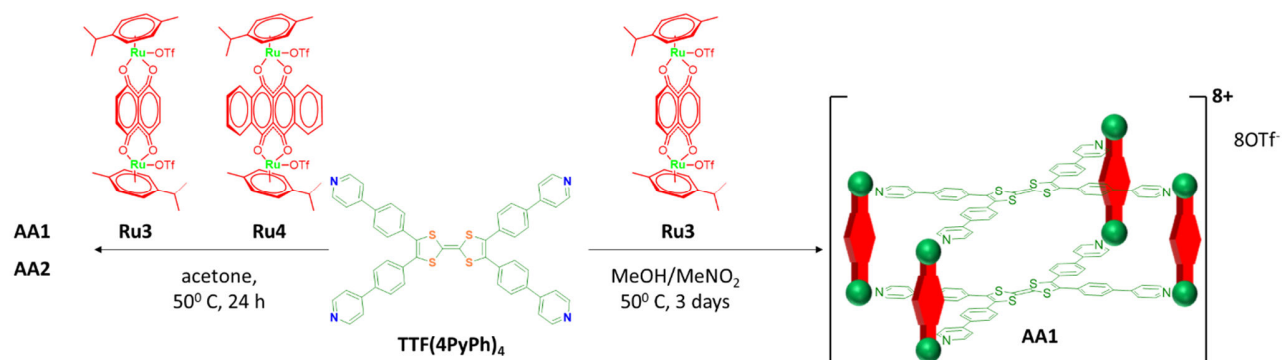
Scheme 2.2.1. Synthesis of the self-assemblies AA1 and AA2.

The reaction was first carried out using acceptor **Ru3** in a methanol/nitromethane 1/1 mixture during 3 days, affording in the self-assembly **AA1** (scheme **2.2.1**). Further optimizations allowed to obtain the same self-assembly **AA1** from **Ru3** in acetone in only 1 day, as well as **AA2** from **Ru4**.

Formation of the cage **AA1** was confirmed ¹H and DOSY NMR (figure **2.2.1**). Upon coordination to the metal center, the signals of α(■) and β(●) pyridil protons shift as expected towards stronger field. Well defined signals are observed, suggesting formation of a discrete self-assembled compound. This is

further confirmed by a DOSY NMR experiment, for which a single set of aligned signals is observed. The corresponding diffusion coefficient ($D = 2,51$ x 10^{-10} m².s^{-1}) allows to estimate the hydrodynamic radius $r_H = 16$ Å for **AA1,** calculated from the Stokes-Einstein equation (equation **1**).[169-170]

$$ D = \frac{k_B T}{6\pi\eta r_H} $$

Equation 1 : Stokes-Einstein Equation; D corresponds to the diffusion coefficient (m².s^{-1}), k_B Boltzmann constant (1,38 x 10^{-23} J.K^{-1}), T absolute temperature (K), η viscosity of the solvent (Pa.s) and r_H hydrodynamic radius (m).

A similar behavior is observed in the case of **AA2** prepared in acetone-d$_6$ (annex **3.1**). Following the same procedure, a r_H value of 17 Å is found for **AA2** ($D = 4,34$ 10^{-11} m².s^{-1}, acetone-d$_6$), which is as expected, slightly larger than for **AA1**.
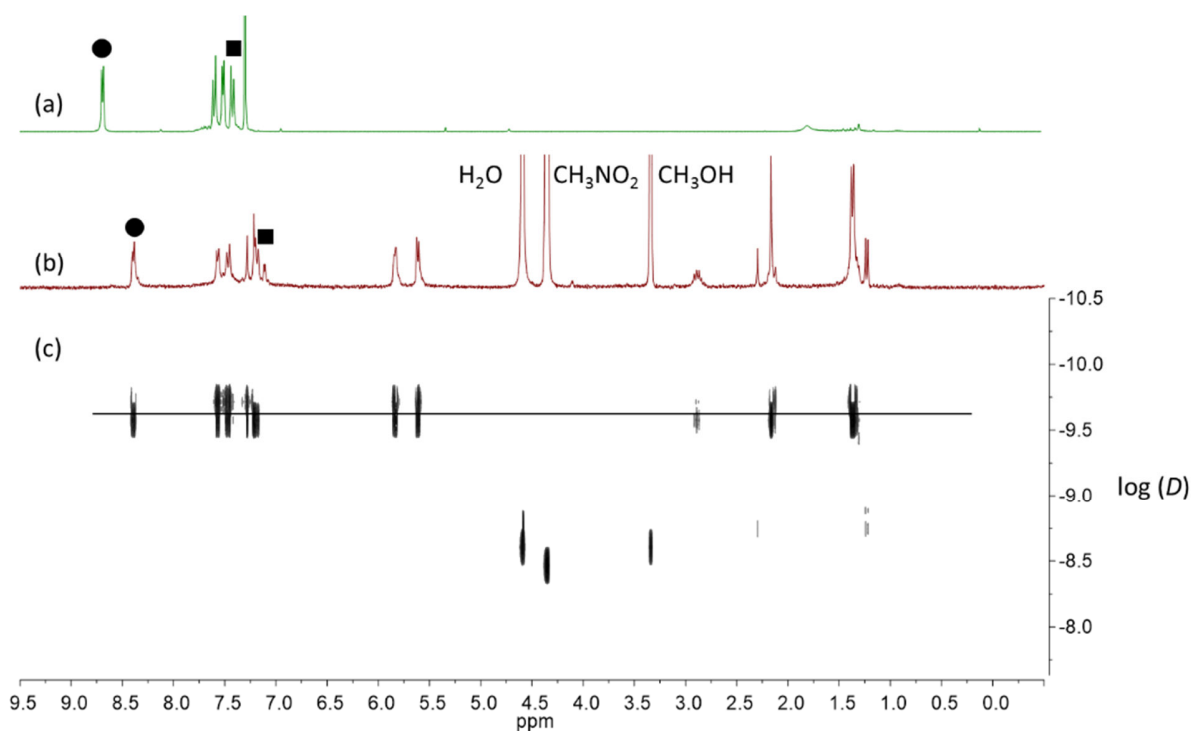
*Figure 2.2.1. ^1H NMR of ligand **TTF(PhPy)$_4$** in CDCl$_3$ (a), self-assembly **AA1** in MeOD/CD$_3$NO$_2$ (b) and corresponding DOSY NMR (c)*

A ESI-FTCIR analysis was carried out in collaboration with Drs Frédéric Aubriet and Vincent Carré in the University of Lorraine. This analysis confirms the M$_8$L$_2$ stoichiometry, which therefore corresponds to four *bis*-Ruthenium acceptor units and two ligands which are assembled in one discrete structure as shown by the characteristic ions [(**TTF(PhPy)$_4$**)$_2$(**Ru3**)$_4$, 5TfO$^-$]$^{3+}$ (m/z = 1671,4093) and [(**TTF(PhPy)$_4$**)$_2$(**Ru3**)$_4$, 4TfO$^-$]$^{4+}$ (m/z = 1216,3185) (figure **2.2.1**, a). Isotopic distribution also correlates well with the theoretical data (figure **2.2.1**, b, c).
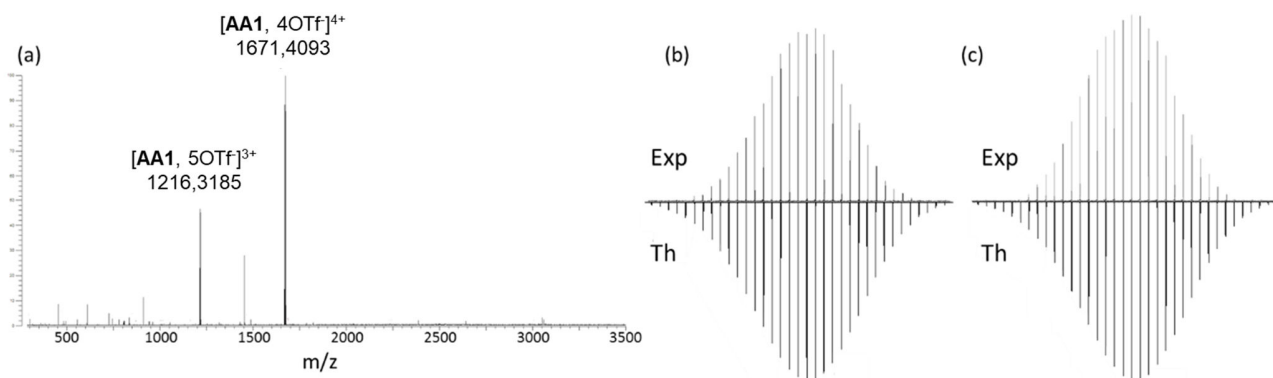
*Figure 2.2.2. ESI-FTCIR of **AA1** (a) and theoretical vs experiment (b, c)*

2.2.2. Structural properties and intercalation attempts

Such metallocages with electron-rich walls should be effective for the intercalation of planar electron-poor guests in a sandwich mode. Nevertheless, all attempts to introduce guest molecules for both cages **AA1** and **AA2** failed. An explanation comes from the short distance existing between facing TTF units, which could be demonstrated in the solid state through a single-crystal X-ray diffraction analysis led on **AA1** (figure **2.2.3**).
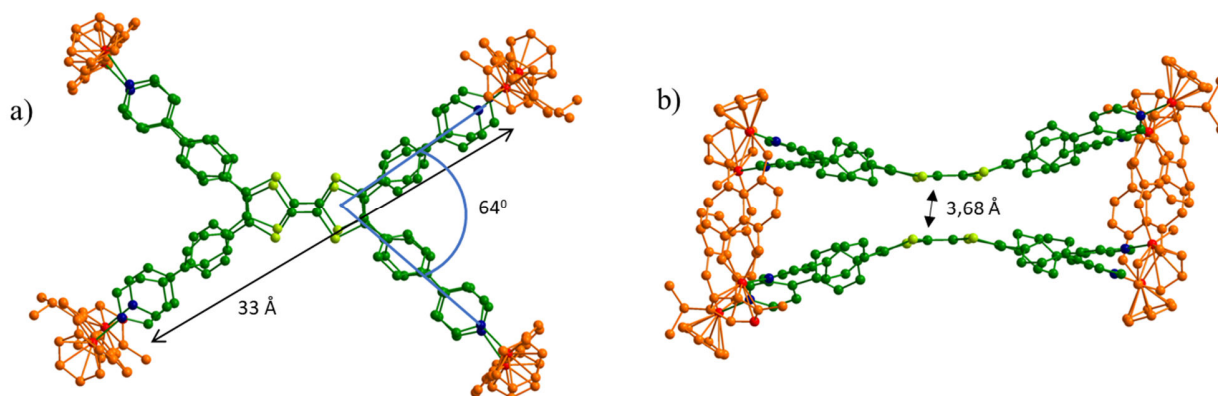
*Figure 2.2.3. X-ray structure of **AA1**. Hydrogens, anions and molecules of solvent omitted for clarity.*

Crystals, suitable for XRD analysis, were obtained by diffusion of methyl-*tert*-butyl ether into a solution of **AA1** in methanol (see X-Ray data in annex **6.2**). From this study, a distance of 33 Å is found between two extreme opposing atoms of **AA1** which correlates well with the above calculations using DOSY NMR. The angle between Nitrogen atoms of pyridil units is 64° in comparison to 84.7° in the free ligand, which illustrates a certain constraint upon self-assembly. But the most striking feature of this solid state structure relies on the close distance of 3.68 Å observed between C atoms of the internal C=C bond in two TTF units (S···S mini: 3.83 Å), which is significantly smaller in comparison to the Ru-Ru distance in the lateral pillar (8.4 Å). This illustrates the significant flexibility of the assembly and results in a severe bending of both TTF units. The latter can be characterized with an angle of 35° between the pyridine-TTF vector and ideal planar geometry of the **TTF(4PhPy)₄** ligand. Such bending justifies why no sandwich host-guest complex could be obtained, despite numerous attempts.

Crystals of **AA2** were obtained using the same conditions. As expected, the spatial organization of **AA2** (figure **2.2.4**) is similar to the above presented **AA1**. Notably, the distance between TTF fragments is of the same order (3.72 Å) as for **AA1**, and is much shorter than the Ru-Ru distance in the lateral pillars (8.34 Å). A noticeable difference with **AA1** comes from the cavity collapse which in the case of **AA2**, is essentially supported by a single TTF unit. The latter displays a severe bending with 33° and 37° angles between the pyridine-TTF vectors and an ideal planar geometry, whereas the second TTF unit remains essentially planar.
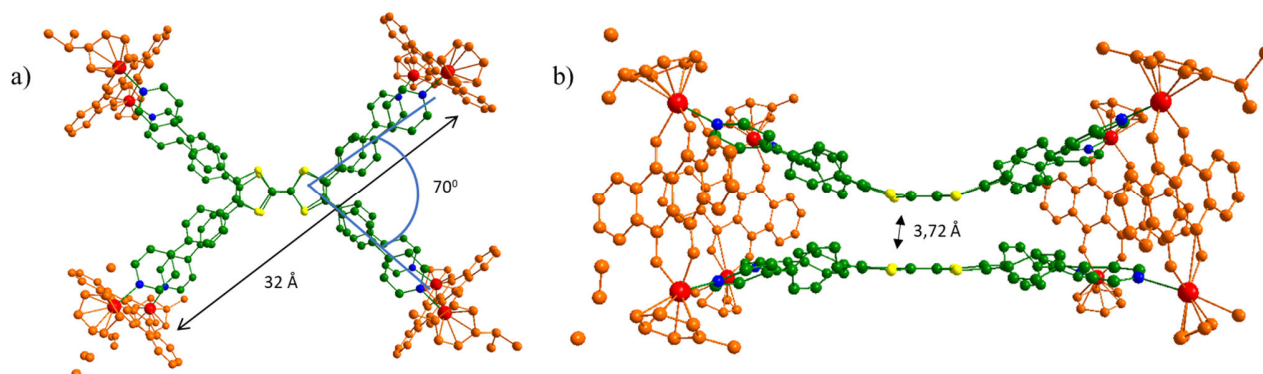
*Figure 2.2.4. X-ray structure of **AA2**. Hydrogens, anions (PF₆) and molecules of solvent omitted for clarity*

2.2.3. Electrochemical properties

The electrochemical behavior of cage **AA1** was studied in a acetonitrile/dichloromethane 1/1 mixture, using ferrocene for calibration (figure **2.2.5**). Interestingly, cage **AA1** shows a splitting of the first oxidation process in two waves (-0.03 V and +0.20 V *vs Fc/Fc⁺*) in comparison to the ligand (+0.06V *vs Fc/Fc⁺*) (figure **2.2.5**, a). This is indicative for the formation of the mixed-valence dimer ((TTF)₂)·⁺ and the corresponding π-dimer (TTF·⁺)₂.[156, 171]
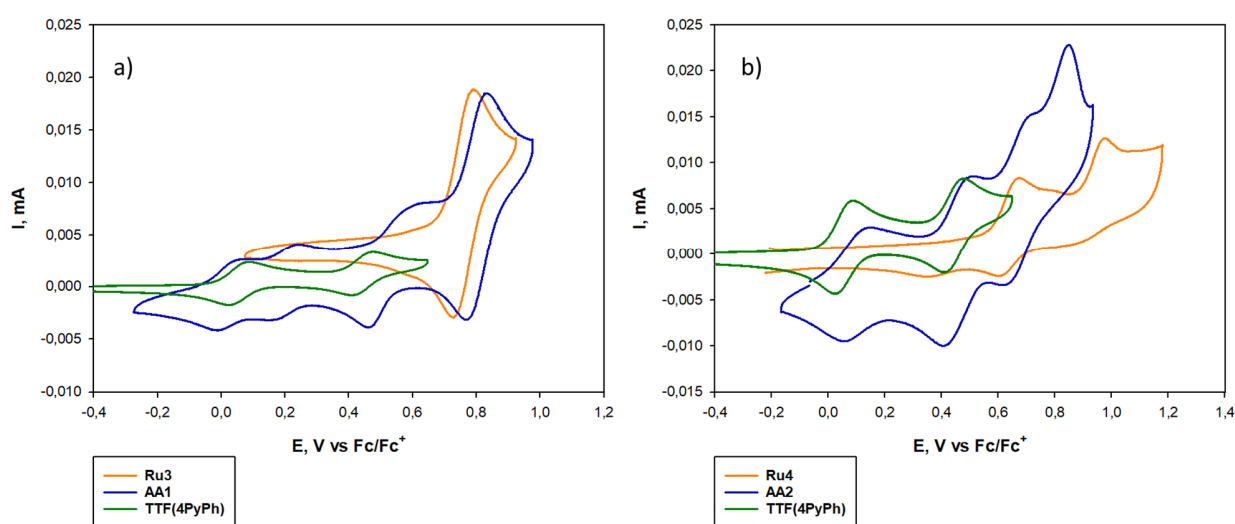
*Figure 2.2.5. Cyclic voltammetry of **AA1** (a) and **AA2** (b) (CH₃CN/CH₂Cl₂ (C = 1 mM, n-Bu₄NPF₆ (0,1 M)), 100 мV.s⁻¹, Pt, vs Fc/Fc⁺)*

Such phenomenon can be explained by the very close distance between facing TTF subunits which are therefore prone to strongly interact upon oxidation. A third reversible oxidation is located at

0.53 V *vs Fc/Fc⁺* and is assigned to the formation of the dication state for each TTF unit resulting in tetracationic cage. Finally, an additional reversible oxidation process is observed at 0.80 V *vs Fc/Fc⁺*, which corresponds to the metal center oxidation, as shown from comparison with **Ru3**. Note that the reversible reduction of the naphthoquinone fragment is observed at -0.87 V *vs Fc/Fc⁺* (not shown in Figure **2.2.5**). Finally, it is worth noting that the self-assembly **AA1** remains stable upon repeated cycles within this potential window, but that higher potentials cause destruction of the cage.

In contrast to **AA1**, self-assembly **AA2** shows the usual two reversible oxidation processes of TTF at 0.17 V and 0.45 V *vs Fc/Fc⁺*. The absence of generation of the oxidized dimeric species is surprising since the Ru-Ru distances are similar for both **Ru3** and **Ru4** pillars. One hypothesis relies on the larger tetracene-based central unit in **Ru4** (naphthalene-based in the case of **Ru3**) which presumably prevents interaction between the TTF planes. These processes are followed by a reversible oxidation at 0.66 V and an irreversible one at 0.85 V *vs Fc/Fc⁺*, which are attributed to the **Ru4** unit. As for **AA1**, scanning the potentials beyond 1.20 V leads to the cage disassembling.

2.2.4. Electrocrystallization studies

The electrocrystallization technique allows to grow single crystals of the oxidized (or reduced) compounds upon a controlled galvanostatic or potentiostatic electrolysis (see annex **2**). The crystals are generally collected directly onto the working electrode. The main principle is based on the slow oxidation (or reduction) of the electro-active molecule giving rise to charged species which cocrystallyze with the counter-ion present used in the supporting electrolyte. After numerous attempts of constant current electrolysis of **AA1**, single crystals suitable for XRD analysis could be collected (conditions: $C_{AA1} = 5 \times 10^{-4}$ mol.L-1; methanol; Bu_4NPF_6 (0.1 mol.L^{-1}); Tre= 20 °C; i= 0.5 μA).
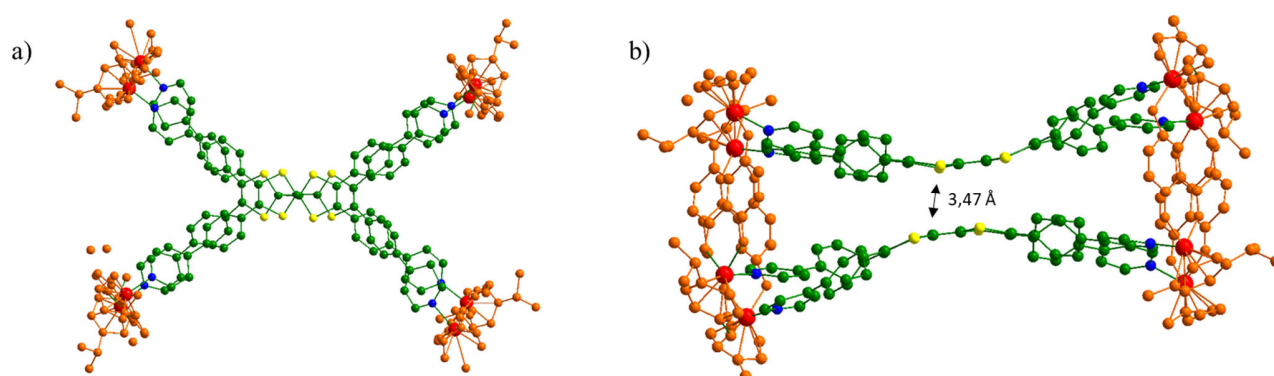
Figure 2.2.6. X-ray structure of oxidized AA1. Hydrogens, anions (PF₆⁻) and molecules of solvent omitted for clarity

The quality of the X-Ray data collection was not optimal, nevertheless the main trends could be drawn. The oxidized form preserves the main geometrical characteristic of the starting **AA1 cage**, but exhibits some significant differences (figure **2.2.6**). Most notably, the TTF planes of both ligands are shifted relative to one another (figure **2.2.6**, a) and a significantly shorter distance is observed between both TTF planes. The shortest interplanar TTF distances are found to be *ca* C···C = 3.47 Å and S···S = 3.70 Å (figure **2.2.6**, b), *i.e.* significantly smaller than in neutral **AA1**. The generation of oxidized TTF units is furthermore confirmed by comparing the length of the central $S_2C - CS_2$ bonds (1.38 Å for both TTF units in the electrocrystallized salt) with the $S_2C = CS_2$ bond in neutral **AA1** (1.33 Å for both TTF units). Such observations are consistent with the formation of a cation-radical dimer $(TTF^{·+})_2$ and

illustrates occurrence of an intramolecular interaction occurring between the facing TTF units upon oxidation at the first redox process (cation-radical generation).

2.2.5. Absorption studies

In order to get a deeper understanding of the electronic properties of these new architectures, we plane to perform some spectroelectrochemistry measurements (annex **1**). This technique allows to follow in real time the changes in the UV-vis spectra during the cyclic voltammetry. These studies are currently done in collaboration with Drs O. Alevêque and E. Levillain (laboratory MOLTECH-Anjou).

Reference UV-vis data of the ligand **TTF(4PyPh)₄** are first needed in order to tune the spectroelectrochemistry analysis. The latter is very sparingly soluble in the standard dichloromethane/acetonitrile system which we used for the above electrochemical experiments. Therefore the more soluble tetrakis(methylpyridinium) derivative **TTF(Me-4PyPh)₄** was synthesized (scheme **2.2.2**). This compound is considered reminiscent of the corresponding **TTF(4PyPh)₄** once the latter is engaged in a coordination bond, as it is the case in **AA1**. Alkylation was carried out in DMF, followed by anion exchange using KPF₆.
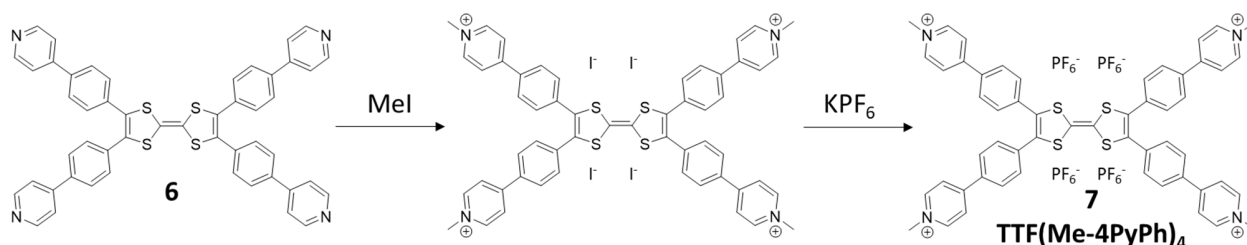
*Scheme 2.2.2. Synthesis of **TTF(Me-4PyPh)₄**.*

The UV-vis spectra of **TTF(Me-4PyPh)₄** (compound **7**) (2.5 x 10^{-5} M), complex **Ru3** (2.5 x 10^{-5} M) and cage **AA1** (1.5 x 10^{-5} M) are shown in figure **2.2.7**. The TTF derivative **7** exhibits two strong absorptions at λ= 325 nm (ε = 41110 l.mol^{-1}.cm^{-1}) and λ = 460 nm (ε = 4220 l.mol^{-1}.cm^{-1}), which are typical for pyridinium salts[172]. The **Ru3** complex exhibits main absorptions at λ = 320 nm (ε = 12600 l.mol^{-1}.cm^{-1}) and λ = 430 nm (ε = 9100 l.mol^{-1}.cm^{-1}), which correspond to the intra-ligand charge transfer in naphthalene and cymene, and minor absorptions at λ = 630 nm (ε = 3300 l.mol^{-1}.cm^{-1}) and λ = 682 nm (ε = 4250 l.mol^{-1}.cm^{-1}), that correspond to the metal-ligand charge transfer due to the coordination with naphthalene and cymene[173]. Finally, the spectrum of cage **AA1** essentially corresponds to the sum of the respective above contributions of **TTF(Me-4PyPh)₄** and **Ru3 with** main absorption at λ = 305 nm (ε = 96200 l.mol^{-1}.cm^{-1}) and less intense ones at λ_m = 435 nm (ε = 26200 l.mol^{-1}.cm^{-1}), λ = 645 nm (ε = 7900 l.mol^{-1}.cm^{-1}) and λ = 695 nm (ε = 7500 l.mol^{-1}.cm^{-1}), which is typical for such systems[174].
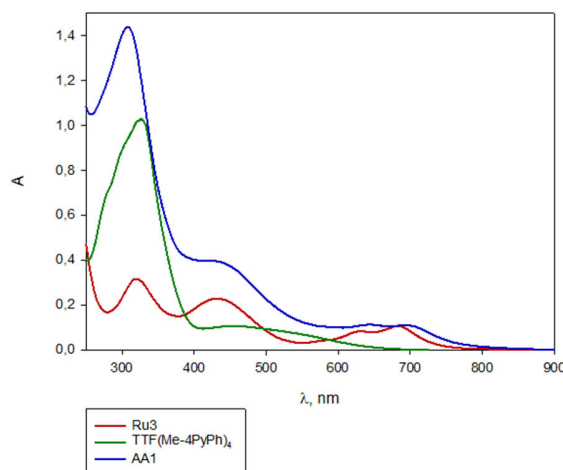
*Figure 2.2.7. UV-vis spectra of **Ru3**, **TTF(Me-4PyPh)₄** and **AA1** (CH₃CN/DCM 1/1)*

The corresponding spectroelectrochemical studies of **AA1** are in due course and should contribute to get a better insight over the oxidized species resulting from oxidation of the cage..

2.3. Conclusion

A new large tetratopic ligand **TTF(4PyPh)₄** was designed in order to favor the formation of a M_8L_2 cage rather than a M_4L_1 metalloplate upon self-assembling with *bis*-Ruthenium complexes. The latter are used as the four pillars separating both TTF planes in the M_8L_2 cage and their respective length is considered to drive the distance between the facing redox-active units. In particular, two self-assemblies **AA1** and **AA2** were synthesized and fully characterized, including in the solid state (XRD). Whereas in both cases the M_8L_2 corner-corner distances Ru-Ru are *ca* 8.3Å, short interplanar C⋯C and S⋯S distances of *ca* 3.68 Å and 3.83 Å respectively are observed between the two TTF units in **AA1** (similar values for **AA2**). This short distance is consecutive to a severe bending of the facing ligands, which collapse towards the center of the cavity. Accordingly, attempts to bind electron-poor planar guests in a sandwich mode, failed from these collapsed M_8L_2 assemblies. It is worth noting that whereas **AA2** exhibits the usual electrochemical two-step oxidation behavior of TTF derivatives, **AA1** clearly shows that the two facing TTF units strongly interact upon oxidation, giving rise to an oxidized TTF dimer. This observation is imputable to the unique geometry of those M_8L_2 assemblies, for which the two TTF units are forced to stack together. Electrocrystallysation experiments where led upon galvanostatic oxidation of **AA1** and afforded single-crystals of the oxidized cage. The latter does not disassemble upon oxidation which confirms the robustness of **AA1**. The resulting oxidized cage shows that the two TTF units are significantly closer than in neutral **AA1**. The shortest interplanar TTF distances are found to be *ca* C⋯C = 3.45 Å and S⋯S = 3.70 Å, *i.e.* significantly smaller than in neutral **AA1** and in the range of twice the van der Waals radii of C and S atoms respectively ($2.R_{vdW}(C)$ = 3.40 Å and $2.R_{vdW}(S)$= S⋯S = 3.60 Å). This observation illustrates an intramolecular interaction occurring between the facing TTF units upon oxidation at the first redox process (cation-radical generation). Given the fundamental interest of such species in the current literature, additional studies have to be led to finely characterized those oxidized species. This work is in progress through spectroelectrochemical analyses.

45

3. Chapter III. Dithiafulvalene-based self-assembly

As previously described in § **1.3.3**, a new class of M_2L_4 "lantern"-shaped self-assemblies has emerged recently. Construction of such structures relies on combination of "naked" square-planar metal centers having all 4 coordination sites available with bent "banana-shaped" ligand.[32, 71, 175] These cages usually possess a well-defined cavity, which is of a particular interest for host-guest chemistry using either anionic or neutral guests.[42] Nevertheless, redox-active M_2L_4 self-assembly are quite rare in literature (see § **1.5.2**). Therefore, an electron-rich redox-active motif suitable for M_2L_4 cages was developed starting from the dithiafulvalene scaffold (scheme **3.1.1**). *Nota:* By extension, the latter is in this work defined as an association between a 1,3-dithiol heterocycle and the fluorene unit.

3.1. Ligands based on dithiafulvalene (DTF)
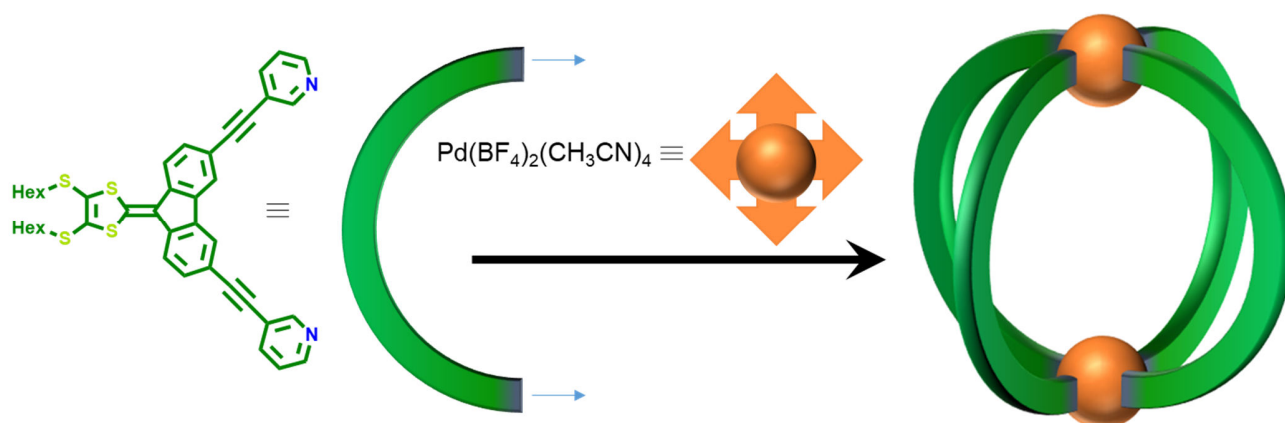
Scheme 3.1.1. Formation of a M_2L_4-type self-assembly using "banana-shaped" ligands and "naked" Palladium.

On this basis and in the course of our study related to the preparation of electron-rich metallacages, we designed the **3Py-DTF** bent ligand involving dithiafulvalene and fluorine fragments (scheme **3.1.2**). Such systems are known to retain interesting electrochemical behavior.[171, 176-177]

In order enlarge the scope of such ligand and to achieve effective coordination in a different orientation, the **4Py-DTF** isomer was also synthetized. This complementary ligand could allow to generate larger M_6L_{12} cages, such as the one recently reported by Fujita and coworkers.[175] Thioalkyl groups on the dithiol ring are added to improve general solubility.
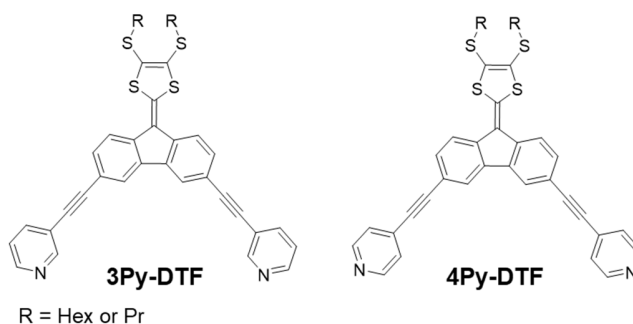
Scheme 3.1.2. Design of DTF-based ligands.

3.1.1. Synthesis

The fluorene core was obtained in two steps starting from commercially available phenanthrene-9,10-dione (scheme **3.1.3**). The first step was performed by radical bromination to compound **21** with 86% yield, followed by oxidation to compound **22** with 60% yield.

Scheme 3.1.3. Synthesis of the SHex DTF based ligands.

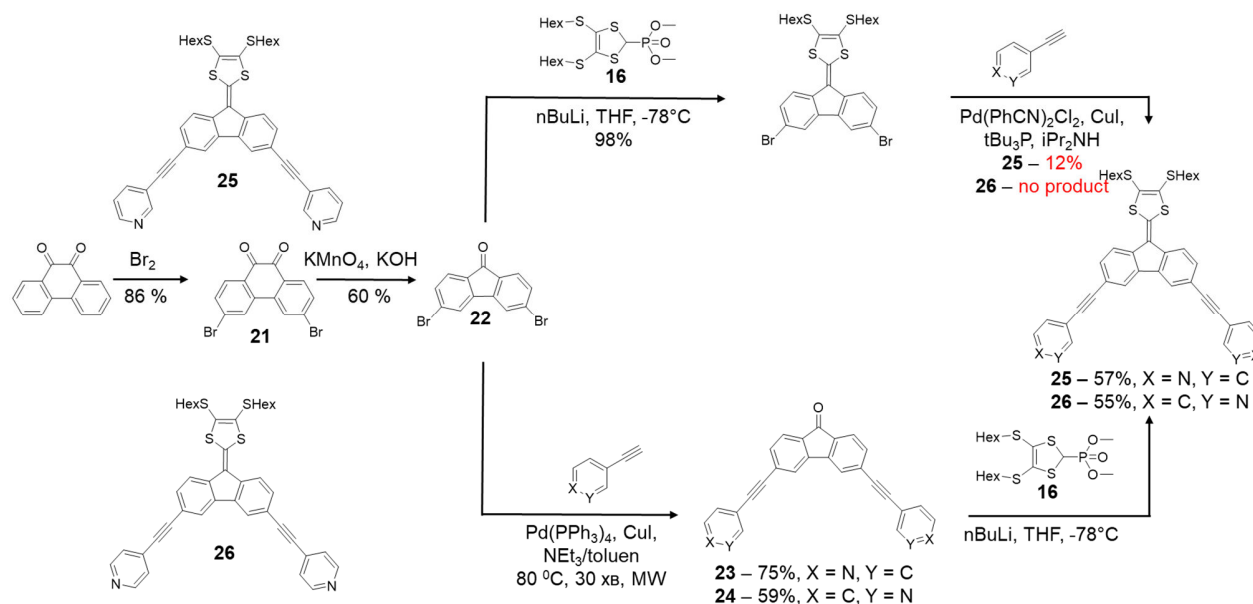At this stage, two routes can be followed to produce target ligands. Initial attempts during the PhD thesis of V. Croue involved first a Horner-Wadsworth-Emmons (HWE) reaction using the previously obtained S-hexyl phosphonate **16** to produce the intermediate dibrominated DTF compound. Unfortunately, the subsequent Sonogashira coupling reaction gave very low yield in case of ligand **25** and only traces in case of **26**. After numerous attempts, it was chosen to first perform a microwave-assisted Sonogashira coupling reaction on derivative **22**. Compounds **23** and **24** were obtained with good yields of 75% and 59% respectively, in only 30 min. Final ligands were obtained after a HWE reaction, with moderate yield of 57% and 55%. Similar ligands **27** (for **3Py-DTF** motif) and **28** (for **4Py-DTF** motif) bearing propyl chains were also synthetized using the same procedure starting from previously obtained phosphonate **17** with 46% and 40% yield respectively.

3.1.2. Characterization and electrochemical properties

Ligands **25**, **27** (**3Py-DTF**)and **26**, **28** (**4Py-DTF**) were characterized using ^{1}H, ^{13}C NMR and high-resolution mass spectrometry. Interestingly, long hexyl chains did not prevent the crystallization and crystals suitable for X-Ray analysis were obtained by slow evaporation of ligands **25** and **26** in a dichloromethane/methanol mixture (figure **3.1.1**). Nevertheless, alkyl chains remain slightly disordered in both cases. Both ligands show a nearly planar geometry with a slight folding of the dithiole rings (3.6° and 6° along the S --- S vector for **25** and **26** respectively). The pyridine units are less twisted in **26** than in **25** in relation to the central planar fluorene core with angles of ca. 5° and 13° respectively. Exocyclic double-bond has slightly longer distance (1.36 Å) than for a standard olefinic bond ($R_2C=CR_2$).[176] The angle between both ethynyl axes is close to 90° in good accordance with the expected structure. This

results in the **3Py-DTF** system for which both nitrogen pyridine atoms point towards *ca* parallel directions, providing therefore a geometry that is suitable for the synthesis of M$_2$L$_4$ coordination cages.
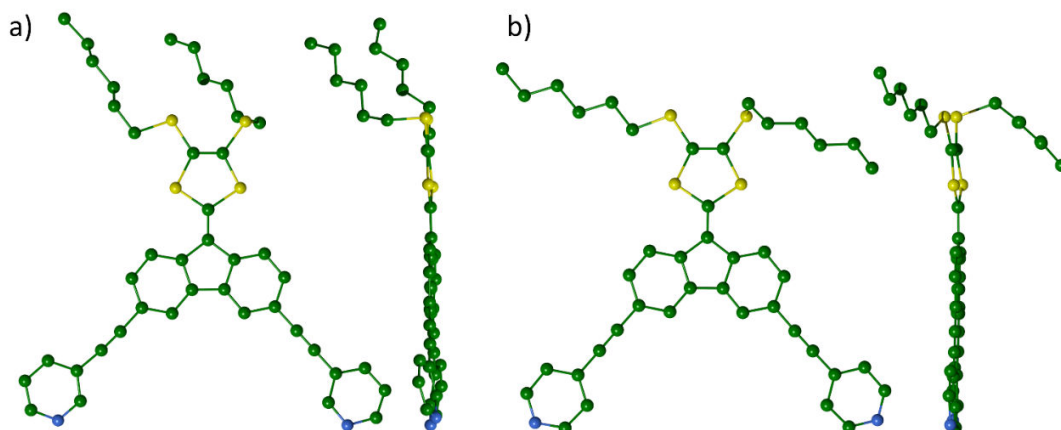

*Figure 3.1.1. X-ray analysis of ligands **25** (a) and **26** (b). Hydrogen atoms omitted for clarity.*

In principle, the DTF fragment shows two oxidation processes when studied by cyclic voltammetry. The first, reversible, corresponds to the formation of a radical-cation and the second, irreversible, to a dication.[176] However, in the case of our DTF ligands, only one irreversible oxidation process was observed in DMF, located at 0.54 V and 0.57 V *vs* Fc/Fc$^+$ for ligands **25** and **26** respectively (figure **3.1.2**, a).
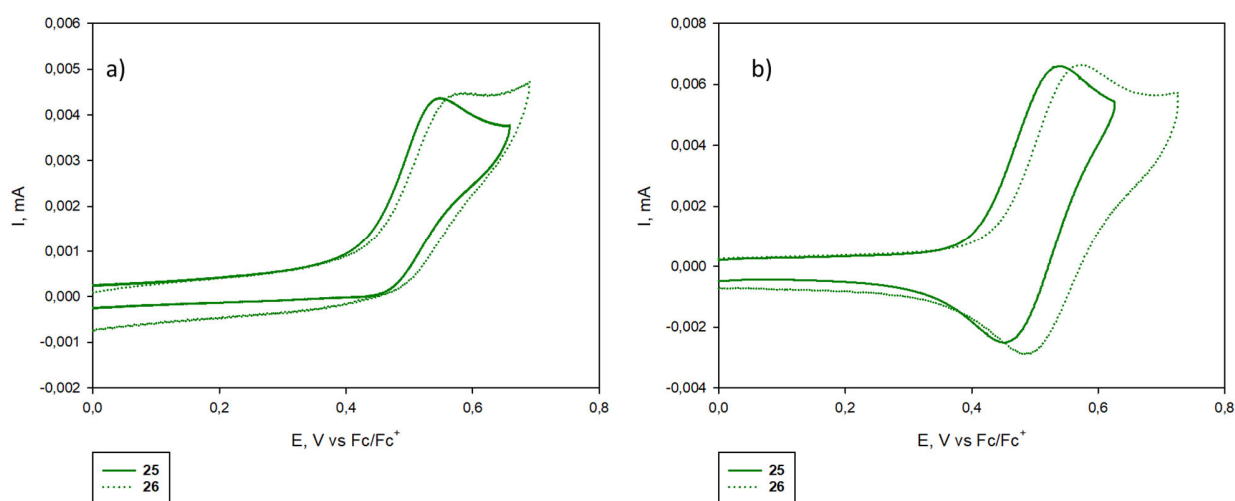
*Figure 3.1.2. Cyclic voltammetry of ligands **25** and **26** in DMF (a) and CH$_3$CN/CH$_2$Cl$_2$ (b) (C = 1 mM, n-Bu$_4$NPF$_6$ (0,1 M)), 100 mV.s^{-1}, Pt, vs Fc/Fc$^+$.*

Changing the solvent to the more conventional CH$_3$CN/CH$_2$Cl$_2$ mixture results in one reversible oxidation at 0.49 V and 0.53 V *vs* Fc/Fc$^+$ for ligands **25** and **26** respectively (figure **3.1.2**, b). Scanning at higher potential does not reveal a second oxidation process, although results in the losing the reversibility for the first oxidation. Similar results were previously obtained for an isomeric DTF compound.[177] As expected, ligands **27** and **28** bearing propyl fragments show similar behavior at the same potential

3.2. Self-assembly using "naked" Palladium[178]

3.2.1. M$_2$L$_4$ self-assembly with 3Py-DTF ligand: AA3

The self-assembly process using ligand **25** (2 equiv.) and complex Pd(BF$_4$)$_2$(CH$_3$CN)$_4$ (1 equiv.) was carried out in DMSO-d_6 at 50 ^{0}C. The reaction was followed by ^{1}H and DOSY NMR (figure **3.2.1**) and converged within 10 minutes resulting in unique species. Cage **AA3** could be easily isolated by precipitation with AcOEt after cooling down to room temperature. ^{1}H NMR spectrum of **AA3** (figure **3.2.1**, b) is characterized by well-defined signals which confirms symmetric discrete compound. Upon formation of the cage, signals of both fluorene and pyridyl moieties are downfield-shifted due to the coordination to the Pd metal center. ^{1}H DOSY NMR spectrum (figure **3.2.1**, c) exhibits a single set of signals, which confirms one discrete species in solution. As expected from a larger self-assembly structure, it exhibits a smaller D value (7.94 x 10^{-11} m^2.s^{-1}) than the corresponding ligand (D = 1.86 x 10^{-11} m^2.s^{-1}).
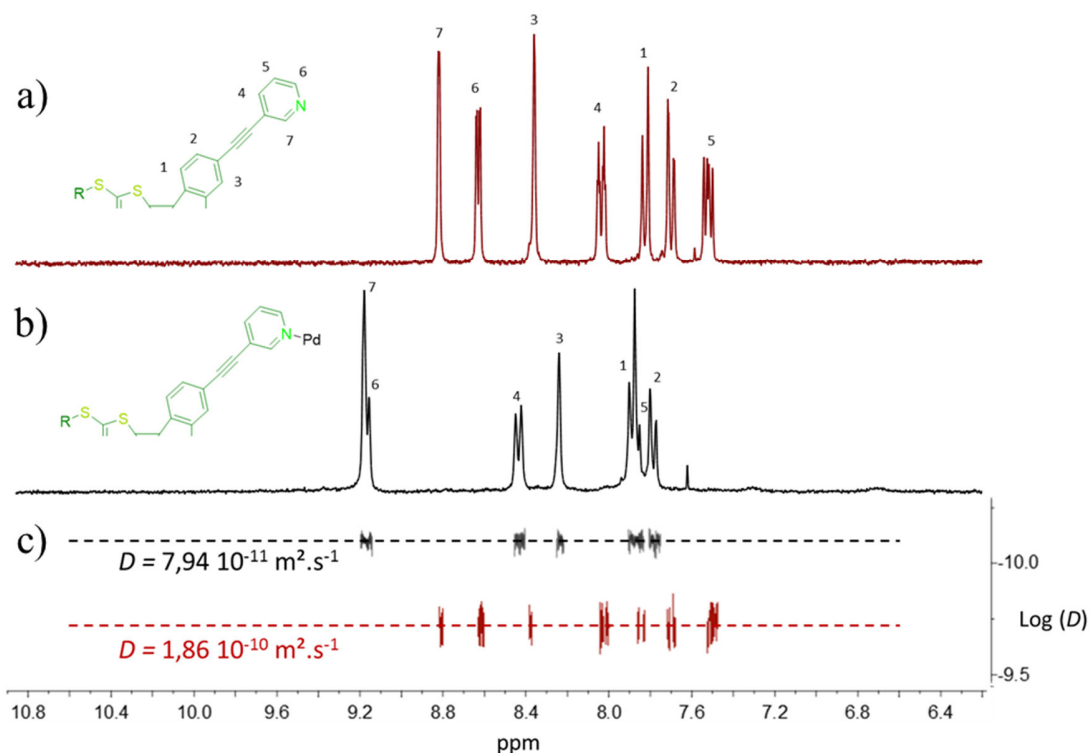
Figure 3.2.1. ^{1}H (a, b) and DOSY (c) NMR for the 25 (a, c) and AA3 (b, c) in DMSO-d$_6$.

High resolution ESI-FTICR-MS spectrometry was performed in collaboration with Drs Frédéric Aubriet and Vincent Carré from the University of Lorraine. However, initial experiments using an isolated **AA3** self-assembled complex resulted in the absence of signal due to its low solubility when analyzed from a DMSO solution. Therefore, we exchanged the BF$_4^-$ anion for the bulky tetrakis[3,5-bis(trifluoromethyl)phenyl]borate (BArF$^-$) anion in order to improve the solubility of the cage. Addition of an excess of NaBArF to the suspension of **AA3** ([**Pd$_2$L$_4$**]$^{4+}$, 4BF$_4^-$) in a CH$_2$Cl$_2$/CH$_3$NO$_2$ (1/1, v/v) mixture allowed to obtain a 10^{-3} M solution of [**Pd$_2$L$_4$**]$^{4+}$, 4BArF$^-$, which was used directly for the analysis. Thus, ESI-FTICR-MS experiment was able to confirm the M$_2$L$_4$ stoichiometry of **AA3**, with

characteristic multi-charged species at m/z = 1293.2367 corresponding to [[**Pd₂L₄**]⁴⁺, 4BArF⁻ – 3BArF⁻]³⁺ . Experimental isotopic pattern also shows good correlation with the theoretical one (figure **3.2.2**).
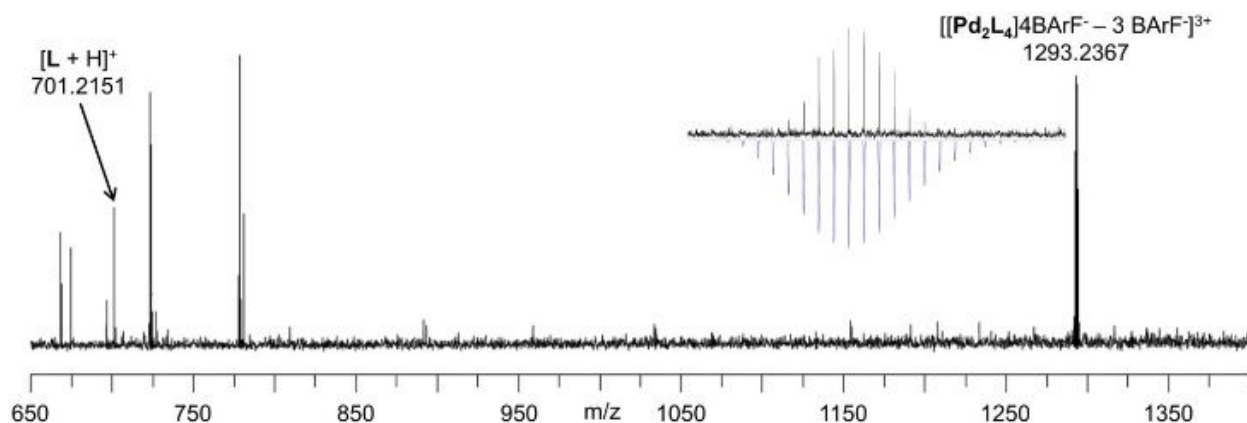
*Figure 3.2.2. ESI-FTICR-MS of cage **AA3** ([Pd₂L₄]⁴⁺,4BArF⁻) in CH₂Cl₂/CH₃NO₂ (C = 10⁻³ M).*

Despite long alkyl chains, single crystals of the self-assembly were obtained by slow vapor diffusion of AcOEt into a DMSO solution of **AA3**. X-ray data shows distance between both Palladium centers of 13.5 Å, which correlates well with DOSY data (figure **3.2.3**). They are connected via four 9-(1,3-dithiol-2-ylidene)fluorene ligands **25**. Geometrical parameters for the ligand **25** inside the cage **AA3** remain mostly the same, which confirms good compatibility of the ligand and metal center. Resulting M₂L₄ self-assembled structure has an internal cavity of approximately 600 Å³ (Figure **3.2.3**, left).[179]

*Figure 3.2.3. X-Ray crystal structure of **AA3**, lateral view (left) and top view through the Pd···Pd axis (right). Counter anions, solvent molecules and hydrogens were omitted for clarity. The cavity is depicted as a grey volume.*

3.2.2. Electrochemical properties

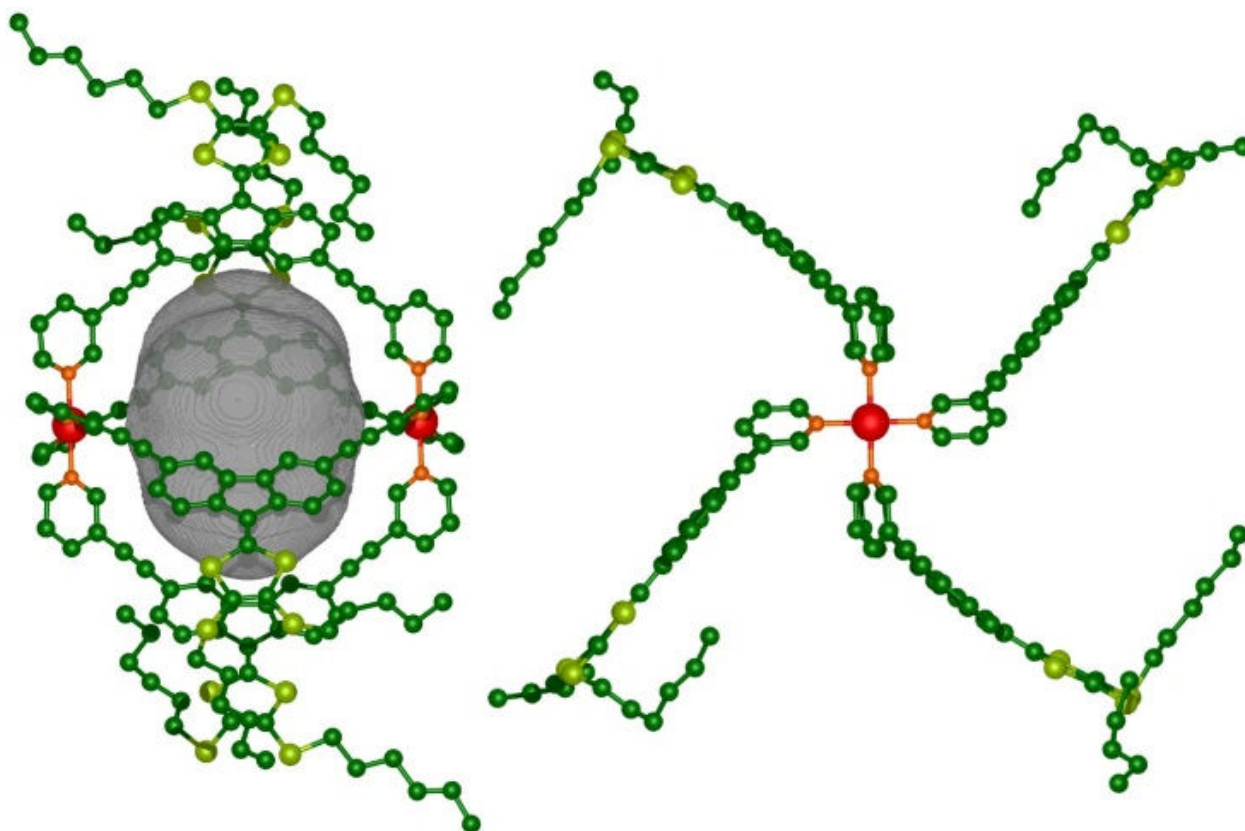The electrochemical behavior of the cage **AA3** in comparison with ligand **25** was investigated by cyclic voltammetry. Due to its solubility, cage **AA3** was first studied in DMF, resulting in one irreversible oxidation process at 0.62 V *vs* Fc/Fc$^+$, therefore having the same behavior as a starting ligand **25** with slightly higher potential (figure **3.2.4**, a). Taking into account reversible oxidation of the starting ligand **25** in the CH$_2$Cl$_2$/CH$_3$CN system, as well as literature data for similar compounds,[180] we decided to exchange initial BF$_4^-$ anion for better solubility. Therefore, 0.05 M solution of NaBArF in CH$_2$Cl$_2$/CH$_3$CN was used, ensuring both anion exchange with formation of soluble cage [**Pd$_2$L$_4$**]$^{4+}$(BArF$^-$)$_4$ and serving as a supporting electrolyte. Resulting cage **AA3BArF$^-$** has one reversible process at E$^{1/2}$ = 0.50 V *vs* Fc/Fc$^+$ (figure **3.2.4**, b), which is again slightly higher due to the coordination to Palladium ions than the initial ligand **25**. Altogether, behavior of the cage is consistent with independent one-electron oxidation of each **DTF** fragment within the cage without any electronic interaction between them.
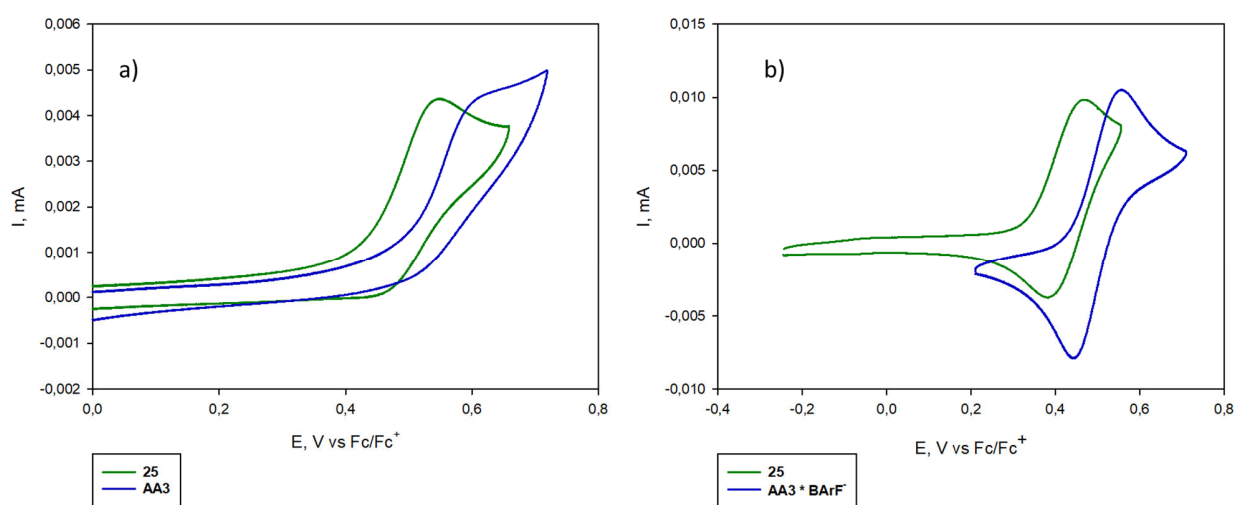
Figure 3.2.4. Normalized cyclic voltammograms of ligand 25 (C = 10^{-3} M, 0.1 M nBu$_4$NPF$_6$, 50 mV·s^{-1}, Pt) and AA3 in DMF (a) and CH$_3$CN/CH$_2$Cl$_2$ (b) (C = 5 × 10^{-4} M, 0.1 M nBu$_4$NPF$_6$ or 0.05 M NaBArF for a) and b) respectively, 50 mV·s^{-1}, Pt), V vs Fc/Fc$^+$.

3.2.3. Attempts towards M$_6$L$_{12}$ cage from 4Py-DTF

As mentioned before, **4Py-DTF** motif can be used to obtain larger M$_6$L$_{12}$ type cages, as demonstrated recently by Fujita and coworkers (figure **3.2.5**).[175] In our case we were interested in obtaining larger cages while the maintaining redox properties of the system.

Figure 3.2.5. Example of M$_6$L$_8$ self-assembly by Fujita and coworkers.

The self-assembly process was carried out in DMSO-d_6 at 50 ^{0}C. The reaction of ligand **26** (2 equiv.) and complex Pd(NO$_3$)$_2$ (1 equiv.) resulted in clear orange solution within 10 minutes. Even though resulting ^{1}H NMR spectra shows clear downfield shift of signal for α pyridil protons, which indicates successful coordination (figure **3.2.6**), lo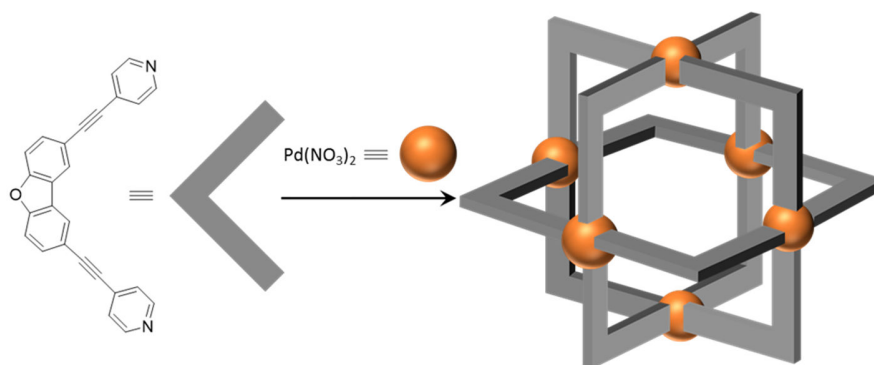w solubility of the resulting compound prevented further characterization using DOSY NMR. Attempts to grow crystal, as well as performing anion exchange using NaBArF did not succeed.
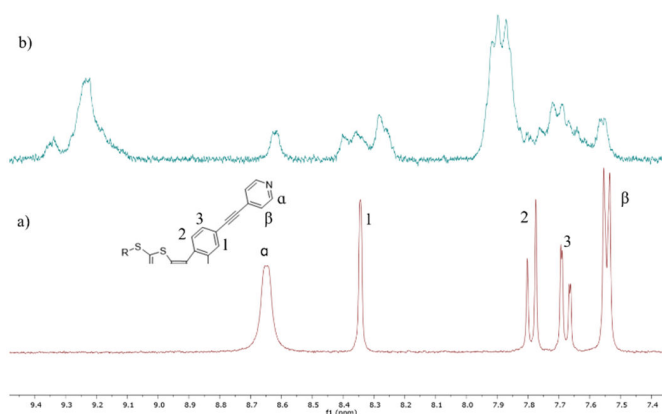
*Figure 3.2.6. ^{1}H NMR for the **26** (a) and corresponding self-assembly (b) (in DMSO-d$_6$)*

3.3. Self-assembly using *cis*-blocked Palladium[181]

Coordination of DTF-based ligands **4Py-DTF** (**26** or **28**) and **3Py-DTF** (**25** or **27**) with *cis*-blocked Pd and Pt complexes should allow for obtaining M$_2$L$_2$ metallocycles (scheme **3.3.1**). Additionally, using ferrocene-containing complexes Pddppf or Ptdppf allows introduction of an additional redox-active ferrocene fragment, which can be used as an internal electrochemical standard (chapter **1.6.2**).

3.3.1. M$_2$L$_2$ clips from 4Py-DTF: AA4 and AA5

Self-assembly process between both ligands **26** and **28** and Pd(dppf)OTf$_2$ were carried out in CD$_2$Cl$_2$, and followed by ^{1}H and DOSY NMR (figure **3.3.1**). After only 10 minutes, both reactions converged to the formation of unique structures **AA4** and **AA5** respectively, that could be isolated by a simple precipitation with Et$_2$O.
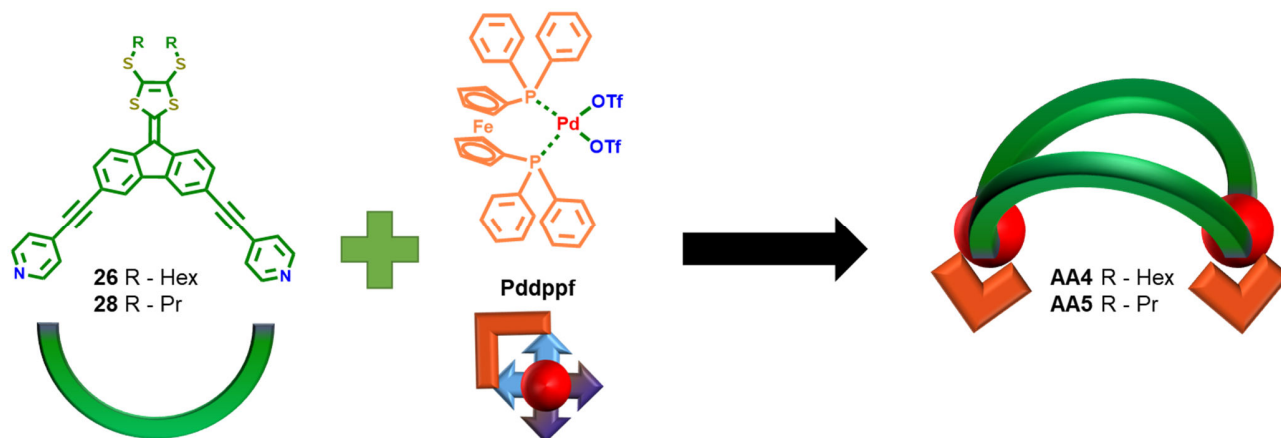
*Scheme 3.3.1. Self-assembly process for M₂L₂ self-assembled clips using **4Py-DTF** ligands.*

¹H NMR spectrum of the resulting solid shows a single set of well resolved signals, which is characteristic for a symmetrical discrete self-assembly structure (figure **3.3.1**, b). Signals of pyridyl protons H_4 and H_5 are upfield shifted in comparison to the starting ligand **26**, as a result of through-space interactions between the pyridyl groups and the coligand phenyl units (dppf), therefore confirming coordination to the acceptor. A ¹H DOSY NMR experiment exhibits a single set of signals with a diffusion value of D = 5.03 x 10⁻¹⁰ m²·s⁻¹, indicating formation of a single discrete structure. Stokes-Einstein equation REF allows to calculate a hydrodynamic radius of ca. 10 Å (T = 298 K), which is consistent with expected M₂L₂ architecture [Pd₂L₂(OTf)₄].
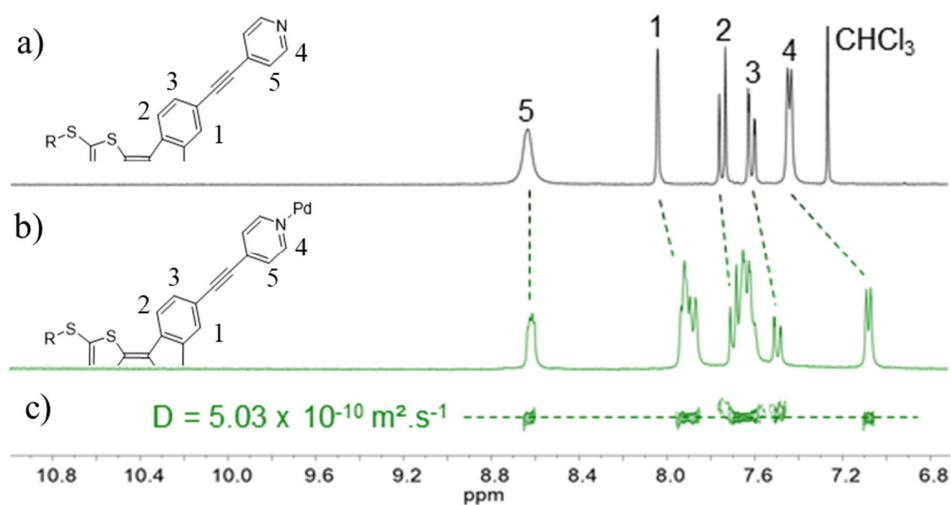
*Figure 3.3.1. ¹H (a, b) and DOSY (c) NMR for the **26** (in CDCl₃) and **AA4** (in CD₂Cl₂).*

High resolution ESI-FTICR-MS spectrometry was done in collaboration with Drs Frédéric Aubriet and Vincent Carré in the University of Lorraine. Surprisingly, in addition to signal of expected M₂L₂ molecular clip ([**Pd₂(25)₂(OTf)₄**] - 2OTf]²⁺; m/z = 1510.1598), peaks of higher molecular mass were observed despite the variation of the instrumental conditions, the concentration (10⁻⁵ M< C < 10⁻³ M) and the solvent (figure **3.3.2**).
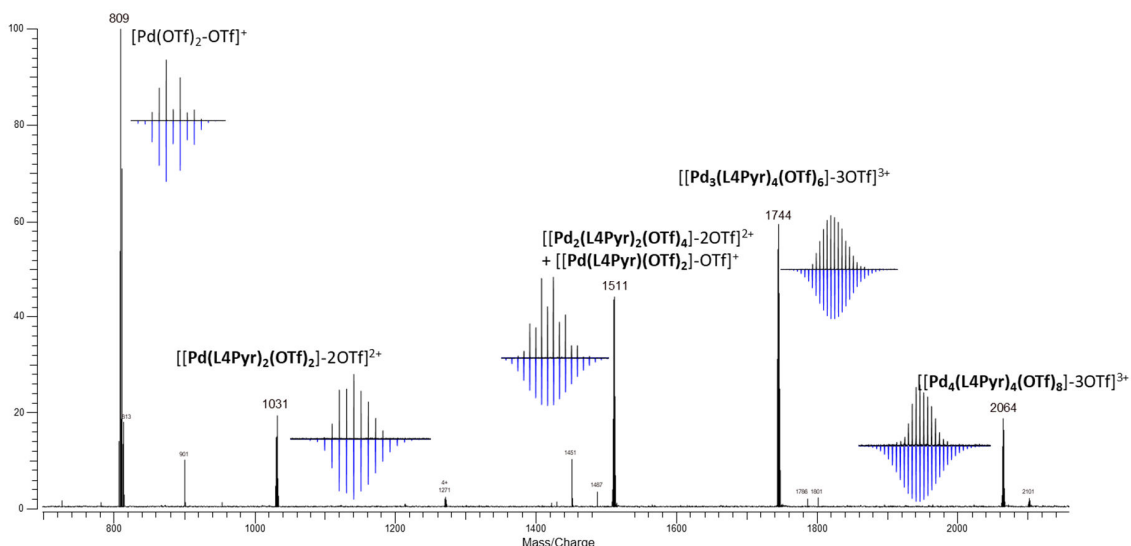
*Figure 3.3.2. ESI-FTICR mass spectrum of **AA4** in CH$_2$Cl$_2$ (9/1) (C = 10^{-3} M), in black experimental isotopic pattern, in blue theoretical isotopic pattern.*

Some additional signals were identified as M$_4$L$_4$ ([[**Pd$_4$(25)$_4$(OTf)$_8$**] - 3OTf]$^{3+}$; m/z = 2064.1986) and sometimes M$_6$L$_6$ species. Taken into account previous DOSY NMR data, this data suggests aggregation of the starting M$_2$L$_2$ cage upon ESI with formation of dimer and trimer associates. Such occurrences are known in literature at high concentration and with soft ionization conditions.[182] Attempts to apply IRMPD technique didn`t give sufficient results.

3.3.2. Structural properties

Fortunately, single crystals could be grown by slow diffusion of MeOtBu in a CH$_2$Cl$_2$ solution containing **AA4** (C = 1 mM). X-ray crystallography analyses confirmed unambiguously the expected M$_2$L$_2$ stoichiometry (figure **3.3.3**).

*Figure 3.3.3. X-ray crystal structure of **AA4**, (a) crystal packing showing two independent discrete assemblies (blue and turquoise respectively), (b) top view and (c) lateral view of turquoise metalla-macrocycle (related to (a)). Counter anions, solvent molecules and hydrogen atoms (b, c) omitted for clarity.*

X-ray structure indicates two separate assemblies within the crystal packing (figure **3.3.3**, a). Both structures have the same stoichiometry and general structure, but differ i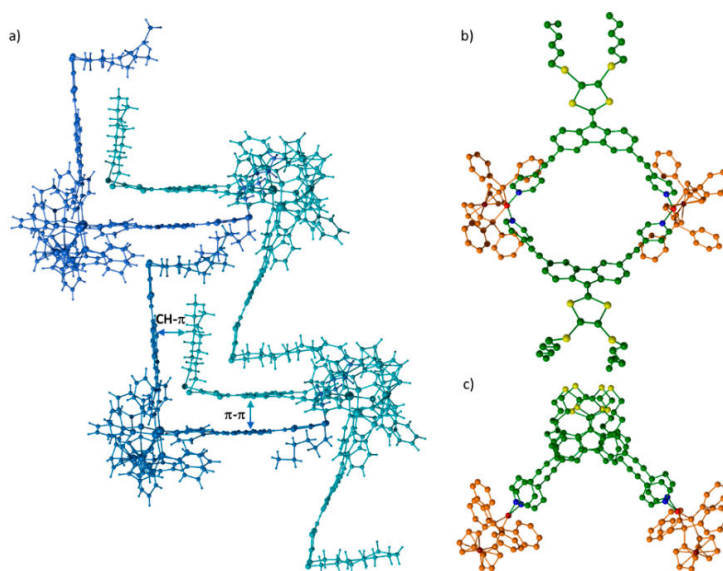n dihedral angle between DTF planes with values of 88.7° and 58.1° for blue and turquoise species respectively. Interplanar distance of 3.45 Å between the respective DTF units of two separate assemblies indicates significant π–π interactions, in addition to CH–π interactions between DTF units and SHex chains. Similar to **AA3**, geometrical parameters of ligand **26** remain mostly the same, despite the increase of twisting between the DTF core and ethynilpyridine units to 12.5°.

3.3.3. Interaction with C_{60} and its derivatives

Since the first isolation of fullerene C_{60}, several artificial π-electron rich supramolecular receptors have been synthesized in the context of selective separation of C_{60} from the fullerite composites containing other large analogues such as C_{70} and C_{120}. It has been concluded in the reported literature that a bowl-shaped host is considered to be an ideal host to embrace the curved-surface of C_{60} through concave−convex, "ball-and-socket" π−π interactions, or C−H−π interactions.[183] Recently, a stable inclusion complex with C_{60} through a π−π interaction by a similar carbazole-based M_2L_2 self-assembly clip was illustrated by Mukherjee and coworkers (figure **3.3.4**).[32] Therefore, metallocycles **AA4** and **AA5** should also present compatible geometries for interaction with C_{60} and should benefit from their electron-rich side walls
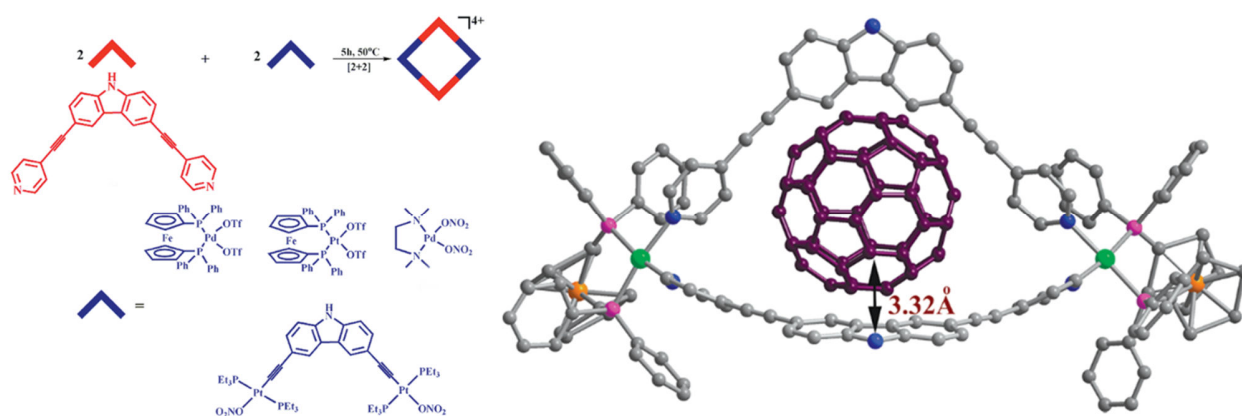
Figure 3.3.4. Example of host-guest complex using C_{60} and M_2L_2 self-assembly clip.[32]

Regarding the lack of solubility of C_{60}, interaction was fist studied by UV-vis absorption. UV-Vis spectra of ligand **26** and metalla-macrocycle **AA4** were recorded in dichloromethane at $C = 1.5 \times 10^{-5}$ M (Figure 3.3.5). Ligand **26** shows two high energy absorption bands at 290 nm and 350 nm, which can be attributed to π–π* transitions located on the fluorene and pyridines units respectively. They are followed by an intense low energy band at 460 nm ($\varepsilon = 46,000$ $M^{-1} \cdot cm^{-1}$), which has an ICT character from the HOMO localized on the DTF unit to the LUMO of the electron accepting pyridyles.[184] Self-assembly **AA4** shows a similar profile. It has its maxima shifted to lower energy ($\lambda_{max} = 483$ nm) in comparison with starting ligand, which is expected from metal coordination. ε values of the **AA4** are also twice higher ($\varepsilon = 102,000$ $M^{-1} \cdot cm^{-1}$), which correlates well with established M_2L_2 composition of the metalla-ring.

Figure 3.3.5. UV-vis absorption spectra of ligand 26 and metalla-macrocycle AA4, r.t. (C = 1.5 × 10⁻⁵ M in CH₂Cl₂).

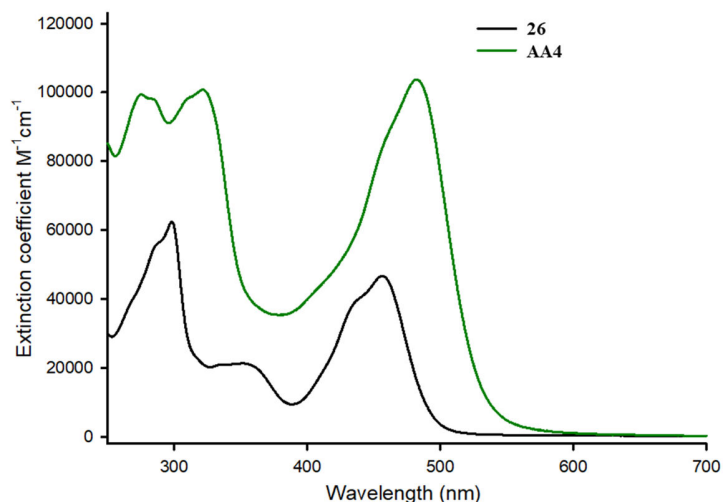Unfortunately, subsequent attempts to evaluate interaction between the supramolecular clip **AA4** and **C₆₀** by UV-vis titration gave conflicting results. Therefore ¹H NMR studies were carried out.

Study by ¹H NMR of a stoichiometric mixture of C_{60} and metallacyle **AA4** in tetrachloroethane-d_2 showed no significant shift in the signals of the cage. However, appearance of new signals in the aromatic region was observed along with the deterioration of the signals belonging the cage (figure **3.3.6**, a). This data suggests photodestruction of the cage. Control experiment using the mixture of starting ligand **26** and C_{60} resulted in the similar ¹H NMR (figure **3.3.6**, b). Interestingly, only the fluorene signals change significantly, while pyridil protons remain the same. Therefore, the most probable mechanism is a photooxidation of the exocyclic double bond resulting in ketone **24**. This was further confirmed by mass-spectra of the fully decomposed mixture, which showed signals of ketone **24** for both self-assembly and pure ligand. However, in the absence of light or in the inert atmosphere the mixture remains stable. Nevertheless, one can note that degradation of ligand **26** in **AA4** occurs much faster indicating efficient interaction between C_{60} and **AA4**.
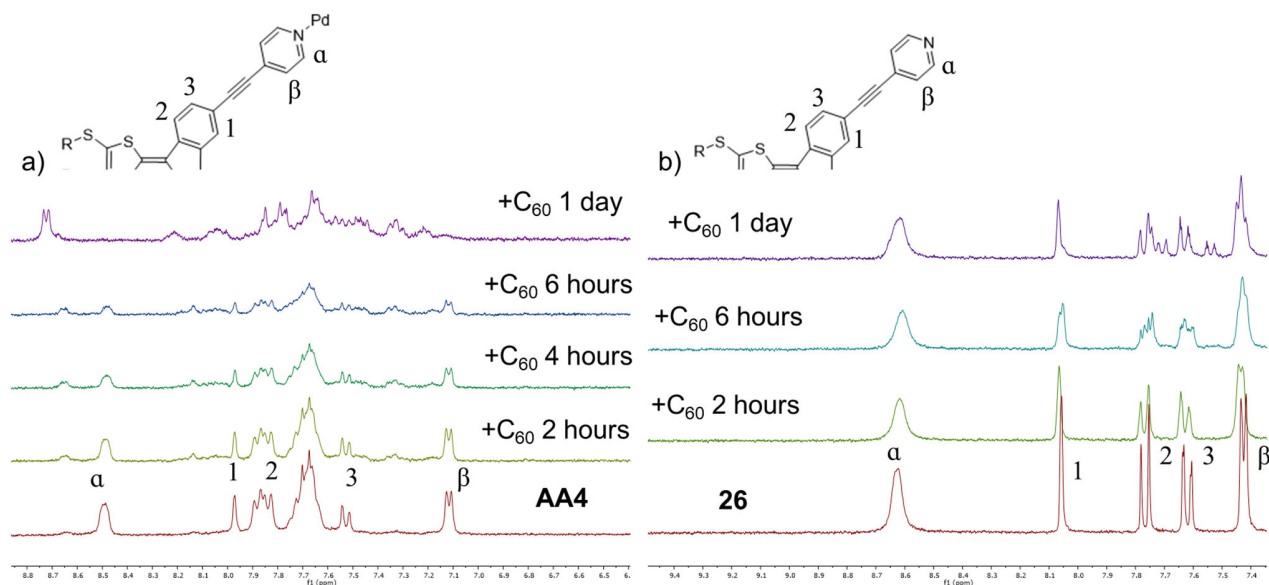
Figure 3.3.6. Progression of ¹H NMR for the mixture of C₆₀ with clip AA4 (a) and ligand 26 (b) upon irradiation, (C₂H₂Cl₄-d₂).

57

To simplify interpretation of the host-guest interaction, we then moved to phenyl-C_{61}-butyric acid methyl ester (PC$_{61}$BM) for its higher solubility. Additionally, it is widely used as a component for solar cells or flexible electronics as an electron acceptor.[185]

^{1}H and DOSY NMR experiments were performed in deuterated chloroform (figure **3.3.8**). Unfortunately, no significant shift for the signals of the clip was observed. Nevertheless, DOSY NMR shows change in the D value of PC$_{61}$BM from 4,23 x 10^{-10} m^{2}s^{-1} to 1,85 x 10^{-10} m^{2}s^{-1}. This confirms substantial interaction between the clip and guest PC$_{61}$BM. However, irradiation of the mixture results in the similar decomposition (figure **3.3.8**, d)
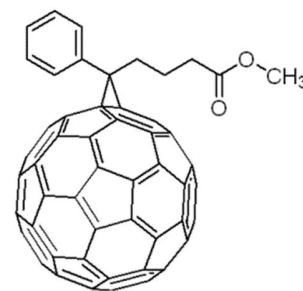
Figure 3.3.7. Phenyl-C_{61}-butyric acid methyl ester (PC$_{61}$BM)

Figure 3.3.8. ^{1}H and DOSY NMR of PC$_{61}$BM (a), AA4 (b) and their mixture as formed (c) and after 2hr irradiation (d).

3.3.4. Electrochemical properties

The electrochemical properties of ligand **26** and complex **AA4** were studied by cyclic voltammetry in CH$_3$CN/CH$_2$Cl$_2$ (1/1, v/v) (figure **3.3.9**).

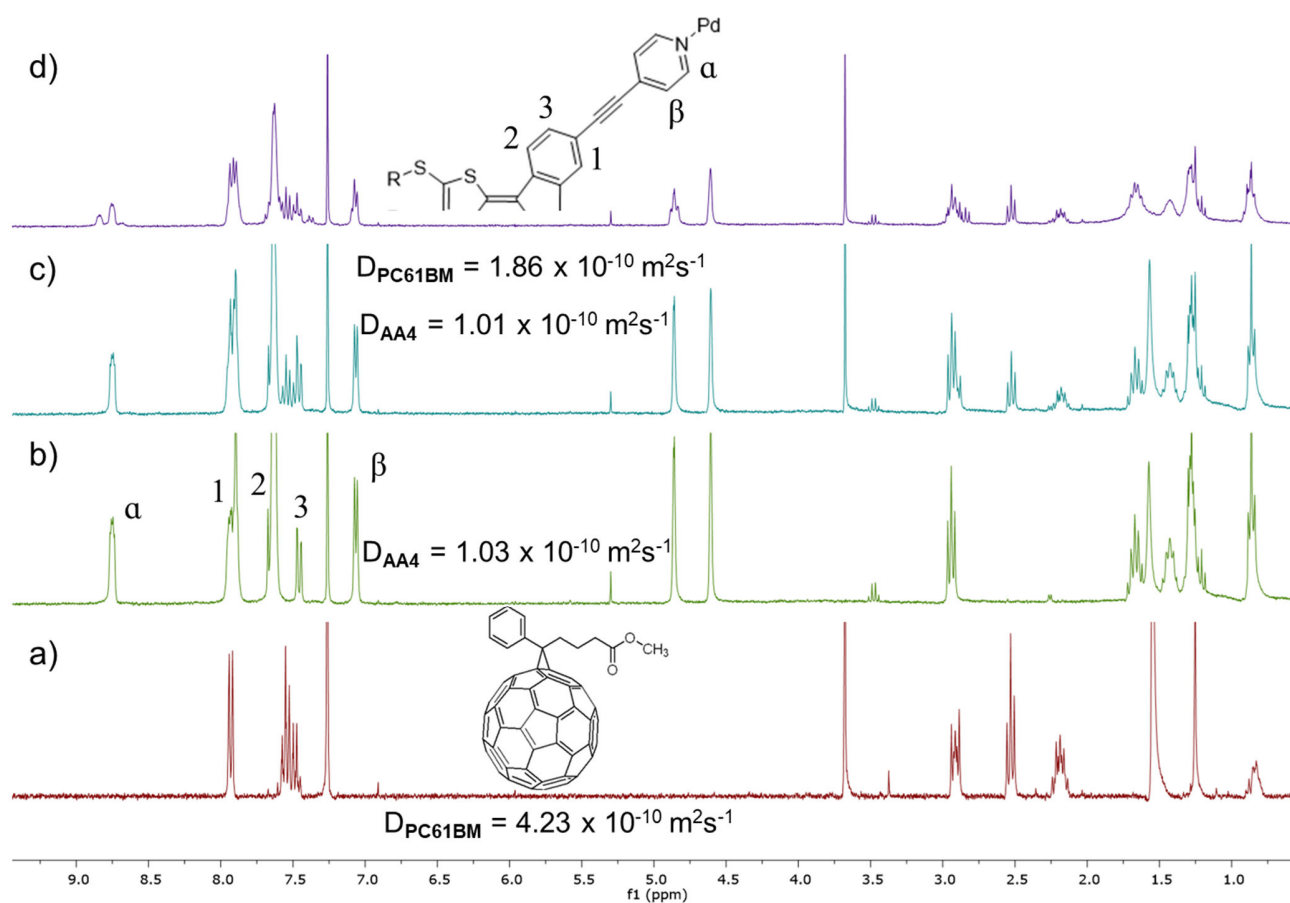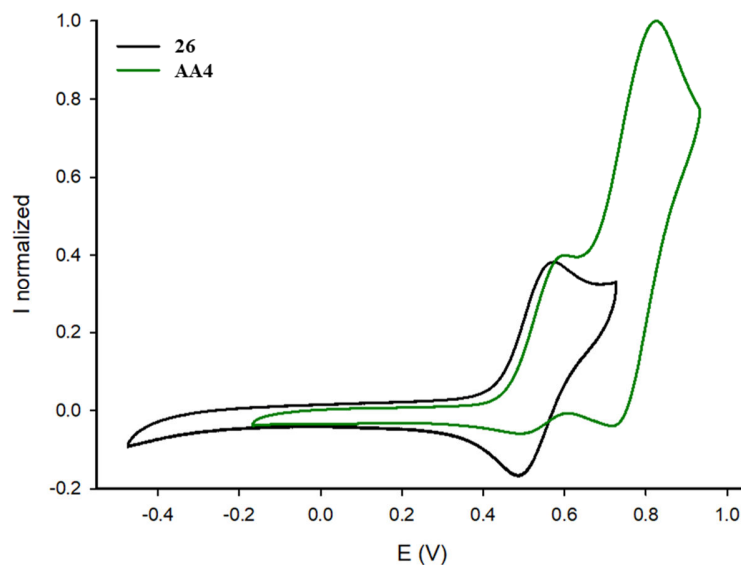*Figure 3.3.9. Normalized cyclic voltammograms of ligand **26** and metalla-ring **AA4** (C = 10^{-3} M, CH$_3$CN/CH$_2$Cl$_2$, 0.1 M nBu$_4$NPF$_6$, 100 mV·s^{-1}, Pt) V vs. Fc/Fc$^+$.*

Metalla-cycle complex **AA4** exhibits two reversible oxidation waves. The first process (E$_1$ = 0.59 V *vs.* Fc/Fc$^+$) can be assigned to the oxidation of the DTF fragment and is anodically shifted by 20 mV regarding the free ligand as a result of coordination to the metal center. Second process (E$_2$ = 0.83 V *vs.* Fc/Fc$^+$) correspond to the oxidation of the ferrocene moieties within the dppf fragment. Both processes present similar intensities, as expected from the M$_2$L$_2$ composition of the self-assembly. Altogether, this behavior suggests that both organic redox active DTF units behave independently upon oxidation to their radical cation state and that they do not interact electronically. Electrochemical behavior of clip **AA5** is similar due to the weak influence of the aliphatic groups.

3.3.5. M$_2$L$_2$ clips from 3Py-DTF: AA6 and AA7

Despite slightly different geometry, **3Py-DTF** ligands can also participate in a self-assembly process with *cis*-blocked acceptors. Reaction of ligand **25** (3Py-DTF SPr) and complex Pd(dppf)OTf$_2$ was carried out in similar conditions and converged within 10 minutes. Presence of the non-symmetric 3-pyridyl unit leads to a more complex ^{1}H NMR spectrum (figure **3.3.10**). Nevertheless, all aromatic signals could be attributed using a COSY experiment (annexes **3.4-3.9**). All pyridyl proton signals are upfield shifted after coordination to the metal except H$_6$, indicating that the latter does not interact with the dppf coligand. The presence of only one discrete species is confirmed by ^{1}H DOSY NMR experiment that show a single set of signals with diffusion coefficients D = 4.96 x 10^{-10} m².s^{-1} respectively. This observation suggests that self-assembly structure has similar size to **AA4**, with an estimated hydrodynamic radius of ca 10 Å extracted from the Stokes-Einstein equation (T = 298K), a value which is compatible with the formation of M$_2$L$_2$ architectures.
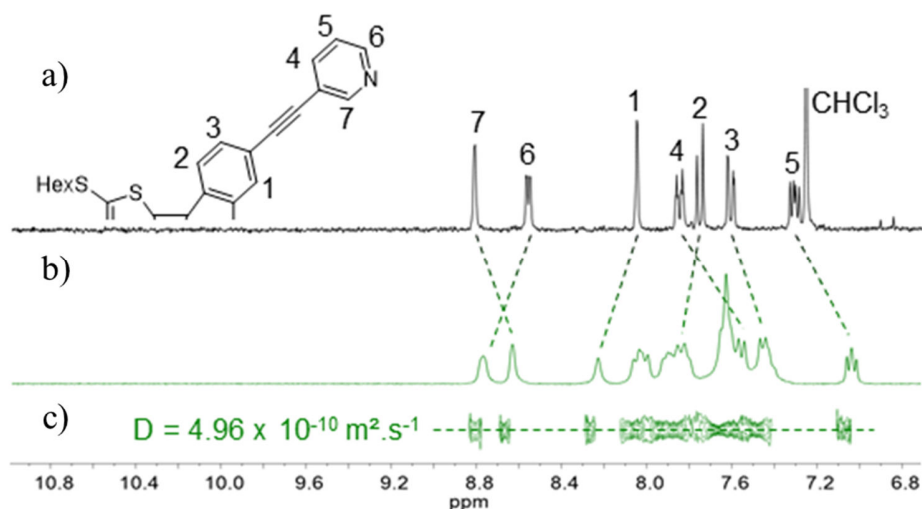
*Figure 3.3.10. ^1H (a, b) and DOSY (c) NMR for the 25 (a) and **AA6** (b,c) (in CD$_2$Cl$_2$).*

High resolution ESI-FTICR-MS spectrometry was done in collaboration with Drs Frédéric Aubriet and Vincent Carré in the University of Lorraine in order to confirm the stoichiometry of self-assembly **AA6**. Surprisingly, in addition to signal of expected M$_2$L$_2$ molecular clip ([**Pd$_2$(25)$_2$(OTf)$_4$**] - 2OTf]$^{2+}$; m/z = 1510.1598), peaks of higher molecular mass were observed despite the variation of the instrumental conditions, the concentration (10^{-5} M< C < 10^{-3} M) and the solvent (annex **5.1**). Some additional signals were identified as M$_4$L$_4$ ([[**Pd$_4$(25)$_4$(OTf)$_8$**] - 3OTf]$^{3+}$; m/z = 2064.1986) and sometimes M$_6$L$_6$ species. Taken into account previous DOSY NMR data, this data suggests aggregation of the starting M$_2$L$_2$ cage upon ESI with formation of dimer and trimer associates. Such occurrences are known in literature and were already observed in case or **AA4**.[182] Attempts to apply IRMPD technique also didn`t give sufficient results, similar to the self-assemblies with **4Py-DTF** ligands.

3.3.6. Electrochemical properties

The electrochemical properties of ligand **26** and complex **AA6** were studied by cyclic voltammetry in CH$_3$CN/CH$_2$Cl$_2$ (1/1, v/v) (figure **3.3.11**).
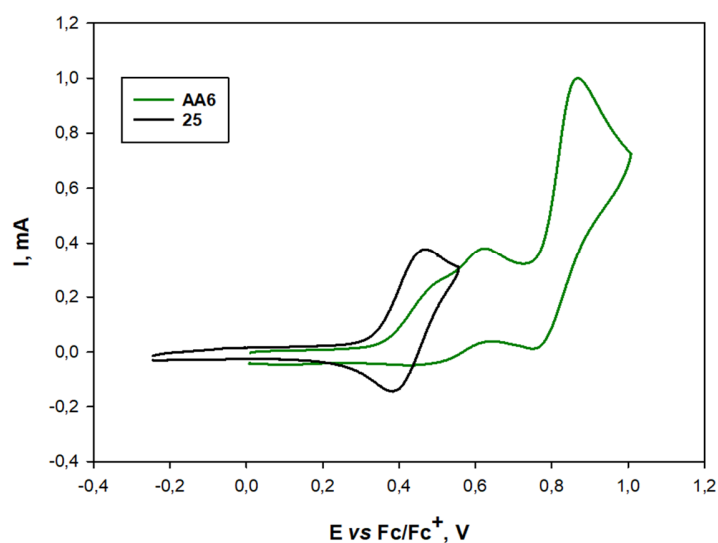
*Figure 3.3.11. Normalized cyclic voltammograms of ligand **25** and metalla-ring **AA6** (C = 10⁻³ M, CH₃CN/CH₂Cl₂, 0.1 M nBu₄NPF₆, 100 mV·s⁻¹, Pt) V vs. Fc/Fc⁺.*

Interestingly, in contrast to the complexes **AA4** and **AA5** obtained from **4Py-DTF** ligands, clip **AA6** presents three reversible oxidation waves. The first two correspond to the oxidation of DTF units, while the second is centered on the ferrocene moieties like the previous examples. The splitting of the first oxidation process is most likely due to the formation of the mixed-valence species during the oxidation process, similar to the cage **AA1**.
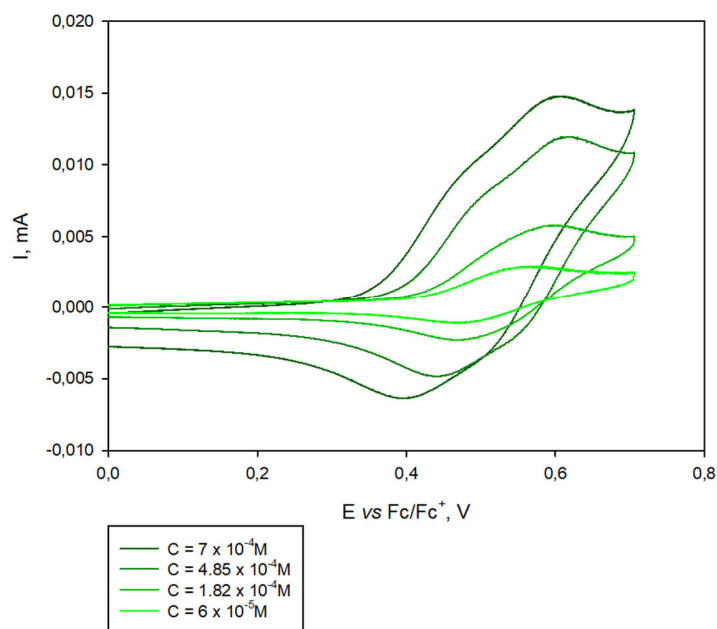
*Figure 3.3.12. Cyclic voltammograms of metalla-ring **AA6** at different concentration (CH₃CN/CH₂Cl₂, 0.1 M nBu₄NPF₆, 100 mV·s⁻¹, Pt) V vs. Fc/Fc⁺.*

This process can occur due to either intermolecular[156] or intramolecular interactions. To check this, cyclic voltammetry experiment was performed with different concentrations. Upon dilution data

shows diminishing of the current power, but the split structure remains (figure **3.3.12**). This confirms that the formation of the mixed-valence species is caused by intramolecular interaction of DTF fragments within one clip.

3.3.7. Structural properties

Unfortunately, attempts to grow single crystal for the x-ray analysis were unsuccessful so far. Nevertheless, theoretical calculations using the MM+ model (HyperChem 8.0.8) for the M_2L_2 complex show much closer position of the DTF fragments with a S---S distance of 3.55 Å (figure **3.3.13**). Such a proximity of the DTF units allows to explain the electrochemical behavior.
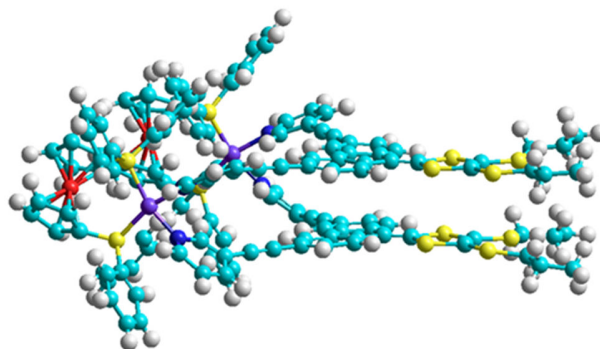
Figure 3.3.13. MM+ model of the self-assembly AA7.

3.3.8. Intercalation attempts using DCTNF

According to the theoretical calculations for **AA7**, close distance between the DTF panels isn`t suitable for interaction with large molecules like C_{60}. Nevertheless, it should efficiently bind planar neutral and specifically electron-accepting molecules. We tested several possible guest molecules, out of which only DCTNF has shown efficient interaction (figure **3.3.14**).

| pyrene | coronene | 9H-fluorene-9-one | DCF | DCTNF |
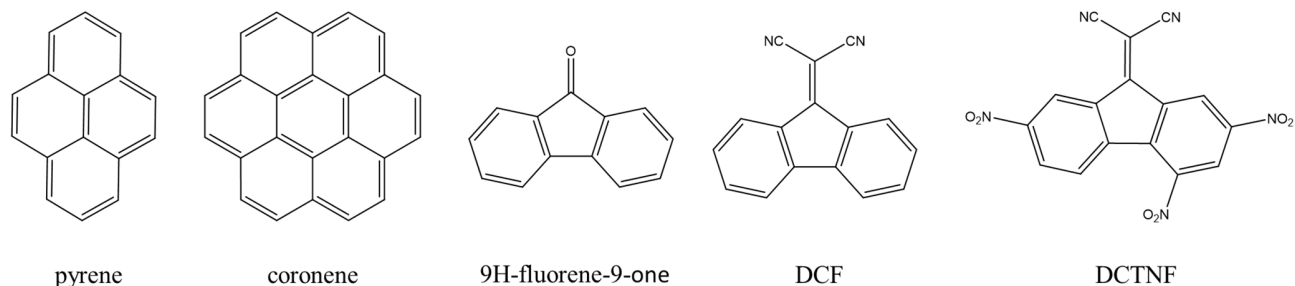
Figure 3.3.14. Possible guest molecules

In this case, the redox-active behavior of the ligand and of the corresponding cage allows to study the host-guest interaction through cyclic voltammetry. Upon intercalating between the DTF panels, guest molecule disrupts formation of the mixed-valence species. This results in recovering the conventional oxidation process (figure **3.3.15**, a). As expected, similar studies with **AA5** did not show significant changes upon interaction with DCTNF (figure **3.3.15**, b).
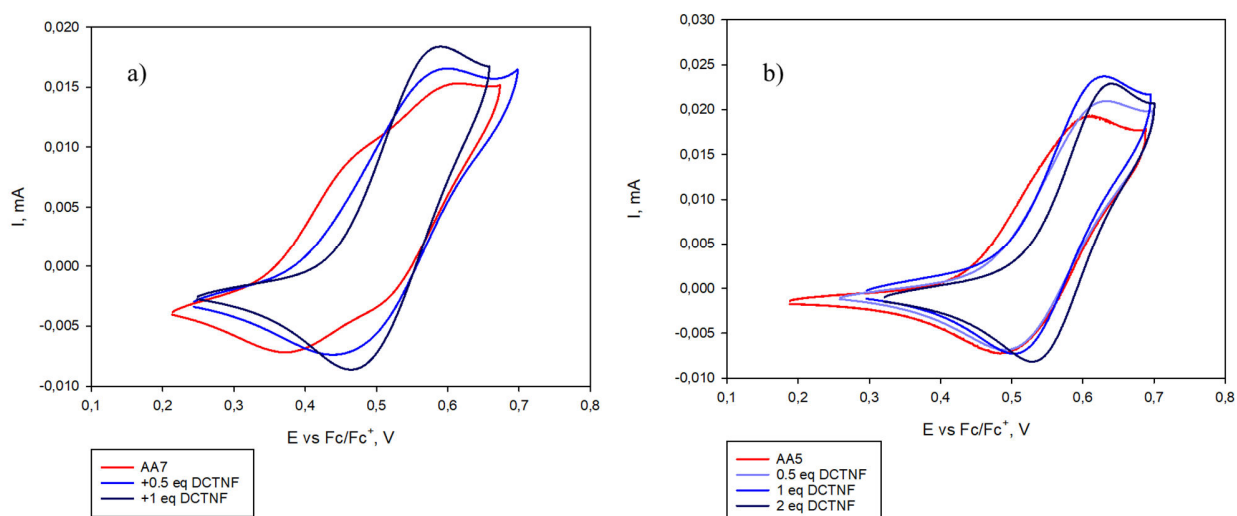
*Figure 3.3.15. Normalized cyclic voltammograms of metalla-ring **AA5 (b)** and **AA7 (a)** with DCTNF guest (C = 5 x 10^{-4}M, CH$_3$CN/CH$_2$Cl$_2$, 0.1 M nBu$_4$NPF$_6$, 100 mV·s^{-1}, Pt) V vs. Fc/Fc$^+$.*

Host-guest interaction was also studied using ^{1}H and DOSY NMR. Even though ^{1}H NMR shows shift in the signals, the resulting broadening and overlap of the signals does not allow to interpret the result (figure **3.3.16**). DOSY NMR does not show significant change in the clip (D = 5.01 x 10^{-10} m^2.s^{-1} for free clip), but confirms binding of the guest (D = 1.12 x 10^{-9} m^2.s^{-1} for free guest in CDCl$_3$).
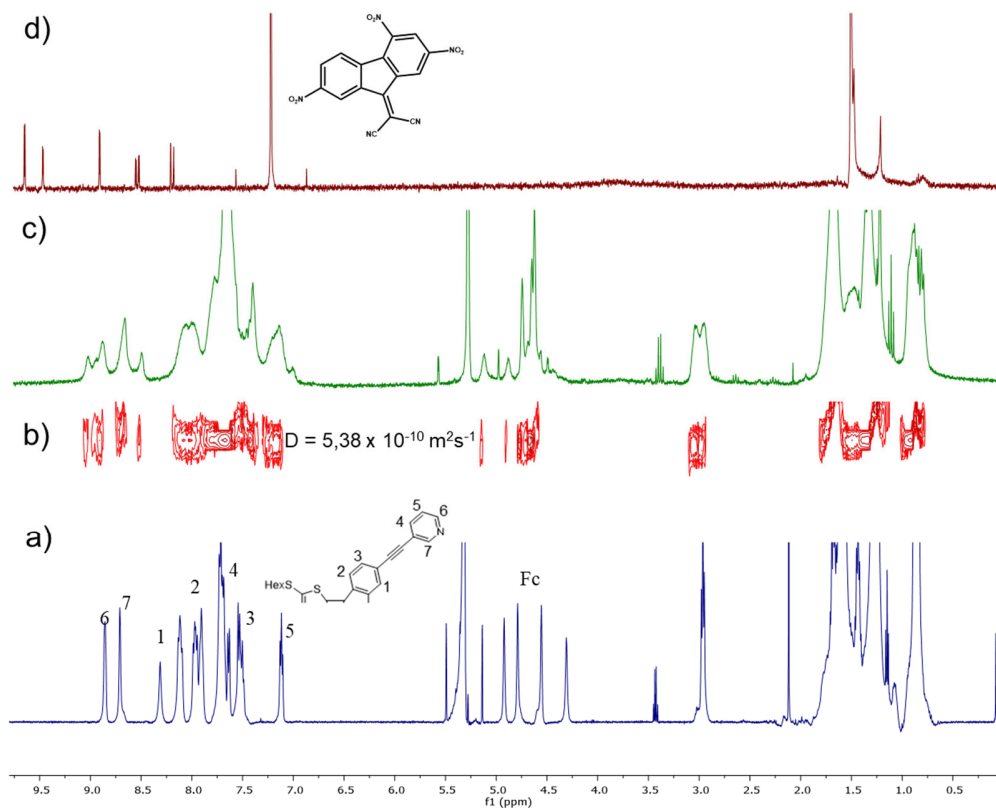
*Figure 3.3.16. ^{1}H (a, c, d) and DOSY (b) NMR for the **AA6, DCTNF** and their mixture 1/1 (in CD$_2$Cl$_2$ for a,b,c and CDCl$_3$ for d)*

In case of self-assemblies **AA4-AA5** constructed from 4PyrDTF ligands, more simple ^{1}H NMR spectra are obtained for a stoichiometric mixture of guest and clip. It allows to better investigate host-guest interaction. ^{1}H NMR shows significant shift for both DCTNF guest and fluorene signals of the clip (figure **3.3.17**). At the same time, signals of pyridyl protons are not shifted, which correlates well with binding of the guest with the DTF unit. A ^{1}H DOSY NMR confirms the interaction between the clip and the DCTNF since the diffusion coefficient of the DCTNF is decreased in presence of **AA5**.
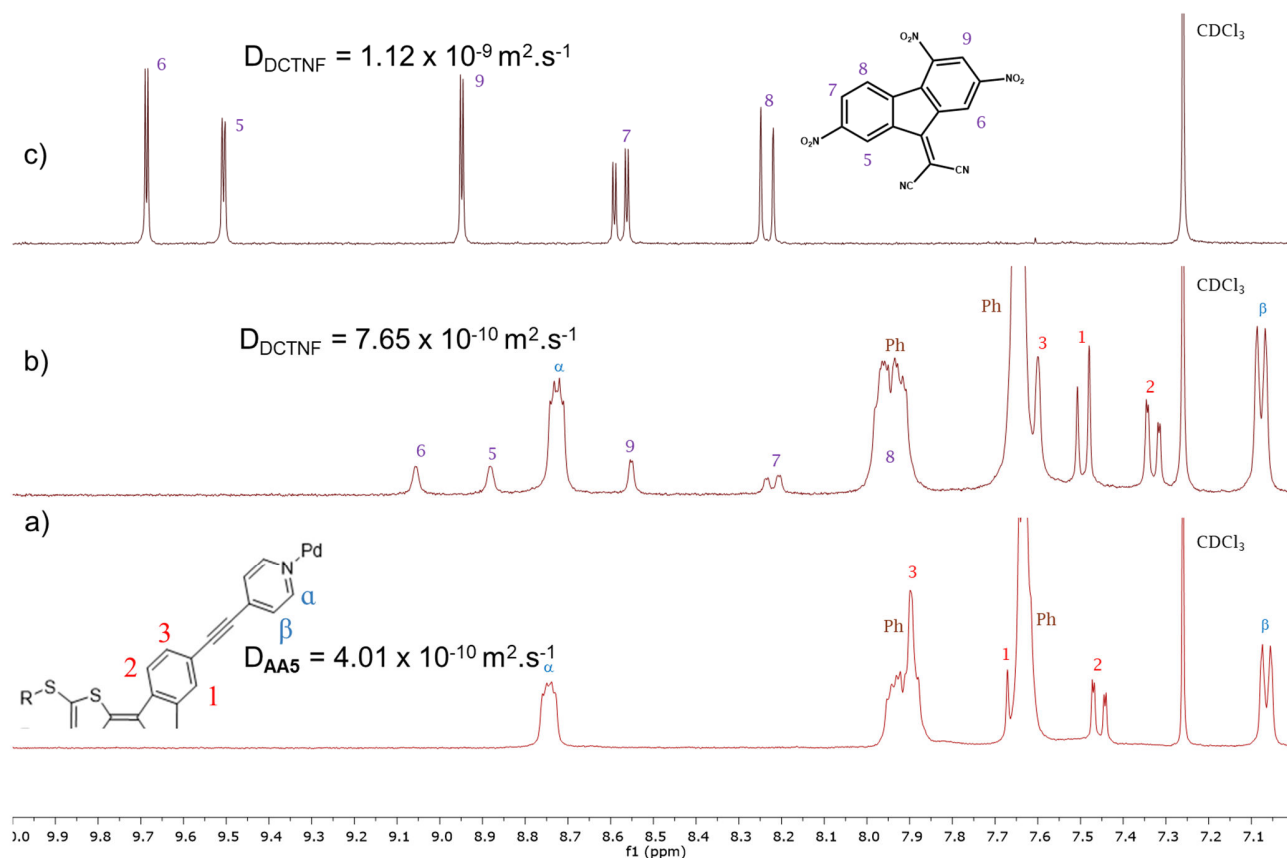
*Figure 3.3.17. ^{1}H and DOSY NMR for the AA5 (a), **DCTNF** (b) and their mixture 1/1 (c) (in CDCl₃).*

Further ^{1}H NMR titration and corresponding Job`s plot indicates a 1:2 interaction with DCTNF, as shown by the shift of H_2 and H_3 protons (figure **3.3.18**). This correlates well with larger distance between DTF fragments and resulting interaction of each DTF panel with one guest molecule separately.

64
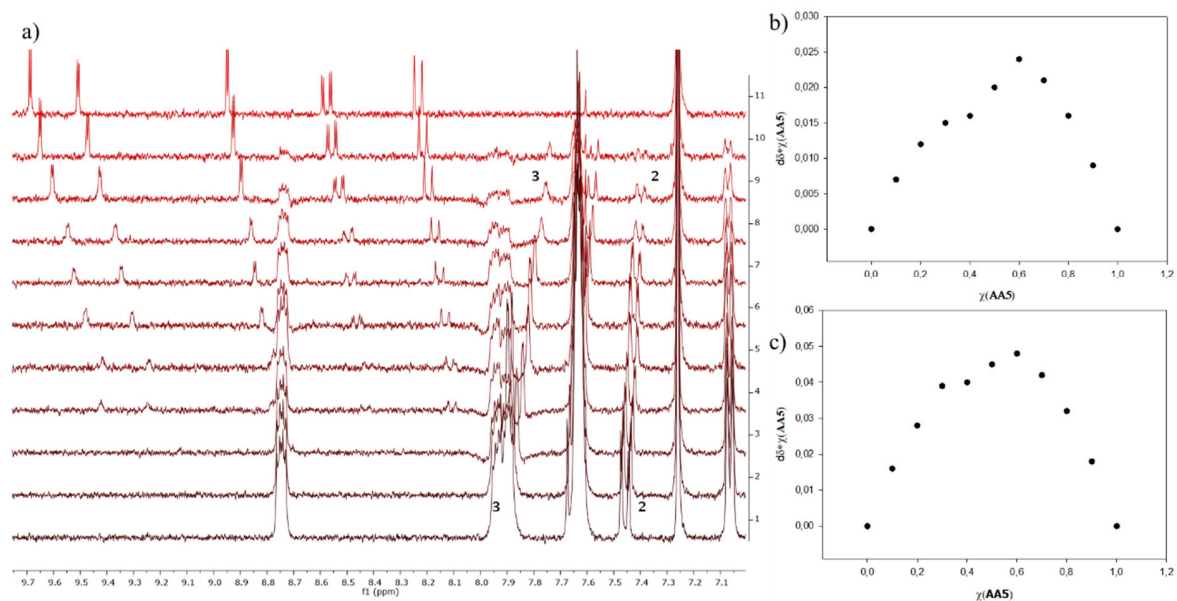
Figure 3.3.18. ^1H NMR for AA5/DCTNF mixture (a) and Job`s plot for H_2 (b) and H_3 (c) (in CDCl₃)

This correlates well with a similar shift for 1/1 mixture of initial ligand 28 and DCTNF guest in pure CDCl3 (figure **3.3.19**).
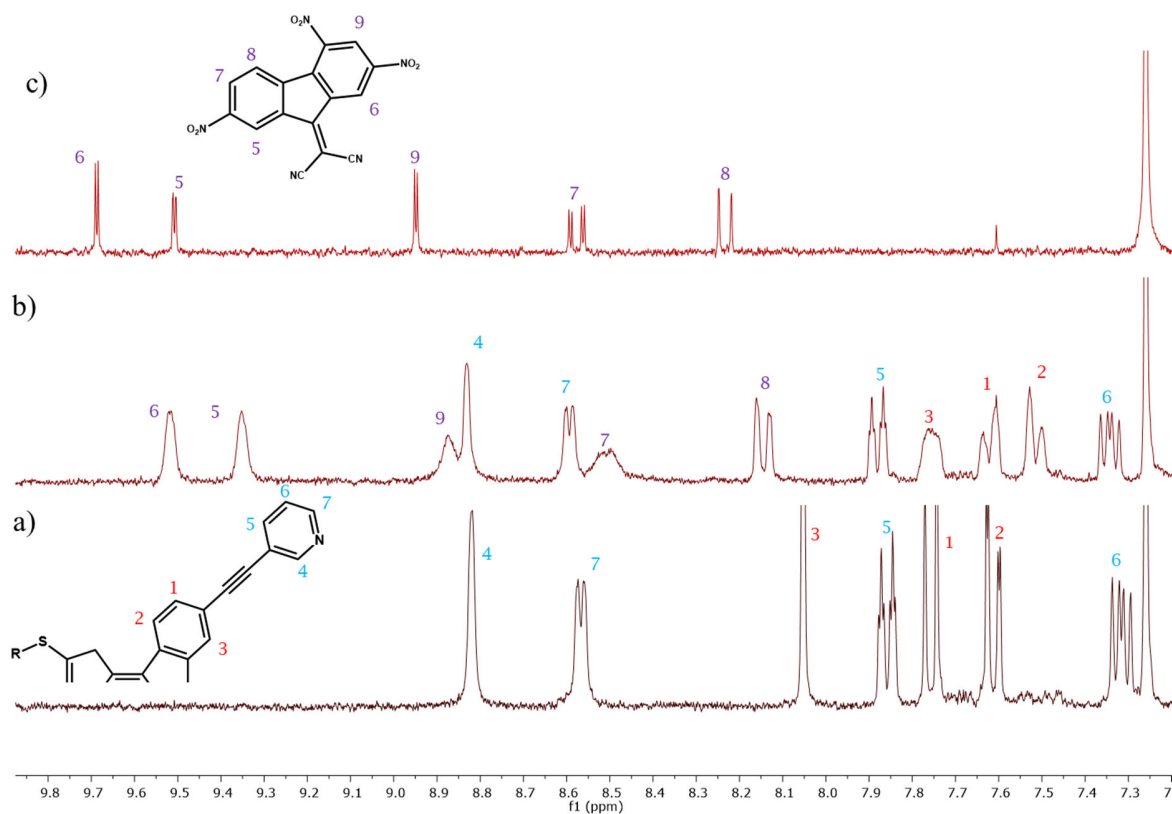
*Figure 3.3.19. ^1H NMR of ligand **27** (a), guest DCTNF (c) and their 1/1 mixture (c) in CDCl₃*

3.4. Self-assembly using *bis*-ruthenium complexes

Bis-ruthenium acceptors were previously described in chapters **1.4.4** and **2.2**. In addition to having compatible geometry with DTF ligands, they allow to fine-tune the properties of the resulting assembly by changing the size of linker unit in the acceptor complex (scheme **3.4.1**).
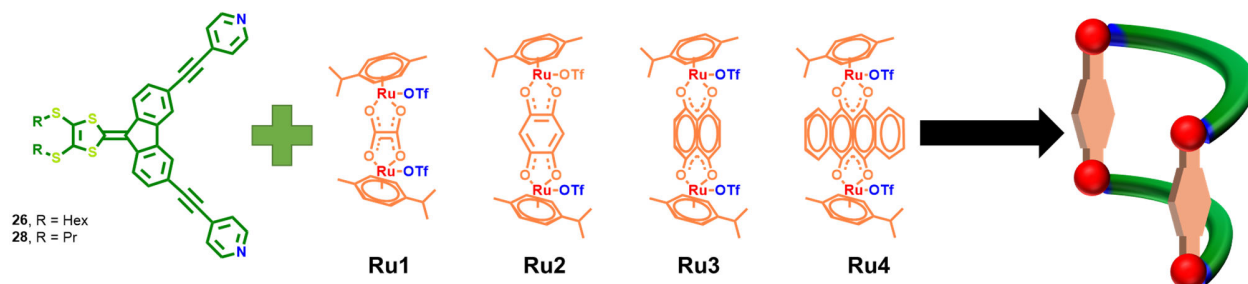
Scheme 3.4.1. Expected of self-assemblies using 4Py-DTF motif in combination with bis-ruthenium acceptors.

3.4.1. Self-assembly using 4Py-DTF and Ru1-4

Only **4Py-DTF** ligands gave discrete assemblies upon interaction with the *bis*-ruthenium acceptors. Reactions were carried out in methanol at 50 ^{0}C for 24h using stoichiometric amounts of ligands **26** or **28** and acceptors **Ru1-4** resulting in self-assemblies **AA8-AA13** and monitored by ^{1}H and DOSY NMR. Final self-assemblies can be isolated by precipitation with diethyl ether or used directly without purification.

Self-assemblies **AA8** and **AA9** obtained from the smallest acceptor **Ru1** and ligands **26** and **28** respectively, show a relatively simple ^{1}H NMR(figure **3.4.1**). Well-defined structure of ^{1}H NMR state for the formation of a probable unique discrete structure. ^{1}H DOSY NMR confirms formation of a single product with corresponding r_H = 13,2 Å for **AA8** and 11,4 Å for **AA9**, which correlates well with expected size of a M_4L_2 assembly (figure **3.4.1)**. After precipitation, self-assembly can be solubilized in dmso-d_6 without structure modification (figure **3.4.1**, b).
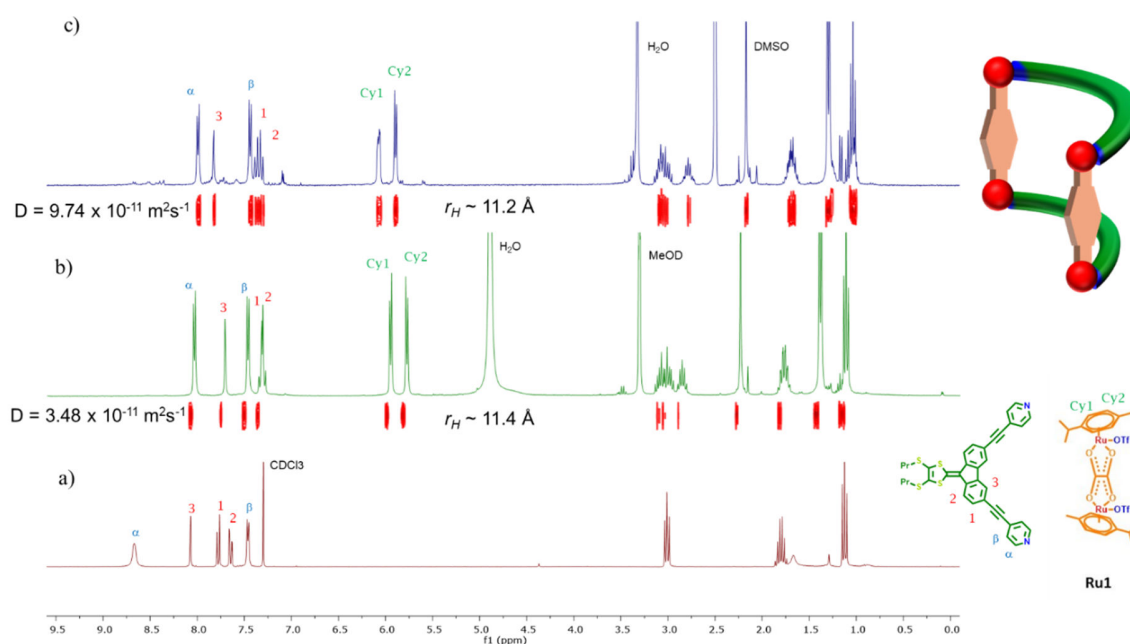
Attempts to obtain single crystal suitable for x-ray diffraction starting from self-assemblies using ligand **26** with thiohexyl groups weren`t successful. However, the ligand **28** with smaller thiopropyl groups allowed to obtain crystals of self-assembly **AA9** by liquid diffusion of methyl tert-butyl ether into the solution of self-assembly in methanol. **AA9** illustrates the expected M$_4$L$_2$ self-assembly clip (figure **3.4.3**). Packing indicates certain degree of π-π interaction between fluorene fragments (with similar distance about 3.4-3.7 Å between two DTF fragments from neighboring clips and within the clip).Mostly unchanged geometry of the ligand indicates good compatibility of the ligand and acceptor.

*Figure 3.4.2. X-ray crystal structure of **AA9** and its schematic representation. Counter anions, solvent molecules and hydrogen atoms omitted for clarity.*

Interestingly, moving to the *bis*-ruthenium acceptor **Ru3** for which distance between both Ru centers is increased to 7.9 Å leads to a drastic change in the NMR spectra (figure **3.4.3**, a) with the presence of aromatic upfield shifted signals and a splitting of α and β protons.

*Figure 3.4.3. ^{1}H and DOSY NMR for the **AA11** (a) and **AA10** (b) in methanol-d$_4$ and dmso-d$_6$ (c)*

Despite the overall complex structure, ^{1}H DOSY NMR confirms formation of a single product with corresponding r_H = 16.4 Å for **AA10** and 14 Å for **AA11**. a size which is much bigger than the one observed for **AA9** using **Ru1** complex (figure **3.4.3**, a and b). Surprisingly, self-assemblies **AA10** and **AA11** also exhibit substantial difference in the aromatic region while having only different thioalkyl groups in ligands **26** and **28** respectively. Unlike **AA8-9**, changing the solvent to dmso-d_6 removes the more complicated signal structure, but also probably leads to partial destruction of the cage due to more competitive nature of the solvent. However, DOSY NMR confirms that the self-assembly structure remains present in the solution (figure **3.4.2**, c).

Further analysis using COSY and ROESY NMR (annexes **3.8-3.18**) shows two distinct sets of signals for both acceptor and ligand. Signals are also better resolved in case of **AA11** in comparison to **AA10**. Therefore, COSY NMR for **AA11** allows to identify clear coupling between two sets of α and β pyridil protons respectively, as well as two sets of fluorene protons using COSY and ROESY NMR. Signals of cymene protons give similar two sets of signals (annex **3.11**). In case of **AA10** COSY and ROESY NMR spectra give similar data, but overlapping signals don`t allow clear identification of all interactions (annex **3.9**). Therefore, such set of signals is probably indicative of the geometrically intertwined structure with several distinct molecules, such as described in chapter **1.3.6**.

High resolution ESI-FTICR-MS spectrometry was done in collaboration with Drs Frédéric Aubriet and Vincent Carré in the University of Lorraine. Experiments confirmed the expected M_4L_2 stoichiometry, along with the aggregation of the higher species (annexes **5.2-5.4**) similar to the Palladium-based self-assemblies **AA4-7**.

Finally, an X-ray analisys allows to explain the difference in the NMR spectra. (figure **3.4.4**). the larger distance between both Ru centers acceptor **Ru3** allowed the formation of a dimer. **AA11** doesn`t create a closed structure similar to the ones described in chapter **1.3.6**, but a dimer from two interfold separate clips. This also allows to explain the difference in the ^{1}H NMR spectra. Most probably one set of signals belongs to the fragments inside the dimer, while second set correspond to the outside protons.
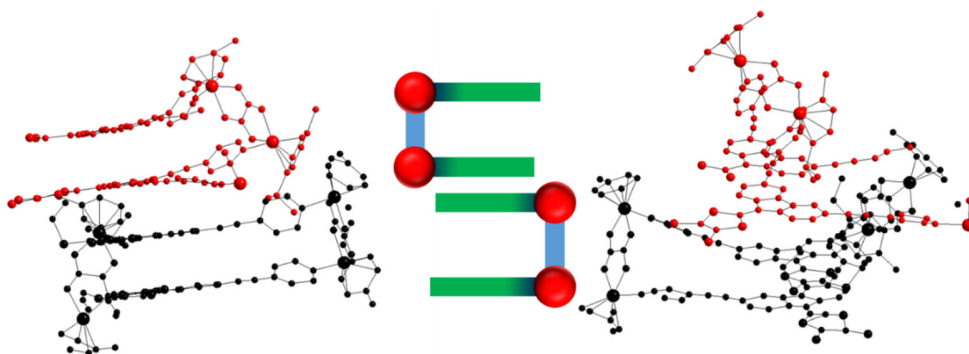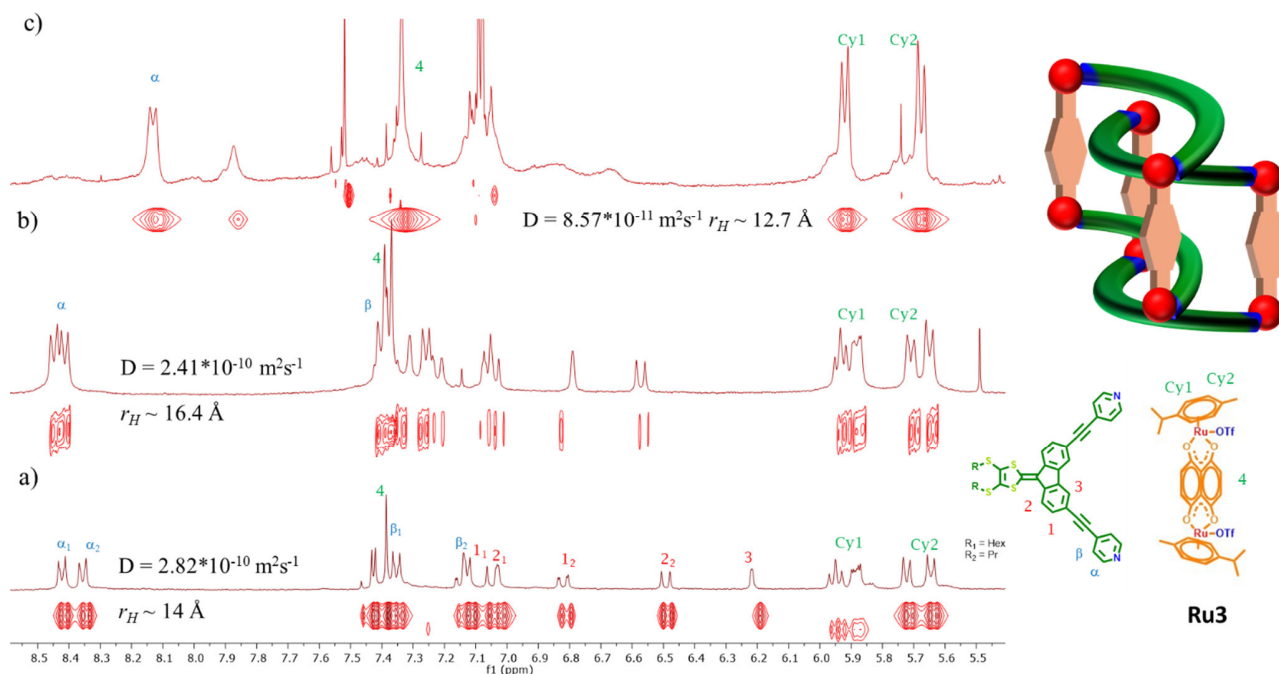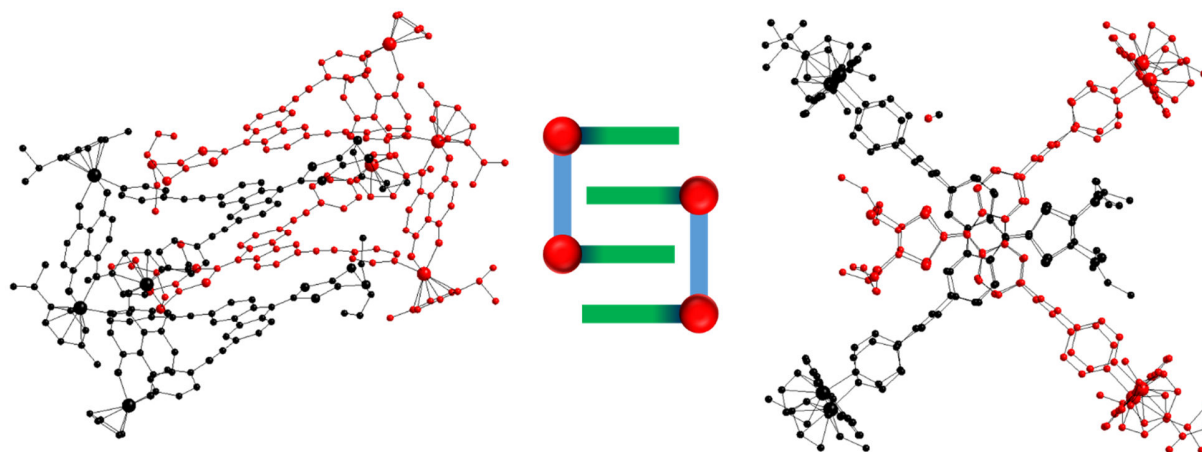

*Figure 3.4.4. X-ray crystal structure of **AA11** (a) and its schematic representation (b). Counter anions, solvent molecules and hydrogen atoms omitted for clarity.*

Acceptors **Ru2** and **Ru4** resulted in corresponding M_4L_2 self-assemblies. However, acceptor **Ru2** gave less distinct ^{1}H NMR, which indicates non-ideal geometrical compatibility between the ligand and acceptor. Therefore, this combination wasn`t studied further. Upon using the biggest acceptor **Ru4**, ^{1}H and DOSY of corresponding self-assemblies **AA12** (figure **3.4.5**) i **AA13** have similar double structure

to **Ru3**. At the same time, additional signal from the tetracene core in the aromatic region complicate already complex NMR while having similar properties to **Ru3**.
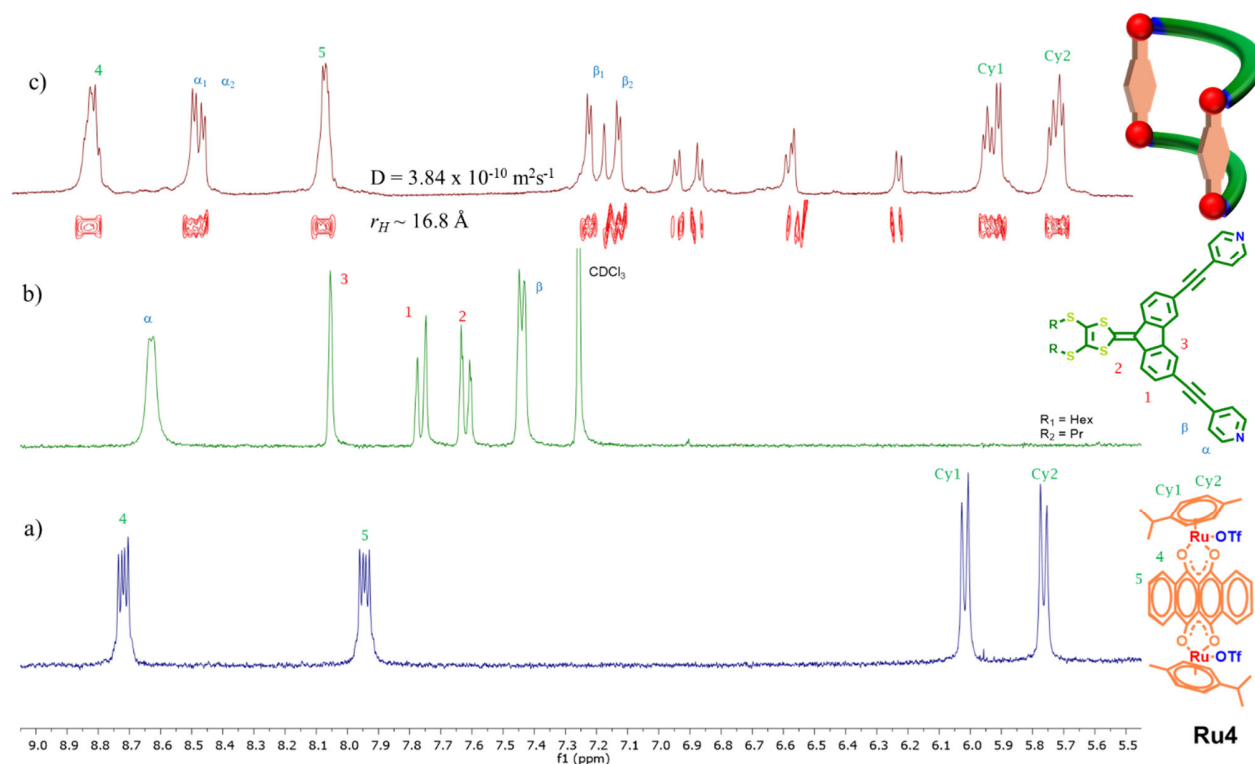
*Figure 3.4.5. ^1H and DOSY NMR for ligand **Ru4** (a), **26** (b) and **AA12** (c) in methanol-d_4, CDCl$_3$ and CD$_3$CN (c) respectively*

3.4.2. Electrochemical properties

The electrochemical behavior of self-assemblies **AA8-13** were studied by cyclic voltammetry in CH$_3$CN/CH$_2$Cl$_2$ (1/1, v/v). Smaller clips **AA8-9** show reversible oxidation to the radical-cation with a formation of intermediate mix-valence species (figure **3.4.6**), similar to the clips **AA6-7**. The intramolecular nature of this process is in good relation to the close distance between DTF fragments within the clip due to the smaller size of the **Ru1** acceptor.

As expected, larger self-assemblies **AA10-11** retain split wave oxidation of the DTF fragment to the radical cation (figure **3.4.7**, a). It is followed by the oxidation of the Ru acceptor unit at higher potential (figure **3.4.7**, b). Scanning at the higher potential leads to the second irreversible oxidation of a Ruthenium fragment.
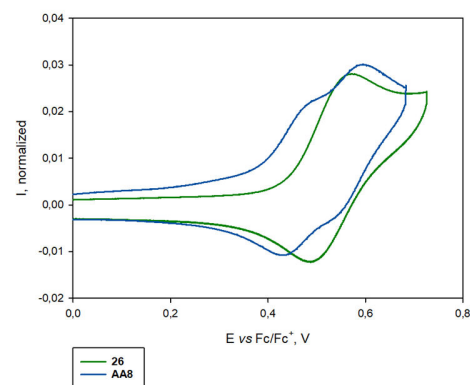
*Figure 3.4.6. Normalized cyclic voltammograms of ligand **26** and metalla-ring **AA8** (C = 10^{-3}M, CH$_3$CN/CH$_2$Cl$_2$, 0.1 M nBu$_4$NPF$_6$, 100 mV·s^{-1}, Pt) V vs. Fc/Fc$^+$.*

69
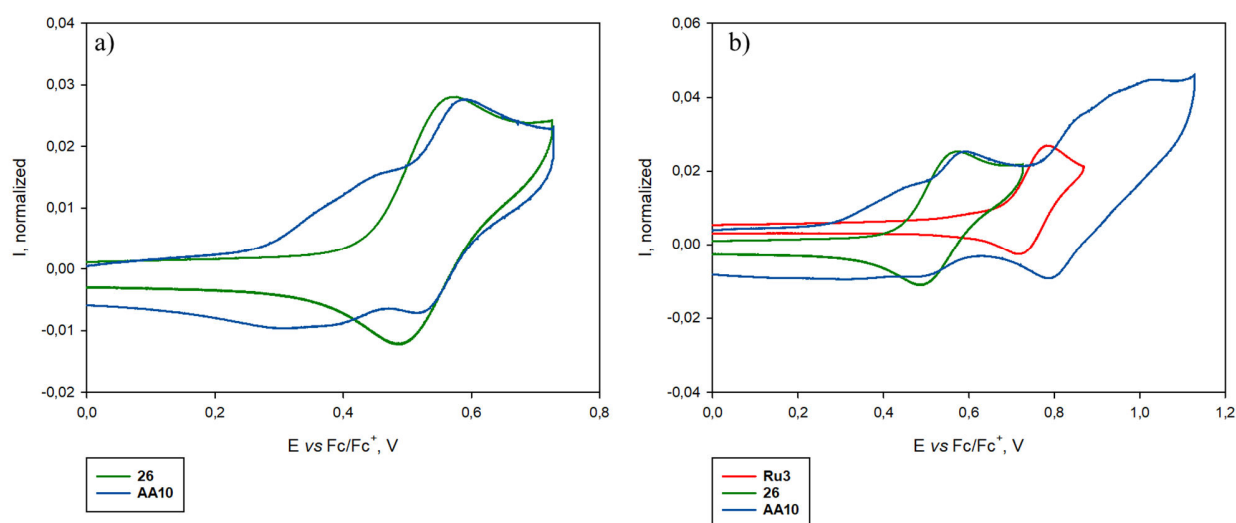
*Figure 3.4.7. Normalized cyclic voltammograms of ligand **26** and metalla-ring **AA10** (C = $10^{-3}M$, CH$_3$CN/CH$_2$Cl$_2$, 0.1 M nBu$_4$NPF$_6$, 100 mV·s^{-1}, Pt) V vs. Fc/Fc$^+$.*

3.4.3. Monomer-dimer transformations

The dimer form of the self-assemblies **AA10-AA11** is not rigidly fixed and can therefore be reversed back to the monomer. Within the current work, we studied the influence of factors as concentration, solvent or addition of a guest molecules (figure **3.4.8**).
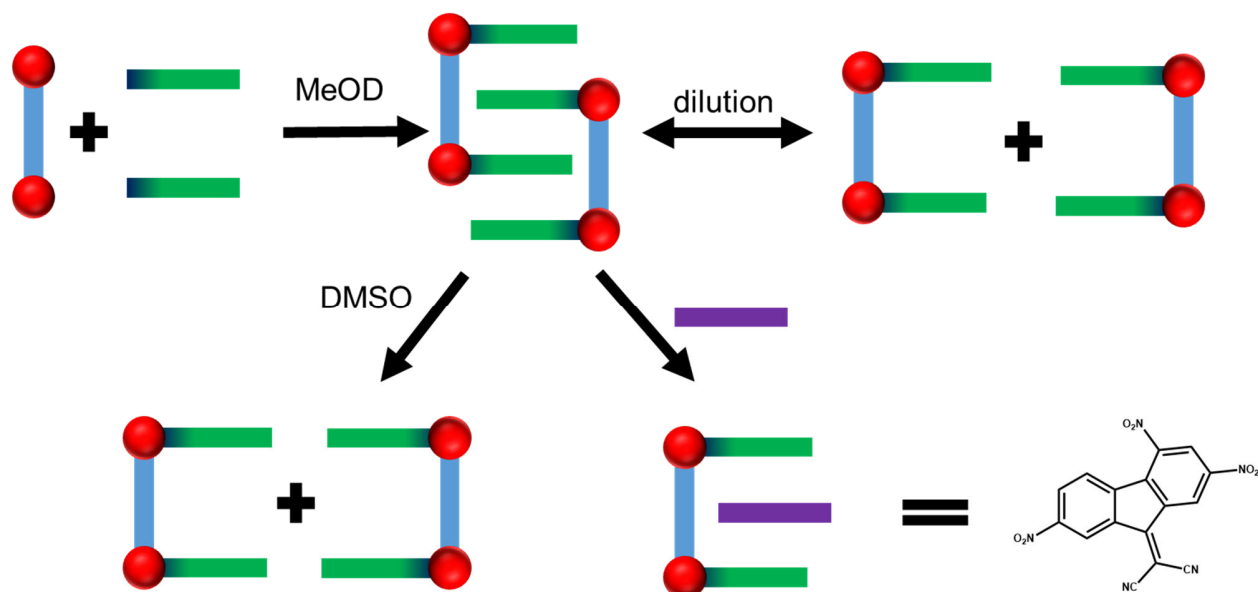
Figure 3.4.8. Schematic representation of a monomer-dimer transformation.

As was previously shown on the figure **3.4.2**, isolation of the self-assembly and subsequent resolubilization in dmso-d$_6$ leads to the formation of a simple ^{1}H NMR, which is characteristic of a monomer species. In other polar solvents such as acetonitrile, acetone or nitromethane dimer remains the prevalent form (annex **3.19**).
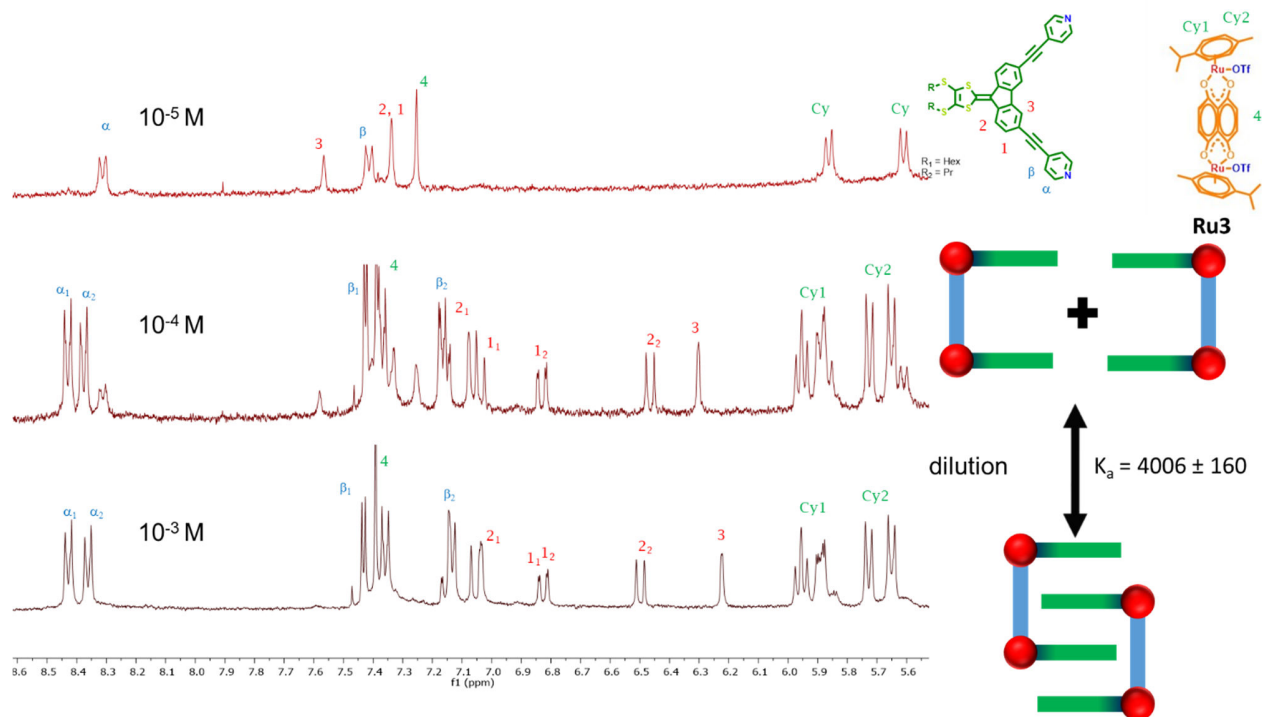
Figure 3.4.9. ^1H NMR of self-assembly AA11 in methanol-d_4

Influence of the concentration was studied in the range 10^{-3} M – 10^{-5} M (figure **3.4.9**). Within the concentration of 10^{-3}M and higher, ^1H NMR spectra shows only signals of the dimer. Upon dilution to 10^{-4} M, signals of a monomer appear and further dilution to 10^{-5} M results in only monomer being present in the solution. Usually, such type of equilibrium can be evaluated via the correlation between the ratio of signals for both forms at different concentrations. Therefore, association constant of $K_a = 4006 \pm 160$ was calculated based on the ^1H NMR experiment using the α pyridil protons (annex **3.20**).

Monomer-dimer equilibrium depending on the concentration was also studied using cyclic voltammetry. Upon dilution to 10^{-5} M, additional oxidation process for the DTF fragment completely disappears (figure **3.4.10**), in contrast to the intramolecular character in **AA6-7**. It allowed to confirm the intermolecular character of the oxidation process, which is consistent with ^1H NMR and crystallographic data.
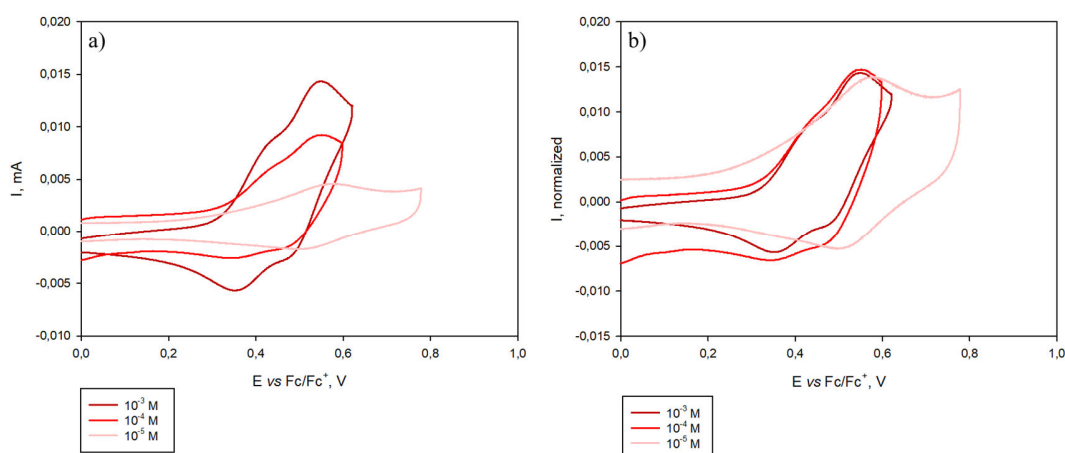
Another possibility to break the dimer is to introduce a competitive guest molecule. From the variety of planar guests (figure **3.3.11**), only the DCTNF molecule showed significant results. ^{1}H NMR shows complete disappearance of signals from the dimer upon addition of 1 equivalent of DCTNF (figure **3.4.11**). At the same time, shift of the ^{1}H NMR signals of the resulting complex isn`t the same as for the pure monomer upon dilution, which confirms interaction between the clip and the guest.
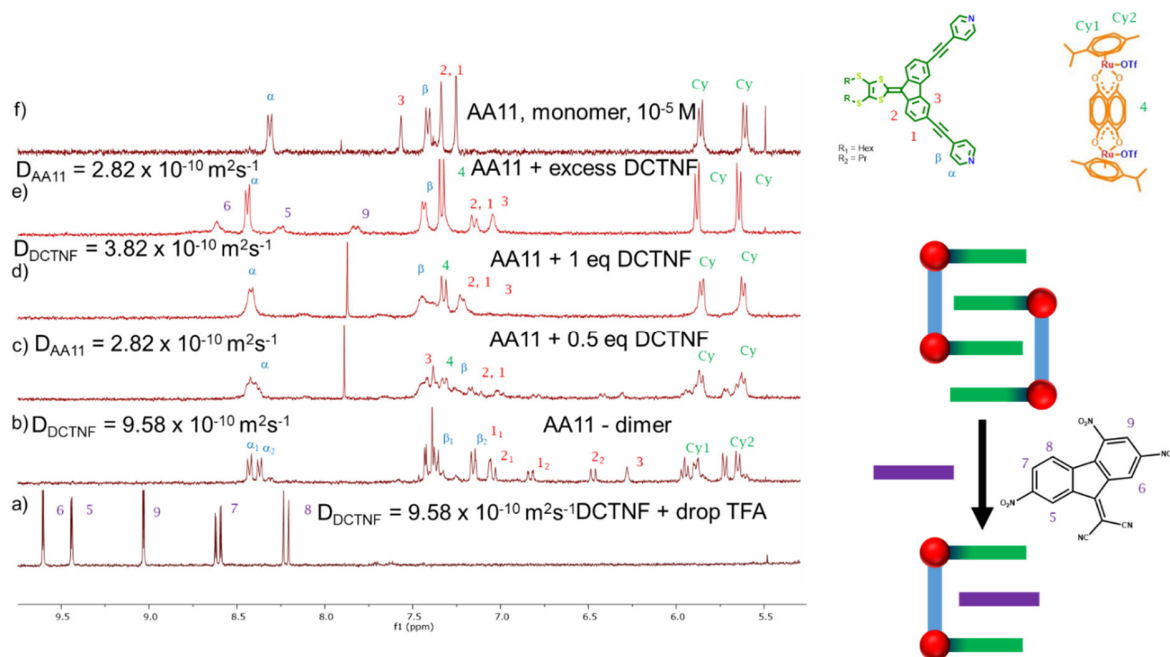
Figure 3.4.11. ^{1}H and DOSY NMR of guest DCTNF (a), self-assembly AA11 (b – dimer, f – monomer) and their mixture (c, d, e) in methanol-d₄

These interactions were also studied by the cyclic voltammetry. Similar to the **AA6-7**, it illustrates recovery of the single oxidation process for the DTF fragment upon addition of 1 equivalent of the DCTNF guest (figure **3.4.12**, a). However, subsequent reduction part of the wave remains splitted, which suggests reformation of the dimer upon oxidation. This assumption correlates well with theoretical calculations for such process (figure **3.4.12**, b). This results are quite interesting and require further studies.
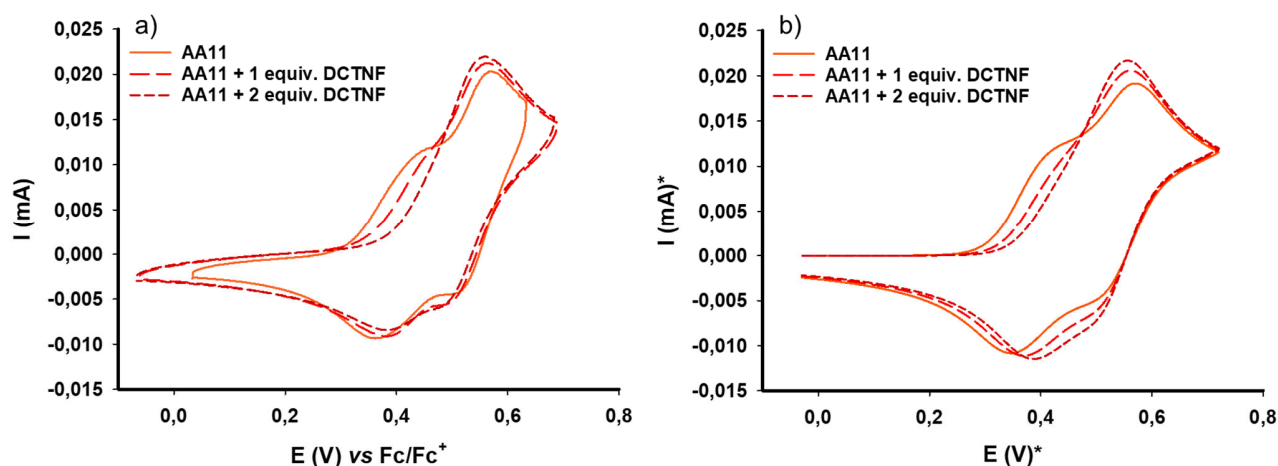
*Figure 3.4.12. Experimental (a) and theoretical (b) cyclic voltammograms of **AA11** and its mixture with DCTNF (1/1) (C = 5 x 10⁻⁴M, CH₃CN/CH₂Cl₂, 0.1 M nBu₄NPF₆, 100 mV·s⁻¹, Pt) V vs. Fc/Fc⁺*

3.5. Conclusions to chapter III.

Two new types of angular ligands were designed based on the dithiafulvalene (DTF) scaffold in combination with ethynylpyridine groups for use in coordination-driven self-assembly. Both **3Py-DTF** and **4Py-DTF** ligands are characterized by one reversible oxidation resulting in the formation of a radical-cation.

Reaction of the **3Py-DTF** ligand with naked palladium ions resulted in a M_2L_4 type cage **AA3**, which exhibits one reversible oxidation upon electrochemical analysis. This suggests that all four DTF fragments are oxidized independently at the same potential. The cage structure was confirmed by HRMS and x-ray analysis, with an internal cavity of ~600 Å^3. Reaction of the **4Py-DTF** ligand with naked palladium ions resulted in the formation of a discrete species which could not be further characterized due to its low solubility.

Combination of *cis*-blocked palladium complexes with ligands **3Py-DTF** and **4Py-DTF** afforded self-assembled M_2L_2 clips **AA4-5** and **AA6-7** respectively. Clips **AA4-5** are characterized by two reversible oxidation, one corresponding to the DTF fragment and the second to the ferrocene unit of Pd*dppf*. Interestingly, in the case of **AA6-7**, the first oxidation process of DTF splits into two waves, suggesting the formation of the mixed-valence species or a π-dimer similar to **AA1**.

AA4-5 were shown to interact with C60 thanks to their "pincer-like" geometry. However, irradiation with visible light led to its photodecomposition. Speed of the process suggests significant interaction between them. The clips **AA6-AA7** were shown to interact with the planar electron-deficient guest DCTNF, resulting in disrupting the formation of a mixed-valence species or a π-dimer.

The **4Py-DTF** ligand in combination with bis-ruthenium complexes involving different bridging groups **Ru1-4** resulted in a series of M_4L_2 type self-assembled metallorings **AA9-13**. Cyclic voltammetry experiments demonstrate the formation of a mixed-valence species or a π-dimer similar to **AA6-7**. Additionally, clips **AA10-11** were shown to form a M_8L_4 dimer in solution, which can be transformed to its monomeric counterpart upon dilution, or inclusion of the electro-deficient DCTNF unit. Remarkably, expulsion of the later in the resulting host-guest complex could be achieved through a redox stimulus, as confirmed by cyclic voltammetry measurements.

4. Chapter IV. π-extended tetrathiafulvalene-based (exTTF) self-assemblies[186]

4.1. exTTF-based ligands

4.1.1. Introduction

Compounds based on π-extended tetrathiafulvalene fragments were introduced in chapter **1.6.4.** In our group, the first ligand constructed from such motif was developed using the dihydroanthracene fragment during the PhD thesis of Dr. S. Bivaud (Figure **4.1.1**).[187] Introduction of 4-pyridil units via direct arylation allowed for creation of **exTTF-4Py₄** ligand, which successfully react with cis-blocked Pd and Pt acceptors to produce M_4L_2 cages, capable of binding the perylene molecule.[149]
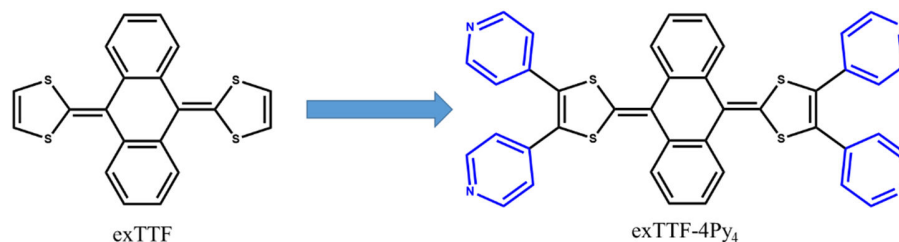
Figure 4.1.1. π-extended tetrathiafulvalene (exTTF) and corresponding ligand exTTF-4Py₄

Characteristic feature of the exTTF scaffold lies on its ability to change reversibly its geometry upon oxidation (figure **4.1.2**). In the neutral form, it adopts a singular bent "butterfly" shape due to steric hindrance between hydrogens from the dihydroanthracene fragment and sulfur of the 1,3-dithiol rings. After oxidation through a double one electron process leading to the dicationic state, the initial bent structure evolves to a fully aromatic species in which both dithiolium rings are almost perpendicular to the planar anthracenyl moiety.
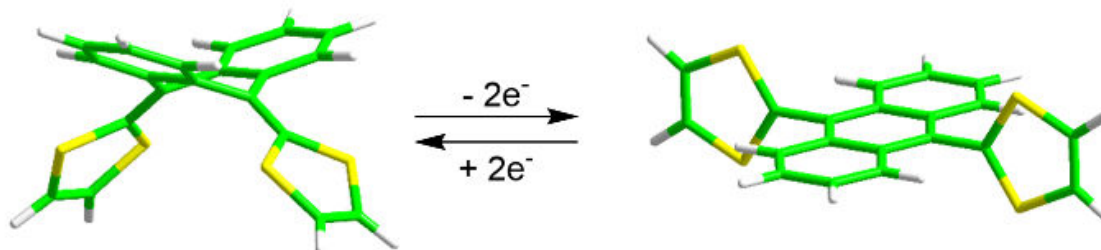
Figure 4.1.2. Conformational change of exTTF molecule upon oxidation/reduction process

4.1.2. Ligand exTTF-TEG

One of the main drawbacks of **exTTF-4Py₄** ligand lies in its relatively low solubility. In order to address this issue, during the PhD thesis of V. Croué, ligand **exTTF-TEG**[150] was developed by addition of four triethyleneglycol fragments (figure. **4.1.3**, a). This allowed to both substantially increase its solubility as well as its donor properties.
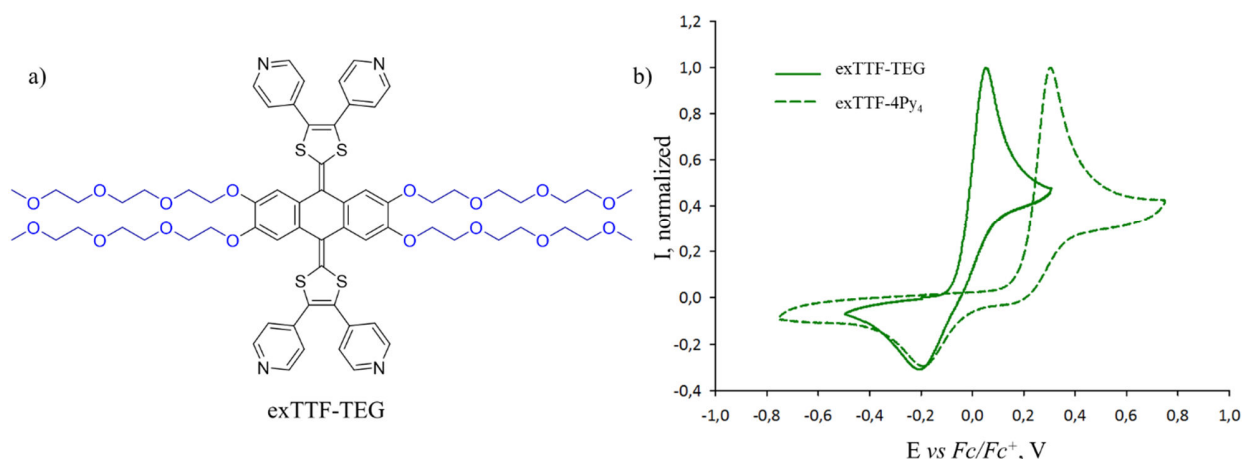
*Figure 4.1.3. Structure (a) and cyclic voltammetry of the **exTTF-TEG** ligand*

It`s worth describing the electrochemical behavior of exTTF-based ligands. The electrochemical oxidation process of exTTF derivatives is usually manifested by a single two-electron oxidation wave to the dicationic state, involving an inverted potential phenomenon ($E_1^{ox} > E_2^{ox}$).[188-189] Both ligands **exTTF-TEG** and **ex-TTF-4Py₄** present a single pseudo-reversible oxidation wave with formation of a dication (figure **4.1.3**, b). Ligand **exTTF-TEG** exhibits a lower oxidation potential (E_{ox} = 0.05 V and E_{red} = -0.20 V *vs*. Fc/Fc$^+$) in comparison to the parent **exTTF-4Py₄** (E_{ox} = 0.30 V *vs*. Fc/Fc$^+$), which is caused by donating mesomeric effect promoted by the TEG groups.

4.2. Self-assembly using exTTF-TEG

4.2.1. Previous works

During the PhD thesis of S. Bivaud and later V. Croué, exTTF-based ligands were used in combination with *cis*-blocked Pd and Pt charged acceptors with different substituents and afforded M_2L_4 type cages, be they neutral or octacationic (figure **4.2.1**). The $M_4L_2^{8+}$ cage has proven to efficiently bind two $B_{12}F_{12}^{2-}$ anions,[150] while the homologue neutral M_4L_2 cage was effective in binding neutral molecules such as coronene.[151-152]
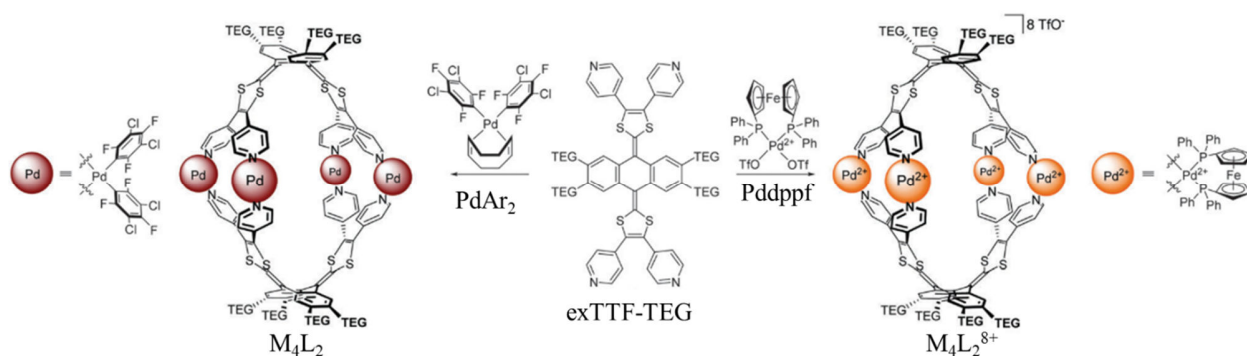
*Figure 4.2.1. Self-assemblies using **exTTF-TEG** ligand in combination with different cis-blocked acceptors*

4.3. Self-assembly $M_{12}L_6$ cages AA14 and AA15

In the current work, we were interested in the self-assembly properties of the ligand **exTTF-TEG** in combination with linear acceptor units. In particular, *trans*-blocked Pd and Pt complexes (chapter **1.4.2**) as well as silver salt were investigated.

4.3.1. Synthesis

Reaction between **exTTF-TEG** ligand (1 equiv.) and trans $PdCl_2(CH_3CN)_2$ (2 equiv.) was carried out in DMSO at 100°C resulting in a neutral self-assembled cage **AA14**. The final compound was isolated by precipitation with ethyl acetate and characterized in $CDCl_3$ by ^1H NMR and ^1H DOSY NMR (figure **4.3.1**). In comparison to the starting ligand **exTTF-TEG** (figure **4.3.1**, a), **AA14** exhibits broader NMR signals, which is common for large discrete structures (figure **4.3.1**, b).[190] ^1H DOSY NMR was able to further confirm the formation of a single discrete compound. A hydrodynamic radius r_H of 21 Å was calculated from the corresponding diffusion value of the cage ($D = 1.93 \times 10^{-10}$ m².s^{-1}), which is consistent with a large size self-assembled structure.
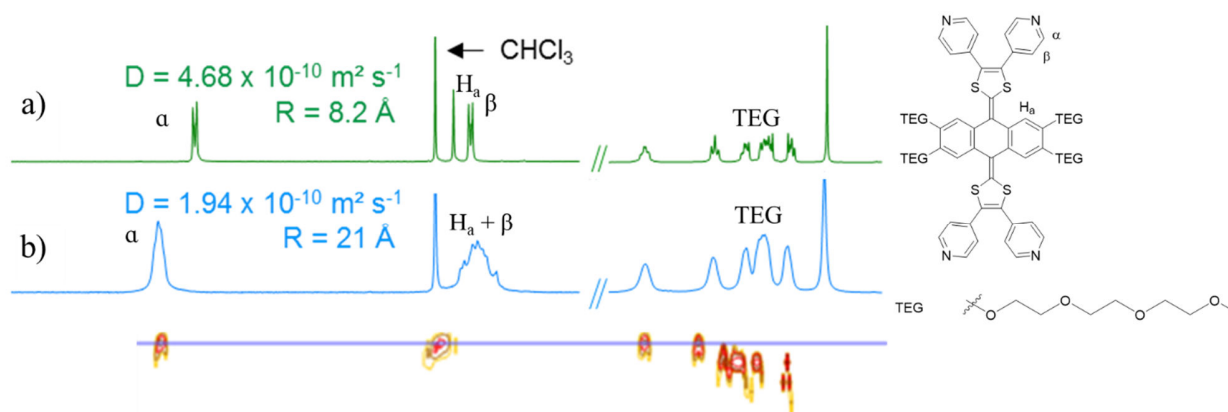
*Figure 4.3.1. ^1H and DOSY NMR for the **exTTF-TEG** ligand (a) and resulting self-assembly **AA14**(b) in dmso-d6*

High resolution ESI-FTICR-MS spectrometry was achieved in collaboration with Drs Frédéric Aubriet and Vincent Carré from the University of Lorraine. As previously described by the group,[151] KOTf was added to the analyzed solution in order to produce ionic species after interaction of the latter with peripheral TEG chains. We were able to determine a $M_{12}L_6$ stoichiometry, for which characteristic peaks corresponding to the $[Pd_{12}(\textbf{exTTF-TEG})_6 + (KOTf)_n = 9\text{-}12 - 7OTf]^{7+}$ and to the $[Pd_{12}(\textbf{exTTF-TEG})_6 + (KOTf)_n = 7\text{-}11 - 6OTf]^{6+}$ cations show good correlation with theoretical estimates (figure **4.3.2**).
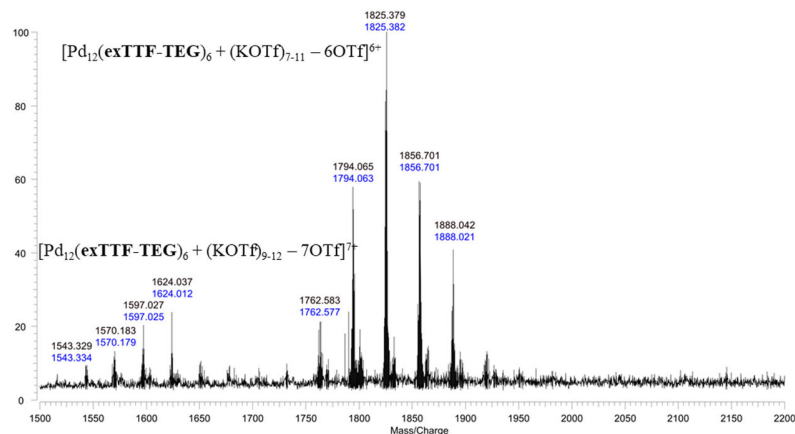
*Figure 4.3.2. ESI-FTICR spectrum of **AA14** recorded in CH₂Cl₂/CH₃NO₂ (C = 5 x 10⁻⁴ M) after addition of 24 equiv. of KOTf (solution in CH₃NO₂)*

A similar reaction was carry out with AgBF₄ in CDCl₃/CD₃NO₂ (1/1) affording a polycationic species. The reaction process was followed by ^{1}H NMR and showed almost instantaneous formation of a single discrete structure, which was further confirmed with ^{1}H DOSY NMR (figure **4.3.3**). The corresponding Stokes radius (R = 20.5 Å) for D = 2.19 x 10⁻¹⁰ m².s⁻¹ is coherent with formation of a large discrete assembly **AA15** having a size similar to the above mentioned palladium cage **AA14**.
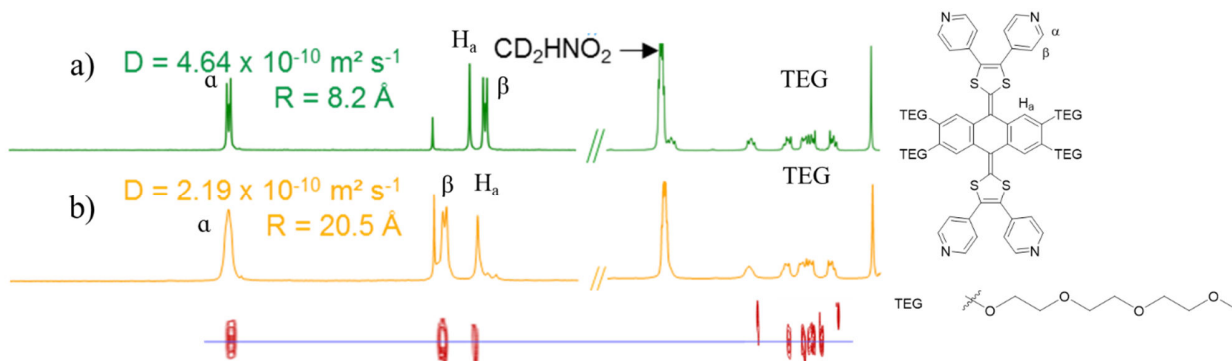
*Figure 4.3.3. ^{1}H and DOSY NMR for the **exTTF-TEG** ligand (a) and resulting self-assembly **AA15** after reaction with AgOTf (b) in CDCl₃/CD₃NO₂*

Interestingly, a similar experiment carried out in pure CH₃CN did not show any formation of the self-assembly structure, which demonstrates the important role of solvents in coordination driven self-assembly processes. Also, since the reaction needs only 2 equiv. of silver cations in order to generate the self-assembly, silver coordination by the TEG chains can be ruled out. This is further confirmed by ^{1}H NMR data that do not show any change in the TEG signals during the reaction (figure **4.3.3**).

Similarly to experiments led with **AA14**, a ESI-FTICR MS analysis of **AA15** was run in presence of 12 equivalents of AgBF₄ in order to stabilize TEG chains. This allowed to confirm a M₁₂L₆ stoichiometry. The characteristic signals $[Ag_{12}(\textbf{exTTF-TEG})_6 + (AgBF_4)_{9-15} - 6BF_4]^{6+}$ and $[Ag_{12}(\textbf{exTTF-TEG})_6 + (AgBF_4)_{8-12} - 5BF_4]^{5+}$ show a good correlation with theoretical estimates (figure **4.3.4**).
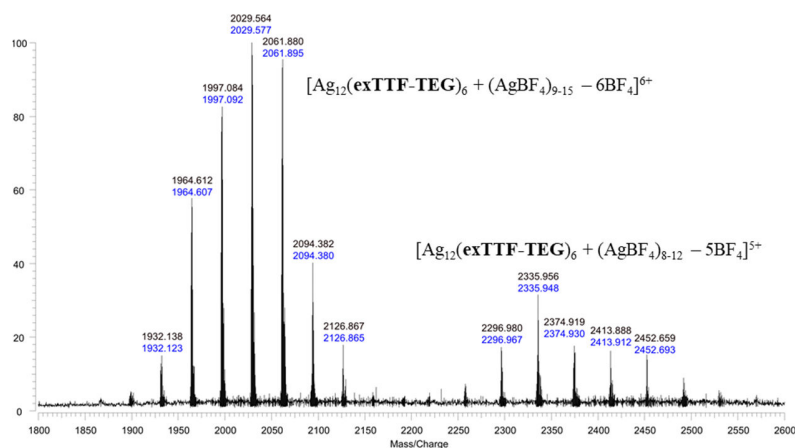
*Figure 4.3.4. ESI-FTICR spectrum of **AA15** recorded in CH_2Cl_2/CH_3NO_2 (C = 5 x 10^{-4} M) after addition of 12 equiv. of $AgBF_4$ (solution in CH_3NO_2).*

4.3.2. Structural properties

Unfortunately, we were unable to obtain single crystal of **AA14** and **AA15** suitable for X-Ray analysis. Therefore, a molecular force field (MM+, HyperChem 8.0.3) optimization was performed for both $M_{12}L_6$ structures (figures **4.3.5** and **4.3.6**). TEG chains and counter anions were omitted to simplify the calculation.
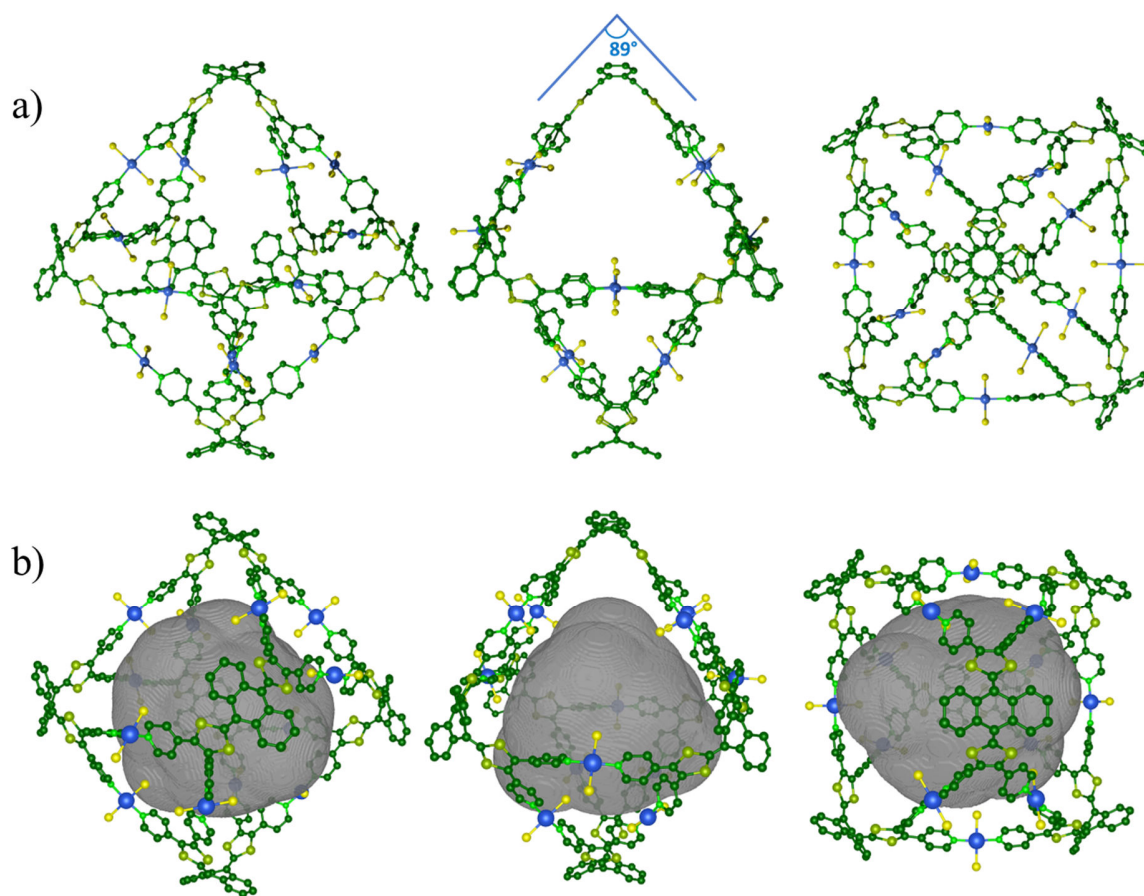
*Figure 4.3.5. MM+ simulation of cage **AA14** (a), cavity is depicted in grey (V = 3658 $Å^3$)(b)*

In both cases, simulations result in structures with a square-based bipyramidal geometry. Metal centers in both silver and palladium cages adopt a nearly linear geometry (Pyr-M-Pyr: *ca.* 175°). **exTTF** fragments within the self-assembly can be described via the intramolecular angle between both 1,3-dithiol-2-ylidene mean plans. The corresponding value for **AA14** and **AA15** are about 87°- 89° (figures **4.3.5**, a and **4.3.6**, a respectively), very similar to the 86° value observed in the free ligand (X-Ray). This data shows that no significant conformational change occurs during the self-assembly process and support therefore a good geometrical compatibility between the ligand and the metal complexes. Both cages present large internal cavities with calculated volume of approximately 3658 and 3954 Å^3 for **AA14** and **AA15** respectively (figures **4.3.5**, b and **4.3.6**, b).[191]
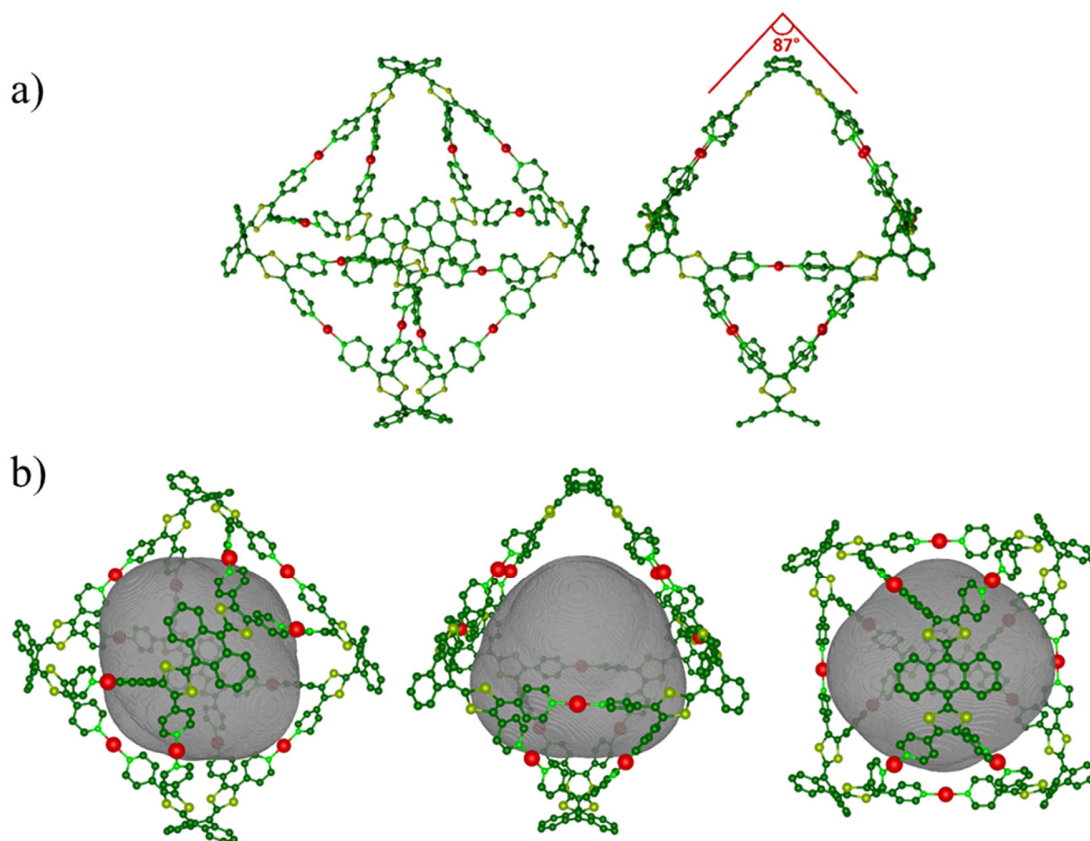
*Figure 4.3.6. MM+ simulation of cage **AA15** (a), cavity is depicted in grey (V = 3954 Å^3)(b)*

4.3.3. Electrochemical properties

The electrochemical behavior of cages **AA14** and **AA15** were studied by cyclic voltammetry and compared to ligand **exTTF-TEG** (figure **4.3.7**). The cage **AA14** exhibits a single redox process involving two electrons (E_1^{ox} = +0.35 V vs Fc/Fc$^+$). Its potential is higher compared to the free ligand (E_1^{ox} = +0.05 V vs Fc/Fc$^+$) as a result of coordination to the metal center. The oxidation process is quasi-reversible in this case, which is consistent with preserving the integrity of the cage (no disassembling) during the redox process. A similar behavior was previously shown for a neutral **Pt$_4$(exTTF-TEG)$_2$** cage.[192]
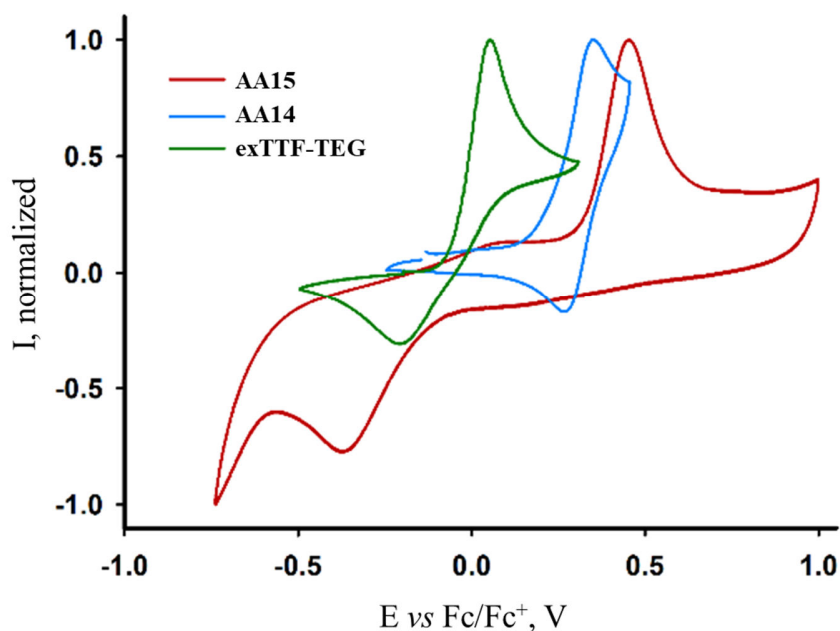
*Figure 4.3.7. Normalized cyclic voltammogram of ligand **exTTF-TEG** (C = 10⁻³ M, CH₃CN) and of cages **AA14** (C = 5 x 10⁻⁴ M, CH₃CN/CH₂Cl₂ (1/1)) and **AA15** (C = 5 x 10⁻⁴ M, CH₃NO₂/CH₂Cl₂ (1/1)), 0.1 M nBu₄NPF₆, 100 mV.s⁻¹, GC, V vs Fc/Fc⁺*

Interestingly, the polycationic cage **AA15** shows quite different behavior. One oxidation wave is observed which, as expected from metal coordination, is located at a higher potential (E_1^{ox} = +0.45 V *vs* Fc/Fc⁺) in comparison to ligand **exTTF-TEG**. In contrast to **AA14**, the reduction process occurs at a much lower potential (E_1^{red} = −0.36 V). A similar behavior was previously shown for a polycationic exTTF based self-assembly **(Pd₄(exTTF-TEG)₂)⁸⁺**, which was assigned to the cage disassembling upon oxidation.[150]

4.4. Supramolecular transformation into [(Ag₂(exTTF-TEG²⁺))²⁺]ₓ

The redox behavior can be investigated by both electrochemical or chemical oxidation/reduction. Therefore, the polycationic **AA15** was further studied upon chemical oxidation in order to identify the products following the cage disassembly process. The reaction was monitored by ¹H and DOSY NMR.
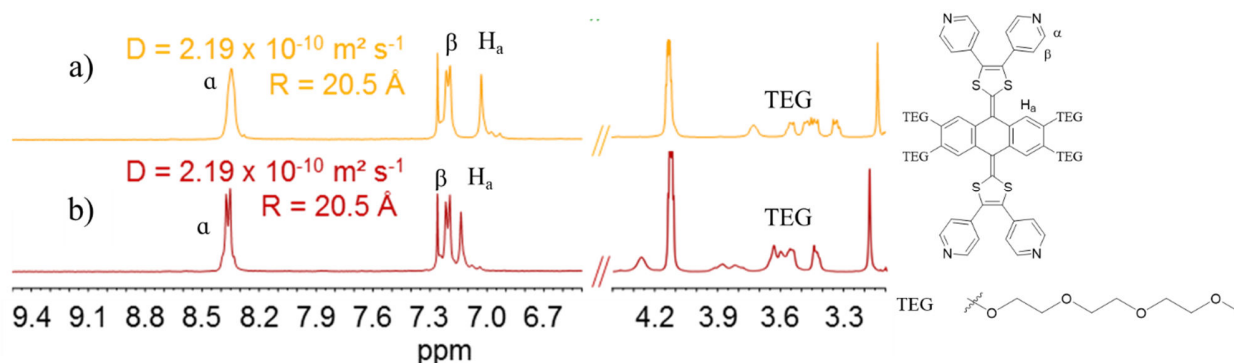
*Figure 4.4.1. ¹H and DOSY NMR for the self-assembly **AA15** (a) and resulting complex [Ag₁₂(Ag₂(exTTF-TEG)₆]²⁴⁺ (b) in CDCl₃/CD₃NO₂*

81

An initial addition of 12 equiv. of AgBF$_4$ to the **AA15** complex resulted in a slight change of the anthracenyl protons. In addition, the TEG signals changed significantly (figure **4.4.1**, b). The corresponding ^{1}H DOSY NMR does not exhibit significant change in the diffusion coefficient value (D). Such observations are consistent with coordination of additional silver cations to the peripheral TEG chains, resulting in a **[Ag$_n$(Ag$_{12}$ exTTF-TEG)$_6$]$^{(n+12)+}$** species. Thus, no oxidation process involving Ag$^+$ was observed, contrary to previous results obtained by the group using other exTTF derivatives.[192] Introduction of a supplementary excess of AgBF$_4$ (up to 30 equiv.) did not result in any additional changes in the ^{1}H NMR spectrum.

Nevertheless, further exposure of the reaction mixture resulted in slight gray powder and formation of light greenish insoluble crystals. The later were easily isolated in 66% yield by filtration. It should be noted that the initial cage **AA15** is stable in the same CD$_3$NO$_2$/CDCl$_3$ system within the same time interval.
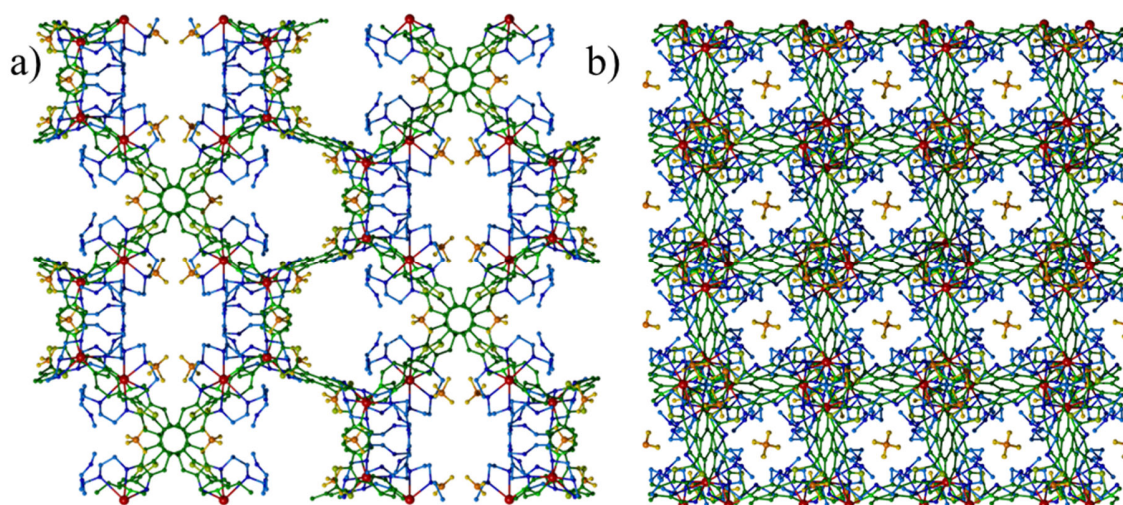
*Figure 4.4.2. X-Ray structure of the **[(Ag$_2$(exTTF-TEG^{2+}))$^{2+}$]$_x$** three-dimensional supramolecular polymer, BF$_4^-$ anions are located in the free space*

Fortunately, we were able to analyze single crystal. An X-Ray diffraction analysis shows the evolution of the initial **[Ag$_{12}$(exTTF-TEG)$_6$]$^{12+}$** discrete structure to an infinite **[(Ag$_2$ exTTF-TEG^{2+})$^{2+}$]$_x$** three-dimensional supramolecular polymer (figure **4.4.2**), according to a self-oxidation process.

The oxidation reaction is most probably due to the coordinated silver cations located in the lateral TEG chains, that generate a kinetically delayed oxidation process. To the best of our knowledge, this constitutes a unique example of a supramolecular transformation from a discrete cage to a 3D-polymer.
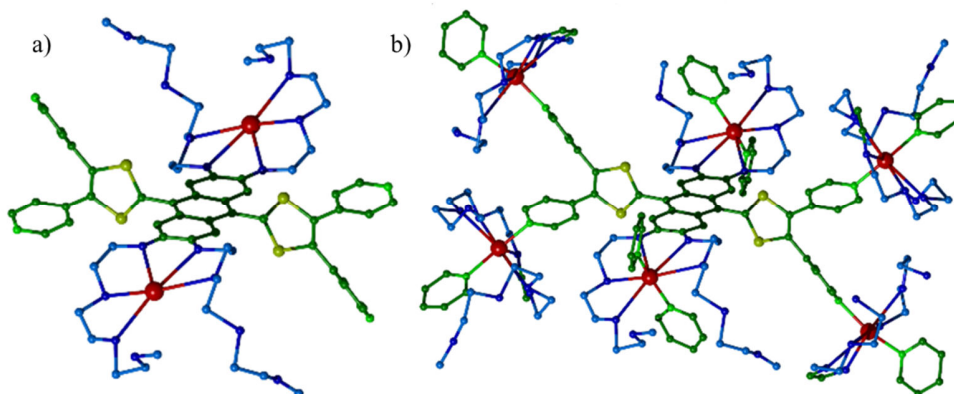
Figure 4.4.3. Partial [(Ag₂(exTTF-TEG²⁺))²⁺]ₓ X-ray structure showing a) the repeating (Ag₂exTTF-TEG ²⁺)²⁺ motifs and b) the silver coordination sphere. BF₄⁻ anions omitted for clarity

X-ray data of **[(Ag₂(exTTF-TEG²⁺))²⁺]ₓ** shows a polycationic polymeric backbone which is constituted from the repeating unit **(Ag₂(exTTF-TEG ²⁺)²⁺** (figure **4.4.3**, a). The dication state of the exTTF fragment (**exTTF-TEG²⁺**) is confirmed by both the length of the C-C bond (1.47 Å) between the planar central anthracene moiety and the 1,3-dithiolium rings and by the corresponding dihedral angles of 83.4°. The TEG fragments play a substantial role in the final structure, since they provide additional coordination sites for silver cations (figure **4.4.3**, b). The pyridine units are slightly distorted (N-Ag-N = 157°) in comparison to the starting cage **AA15** (N-Ag-N: *ca.* 175°). In general, three independent exTTF ligands take part simultaneously to the silver coordination.

A chemical reduction was further achieved in an attempt to recover the starting cage **AA15**. Upon addition of a reducing agent (tetrakis(dimethylamino)ethylene, TDAE) to a suspension of **[(Ag₂(exTTF-TEG²⁺))²⁺]ₓ** in a CD₃NO₂/CDCl₃ system, the ¹H NMR shows almost instantaneous reappearance of the starting neutral ligand **exTTF-TEG** and no reformation of the starting cage.

4.5. Conclusions to chapter IV

Further exploitation of the **exTTF-TEG** ligand in combination with 180° palladium and silver complexes allowed to obtain two new electro-active large M₁₂L₆ metallocages **AA14** and **AA15**. The resulting spherical cages are predicted to have large internal cavities of ca. 4000 Å³. Despite similar structure, while cage **AA14** remains stable during the electrochemical oxidation, cyclic voltammetry experiment of cage **AA15** demonstrates its disassembling.

The chemical oxidation of self-assembly **AA15** using silver cations leads to an unprecedented transformation of a discrete cage into an infinite polycationic 3D polymer **[(Ag₂ exTTF-TEG²⁺)²⁺]ₓ**. Even though several examples of coordination polymers based on the parent tetrathiafulvalene unit are described,[193] this polymer constitutes the first example of a three dimensional coordination network involving an exTTF derivative. The experimental data suggest an initial binding of the silver cations to the TEG chains promoting a kinetically delayed oxidation process. As a result, the **exTTF-TEG** fragment is oxidized to the dication state causing a drastic conformational change. The TEG chains also play an important role in the final structure, providing additional coordination sites for the silver cations. Finally, a chemical reduction allows to recover the starting ligand without reformation of the cage.

5. Chapter V. Compounds based on π-extended dithieno-tetrathiafulvalene (S-exTTF)[194]

5.1. Introduction

As was shown in a previous chapter, π-extended tetrathiafulvalene corresponds to an efficient structural system for application in self-assembly methodology, along with more traditional use in organic electronics.[195-201] The *π-extension*, in addition to be possibly promoted by an anthracene spacer bridging both 1,3-dithiol units (as in Chp 4), can be produce by a variety of conjugated units. Examples of alternative π-systems inspired by exTTF include the usage of extended aromatic spacers such as indenofluorene,[202] diindenothienoacene,[203] indacene[204] or large polycyclic aromatic hydrocarbons (PAHs).[205-206]

Another possibility to control the planarity of the molecule, in contrast to the covalent construction of related π-extended molecules, can be achieved via fine-tuning intramolecular non-covalent interactions between heteroatoms.[142] Importance of such interactions to the conformation has been very recently illustrated for a rationally designed series of benzo bis(thiazole) (BBT) derivatives in the gas phase (computation) and in the solid state.[207]

On this basis, we have designed π-system **S-exTTF**, inspired from the exTTF framework but which, contrary to the latter, should be able to generate planar oxidized states thanks to intramolecular non-covalent interactions. The benzo[1,2-b:4,5-b']dithiophene fragment was chosen as a new central core (scheme **5.1.1**).
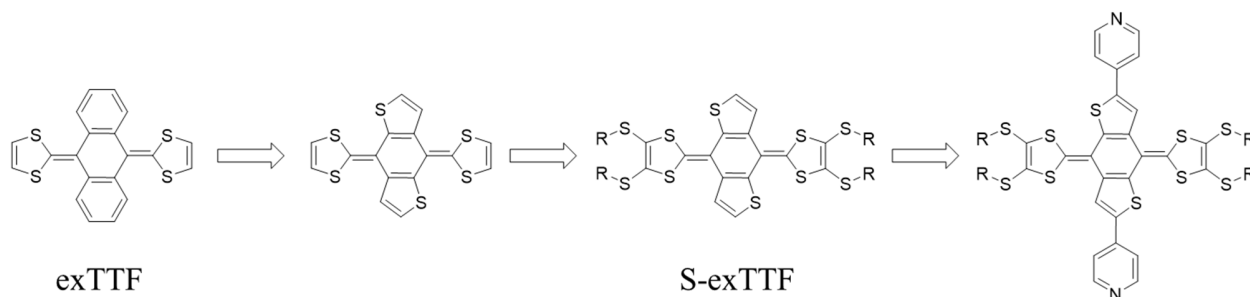
Scheme 5.1.1. Design of the S-exTTF-based ligands.

Changing the six-membered rings in the anthracene for five-membered thiophene rings is expected to substantially reduce steric strain with 1,3-dithiol rings, while intramolecular S-S interactions are supposed to stabilize more planar conformation in the neutral state. Thioalkyl peripheral groups were added in order to increase solubility, while pyridine fragments could be added to the central core to provide coordination to the metal center. Alternatively, pyridine groups can be added onto the 1,3-dithiol rings, similar to exTTF-4Py$_4$ ligand.

5.2. Synthesis

The synthesis of compound **S-exTTF** was performed according to scheme **5.2.1**. Commercially available benzo[1,2-*b*:4,5-*b'*]dithiophene-4,8-dione was modified via the two-step bis(olefination) using phosphonate esters.[208] First, Horner-Wadsworth-Emmons coupling resulted in the intermediate compounds **29** and **31**. The latter was then again treated following similar procedure with an excess of phosphonate ester **18** or **16** respectively. This allowed to obtain the target product **30** (**S-exTTF**, R=CH$_3$)

in a satisfactory yield, taken into account the lowered electrophilic character of the remaining keto function in the mono-substitute intermediates, whereas the corresponding product with R=n-C$_6$H$_{13}$ could not be obtained from phosphonate ester **16.**

18, R = Me
16, R = n-C$_6$H$_{13}$

29, R = Me (63%)
31, R = n-C$_6$H$_{13}$ (20%)

30, **S-exTTF**, R = Me (30%)
R = n-C$_6$H$_{13}$ (0 %)
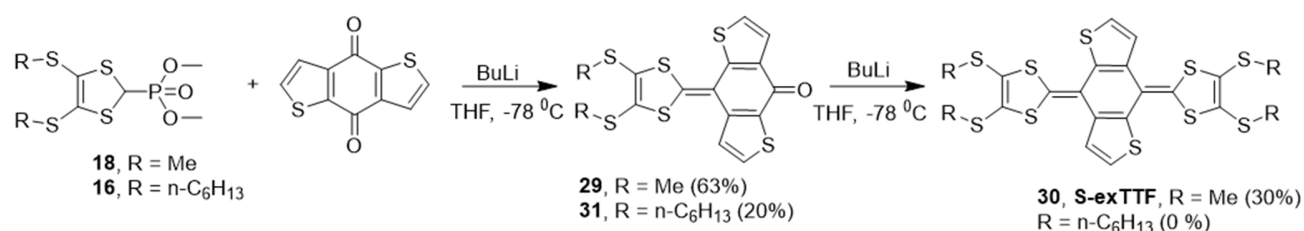
Scheme 5.2.1. Synthesis of the S-exTTF

Unlike the intermediate compound **29** and **31**, **S-exTTF** was found to be highly sensitive to acidic conditions. Therefore, all purification steps were performed using chromatography with basic aluminum oxide instead of classic silica gel. For the same reasons, NMR experiments in deuterated chloroform were performed with addition of few drops of triethylamine.

5.3. Structural properties of the neutral form

Slow vapor diffusion of methanol in a dichloromethane solution of the **S-exTTF** afforded single crystals, which were then analyzed by X-ray diffraction (figure **5.3.1**).
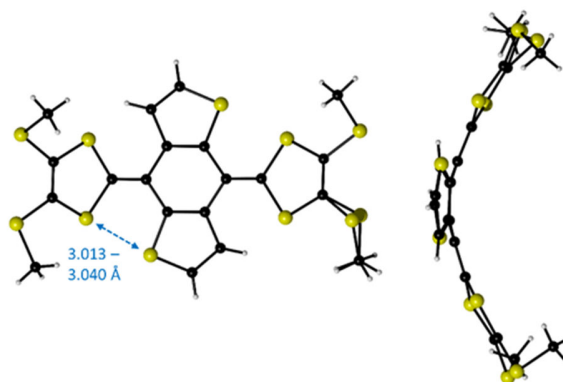
*Figure 5.3.1. Molecular structure determined by single crystal X-ray diffraction of dithieno-exTTF **S-exTTF**. Top (left) and side (right) views, respectively.*

Similarly to the other exTTF derivatives, it appears from these data that the dithieno-TTF derivative **S-exTTF** possesses a butterfly-shape bent structure in the solid state. This can be illustrated by 1,3-dithiolyliden rings pointing in the opposite direction as well as slight folding of the central dihydrobenzodithiophene moiety. However, the distortion appears less pronounced, as shown below by comparing with its exTTF analogs **exTTF** and **exTTF'** (figure **5.3.2**)
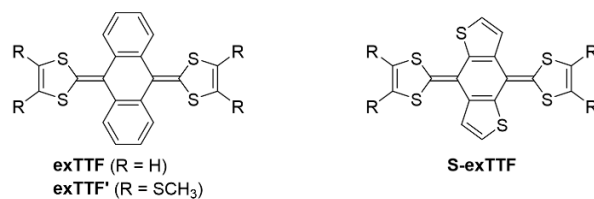
*Figure 5.3.2. Molecular structure of **exTTF**, **exTTF'** and **S-exTTF***

Main common parameters characterizing the geometrical structure of these systems can be defined by *i)* the folding angle of the central quinoidal ring (angle α), *ii)* the tilting angle defined by the 1,3-dithiolyliden rings with respect to the plane formed by the central four carbon atoms of the quinoidal ring (angle β), and iii) the 1,3-dithiolyliden folding angle along the S···S axis (angle γ). (figure **5.3.3**)
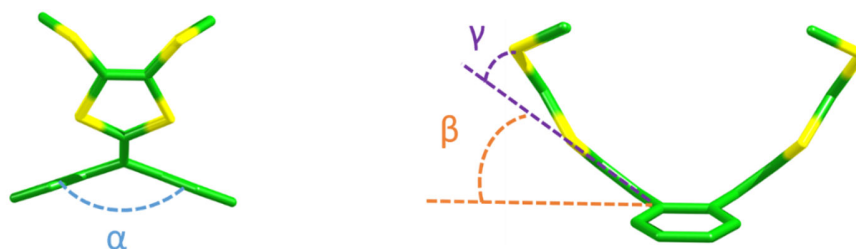
*Figure 5.3.3. Schematic view of the most relevant angles that characterize the butterfly-shape folded structures of **S-exTTF** and **exTTF'**. Hydrogen atoms have been omitted for clarity.*

In the neutral state, X-ray data for **S-exTTF** shows values of α = 22.6°, β = 17.1° and γ = 11.6°. In comparison, all these values are significantly lower than those extracted from the X-ray structures of the parent **exTTF** (α = 36.6°, β = 30.6° and γ = 14.0°)[209] and **exTTF'** (α ~38°, β ~31° and γ ~8–12°).[210]

The main reason for the distortion in the **exTTF** motif is due to the close steric repulsion between periplanar hydrogens of the dihydroanthracene unit and S atoms. On the contrary, **S-exTTF** is able to diminish steric constraint due to the conjunction of: *i)* occurrence of peripheral five-membered rings (instead of six-membered rings for **exTTF**) provides more space for periplanar hydrogen atoms, and *ii)* occurrence of attractive 1,5-S···S intramolecular contacts in the range 3.01–3.04 Å, which are far shorter than twice the van der Waals radii for S atoms (1.80 Å).

At the same time, C=C bond lengths between the central fragment and 1,3-dithiolyliden rings present similar typical values (1.36–1.37 Å) in both **S-exTTF** and **exTTF'**.

5.3.1. Electronic structure

In order to thoroughly characterize the structural, electronic and optical properties, a quantum-chemical study was performed for **S-exTTF** and its analogue **exTTF'** using the density functional theory (DFT) framework at the B3LYP-D3/6-31G** level in the presence of CH_2Cl_2. These calculations were performed by Prof E. Ortí and Dr J. Aragó (Universidad de Valencia, Spain).

In both cases, these compounds maintain saddle-like folded structures (figure **5.3.4**). In good correlation with the solid-state structure, both show folding to a boat conformation for the central quinoidal ring, while the 1,3-dithiolyliden rings are tilted up. Calculation show smaller distortion for **S-exTTF** comparing to the **exTTF'**. Computed α, β and γ angles of **S-exTTF** (24.6°, 18.9° and 6.7°

respectively; figure **5.3.4**) are significantly smaller compared with those of **exTTF'** (38.1°, 32.1° and 20.7° respectively), and correlates nicely with X-ray data in both cases.
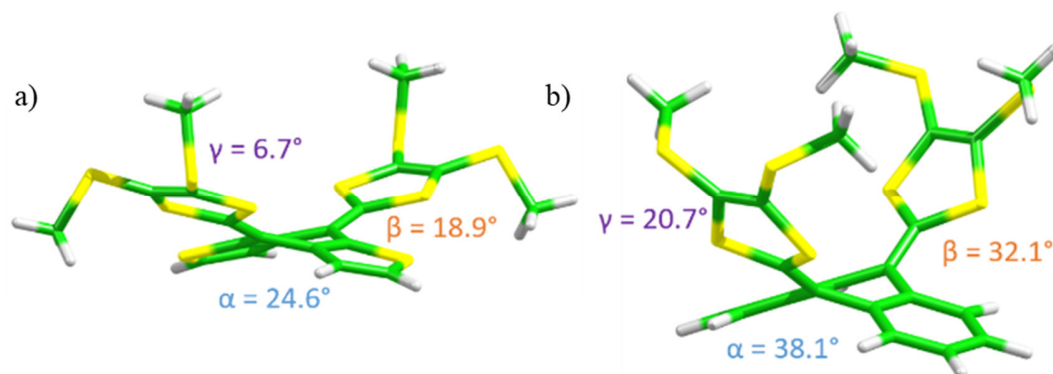
*Figure 5.3.4. Minimum-energy B3LYP-D3/6-31G**-optimized geometries calculated for compound **S-exTTF** (a) and **exTTF'** (b) in CH$_2$Cl$_2$*

The bond lengths show similar values for the dithiole rings of both compounds **S-exTTF** and **exTTF'** (figure **5.3.5**), and are consistent with the X-ray data. For instance, the exocyclic C=C bonds connecting the 1,3-dithiolyliden rings are calculated to be 1.371 Å (**S-exTTF**) and 1.361 Å (**exTTF'**).
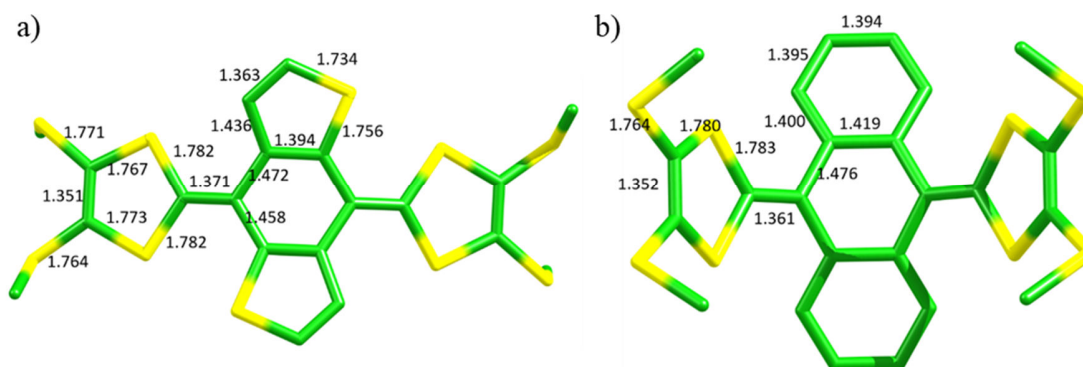
*Figure 5.3.5. B3LYP-D3/6-31G**-optimized bond lengths (in Å) computed for compound **S-exTTF** (a) and **exTTF'** (b) in CH$_2$Cl$_2$. Hydrogen atoms have been omitted for clarity*

Alongside with the minimum-energy butterfly-like structures, the fully planar structures of **S-exTTF** (C_{2h} symmetry) and **exTTF'** (D_{2h} symmetry) were also optimized at the same conditions (figure **5.3.6**). Energy difference for **S-exTTF** between the planar structure is predicted to be 13.03 kcal mol^{-1} higher in energy, in comparison to a 46.36 kcal mol^{-1} increase for **exTTF'**. Such energy difference is due to the much shorter S···H intramolecular contact occurring between the sulfur atoms and the periplanar hydrogens in the hypothetical planar conformations of **exTTF'** (1.981 Å) compared to **S-exTTF** (2.247 Å).
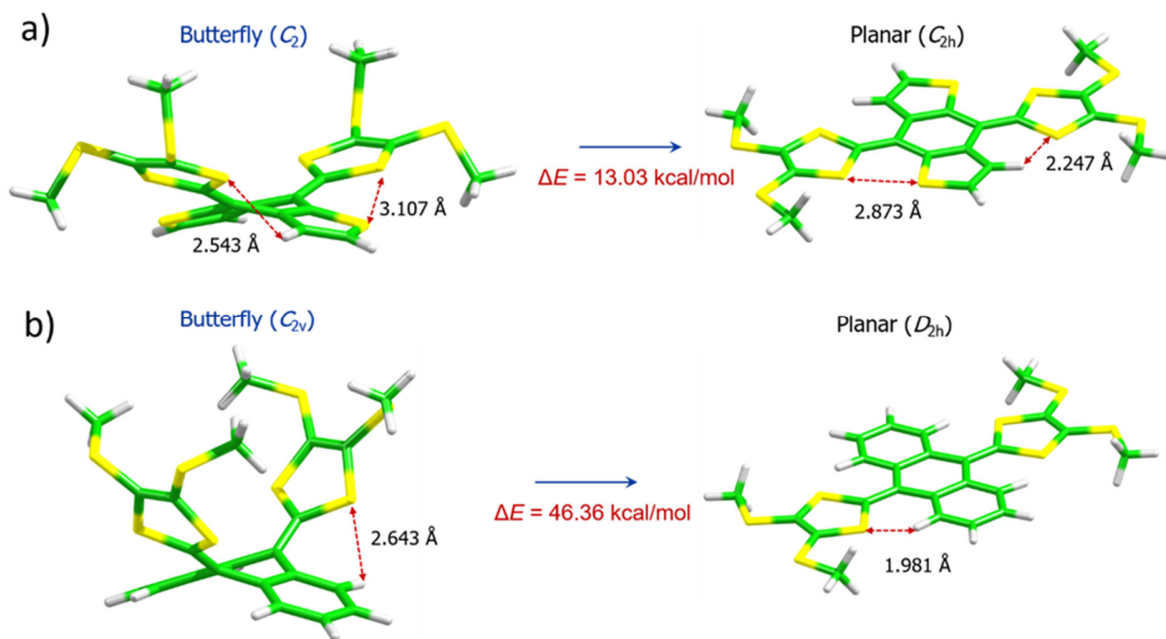
*Figure 5.3.6 B3LYP-D3/6-31G**-optimized butterfly and planar structures computed for compound **S-exTTF** (a) and **exTTF'** (b) in CH$_2$Cl$_2$. The molecular symmetry, the intramolecular contacts and the energy difference between both structures are indicated.*

Frontier molecular orbitals calculated for **S-exTTF** and **exTTF'** at their minimum-energy geometries are shown in figure **5.3.7**. Swapping the benzene rings for thiophene rings in the central fragment of **S-exTTF** leads to a very significant energy destabilization/stabilization of the highest-occupied/lowest-unoccupied molecular orbital (HOMO/LUMO) by 0.44/0.09 eV in comparison to the **exTTF'**. This causes a narrower HOMO−LUMO energy gap in **S-exTTF** (2.89 eV) compared to **exTTF'** (3.41 eV). Therefore, the electron-donor character of compound **S-exTTF** is significantly increased comparing to **exTTF'** due to a much more efficient electronic delocalization (π-conjugation). The latter is ascribed to both a more planar central dihydrobenzodithiophene unit of **S-exTTF**, and to the larger electronic polarizability of the sulfur atoms.
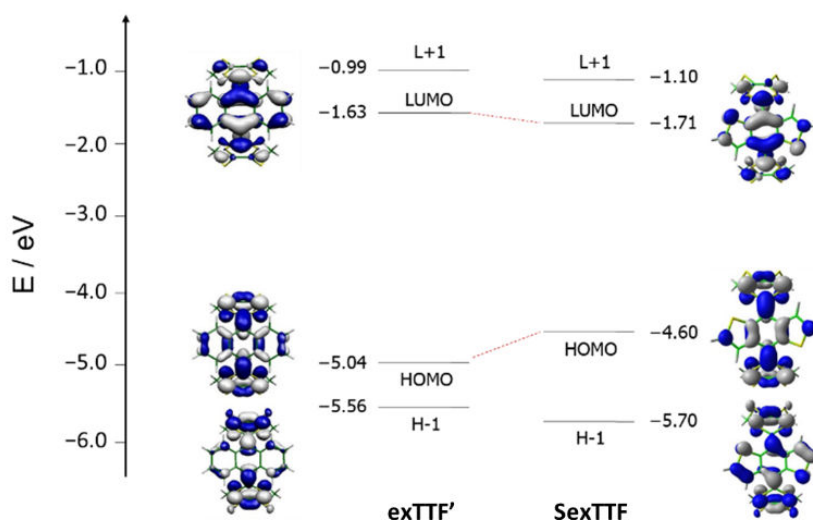
*Figure 5.3.7 Energy diagram showing the frontier molecular orbitals computed for **exTTF'** and **S-exTTF** at the B3LYP-D3/6-31G** level in CH$_2$Cl$_2$. H and L denote HOMO and LUMO, respectively.*

UV-vis spectroscopy was used in order to analyze the electronic absorption properties of compounds **S-exTTF** and its push-pull precursor **29** (figure **5.3.8**). Well-resolved and relatively sharp peaks are observed for both **S-exTTF** and **29** which is consistent with relatively rigid structures. **S-exTTF** exhibits an intense absorption band peaking at *ca.* 495 nm ($\varepsilon = 55000$ M^{-1} cm^{-1}) with a shoulder at 467 nm ($\varepsilon = 35000$ M^{-1} cm^{-1}) whereas **29** shows a less intense band centered at 486 nm ($\varepsilon = 35000$ M^{-1} cm^{-1}).
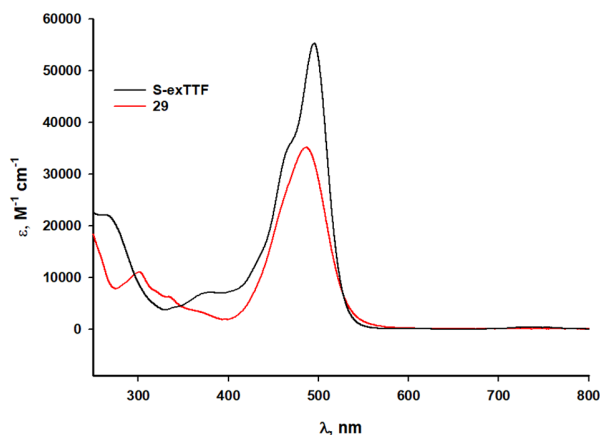
*Figure 5.3.8. UV-vis spectra of **29** and **S-exTTF** in CH$_2$Cl$_2$ (C = 1.38 × 10^{-5} M)*

To complete the study, time-dependent DFT (TDDFT) calculations of the lowest-energy singlet excited electronic states (S$_n$) were performed for compounds **S-exTTF** and **29** as well as for **exTTF'** at the B3LYP/6-31G** level in CH$_2$Cl$_2$. The main experimental absorption bands recorded for **S-exTTF** and **29**, are attributed to intense S$_0$ → S$_1$ electronic transitions predicted at 483 and 445 nm, respectively (figure **5.3.9**, a). These electronic transitions are of $\pi \rightarrow \pi^*$ nature and mainly imply the HOMO → LUMO one-electron excitation (figure **5.3.9**, b). Calculations for **exTTF'** show an intense S$_0$ → S$_1$ electronic transition at 423 nm, which has a dominant HOMO → LUMO character. The narrower HOMO−LUMO gap in the **S-exTTF** and **29** compared to **exTTF'** explains the corresponding red shift between them and is likely due to the smaller distortion from planarity of the molecular structure for the **S-exTTF** compared to **exTTF'**.

Compound	State	E (eV/nm)	f	Description[a]
S-exTTF	S_1	2.56 / 483	0.851	H → L (98)
	S_3	3.22 / 385	0.063	H → L+1 (96)
1	S_1	2.79 / 445	0.583	H → L (96)
	S_3	3.44 / 360	0.036	H−1 → L (93)
exTTF'	S_1	2.93 / 423	0.460	H → L (98)
	S_3	3.52 / 352	0.171	H−1 → L (35)
				H → L+1 (58)
[a] H and L denote HOMO and LUMO, respectively.				

*Figure 5.3.9. a) Lowest singlet excited states calculated at the TDDFT B3LYP-D3/6-31G** level for S-exTTF, intermediate 1S-exTTF and exTTF' in CH₂Cl₂ solution. Vertical excitation energies (E), oscillator strengths (f) and dominant monoexcitations with contributions (within parentheses) greater than 10%. b) frontier molecular orbitals computed for **S-exTTF**, **29** and **exTTF'** at the B3LYP-D3/6-31G** level in CH₂Cl₂. Isovalue contours (±0.03 a.u.) were used. Molecular orbital energies are given within parentheses in eV.*

5.3.2. Electrochemical properties

The electrochemical behavior of compound **S-exTTF** was studied by cyclic voltammetry in CH₂Cl₂. A single reversible oxidation wave is observed, located at $E^{1/2} = -0.18$ V *vs* Fc/Fc⁺ (figure **5.3.10**, a).

It appears of course of interest to compare this redox behavior with the one of the π-isoelectronic analogue **exTTF'** (figure **5.3.10**, b). The latter, as well as exTTF derivatives in general, exhibits a characteristic single two-electron oxidation wave, resulting in formation of a dicationic state.[188-189] This process is electrochemically irreversible, with a peak-to-peak potential separation ($\Delta E_p = E_{pa} - E_{pc}$) often higher than 200 mV[211] and involving an inverted potential phenomenon ($E_1^{ox} > E_2^{ox}$). Other similar illustrative examples of exTTF derivatives are provided above, with compounds **exTTF-4Py₄** and **exTTF-TEG** (chapter **4.1.2**).
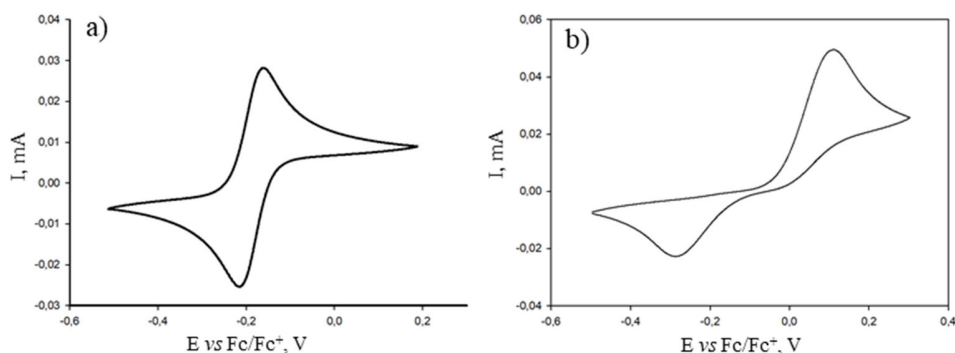

*Figure 5.3.10. Cyclic voltammograms of **S-exTTF** (a) and **exTTF'** (b), CH₂Cl₂, C = 1 mM, Bu₄NPF₆ (0.1 M), 100mV.s⁻¹, Pt working electrode;*

Therefore, in contrast to **exTTF'**, dithieno-exTTF (**S-exTTF**) exhibits a fully reversible process (figure **5.3.10**, a), illustrating a drastically different redox process, despite both are π-isoelectronic

analogs. A plausible reason for that, lies on their different respective geometries in both the neutral and oxidized states. More specifically, it indicates that compound **S-exTTF**, unlike **exTTF'**, does not undergo a large conformational change upon oxidation.[212]

As shown in the above-mentioned calculations, the π-donating ability of **S-exTTF** and **exTTF'** are significantly different. Compared to the irreversible oxidation process occurring at E_{pa}= +58 mV *vs* Fc/Fc$^+$ for **exTTF'**[211], compound **S-exTTF** exhibits a remarkably higher π-donating ability with a redox potential ($E_{1/2}$) located at −180 mV *vs* Fc/Fc$^+$. Such difference is fully consistent with the higher HOMO energy predicted for **S-exTTF** (−4.60 eV) compared to **exTTF'** (−5.04 eV).

The redox behavior of **S-exTTF** was further studied by thin-layer cyclic voltammetry (TLCV) (figure **5.3.11**). This technique[213] allows to analyze specifically the redox processes of all the species which are confined within the thin layer, avoiding the contribution of diffusion ones. Therefore, it allows to determine the charge exchanged during the redox process and to deduce the number of electrons(s) which take part in the process.

Introduction of a reference compound with a known redox behavior, is therefore required. A quinone derivative (2,3-dichloronaphthoquinone (**NQ**)) was used as the coulometric standard. The latter exhibits a one-electron reversible reduction. Figure **5.3.11** shows two redox waves, respectively assigned to the reversible oxidation of **S-exTTF** (positive potentials) and to the reversible reduction of **NQ** (negative potentials). The ratio of the exchanged charges for each process, calculated from the respective wave areas, is very close to one ($Q_{NQ}/Q_{S-exTTF}$ = 1.01). Taking into account that a 2/1 concentrations ratio was used, this observation indicates a two-electron nature for the oxidation process of **S-exTTF** and therefore formation of a dication species.
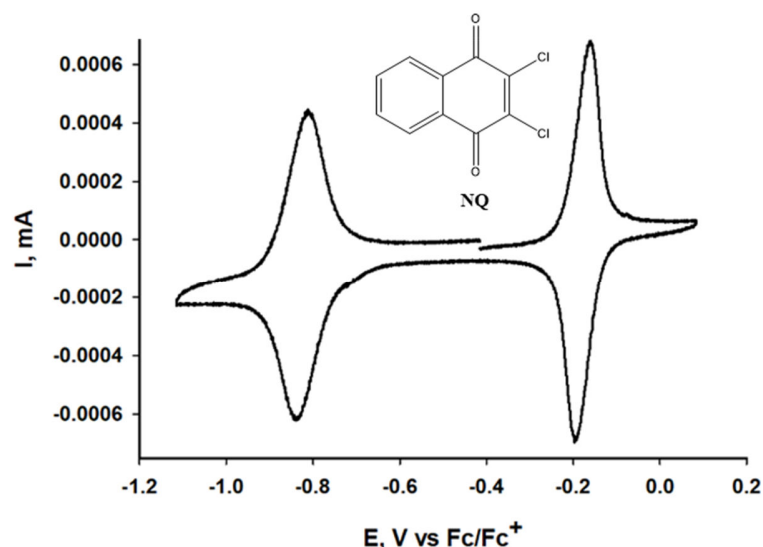
Figure 5.3.11. Thin-layer cyclic voltammogram ([S-exTTF] = 1.3 mM) in presence of 2,3-dichloronaphthoquinone (NQ) as a coulometric standard ([NQ] = 2.6 mM), CH₂Cl₂/CH₃CN 2/1 (v/v), Bu₄NPF₆ (0.1M)), 10mV.s⁻¹, r.t., Pt working electrode.

5.4. Structural properties of the oxidized form

The electrocrystallization technique (annex **2**) was used in order to obtain single crystals of the oxidized form. Slow oxidation with a constant low-current density (0.5 μA cm^{-2}) allowed to obtain shiny, dark-red, needle-like single crystals, which were grown on a platinum electrode. The latter were analyzed by X-ray diffraction. The resulting structure corresponds to a cation-radical salt formulated as [**S-**

exTTF][PF$_6$]·THF (figure **5.4.1**). Two immediate observations can be drawn from this 1:1 stoichiometry: 1/ this salt strongly differs from the electrocrystallized salts based on the exTTF skeleton, from which dicationic species (exTTF)$_1$(anion)$_2$ are usually formed,[196, 214-215]. This was expected given the strong electronic and geometric differences observed between **S-exTTF** and exTTF derivatives; 2) this 1:1 stoichiometry was unexpected from the above electrochemical studies, for which a two-electron oxidation process was anticipated. One possible explanation is a comproportionation reaction in the electrocrystallization cell, involving neutral **S-exTTF** and the corresponding dication.
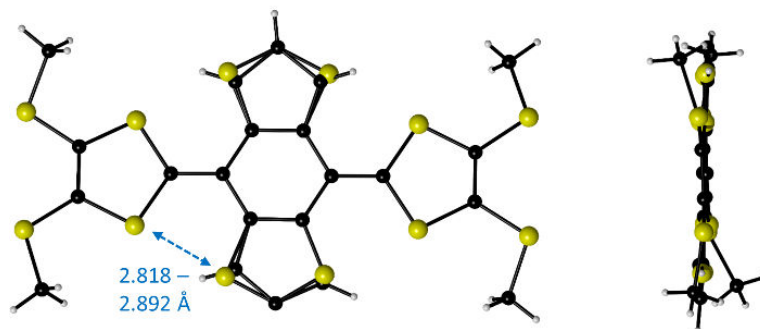
*Figure 5.4.1. Molecular structures determined by single crystal X-ray diffraction of the electrocrystallized salt [**S-exTTF**].[PF$_6$]·THF. Top (left) and side (right) views, respectively. Note that a the thiophene rings are disordered and the occupation ratios of S and C atoms in respective 1,3-positions have been refined till a convergence value of ca. 0.5.*

Analysis of the molecular structure of shows that the extended π-system of the oxidized form **S-exTTF$^{•+}$** has a planar geometry, with only two methyl substituents out of plane. Value for bond lengths within the π-framework of **S-exTTF$^{•+}$** correspond to expectation for a cation-radical salt, with in particular the exocyclic C–C bonds having a value of 1.42 Å (*vs* 1.37 Å for neutral **S-exTTF**).

However, the planar molecular structure of **S-exTTF$^{•+}$** is also quite different compared to its **exTTF^{2+}** analog. The latter is characterized by a twisting of both 1,3-dithiolium rings perpendicular to the anthracene platform[196, 214-215]. This is not the case with **S-exTTF$^{•+}$** for which a fully planar conformation is observed, resulting in an exceptionally short S⋯S intramolecular distances of 2.82–2.89 Å. This value is intermediate between the sum of the van der Waals radii for S atoms (3.60 Å) and a S–S disulfide bond (2.06 Å). Such short S⋯S contacts are quite rare in the literature. Actually, a search using the Cambridge Crystallographic Data base (CCDC), and focusing on conformationally flexible species with divalent sulfur atoms, resulted in only four cases of intramolecular S⋯S distances lower than 2.90 Å. [216-219] Interestingly, all of them are found in positively charged species. Therefore, such a remarkably short S⋯S distance may correspond from the contraction of the sulfur sp^2 lone pairs upon oxidation of the molecule.

In order to confirm this hypothesis, theoretical calculations of the charge distribution were performed by E. Ortí and Dr J. Aragó (*vide infra*, § **5.4.1**). They confirm a decrease of the Pauli exchange repulsion between the interacting S atoms upon oxidation to **S-exTTF$^{•+}$**. This then leads to a change from a repulsive S⋯S interaction in neutral **S-exTTF** which has become now attractive in **S-exTTF$^{•+}$**, justifying in part the planarization found for the [**S-exTTF**][PF$_6$]·THF salt (scheme **5.4.1**, a).
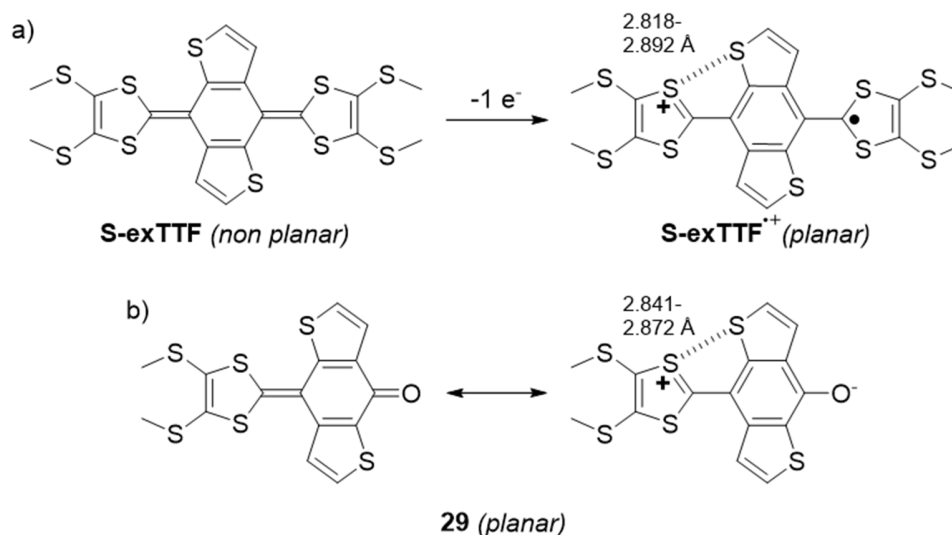
Scheme 5.4.1 Scheme figuring the S···S interaction in planar **S-exTTF·⁺** (a) and **29** (b).

Importantly and in line with the latter observation, single crystals of the intermediate push-pull compounds **29** (figure **5.4.2**) and **31** (annex **6.10**) could be obtained by slow evaporation of a methanol/dichloromethane solution. Both compounds appear essentially planar in the solid state, with only alkyl chains being out of plane. Interestingly, they both present remarkably short S···S contacts in the range of 2.84–2.87 Å (i.e. similar as in **S-exTTF·⁺**). As a result, while neutral, the push-pull compounds **29** and **31** exhibits the same unique features as does **S-exTTF·⁺**. A plausible explanation lies on a high contribution of a charged mesomeric form in the case of **29** (and **31**), which results from the π-delocalization between the electron donating 1,3-dithiole unit and the quinone accepting group, and which affords two aromatic moieties (1,3-dithiolium and benzene rings) (scheme **5.4.1**, b). Such mesomeric form promotes a certain degree of positive charge over the S atoms, showing therefore a clear analogy with the case of **S-exTTF·⁺** and resulting in exceptionally short S···S intramolecular distances.
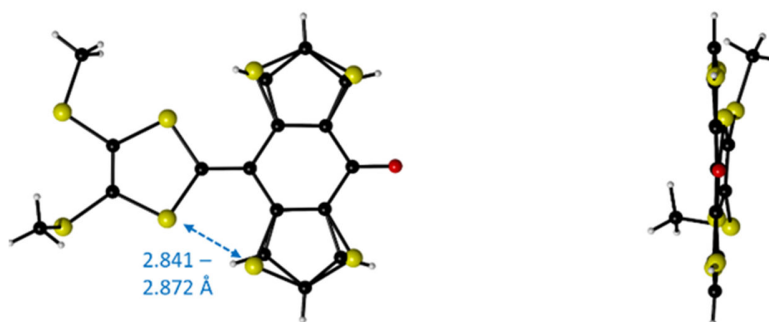
Figure 5.4.2. Molecular structures determined by single crystal X-ray diffraction of the push-pull derivative **29**. Left and right columns correspond to top and side views, respectively. Both thiophene rings are disordered with an occupation ratios of S / C atoms of 0.5.

5.4.1. Theoretical calculations

In order to further characterize the oxidized states, DFT theoretical calculation were performed at the B3LYP-D3/6-31G** level in CH₂Cl₂. The oxidized compounds (**S-exTTF·⁺**, **S-exTTF²⁺** and **exTTF'²⁺**) were optimized starting from the neutral **S-exTTF** and **exTTF'** derivatives. In the case of **S-exTTF**, the butterfly-shape conformation observed in the neutral state (see above, Figure **5.3.4**: α = 24.6°,

94

$\beta = 18.9°$ and $\gamma = 6.7°$) tends to planarize significantly upon oxidation. This is notably illustrated by the significant decrease of the folding angles in **S-exTTF**$^{•+}$ ($\alpha = 16.7°$, $\beta = 13.1°$, $\gamma = 0.9°$, figure **5.4.3**, a).
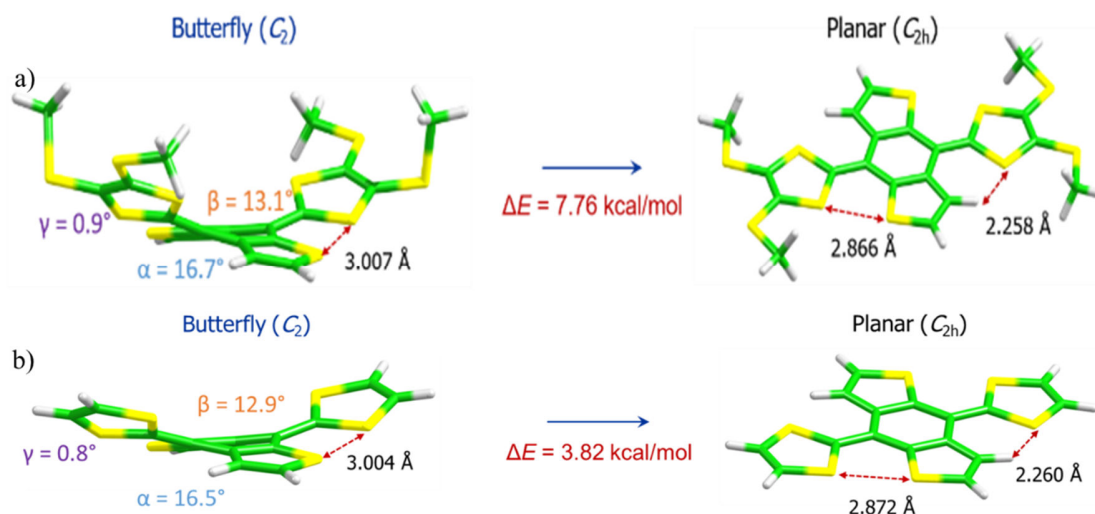
Figure 5.4.3 B3LYP-D3/6-31G**- optimized structure (left) and forced planar structure (right) computed for the radical cation **S-exTTF**$^{•+}$ *(a) and* **S-exTTF**$^{•+}$ *in which the thiomethyl groups have been removed (b) in CH$_2$Cl$_2$. The molecular symmetry, the intramolecular contacts and the energy difference between both structures are indicated.*

In the latter case, the dithiole rings of the C_2-butterfly **S-exTTF**$^{•+}$ are twisted in such a way that attractive S···S interactions with short distances (3.01 Å) are favored, whereas S···H interactions are avoided. In order to create a fully-planar C_{2h}-structure of **S-exTTF**$^{•+}$, additional difference of 7.76 kcal mol^{-1} has to be applied (**5.4.3**, a). In order to fully planarize, thiomethyl groups have to be forced to be in the molecular plane, which requires a significant additional energy. Calculations were made also without thiomethyl groups (**5.4.3**, b), leading to an energy state which is only 3.82 kcal mol^{-1} higher than for the starting C_2-butterfly structure. Consequently, very short S···S distances (2.87 Å) are found in this C_{2h}-structure, in very good agreement with those obtained from X-ray diffraction (2.82–2.89 Å). Therefore, those calculated energies confirm the possibility of a fully planar **S-exTTF**$^{•+}$ unit, with thiomethyl groups which are prone to be impacted by solid-state packing effects in the crystal. Therefore, these calculations correlate well with the X-ray structure obtained for the [**S-exTTF**][PF$_6$]·THF salt.

Further oxidation to **S-exTTF**$^{2+}$ leads to the fully planar central dihydrobenzodithiophene core (figure **5.4.4**, a), while dithiole rings are tilted by ~50° with respect to the plane formed by the central unit, similarly to what is observed with the **exTTF**$^{2+}$ parent molecule (figure **5.4.4**, b). Therefore, the structural transformation upon oxidation follows the same trend as for **exTTF**$^{2+}$ or **exTTF'**$^{2+}$. Nevertheless, a significant difference occurs with **S-exTTF**$^{2+}$, since the latter involves short S···S intramolecular contacts (3.30 Å) (2R$_{vdw}$(S)= 3.60 Å), which therefore also occurs in the dication states.
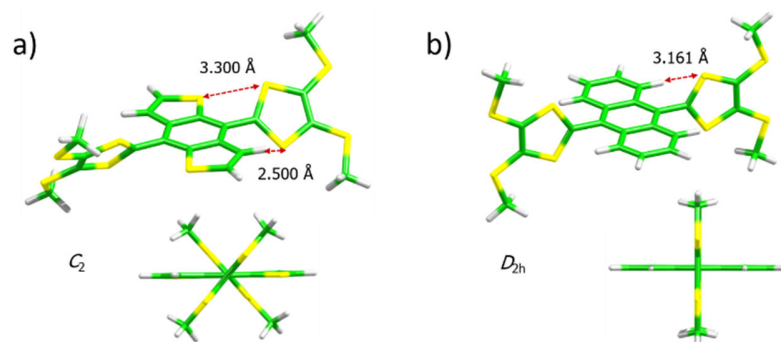
*Figure 5.4.4. Minimum-energy B3LYP-D3/6-31G**-optimized geometries computed for **S-exTTF**$^{2+}$ (a) and **exTTF'**$^{2+}$ (b) in CH$_2$Cl$_2$.*

Further analysis of the Mulliken atomic charges calculated for **S-exTTF**, **S-exTTF**$^{•+}$ and **S-exTTF**$^{2+}$ allows to investigate charges localization in the neutral and oxidized states. Data clearly show that upon oxidation, the charge is essentially located on the dithiole rings with a noticeable contribution of the thiomethyl groups (figure **5.4.5**). Upon passing from **S-exTTF** to **S-exTTF**$^{•+}$, 0.75e are extracted from the dithiole rings and the thiomethyl groups and especially from the S atoms of the dithiol groups (0.51e, figure **5.4.5**, a). Such data correlate well with the contraction of the sulfur sp^2 lone pairs upon oxidation. It in turn leads to the diminishing of the Pauli exchange repulsion, resulting in shorter S···S contacts observed for **S-exTTF**$^{•+}$.
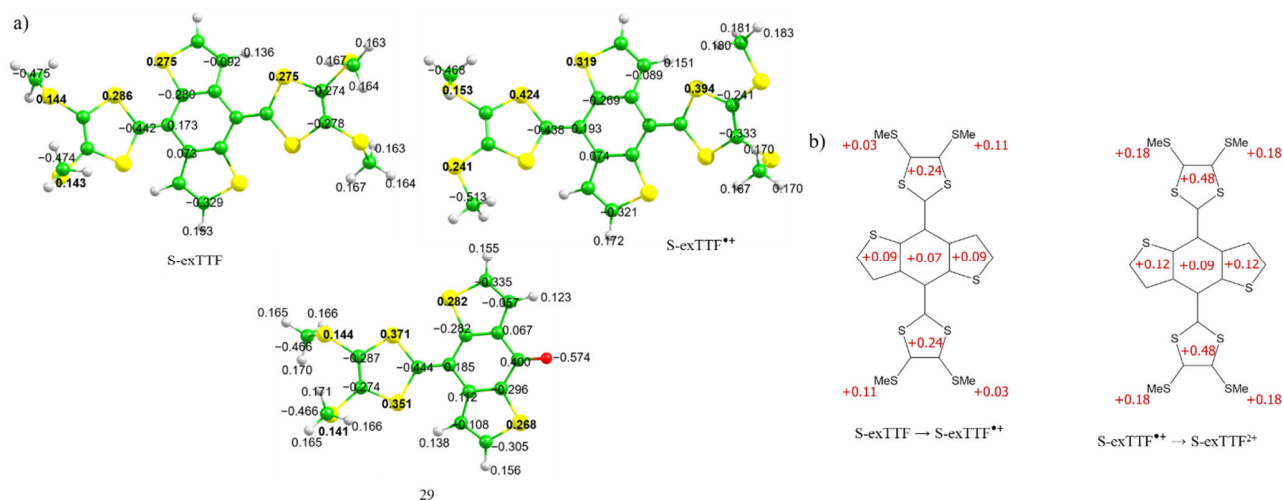
*Figure 5.4.5. Mulliken atomic charges computed for **S-exTTF**, **S-exTTF**$^{•+}$ and **29** (a) and extracted from the different molecular fragments in passing from **S-exTTF** to **S-exTTF**$^{•+}$ (left) and from **S-exTTF**$^{•+}$ to **S-exTTF**$^{2+}$ (right) computed at the B3LYP-D3/6-31G** level in CH$_2$Cl$_2$ (b)*

Interestingly, the dithiol sulfur involved in the S···S interaction for compound **29** presents a positive charge (+0.37e, figure **5.4.5**) having a value which is closer to that found for **S-exTTF**$^{•+}$ (+0.42e) than for **S-exTTF** (+0.29e). This outcome supports the experimental data for **29** and confirms the significant contribution of the charged mesomeric form in the neutral push-pull compound **29** (Scheme **5.4.1**) and the contraction of the sulfur sp^2 lone pairs giving rise to short S···S contacts.

The most striking calculated structural and electronic changes observed for **S-exTTF** and **exTTF'** upon oxidation are summarized in figure **5.4.6**. The exocyclic C=C bonds appears particularly impacted as expected from its transformation into a single C–C bond. As a result, this bond lengthens from 1.371 Å (**S-exTTF**) to 1.413 (**S-exTTF**$^{•+}$) and to 1.461 Å (**S-exTTF**$^{2+}$), which corresponds well to the experimental X-ray data – from neutral **S-exTTF** (1.37 Å) to the radical cation **S-exTTF**$^{•+}$ (1.42 Å). This transformation allows the rotation of the dithiole rings in the dication **S-exTTF**$^{2+}$ species (figure **5.4.6**, a). Calculations made on **exTTF'** used as a model, show similar changes from 1.361 to 1.476 Å predicted for the exocyclic C=C bonds upon oxidation to the dication (figure **5.4.6**, b). Further details about the evolution of the bond lengths calculated for **S-exTTF** and **exTTF'** are shown in figure **5.4.7**.
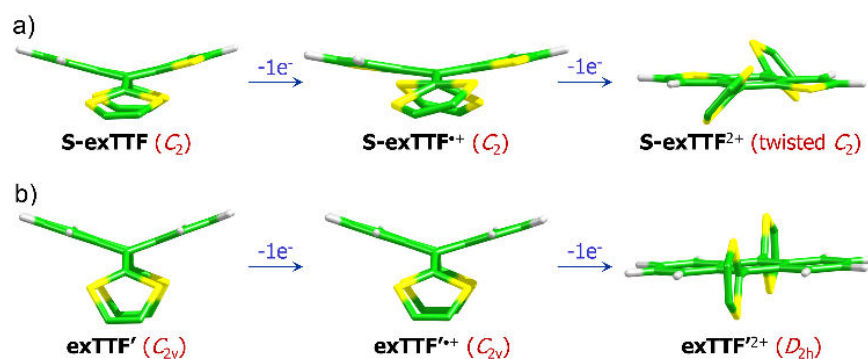
*Figure 5.4.6. Summary of the structural evolution of **S-exTTF** (a) and **exTTF'** (b) upon oxidation calculated at the B3LYP-D3/6-31G** level in CH$_2$Cl$_2$. The thiomethyl groups have been omitted for clarity. A scheme of the aromatization achieved by the **exTTF'**$^{2+}$ dication species is also given*
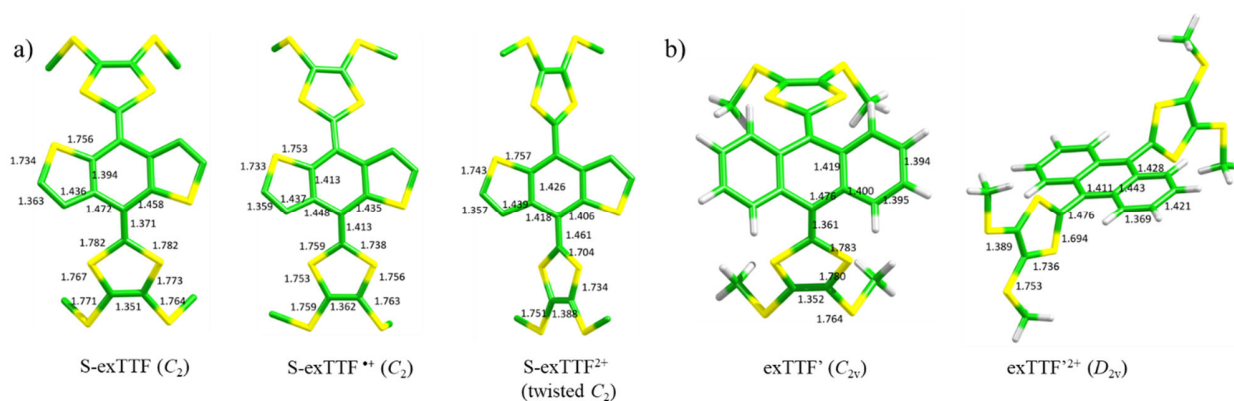
*Figure 5.4.7. B3LYP-D3/6-31G**-optimized bond lengths (in Å) calculated for **S-exTTF**, **S-exTTF**$^{•+}$ and **S-exTTF**$^{2+}$ (a) and **exTTF'** and **ex-TTF'**$^{2+}$ (b) in CH$_2$Cl$_2$*

As sketched in figure **5.4.6**, the generation of the dication species for both **S-exTTF**$^{2+}$ and **exTTF'**$^{2+}$ is favored by the combined formation of aromatic 1,3-dithiolium rings (6π electrons) and aromatic planar benzodithiophene/anthracene units central units (14π electrons). This process is accompanied by a drastic conformational change, occurring through rotation of the dithiolium ring around the C-C bond. It appears that the conformational changes predicted for dithieno-exTTF upon oxidation are significantly less drastic than those occurring for **exTTF'**, justifying a reversible two-

electron oxidation process observed experimentally for **S-exTTF** in comparison with the electrochemically irreversible two-electron oxidation observed for **exTTF'**.

5.5. Conclusions to chapter V

Further investigation of the π-extended tetrathiafulvalene scaffold allowed to create new π - isoelectronic dithieno-exTTF derivative **S-exTTF** using dihydrobenzodithiophene core instead of anthracene fragment. Introduction of additional non-covalent interactions allowed to assert further control over the conformation and planarity of the molecule in both neutral and oxidized states. Comparison with the parent **exTTF** allowed to highlight the prominent role of 1,5 S···S interactions on the fundamental level. DFT calculation shows significant destabilization in HOMO (+0.44 eV) of the **S-exTTF** in comparison to **exTTF`** as a consequence of more planar conformation. This data is further collaborated by X-ray comparison of neutral **S-exTTF** and **exTTF'**. Stronger π-donating character of the **S-exTTF** leads to lower oxidation potential in comparison with **exTTF`** ($E_{1/2}$ = 180 mV and E_{pa} = +58 mV *vs* Fc/Fc$^+$, respectively). Fully reversible character of the oxidation process for **S-exTTF** also suggests absence of strong conformational changes during the oxidation unlike the **exTTF'**.

Analysis of the oxidized states further highlights attractive character of 1,5 S···S interactions, with good correlation between experimental and theoretical data. X-ray data of the oxidized [**S-exTTF**][PF$_6$]·THF salt shows fully planarized molecule with remarkably short S···S distance of 2.82-2.89 Å. Theoretical calculations on the B3LYP-D3/6-31G** level assign it to the contraction of sp^2 lone pair of the dithiole rings in the oxidized state. This further causes lower Pauli repulsion, leading to shorter S···S contacts. Interestingly, push-pull intermediates **29** and **31** show similar S···S distance, which suggests high contribution of the charged mesomeric form.

6. Experimental section

6.1. Metal complexes
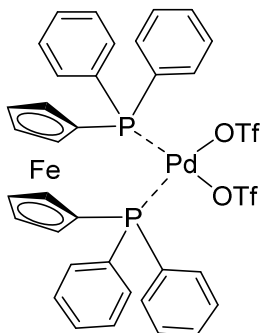
Bis(diphenylphosphino)ferrocenepalladium(II) triflate 1 [125]

To a degassed solution of commercially available bis(diphenylphosphino)ferrocenedichloropalladium (II) (300 mg, 0.37 mmol) in dichloromethane (50 mL), was added silver triflate (220 mg, 0.85 mmol). The solution was stirred at room temperature for 15 h in the dark. The mixture was filtered on hyflosupersel to remove silver chloride. Diethyl ether (100 mL) was added to the filtrate. The flask was transferred in a freezer until complete crystallization (24 h). The compound **1** was isolated as dark purple crystals (285 mg, 80 %) after filtration.

^{1}H NMR (300 MHz, CD$_3$CN) δ 7.80 (H$_{Ph}$, m, 12H), 7.58 (H$_{Ph}$, m, 8H), 4.76 (H$_{Fc}$, s, 4H), 4.58 (H$_{Fc}$, s, 4H). ^{31}P NMR (122 MHz, CD$_3$CN) δ 42.82. ^{1}H NMR (300 MHz, CD$_3$OD) δ 7.95 (H$_{Ph}$, m, 8H), 7.83 (H$_{Ph}$, m, 4H), 7.69 (H$_{Ph}$, m, 8H), 4.82 (H$_{Fc}$, s, 4H), 4.70 (H$_{Fc}$, s, 4H). ^{31}P NMR (122 MHz, CD$_3$OD) δ 48.21. ^{1}H NMR (300 MHz, CD$_3$NO$_2$): 7.92 (H$_{Ph}$, m, 8H), 7.78 (H$_{Ph}$, m, 4H), 7.60 (H$_{Ph}$, m, 8H), 4.81 (H$_{Fc}$, s, 4H), 4.69 (H$_{Fc}$, s, 4H). ^{31}P NMR (122 MHz, CD$_3$NO$_2$) δ 47.31.
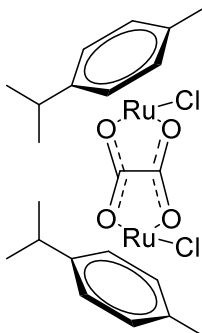
Bis(chloro (p-cymene)Rhuthenium(II))oxalato-1,4-bis(olate) 2 [220]

To a solution of [RuCl$_2$(h$_6$-p-PriC$_6$H$_4$Me)$_2$] (306 mg, 0.5 mmol) in CHCl$_3$–MeOH (1:1, 30 ml) was added (NH$_4$)$_2$C$_2$O$_4$*H$_2$O (71 mg, 0.5 mmol). The mixture was refluxed for about 6 h, then the solvent was removed. The residue was taken up in CH$_2$Cl$_2$ and the resulting mixture was filtered. The filtrate was evaporated to dryness *in vacuo* to give compound **2** as an orange powder (280 mg, 89%).

^{1}H NMR (CDCl$_3$) δ 5.57 (d, J = 6.4, 4H), 5.33 (d, J = 6.4 Hz, 4H), 2.88 (m, 2H), 2.22 (s, 6H), 1.33 (s, 6H), 1.29 (s, 6H).
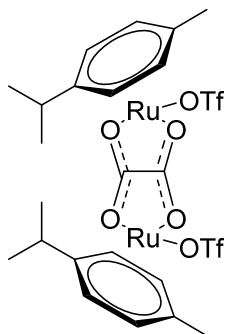
Bis(triflate (p-cymene)Rhuthenium(II))oxalato-1,4-bis(olate) Ru1 [220]

Solid silver triflate (102.8 mg, 0.40 mmol) was added to a solution of compound **2** (126 mg, 0.2 mmol) in methanol (20 ml). The mixture was stirred at room temperature for 2 h, then filtered. The filtrate was evaporated to dryness to give **Ru1** as a yellow solid(184 mg, 99%).

^{1}H NMR (methanol-d_4) δ 5.97 (d, J = 6.2, 4H), 5.77 (d, J = 6.2 Hz, 4H), 2.88 (m, 2H), 2.27 (s, 6H), 1.39 (s, 6H), 1.36 (s, 6H).
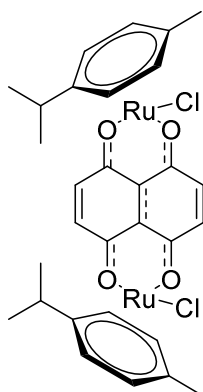
Bis(chloro(p-cymene)ruthenium(II)) 5,8-dioxo-5,8-dihydronaphthalene-1,4-bis(olate) 3 [221]

To a solution of dichloro(p-cymene)ruthenium (150 mg, 0.25 mmol) in anhydrous ethanol (20 mL), were added 5,8-dihydroxynaphthalene-1,4-dione (47 mg, 0.25 mmol) and sodium acetate (40 mg, 0.49 mmol). The solution was stirred at 90°C overnight and the suspension was filtered and the solid washed successively with: ethanol, water, acetone, diethyl ether and pentane to afford **3** as a dark green powder (136 mg, 76 %).

^{1}H NMR (300 MHz, CDCl₃) δ 6.95 (s, 4H), 5.49 (d, J = 6.0 Hz, 4H), 5.23 (d, J = 6.0 Hz, 4H), 2.86 (m, 2H), 2.22 (s, 6H), 1.31 (d, J = 6.9 Hz, 12H).
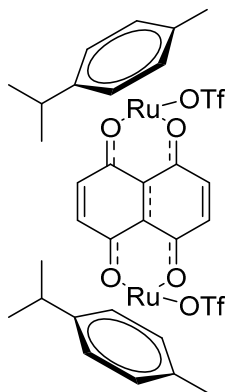
Bis(triflate(p-cymene)ruthenium(II)) 5,8-dioxo-5,8-dihydronaphthalene-1,4-bis(olate) Ru3 [221]

To a solution of **3** (100 mg, 0.14 mmol) in dichloromethane (10 mL) was added silver triflate (70 mg, 0.28 mmol). The solution was stirred in the dark overnight and the suspension was filtered on hyflosupersel to remove silver chloride. Diethyl ether was added (20 mL) to the filtrate and the flask was placed in a freezer until complete precipitation. The solid was filtered, washed with diethyl ether and dried under vacuum. The compound **Ru3** was isolated as a dark green powder (84 mg, 64 %).

^{1}H NMR (300 MHz, Methanol-d_4) δ 7.39 (s, 4H), 5.92 (d, J = 5.7 Hz, 4H), 5.67 (d, J = 5.7 Hz, 4H), 2.93 (m, 2H), 2.30 (s, 6H), 1.42 (d, J = 6.9 Hz, 12H).

Bis(chloro(p-cymene)ruthenium(II)) 6,11-dihydroxy-6,11-dihydrotetracene-5,12-bis(olate) 4 [221]

To a solution of dichloro(p-cymene)ruthenium (410 mg, 0.70 mmol) in anhydrous ethanol (20 mL), were added 6,11-dihydroxytetracene-5,12-dione (194.3 mg, 0.70 mmol) and sodium acetate (109.8 mg, 1.33 mmol). The solution was stirred at 80°C overnight and the suspension was filtered and the solid washed successively with: ethanol, water, acetone, diethyl ether and pentane to afford **4** as a dark green powder (445.2 mg, 80 %).
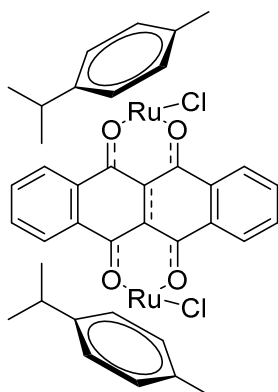
^{1}H-NMR (400 MHz, CDCl$_3$) δ 8.50 (d, J = 8.1 Hz, 4H), 7.72 (d, J = 8.1 Hz, 4H), 5.68 (d, J = 5.4, 4H), 5.33 (d, J = 5.4 Hz, 4H), 3.06 (sept., J = 3.0 Hz, 2H), 2.42 (s, 6H), 1.57 (d, J = 6.9 Hz, 12H).
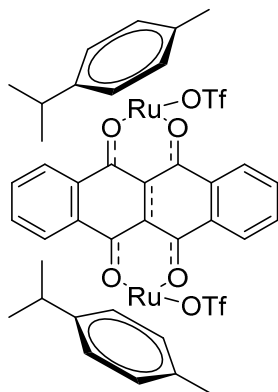
Bis(triflate(p-cymene)ruthenium(II))6,11-dihydroxy-6,11-dihydrotetracene-5,12-bis(olate) Ru4 [221]

To a solution of **4** (100 mg, 0.12 mmol) in dichloromethane (10 mL) was added silver triflate (62 mg, 0.24 mmol). The solution was stirred in the dark overnight and the suspension was filtered on hyflosupersel to remove silver chloride. Diethyl ether was added (20 mL) to the filtrate and the flask was placed in a freezer until complete precipitation. The solid was filtered, washed with diethyl ether and dried under vacuum. The compound **Ru4** was isolated as a dark green powder (82 mg, 62 %).

^{1}H NMR (300 MHz, Methanol-d_4) δ 8.72 (dd, J = 6.0, 3.3 Hz, 4H), 7.95 (dd, J = 6.1, 3.3 Hz, 4H), 6.03 (d, J = 6.1 Hz, 4H), 5.77 (d, J = 6.1 Hz, 4H), 3.04 (dt, J = 13.8, 6.9 Hz, 2H), 2.40 (s, 6H), 1.46 (d, J = 6.9 Hz, 12H).

6.2. TTF family
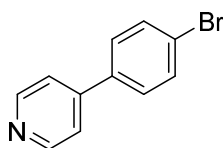
4-(4-bromophenyl)pyridine 5 [169]

To an argon degassed solution of pyridin-4-ylboronic acid (250 mg, 2.03 mmol), 1-bromo-4-iodobenzene (863 mg, 3.05 mmol) and potassium carbonate (843 mg, 6.10 mmol) in dioxane (20 mL) and water (2 mL), was added tetrakis(triphenylphosphine)palladium (II) (117 mg, 0.10 mmol). The mixture was stirred over night at 110°C and the solvent was removed under vacuum. The residue was treated with water and extracted with dichloromethane. The organic extracts were washed with water, and dried over magnesium sulfate. The solvent was removed under vacuum. A chromatography column on silica gel was performed using a gradient of eluent: from dichloromethane to dichloromethane/methanol (99/1). The compound **5** was isolated as a white powder (340 mg, 72 %).

^{1}H NMR (300 MHz, CDCl$_3$) δ 8.67 (d, J = 6.2 Hz, 2HαPy), 7.63 (d, J = 8.6 Hz, 2HPh), 7.51 (d, J = 8.6 Hz, 2HPh), 7.47 (d, J = 6.2 Hz, 2HβPy).
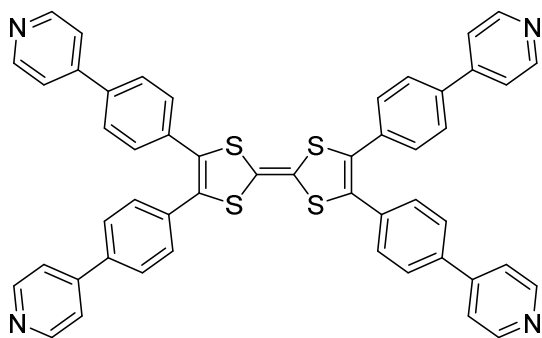
4,4',5,5'-tetrakis(4-(pyridin-4-yl)phenyl)-2,2'-bi(1,3-dithiolylidene) 6

To a suspension of palladium acetate (32 mg, 0.143 mmol), tri-tert-butylphosphonium tetrafluoroborate (104 mg, 0.358 mmol) and cesium carbonate (812 mg, 2.49 mmol) in distilled and argon degassed dioxane (3 mL) at 110°C, was added *via* cannula an argon degassed solution of TTF (100 mg, 0.489 mmol) and 4-(4-bromophenyl)pyridine **5** (420 mg, 1.790 mmol) in distilled dioxane (3 mL). The mixture was stirred at 110°C for 48h. The solvent was evaporated and dichloromethane (20 mL) was added. The resulting suspension was filtered and the filtrate was washed three times with water (20 mL). The organic phase was dried on magnesium sulfate and filtered on cotton. The solvent was evaporated and a chromatography column on silica gel was realized using a gradient of eluent: from dichloromethane/methanol (99/1) to dichloromethane/methanol (92/8) with a constant portion of triethylamine of 0.5%. Compound **6 (TTF(PhPy)₄)** was isolated as a red powder (251 mg, 86%).

^{1}H NMR (300 MHz, CDCl₃) δ 8.65 (HαPy,d, J = 5.7 Hz, 8H), 7.55 (HPh, d, J = 8.4 Hz, 2H), 7.47 (HβPy d, J = 5.7 Hz, 2H), 7.38 (HPh, d, J = 8.4 Hz, 2H). ^{13}C NMR (76 MHz, CDCl₃) δ 150.41, 147.14, 138.21, 133.30, 129.88, 129.23, 127.35, 121.36, 108.54. HRMS m/z found 816.1503, *m/z* calculated 816.1510.
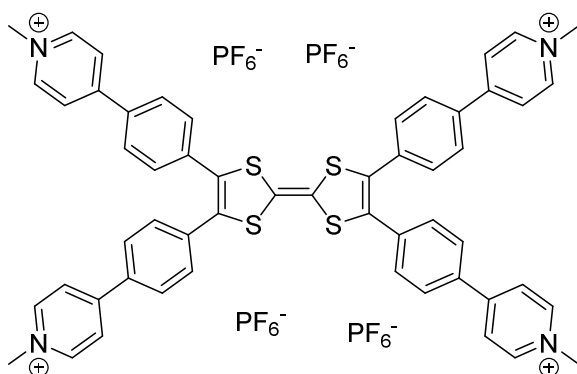
4,4',4'',4'''-([2,2'-bi(1,3-dithiolylidene)]-4,4',5,5'-tetrayltetrakis(benzene-4,1-diyl))tetrakis(1-methylpyridin-1-ium) hexafluorophosphate(V) 7

To a suspension of **TTF(PhPy)₄** (40 mg, 0.049 mmol) in dry DMF (4 mL) was added large excess of iodomethane (120 uL, 278 mg, 1.96 mmol,). The mixture was stirred overnight until formation of clear intense red solution. After cooling down, Et₂O was added and the resulting solid was filtered and dried to give dark powder. Anion exchange from SO₄²⁻ to PF₆⁻ was performed by adding a concentrated solution of potassium hexafluorophosphate in water and stirring for 2 hr. Resulting precipitate was centrifuged, washed with minimum methanol, Et₂O and dried in vacuo to give **7 (TTF(PhPy-Me)₄**) as a dark powder (25 mg, 35 %).

^{1}H NMR (300 MHz, Acetonitrile-d_3) δ 8.61 (d, J = 6.9 Hz, 8H), 8.20 (d, J = 7.0 Hz, 8H), 7.86 (d, J = 8.6 Hz, 8H), 7.53 (d, J = 8.5 Hz, 8H), 4.28 (s, 12H). ^{13}C NMR (76 MHz, CD$_3$CN) δ 251.21, 155.63, 146.27, 136.57, 135.11, 131.33, 130.66, 129.56, 125.71, 108.52, 48.53, 2.08, 1.80, 1.53, 1.25, 0.98, 0.70. ^{31}P NMR (122 MHz, Acetonitrile-d_3) δ -130.72 – -157.80 (m). ^{19}F NMR (283 MHz, Acetonitrile-d_3) δ -72.84 (d, J = 706.6 Hz). HRMS – m/z [TTΦ(Me-4PyPh)$_4$$^{4+}$(PF$_6$$^-$)$_4$ - 2(PF$_6$$^-$)]$^{2+}$ found 583.0842, calculated 583,0860. [TTF(Me-4PyPh)$_4$$^{4+}$(PF$_6$$^-$)$_4$ – 3(PF$_6$$^-$)]$^{3+}$ found 340.4006, calculated 340.4102.
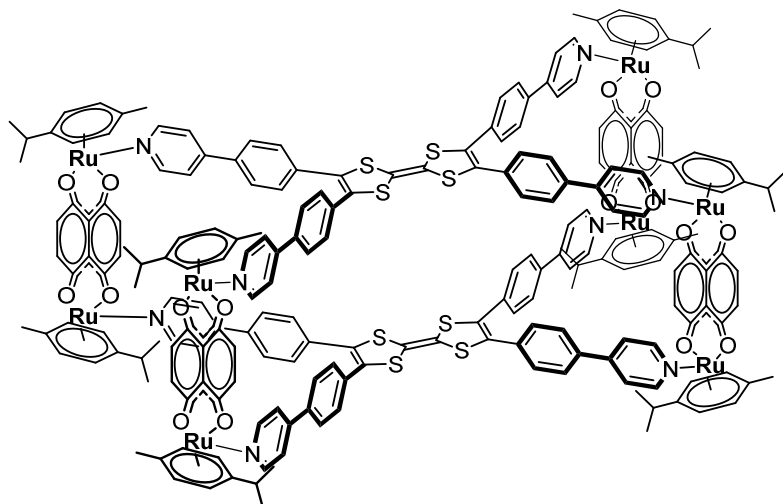
AA1

Ruthenium complex **Ru3** (10.63 mg, 11 μmol) and **TTF(PhPy)$_4$** (4.51 mg, 5.5 μmol) were dissolved in deuterated methanol or acetone (0.5 mL) and the solution was stirred at 50°C overnight. After cooling at room temperature, Et$_2$0 was added to the solution and the resulting solid was filtered and dried under vacuo to give cage **AA1** as a black solid (13.17, 86 %).

^{1}H NMR (300 MHz, MeOD) δ 8.40 (d, J = 6.7 Hz, 16H), 7.62 (d, J = 6.7 Hz, 16H), 7.49 (d, J = 8.5 Hz, 16H), 7.28 (s, 8H), 7.23 (s, 8H), 7.17 (d, J = 8.5 Hz, 16H), 5.88 (d, J = 6.0 Hz, 16H), 5.65 (d, J = 6.0 Hz, 16H), 2.87 (m, 4H), 2.16 (s, 24H), 1.37 (d, J = 6.9 Hz, 48H). ^{1}H NMR (300 MHz, MeOD/MeNO$_2$ 50/50) δ 8.39 (d, J = 6.6 Hz, 16H), 7.57 (d, J = 6.6 Hz, 16H), 7.47 (d, J = 8.0 Hz, 16H), 7.22 (ovelap, 32H), 5.83 (m, 16H), 5.61 (d, J = 6.5 Hz, 16H), 2.89 (m, 8H), 2.16 (s, 24H), 1.37 (d, J = 6.9 Hz, 48H). ^{1}H DOSY NMR (MeOD/MeNO$_2$ 50/50) D = 3.16 x 10^{-10} m^{2}s^{-1}. HRMS-ESI-FTICR: *m/z* calculated: [Ru$_8$TTF$_2$, 5OTf$^-$]$^{3+}$: 1671.4091; [Ru$_8$TTF$_2$, 4OTf$^-$]$^{4+}$ 1216.3187; *m/z* found: [Ru$_8$TTF$_2$, 5OTf$^-$]$^{3+}$: 1671.4093, [Ru$_8$TTF$_2$, 4OTf$^-$]$^{4+}$: 1216.3185.
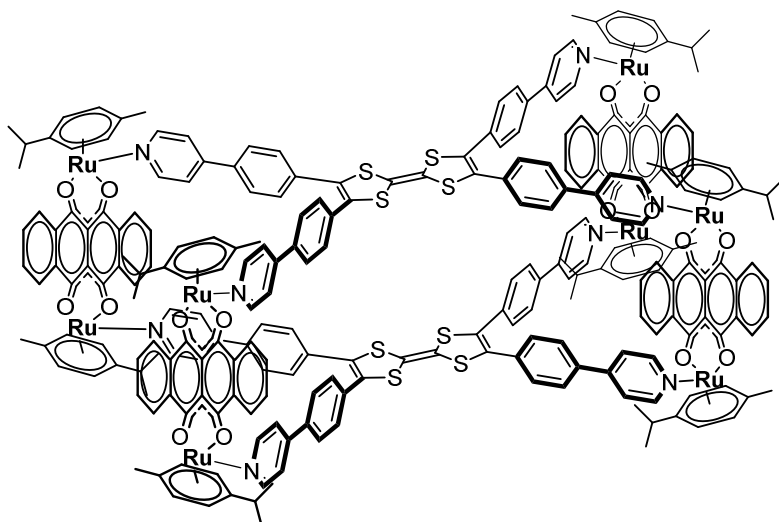
AA2

Ruthenium complex **Ru4** (11.74 mg, 11 μmol) and **TTF(PhPy)4** (4.51 mg, 5.5 μmol) were dissolved in deuterated acetone (0.5 mL) and the solution was stirred at 50°C overnight. After cooling at room temperature, Et₂0 was added to the solution and the resulting solid was filtered and dried under vacuo to give cage **AA1** as a black solid (13.49, 83 %). Formation of the cage **AA2** was quantitative according to ^{1}H NMR, ^{1}H DOSY NMR and HRMS-ESI-FTICR.

^{1}H NMR (300 MHz, Acetone-d_6) δ 8.80 – 8.65 (m, 16H), 8.50 (d, J = 6.2 Hz, 8H), 7.89 (dt, J = 5.9, 4.1 Hz, 16H), 7.38 (d, J = 6.1 Hz, 8H), 7.26 (d, J = 8.1 Hz, 8H), 6.87 (d, J = 7.9 Hz, 8H), 6.10 (dd, J = 12.5, 6.1 Hz, 16H), 5.84 (t, J = 5.8 Hz, 16H), 2.94 (m, 8H), 2.12 (s, 24H), 1.37 (d, J = 6.9 Hz, 48H). ^{1}H DOSY NMR (acetone-d_6) D = 6.62 x 10^{-10} m²s^{-1}.

6.3. DTF family

Bis(tetraethylammonium) bis(1,3-dithiole-2thione-4,5-dithiol) zincate 8

Dimethylformamide (480 mL) and carbon disulfide (240 mL, 4 mol, d = 1.266) were placed in an Erlenmeyer flask and degassed at 0°C. In a three neck round bottom flask with mechanical stirrer, were placed small pieces of sodium (23 g, 1.0 mol) in xylene (80 mL) under argon. The suspension was heated until sodium fusion and then stirred very vigorously to form small balls. The mixture was then cooled to room temperature and xylene was decanted. The sodium balls were cooled at 0°C for 30 min and the dimethylformamide/carbon disulfide solution was added carefully. The mixture was then stirred overnight for 14 h at room temperature and then, methanol (50 mL) was added at 0°C. To the resulting solution was added a solution of zinc chloride (21.3 g, 0.156 mol) in ammonia (35 %, 360 mL) and water (100 mL). Then, a solution of tetraethyl ammonium bromide (66 g, 314 mmol) in water (500 mL) was added slowly *via* dropping funnel. Then, the solution was stirred overnight until complete precipitation. The red solid was filtered and washed with water (500 mL), methanol (2 x 500 mL) and diethyl ether (500 mL). After drying under vacuum, the zincate **8** was obtained as a red solid (99.12 g, 88%).

General protocol for compounds 9-11

To a solution of zincate **8** (10 g, 13.91 mmol) in acetonitrile (80 mL), was added corresponding alkyl halide (4,5 eq., 61.23 mmol, d = 1.44). The resulting solution was stirred at reflux for 1 h 30 min and the

solvent was removed. The residue was partially dissolved in dichloromethane (200 mL), the organic phase was washed with water (2 x 200 mL) and dried with magnesium sulfate. The solvent was removed under vacuum. A chromatography column on a silica gel using appropriate system to obtain a final compound.
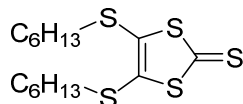
4,5-bis(hexylthio)-1,3-dithiole-2-thione 9

A chromatography column on a silica gel was performed using dichloromethane/petroleum ether (20/80) as eluent. The compound **9** was isolated as an orange oil (8.91 g, 87 %).

^{1}H NMR (300 MHz, CDCl3) δ 2.86 (HSCH2, t, J = 7.2 Hz, 4 H), 1.65 (HCH2, m, 4H), 1.41 (HCH2, m, 4H), 1.29 (HCH2, m, 8H), 0.88 (HCH3, m, 6H).
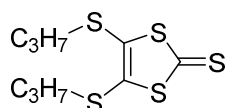
4,5-bis(propylthio)-1,3-dithiole-2-thione 10

A chromatography column on a silica gel was performed using dichloromethane/petroleum ether (10/90) as eluent. The compound **10** was isolated as an orange oil (14.47 g, 92 %).

^{1}H NMR (300 MHz, CDCl3-d) δ 2.85 (dd, J = 7.6, 6.9 Hz, 4H), 1.70 (h, J = 7.3 Hz, 4H), 1.03 (t, J = 7.3 Hz, 6H).
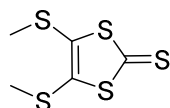
4,5-bis(methylthio)-1,3-dithiole-2-thione 11

A chromatography column on a silica gel was performed using dichloromethane/petroleum ether (1/1) as eluent. The compound **11** was isolated as yellow needle crystals (11.5 g, 91 %).

^{1}H NMR (300 MHz, CDCl3-d) δ 2.49 (s, 6H).

General protocol for compounds 12-15

To a solution of compounds **9-11** or commercially available vinylene tricarbonate (24.27 mmol) in dichloromethane (34 mL), was added under argon methyl trifluoromethanesulfonate (2.9 mL, 24.48 mmol, d = 1.05). After 1 h 30 min at room temperature the solvent was removed under vacuum and an orange oil was obtained (12.21 g). The resulting oil (or a powder in case of vinylene tricarbonate) was dissolved in acetonitrile (55 mL) and isopropanol (25 mL) at 0°C. Sodium borohydride (477 mg, 12.6 mmol) was added in small portions until no degassing was observed. After 2 h at room temperature, the solvents were evaporated. The oily residue was partially dissolved in dichloromethane 200 mL), the

organic phase was washed with brine (2 x 200 mL), dried over magnesium sulfate. After evaporation of the solvent product can be used without purification in the next stage. If needed, a chromatography column on silica gel can be perfomed using petroleum ether/dichoromethane (80/20) as eluent.
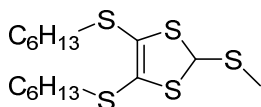
4,5-bis(hexylthio)-2-(methylthio)-1,3-dithiole 12

Compound **12** was obtained as an orange oil (4.15 g, 91%).

^{1}H NMR (300 MHz, CDCl$_3$) δ 5.73 (s, 1H), 2.81 (m, 4H), 2.25 (s, 3H), 1.65 (m, 4H), 1.44 – 1.22 (m, 12H), 0.88 (m, 6H).
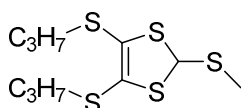
4,5-bis(propylthio)-2-(methylthio)-1,3-dithiole 13

Compound **13** was obtained as an orange oil (14.85 g, 97%).

^{1}H NMR (300 MHz, CDCl$_3$) δ 5.78 (s, 1H), 3.02 – 2.65 (m, 4H), 2.29 (s, 3H), 1.86 – 1.60 (m, 4H), 1.05 (t, J = 7.3 Hz, 6H).
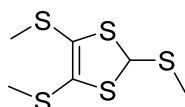
4,5-bis(methylthio)-2-(methylthio)-1,3-dithiole 14

Compound **14** was obtained as a colorless oil (1.55 g, 98%).

^{1}H NMR (300 MHz, CDCl$_3$): 5.83 (s, 1H), 2.46 (s, 6H), 2.31 (s, 3H).
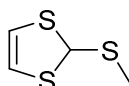
2-(methylthio)-1,3-dithiole 15

Compound **15** was obtained as a colorless oil (1.55 g, 98%).

^{1}H NMR (300 MHz, CDCl$_3$): 6.07 (s, 2H), 3.15 (s, 1H), 2.39 (s, 3H).

General protocol for compounds 16-19

To a solution of compound **12-15** (10.87 mmol) in acetic anhydride (10 mL) at 0°C under argon, was added carefully tetrafluoroboric acid diethyl ether complex (1.78 mL, 13.04 mmol, d = 1.18). After 1 h of stirring at room temperature, the solvent was removed under reduced pressure. The residue was dissolved in anhydrous acetonitrile (70 mL) and sodium iodide (1.79 g, 11.95 mmol) and trimethylphosphite (1.54 mL, 13.04 mmol, d = 1.05) were added. The mixture was stirred for 4 h under

argon and then the solvents were removed. The residue was partially dissolved in dichloromethane (200 mL) and the organic phase was washed with water (2 x 50 mL), dried over magnesium sulfate and the solvent was evaporating. A chromatography column on silica gel was performed to isolate final compound **16-20** respectively.
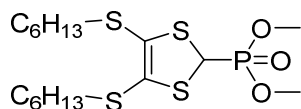
Dimethyl (4,5-bis(hexylthio)-1,3-dithiol-2-yl)phosphonate 16

A chromatography column on a silica gel was performed using ethyl acetate/petroleum ether (4/6) as eluent. The compound **16** was isolated as an orange oil (2.99 g, 62 %).

^{1}H NMR (300 MHz, CDCl$_3$) δ 4.74 (d, J = 5.4 Hz, 1H), 3.88 (d, J = 10.6 Hz, 6H), 2.81 (m, 4H), 1.66 (m, 4H), 1.51 – 1.14 (m, 12H), 0.89 (t, J = 6.8 Hz, 6H).
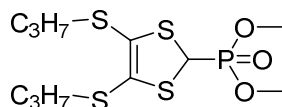
Dimethyl (4,5-bis(propylthio)-1,3-dithiol-2-yl)phosphonate 17

A chromatography column on a silica gel was performed using ethyl acetate/petroleum ether (1/1) as eluent. The compound **17** was isolated as a brown oil (3,08 g, 78.6 %).

^{1}H NMR (300 MHz, CDCl$_3$) δ 4.71 (d, J = 5.5 Hz, 1H), 3.88 (d, J = 10.6 Hz, 6H), 2.98 – 2.62 (m, 4H), 1.85 – 1.58 (m, 5H), 1.01 (t, J = 7.3 Hz, 7H).
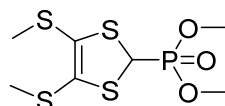
Dimethyl (4,5-bis(methylthio)-1,3-dithiol-2-yl)phosphonate 18

A chromatography column on a silica gel was performed using ethyl acetate/petroleum ether (1/1) as eluent. The compound **18** was isolated as a yellow oil, which solidified in the freezer (4.14 g, 69 %).

^{1}H NMR (300 MHz, CDCl$_3$) δ 4.73 (d, J = 5.6 Hz, 1H), 3.88 (d, J = 10.6 Hz, 6H), 2.41 (s, 6H).
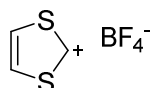
1,3-dithiol-2-ylium tetrafluoroborate 19

Compound **19** was obtained as a white powder after precipitating with diethyl ether and used without purification (1.71 g, 87 %).

^{1}H NMR (300 MHz, DMSO-d_6) δ 11.64 (t, J = 2.0 Hz, 1H), 9.40 (d, J = 2.0 Hz, 2H).
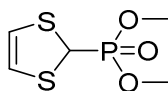
Dimethyl (1,3-dithiol-2-yl)phosphonate 20

A chromatography column on a silica gel was performed using ethyl acetate/petroleum ether (1/1) as eluent. The compound **20** was isolated as a colorless oil (1.41 g, 80 %).

^{1}H NMR (300 MHz, CDCl$_3$) δ 5.97 (s, 2H), 5.03 (d, J = 3.9 Hz, 1H), 3.89 (d, J = 10.5 Hz, 6H). ^{31}P NMR (122 MHz, CDCl$_3$): 19.99.
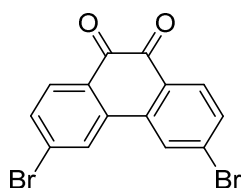
3,6-dibromophenanthrene-9,10-dione 21 [222]

To a suspension of phenanthrene-9,10-dione (5 g, 25.0 mmol) and benzoyl peroxide (0.29 g, 0.9 mmol, 0.75 equiv.) in nitrobenzene (25 mL), was added slowly and with precaution (bromine trap with sodium thiosulfate solution) bromine (1.86 g, 0.6 mL, 11.6 mmol, d = 3,10) through a septum. After heating at 120°C, bromine (6.9 g, 2.24 mL, 13.2 mmol, 2.2 equiv.) was added very carefully dropwise. After heating one hour at 120°C, the dark orange solution was cooled to room temperature. Ethanol (25 mL) was then added to precipitate the product. This suspension was filtered under vacuum and washed with ethanol until the filtrate was completely colorless to give **21** as a shiny orange product (9.15 g, 81 %).

^{1}H NMR (300 MHz, CDCl$_3$) δ 8.12 (d, ^4J = 1.8 Hz, 2H), 8.07 (d, J = 8.1 Hz, 2H), 7.66 (dd, J = 1.8 Hz, J = 8.1 Hz, 2H).
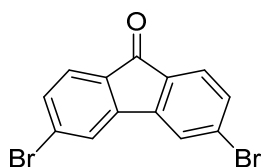
3,6-dibromo-9H-fluoren-9-one 22 [222]

To a solution of potassium hydroxide (12.34 g, 220 mmol) in water (15 mL) at 130°C, was added 3,6-dibromophenanthrene-9,10-dione **21** (6.00 g, 16.4 mmol). After 30 min, potassium permanganate (14.15 g, 89.5 mmol) was added by small portions over 1 h 30 min. The solution was stirred for 1 h and cooled to room temperature. The suspension was neutralized with sulfuric acid and then sodium bisulfite was added. The suspension became white. Then the precipitate was filtered and dried over vacuum to give **22** as a white powder (3.34 g, 60 %).

^{1}H NMR (300 MHz, CDCl$_3$) δ 7.67 (d, J = 1.4 Hz, 2H), 7.55 (d, J = 7.9 Hz, 2H), 7.49 (dd, J = 7.9, J = 1.4 Hz, 2H).
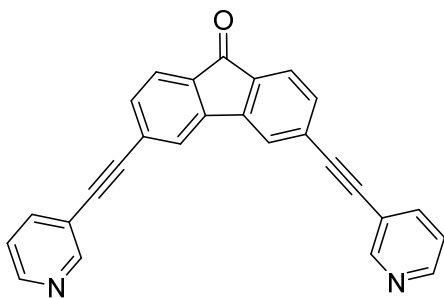
3,6-bis(pyridin-3-ylethynyl)-9H-fluoren-9-one 23

Reaction was carried in the MW tube. To an argon degassed solution of 3,6-dibromo-9H-fluoren-9-one **22** (100 mg, 0.295 mmol) and 3-ethynylpyridine (122 mg, 1.18 mmol, 4 equiv.) in diisopropylamine/toluene (v/v 1/1, 4 mL), Pd(PPh$_3$)$_4$ (68.3 mg, 0.059 mmol, 0.2 equiv.) and CuI (11.3 mg, 0.059 mmol, 0.2 equiv.) were added under argon. Tube was irradiated for 30 min at constant 250 W. The solvent was evaporated under vacuum. The residue was treated with water and extracted with dichloromethane (50 mL). The organic extracts were washed with water (3 x 50 mL) and dried over magnesium sulfate. The solvent was evaporated under vacuum. A chromatography column on silica gel was performed using mixture dichloromethane/petroleum ether (1/1). Compound was further purified by recrystallization with a mixture of dichloromethane/pentane. Compound **23** was obtained as yellow powder (85 mg, 75 %).

^{1}H NMR (300 MHz, CDCl$_3$) δ 8.80 (s, 1H), 8.59 (s, 1H), 7.84 (d, J = 7.9 Hz, 1H), 7.74 – 7.64 (m, 2H), 7.51 (d, J = 7.7 Hz, 1H), 7.37 – 7.29 (m, 1H). ^{13}C NMR (76 MHz, CDCl$_3$) δ 191.77, 152.08, 152.08, 148.88, 148.88, 143.71, 138.97, 134.09, 133.00, 128.99, 124.54, 123.56, 123.35, 119.95, 92.21, 89.45. FAB-HRMS: found: 382.1104, calculated: 382.1106.
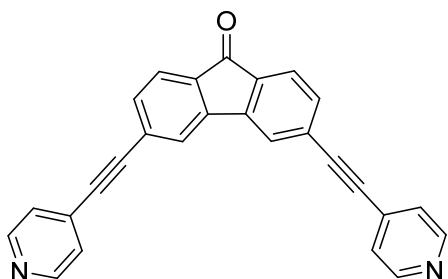
3,6-bis(pyridin-4-ylethynyl)-9H-fluoren-9-one 24

Reaction was carried in the MW tube. To an argon degassed solution of 3,6-dibromo-9H-fluoren-9-one **22** (100 mg, 0.295 mmol) and 3-ethynylpyridine (122 mg, 1.18 mmol, 4 equiv.) in diisopropylamine/toluene (v/v 1/1, 4 mL), Pd(PPh$_3$)$_4$ (68.3 mg, 0.059 mmol, 0.2 equiv.) and CuI (11.3 mg, 0.059 mmol, 0.2 equiv.) were added under argon. Tube was irradiated for 30 min at constant 250 W. The solvent was evaporated under vacuum. The residue was treated with water and extracted with dichloromethane (50 mL). The organic extracts were washed with water (3 x 50 mL) and dried over magnesium sulfate. The solvent was evaporated under vacuum. A chromatography column on silica gel was performed using a gradient of eluent: from dichloromethane/petroleum ether (80/20) to dichloromethane/methanol (98/2). Compound was further purified by recrystallization dichloromethane/pentane. Compound **24** was obtained as yellow powder (67 mg, 59 %).

^{1}H NMR (300 MHz, CDCl$_3$) δ 8.64 (d, J = 5.8 Hz, 2H), 7.73 – 7.67 (m, 2H), 7.51 (dd, J = 7.6, 1.1 Hz, 1H), 7.40 (dd, J = 4.6, 1.4 Hz, 2H). ^{13}C NMR (76 MHz, CDCl$_3$) δ 191.64, 149.95, 143.65, 134.30, 133.28, 130.67, 128.62, 125.59, 124.57, 123.71, 92.93, 90.05. FAB-HRMS: found: 382.1099, calculated: 382.1106.

General protocol for ligands 25-28

To a solution of corresponding phosphonate **16** or **17** (0.37 mmol, 1.5 equiv.) in anhydrous tetrahydrofuran (10 mL) at -78°C, was slowly added *n*-butyl lithium (0.149 mL, 0.37 mmol, 1.6 M, 1.5 equiv.). The mixture was stirred one hour at -78°C and a suspension of compound **23** or **24** respectively (0.25 mmol, 1 equiv.) in anhydrous tetrahydrofuran (10 mL) at -78°C was added *via* cannula. The mixture was stirred 1 h at -78°C and overnight at room temperature. The solvent was removed under vacuum. The residue was treated with water and extracted with dichloromethane. The organic extracts were washed with water, and dried over magnesium sulfate. The solvent was removed under vacuum and the residue was purified by chromatography on silica gel using a gradient of eluent: petroleum ether/dichloromethane (1/1) to dichloromethane/methanol (98/2) with constant 1% of trimethylamine followed by recrystallization using a dichloromethane/methanol mixture.
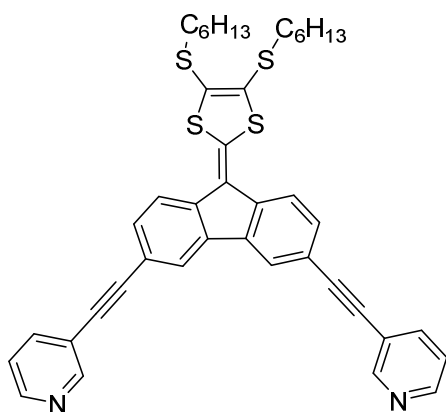
3,3'-((9-(4,5-bis(hexylthio)-1,3-dithiol-2-ylidene)-9H-fluorene-3,6-diyl)bis(ethyne-2,1-diyl))dipyridine 25

Compound **25** was obtained as red crystals (94 mg, 54 %).

^{1}H NMR (300 MHz, CDCl$_3$) δ 8.82 (d, J = 1.8 Hz, 2H), 8.57 (dd, J = 4.9, J = 1.8 Hz, 2H), 8.06 (d, J = 1.6 Hz, 2H), 7.86 (ddd, J = 7.9, J = 1.8, J = 1.8 Hz, 2H), 7.76 (d, J = 8.2 Hz, 2H), 7.62 (dd, J = 8.2, J = 1.6 Hz, 2H), 7.31 (dd, J = 7.9, 4.9 Hz, 2H), 2.99 (m, 4H), 1.71 (m, 4H), 1.48 (m, 4H), 1.33 (m, 8H), 0.90 (t, J = 6.8 Hz, 6H). ^{13}C NMR (76 MHz, CDCl$_3$) δ 152.27, 148.43, 141.61, 138.38, 137.04, 136.80, 130.49, 129.22, 123.08, 123.04, 122.57, 120.70, 119.55, 119.04, 93.64, 86.37, 36.67, 31.37, 29.74, 28.29, 22.57, 14.08. FAB-HRMS: found: 700.2067, calculated: 700.2074.
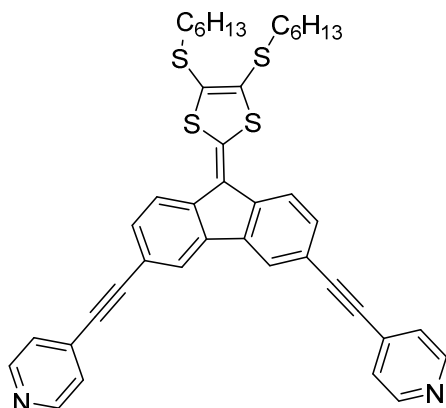
4,4'-((9-(4,5-bis(hexylthio)-1,3-dithiol-2-ylidene)-9H-fluorene-3,6-diyl)bis(ethyne-2,1-diyl))dipyridine 26

Compound **26** was obtained as red crystals (84 mg, 75 %).

^{1}H NMR (300 MHz, CDCl$_3$) δ 8.82 (d, J = 1.4 Hz, 1H), 8.57 (dd, J = 4.7, 1.4 Hz, 1H), 8.06 (d, J = 0.9 Hz, 1H), 7.86 (dt, J = 7.9, 1.8 Hz, 1H), 7.76 (d, J = 8.2 Hz, 1H), 7.62 (dd, J = 8.2, 1.6 Hz, 1H), 7.42 – 7.30 (m, 1H), 3.13 – 2.84 (m, 2H), 1.71 (dd, J = 15.0, 7.6 Hz, 4H), 1.48 (s, 4H), 1.38 – 1.16 (m, 8H), 0.90 (t, J = 6.8 Hz, 6H). ^{13}C NMR (76 MHz, CDCl$_3$) δ 149.58, 142.70, 137.52, 136.81, 131.86, 130.92, 129.64, 125.63, 123.39, 122.70, 119.49, 118.64, 95.12, 87.17, 36.78, 31.35, 30.96, 28.26, 22.56, 14.05. FAB-HRMS: found: 700.2082, calculated: 700.2074.
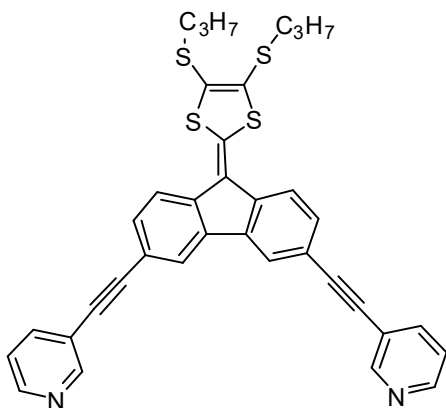
3,3'-((9-(4,5-bis(propylthio)-1,3-dithiol-2-ylidene)-9H-fluorene-3,6-diyl)bis(ethyne-2,1-diyl))dipyridine 27

Compound **27** was obtained as red crystals (132 mg, 46 %).

^{1}H NMR (300 MHz, CDCl$_3$) δ 8.83 (bs, 2H), 8.57 (bs, 2H), 8.05 (dd, J = 1.6, 0.7 Hz, 2H), 7.86 (d, J = 8.0 Hz, 3H), 7.76 (dd, J = 8.2, 0.7 Hz, 2H), 7.61 (dd, J = 8.2, 1.6 Hz, 2H), 7.35 – 7.27 (m, 2H), 3.03 – 2.92 (m, 4H), 1.77 (h, J = 7.3 Hz, 4H), 1.09 (t, J = 7.3 Hz, 6H). ^{13}C NMR (76 MHz, CDCl$_3$) δ 152.29, 148.50, 141.62, 138.39, 137.16, 136.93, 130.63, 129.49, 123.16, 122.69, 119.69, 119.20, 93.49, 86.46, 77.47, 77.05, 76.63, 38.68, 23.18, 13.26. FAB-HRMS: found: 616.1136, calculated: 616.1135.
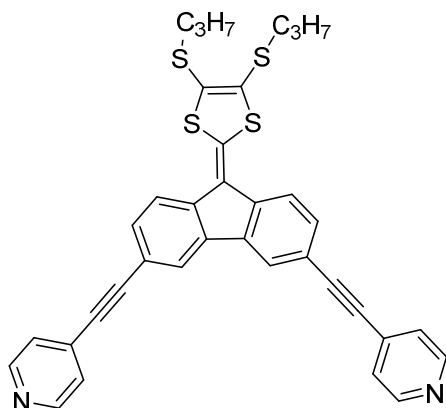
4,4'-((9-(4,5-bis(propylthio)-1,3-dithiol-2-ylidene)-9H-fluorene-3,6-diyl)bis(ethyne-2,1-diyl))dipyridine 28

Compound **28** was obtained as red crystals (105 mg, 40 %).

^{1}H NMR (300 MHz, CDCl$_3$) δ 8.63 (bs, 4H), 8.03 (dd, *J* = 1.6, 0.7 Hz, 2H), 7.74 (dd, *J* = 8.2, 0.7 Hz, 2H), 7.61 (dd, *J* = 8.2, 1.5 Hz, 2H), 7.45 – 7.39 (m, 5H), 2.97 (t, *J* = 7.2 Hz, 4H), 1.75 (h, *J* = 7.3 Hz, 4H), 1.09 (t, *J* = 7.3 Hz, 6H). ^{13}C NMR (76 MHz, CDCl$_3$) δ 149.78, 142.49, 137.44, 136.80, 130.87, 129.62, 123.35, 122.69, 119.51, 118.68, 94.83, 87.26, 77.48, 77.26, 77.06, 76.64, 38.70, 23.18, 13.26. FAB-HRMS: found: 616.1129, calculated: 616.1135.

6.3.1. Self-assemblies based on the dithiafulvalene fragment
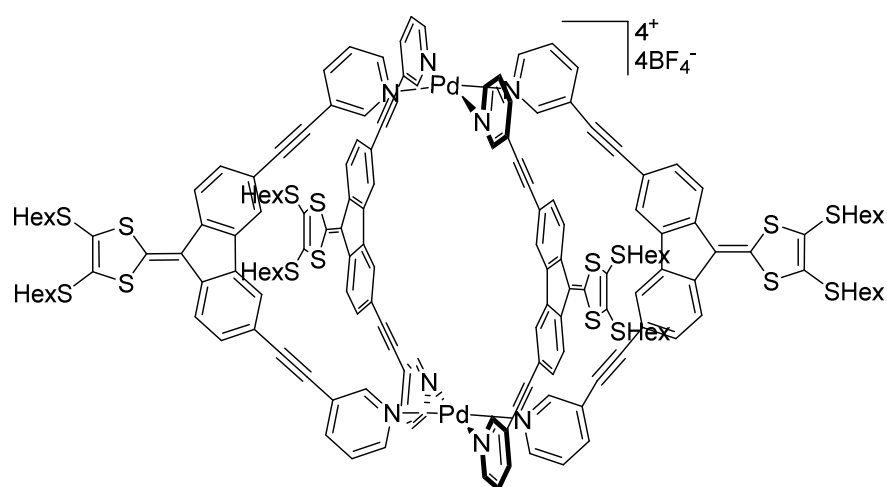
Self-Assembly AA3

A mixture of ligand **25** (10.00 mg, 14.2 μmol) and Pd(BF$_4$)$_2$(CH$_3$CN)$_4$ (3.16 mg, 7.10 μmol) in DMSO (0.5 mL) was heated at 50°C for 5 min until complete dissolution. Then, ethyl acetate was added and resulting suspension was centrifuged. The residue was washed with diethyl ether and dried under vacuum to give **AA3** as a dark red solid (10.5 mg, 80 %). Crystals suitable for analysis were obtained by slow diffusion of ethyl acetate in DMSO (gas-liquid).

^{1}H NMR (300 MHz, DMSO) δ 9.17 (d, J = 6.7 Hz, 2H), 8.43 (d, J = 8.1 Hz, 1H), 8.23 (s, 1H), 7.98 – 7.70 (m, 3H), 3.06 (t, J = 7.0 Hz, 2H), 1.69 – 1.52 (m, 2H), 1.40 (s, 2H), 1.32 – 1.16 (m, 4H), 0.83 (t, J = 6.7 Hz, 3H). FTICR-HRMS: found for [[**Pd$_2$L$_4$**]$^{4+}$, 4BArF$^-$- 3BArF$^-$]$^{3+}$: 1293.2362, calculated: 1293.2350.

General protocol for self-assemblies AA4-6

A stoichiometric mixture of ligand **25-28** (7.01 mg, 0.01 mol) and Pddppf **1** (9.57 mg, 0.01 mol) in CH$_2$Cl$_2$ (1 mL) was stirred at room temperature for 2 hr at room temperature. Then, Et$_2$O was added, resulting suspension was centrifuged and dried under vacuum to give self-assembly **AA4-6** respectively.
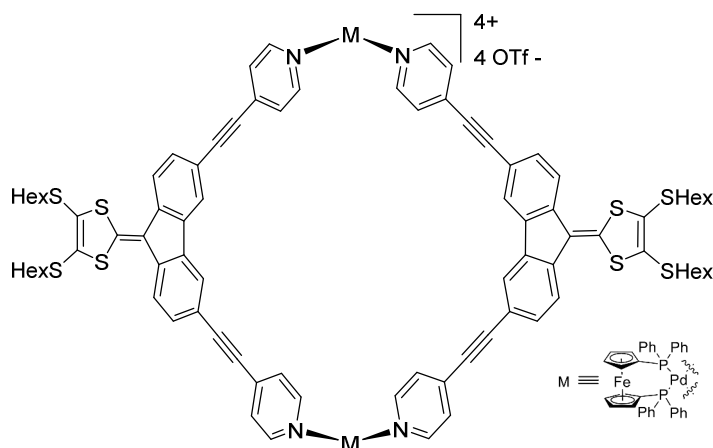
Self-assembly AA4

Self-assembly **AA4** was obtained as a red powder (14.25 mg, 86%). Crystals suitable for analysis were obtained by slow liquid diffusion CH$_2$Cl$_2$/MTBE in a NMR tube.

^{1}H NMR (300 MHz, CD$_2$Cl$_2$)) δ 8.64 (dd, J = 6.6, 3.0 Hz, 8H), 8.04 – 7.82 (m, 20H), 7.77 – 7.57 (m, 28H), 7.51 (dd, J = 8.2, 1.6 Hz, 4H), 7.10 (d, J = 5.4 Hz, 8H), 4.83 (d, J = 1.9 Hz, 8H), 4.65 (s, 8H), 2.96 (t, J = 7.3 Hz, 8H), 1.68 (p, J = 7.3 Hz, 8H), 1.43 (p, J = 7.2, 6.6 Hz, 8H), 1.29 (dd, J = 7.3, 3.9 Hz, 16H), 0.86 (t, J = 7.8, 7.0 Hz, 12H). ^{13}C NMR (126 MHz, CDCl$_3$) δ 150.06, 144.93, 137.79, 136.21, 134.89, 134.15, 134.05, 132.84, 130.76, 129.79, 129.70, 127.78, 127.50, 127.04, 123.96, 122.43, 122.33, 119.77, 118.64, 117.22, 99.73, 85.66, 76.83, 76.77, 76.73, 75.35, 75.29, 70.10, 70.06, 69.58, 69.54, 36.55, 31.14, 29.59, 28.02, 22.38, 13.63. FTICR-HRMS (m/z), [**[Pd$_2$L$_2$]$^{4+}$** - 2TfO$^-$]$^{2+}$: found: 1510.1598, calculated 1510.1660.
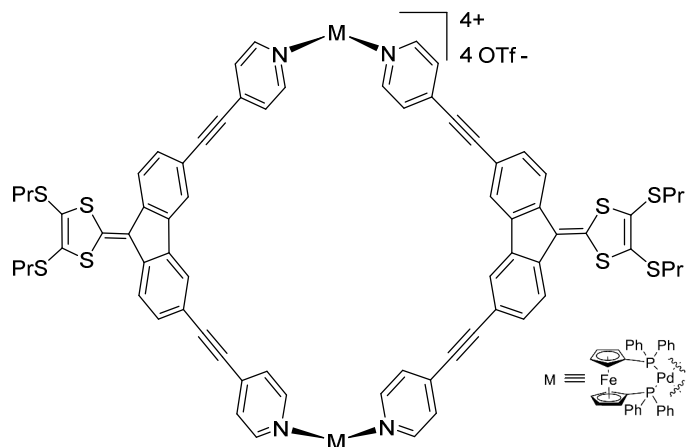
Self-assembly AA5

Self-assembly **AA5** was obtained as a red powder (11.5 mg, 86%). Crystals suitable for analysis were obtained by slow liquid diffusion CH$_2$Cl$_2$/MTBE in a NMR tube.

^{1}H NMR (300 MHz, CDCl$_3$) δ 8.74 (dd, *J* = 6.6, 3.1 Hz, 8H), 7.97 – 7.85 (m, 20H), 7.64 (t, *J* = 6.4 Hz, 28H), 7.46 (dd, *J* = 8.3, 1.6 Hz, 4H), 7.07 (d, *J* = 5.7 Hz, 8H), 4.86 (d, *J* = 2.0 Hz, 8H), 4.61 (s, 8H), 2.93 (t, *J* = 7.2 Hz, 8H), 1.71 (h, *J* = 7.3 Hz, 8H), 1.04 (t, *J* = 7.3 Hz, 12H). FTICR-HRMS (m/z), [**[Pd$_2$L$_2$]$^{4+}$** - 2TfO$^-$]$^{2+}$: found: 1427.0580, calculated 1426,0779.
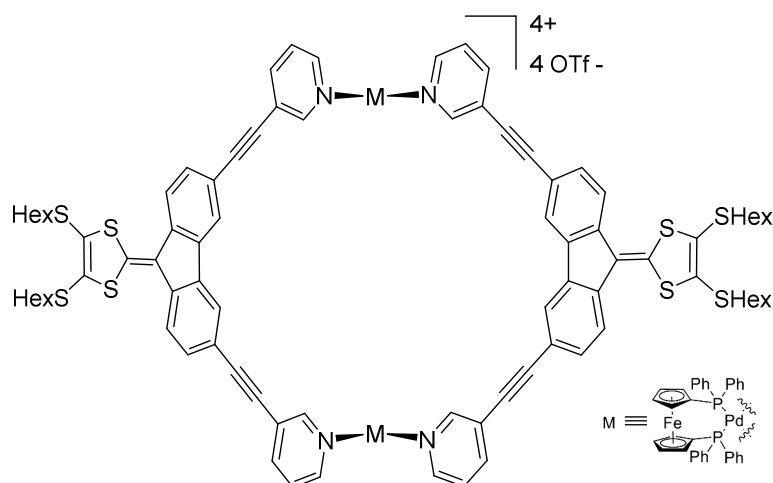
Self-assembly AA6

Self-assembly **AA6** was obtained as a red powder (15.10 mg, 89%).

^{1}H NMR (499 MHz, CD$_2$Cl$_2$) δ 8.86 (s, 4H), 8.71 (s, 4H), 8.31 (s, 4H), 8.18 – 8.07 (m, 8H), 7.97 (dd, J = 12.9, 7.6 Hz, 8H), 7.91 (s, 4H), 7.71 (dd, J = 15.6, 7.7 Hz, 20H), 7.64 (d, J = 8.0 Hz, 4H), 7.52 (dd, J = 20.9, 8.2 Hz, 8H), 7.12 (t, J = 6.9 Hz, 4H), 4.92 (s, 4H), 4.79 (s, 4H), 4.56 (s, 4H), 4.31 (s, 4H), 2.96 (t, J = 7.3 Hz, 8H), 1.68 (p, J = 7.3 Hz, 8H), 1.43 (p, J = 7.2, 6.6 Hz, 8H), 1.29 (dd, J = 7.3, 3.9 Hz, 16H), 0.86 (t, J = 7.8, 7.0 Hz, 12H). FTICR-HRMS (m/z), **[[Pd$_2$L$_2$]$^{4+}$** - 2TfO$^-$]$^{2+}$: found: 1510.1567, calculated 1510.1660.
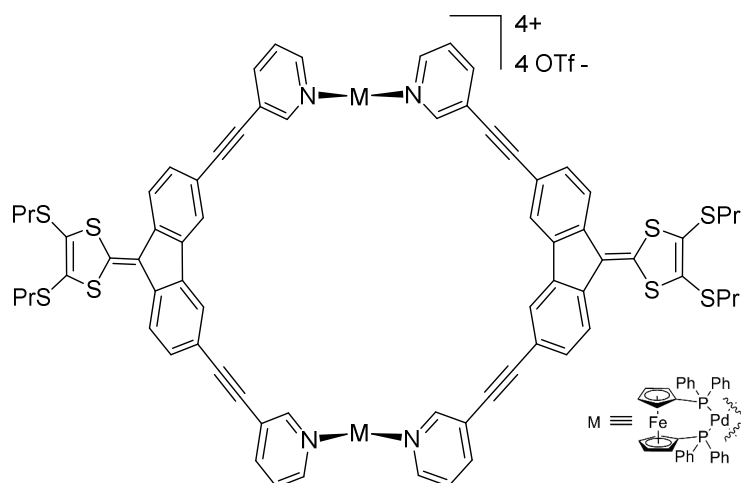
Self-assembly AA7

Self-assembly **AA7** was obtained as a red powder (12.15 mg, 91%).

^{1}H NMR (300 MHz, CD$_2$Cl$_2$) δ 8.86 (s, 4H), 8.65 (s, 4H), 8.30 (s, 4H), 8.11 (t, J = 10.2 Hz, 8H), 7.95 (d, J = 27.4 Hz, 16H), 7.71 (bs, 20H), 7.63 (d, J = 8.1 Hz, 4H), 7.53 (d, J = 8.4 Hz, 8H), 7.19 – 7.03 (m, 4H), 4.94 (s, 4H), 4.77 (s, 5H), 4.57 (s, 7H), 4.33 (s, 4H), 2.95 (t, J = 7.2 Hz, 8H), 1.72 (q, J = 7.2 Hz, 8H), 1.04 (t, J = 7.3 Hz, 12H). FTICR-HRMS (m/z), **[[Pd$_2$L$_2$]$^{4+}$** - 2TfO$^-$]$^{2+}$: found: 1427.0420, calculated 1426,0779.

General protocol for self-assemblies AA8-12

A stoichiometric mixture of ligand **26** or **28** (0,01 mol) and corresponding acceptor **Ru1**, **Ru3** or **Ru4** (0.01 mol) in 2 ml methanol were stirred at 50 ^{0}C overnight solution. Then, Et$_2$O was added, resulting suspension was centrifuged and dried under vacuum to give self-assembly **AA8-12** respectively.
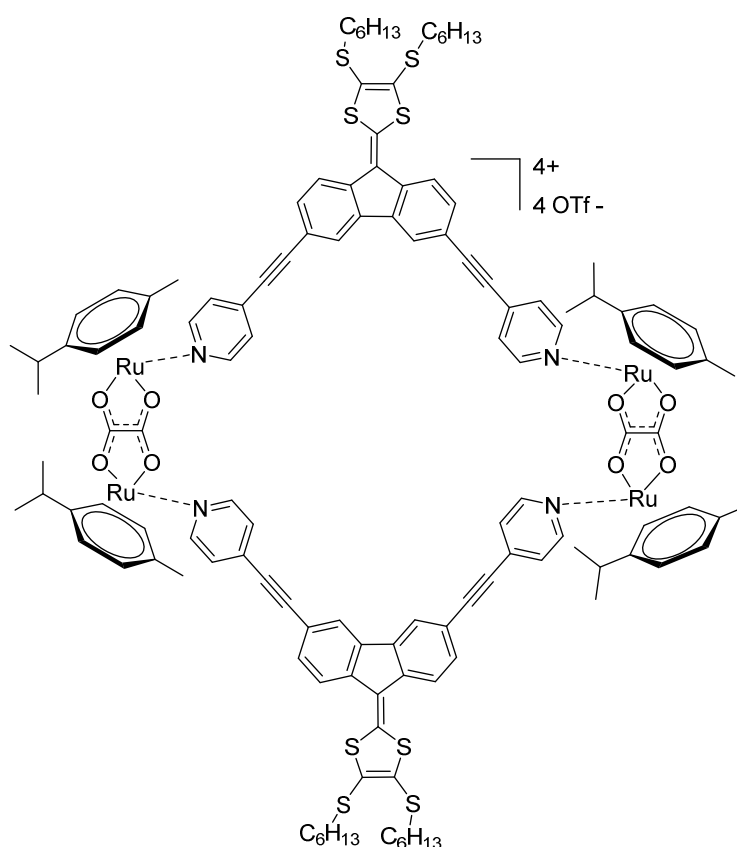
Self-assembly AA8

Self-assembly **AA8** was obtained as a red powder (9,55 mg, 86%). Crystals suitable for x-ray analysis were obtained by liquid diffusion in NMR tube with acetone/MTBE system.

^{1}H NMR (300 MHz, MeOD) δ 8.04 (d, 8H), 7.74 (s, 4H), 7.47 (d, J = 2.0 Hz, 8H), 7.40 – 7.28 (m, 8H), 5.95 (d, J = 4.5 Hz, 8H), 5.78 (d, J = 4.4 Hz, 8H), 3.23 – 2.94 (m, 8H), 2.91 – 2.81 (m, 4H), 2.23 (s, 12H), 1.82 – 1.67 (m, 8H), 1.59 – 1.45 (m, 8H), 1.43 – 1.31 (m, 40H), 0.94 (t, J = 6.5, 2.6 Hz, 12H). FTICR-HRMS (m/z), **[[Ru1$_4$L$_2$]$^{4+}$ - 2TfO$^-$]$^{2+}$**: found: 1409.1616, calculated 1409,1663.

Self-assembly AA9

Self-assembly **AA9** was obtained as a red powder (9,23 mg, 82%). Crystals suitable for x-ray analysis were obtained by liquid diffusion in NMR tube with acetone/MTBE system.

^{1}H NMR (300 MHz, MeOD) δ 8.04 (d, J = 6.7 Hz, 8H), 7.71 (d, J = 1.5 Hz, 4H), 7.47 (d, J = 6.7 Hz, 8H), 7.36 – 7.26 (m, 8H), 5.95 (d, J = 6.2 Hz, 8H), 5.78 (d, J = 6.2 Hz, 8H), 3.17 – 2.92 (m, 8H), 2.86 (p, J = 6.9 Hz, 4H), 2.24 (s, 12H), 1.77 (hd, J = 7.1, 1.8 Hz, 8H), 1.39 (d, J = 6.9 Hz, 24H), 1.11 (t, J = 7.3 Hz, 12H).

Self-assembly AA10

Self-assembly **AA10** was obtained as a dark-green powder (9,69 mg, 83%). Crystals suitable for x-ray analysis were obtained by liquid diffusion in NMR tube with acetone/MTBE system.

^{1}H NMR (499 MHz, MeOD) δ 8.44 (dd, J = 11.3, 6.2 Hz, 8H), 7.45 – 7.40 (m, 4H), 7.40 – 7.34 (m, 8H), 7.30 (d, J = 5.7 Hz, 4H), 7.26 – 7.21 (m, 2H), 7.11 (d, J = 7.9 Hz, 2H), 7.03 (d, J = 7.9 Hz, 2H), 6.90 (s, 2H), 6.58 (d, J = 8.0 Hz, 2H), 5.93 (t, J = 6.7 Hz, 4H), 5.88 (t, J = 5.1 Hz, 4H), 5.73 – 5.68 (m, 4H), 5.65 (dd, J = 6.1, 2.6 Hz, 4H), 2.85 (tdd, J = 36.2, 13.6, 6.7 Hz, 8H), 2.31 (d, J = 7.6 Hz, 4H), 2.20 (s, 6H), 2.12 (s, 6H), 1.56 (p, J = 7.7 Hz, 4H), 1.40 (dd, J = 6.9, 4.4 Hz, 12H), 1.36 (dd, J = 7.0, 5.0 Hz, 12H), 1.27 (dd, J = 9.8, 5.1 Hz, 8H), 1.11 (dd, J = 23.9, 7.6 Hz, 8H), 0.84 (t, J = 6.9 Hz, 12H), 0.61 (d, J = 8.2 Hz, 6H), 0.42 (t, J = 7.3 Hz, 6H). FTICR-HRMS (m/z), $[[\mathbf{Ru1_4L_2}]^{4+} - 2TfO^-]^{2+}$: found: 1509.3691, calculated 1509,1976.

Self-assembly AA11

Self-assembly **AA11** was obtained as a dark-green powder (9,58 mg, 82%). Crystals suitable for x-ray analysis were obtained by liquid diffusion in NMR tube with acetone/diisopropyl ether system.

^{1}H NMR (499 MHz, MeOD) δ 8.44 – 8.41 (m, 4H), 8.38 – 8.34 (m, 4H), 7.47 – 7.40 (m, 4H), 7.39 (s, 4H), 7.36 (d, J = 6.4 Hz, 4H), 7.15 (dd, J = 8.0, 1.5 Hz, 2H), 7.14 – 7.11 (m, 4H), 7.06 (d, J = 8.0 Hz, 2H), 7.02 (d, J = 1.6 Hz, 2H), 6.82 (dd, J = 8.0, 1.5 Hz, 2H), 6.50 (d, J = 7.9 Hz, 2H), 6.20 (d, J = 1.6 Hz, 2H), 5.96 (dd, J = 10.5, 6.1 Hz, 4H), 5.89 (dd, J = 6.1, 4.6 Hz, 4H), 5.77 – 5.70 (m, 4H), 5.69 – 5.62 (m, 4H), 3.06 – 2.92 (m, 4H), 2.87 (dt, J = 14.0, 7.2 Hz, 4H), 2.50 (t, J = 7.4 Hz, 4H), 2.24 (s, 6H), 2.12 (s, 6H), 1.65 (ddt, J = 19.7, 14.1, 7.1 Hz, 4H), 1.43 (dd, J = 7.0, 4.8 Hz, 12H), 1.36 (dd, J = 6.9, 5.2 Hz, 12H), 1.04 (t, J = 7.3 Hz, 6H), 0.86 (t, J = 7.3 Hz, 6H).
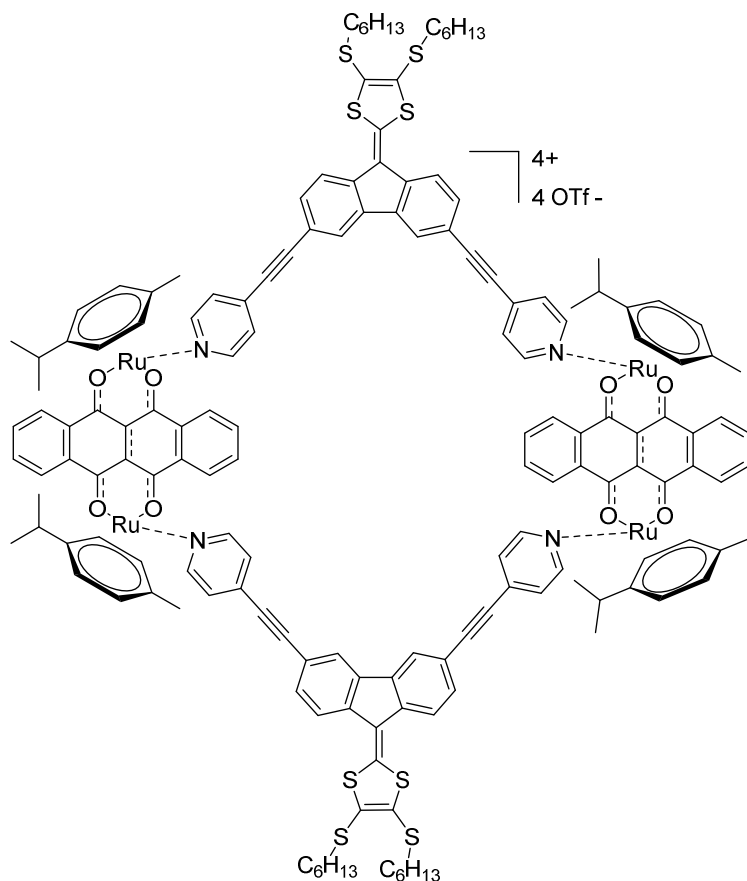
Self-assembly AA12

Self-assembly **AA12** was obtained as a dark-green powder (9.53 mg, 76%).

^{1}H NMR (499 MHz, CD$_3$CN) δ 8.81 (dd, J = 10.8, 7.1 Hz, 8H), 8.46 (dd, J = 14.2, 5.8 Hz, 8H), 8.14 – 7.97 (m, 8H), 7.30 – 7.06 (m, 8H), 6.97 – 6.82 (m, 4H), 6.60 – 6.53 (m, 4H), 6.21 (d, J = 8.0 Hz, 2H), 5.96 – 5.87 (m, 8H), 5.76 – 5.66 (m, 8H), 2.98 (dt, J = 9.4, 6.8 Hz, 4H), 2.82 (ddt, J = 40.4, 13.7, 7.3 Hz, 4H), 2.09 (s, 6H), 1.59 – 1.51 (m, 6H), 1.40 – 1.31 (m, 12H), 1.26 – 1.20 (m, 6H), 1.12 (t, J = 7.0 Hz, 6H). FTICR-HRMS (m/z), [[**Ru1$_4$L$_2$**]$^{4+}$ - 2TfO$^-$]$^{2+}$: found: 1609.7412, calculated 1609,2289.
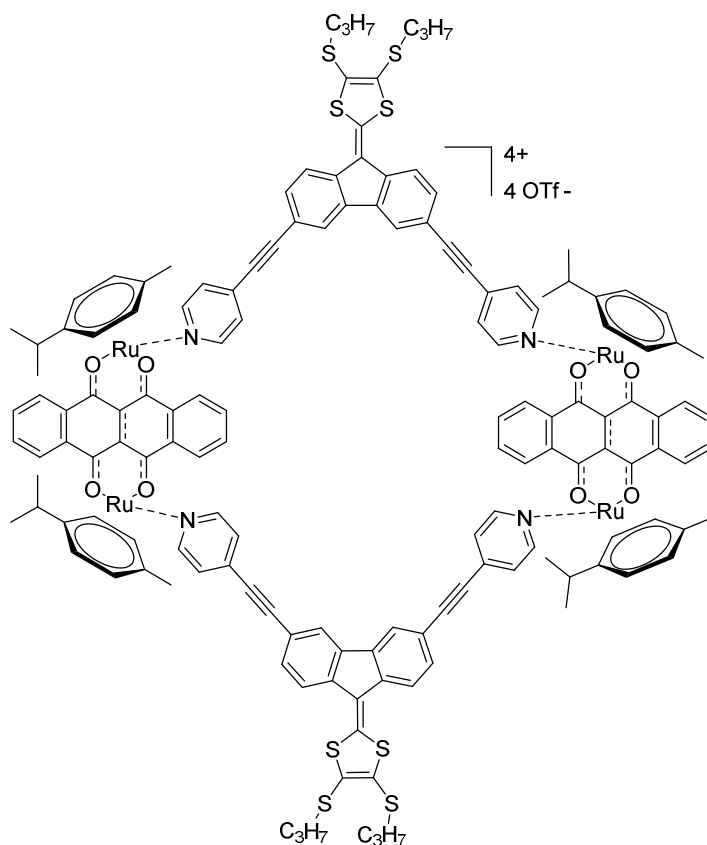
Self-assembly AA13

Self-assembly **AA13** was obtained as a dark-green powder (9.21 mg, 79%).

^{1}H NMR (300 MHz, MeOD) δ 8.99 – 8.77 (m, 8H), 8.62 (q, *J* = 5.9 Hz, 8H), 8.07 (d, *J* = 30.1 Hz, 18H), 7.35 – 6.85 (m, 8H), 6.32 – 6.04 (m, 8H), 6.02 – 5.73 (m, 8H), 3.06 – 2.92 (m, 4H), 2.87 (dt, *J* = 14.0, 7.2 Hz, 4H), 2.50 (t, *J* = 7.4 Hz, 4H), 2.24 (s, 6H), 2.12 (s, 6H), 1.65 (ddt, *J* = 19.7, 14.1, 7.1 Hz, 4H), 1.43 (dd, *J* = 7.0, 4.8 Hz, 12H), 1.36 (dd, *J* = 6.9, 5.2 Hz, 12H), 1.04 (t, *J* = 7.3 Hz, 6H), 0.86 (t, *J* = 7.3 Hz, 6H).

6.4. exTTF family
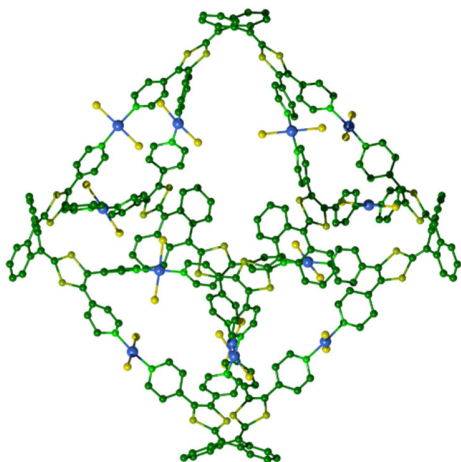
Self-assembly AA14

Ligand **exTTF-TEG** (100 mg, 0.075 mmol) and $PdCl_2(CH_3CN)_2$ (39 mg, 0.150 mmol, 2 equiv.) were heated in DMSO (10 mL) for 1 h. Then, the solution was cooled to room temperature and EtOAc was added. The resulting precipitate was centrifuged and washed 3 times with EtOAc, and dried under vacuum to give **AA14 Pd$_{12}$(LTEG)$_6$** (103 mg, 82%) as a dark red solid.

^{1}H NMR (300 MHz, CDCl$_3$) δ 8.72 (s(br), 48H), 7.04 (72H, m), 4.23 (s(br), 48H), 3.90 (s(br), 48H), 3.74 – 3.55 (m, 192H), 3.37 (s, 72H); ^{13}C NMR (300 MHz, CDCl$_3$) δ 154.16, 147.24, 141.42, 128.25, 127.53, 126.04, 125.05, 124.17, 123.89, 112.66, 71.96, 70.92, 70.71, 70.60, 69.71, 69.33, 59.10. ESI-FTICR (CH$_2$Cl$_2$/CH$_3$NO$_2$) m/z calculated: $[Pd_{12}(exTTF\text{-}TEG)_6 + (KOTf)_{n=9\text{-}12} - 7OTf]^{7+}$ n = 9: 1543.334, n = 10: 1570.179, n = 11: 1597.025, n = 12: 1624.012; $[Pd_{12}(exTTF\text{-}TEG)_6 + (KOTf)_{n=7\text{-}11} - 6OTf]^{6+}$ n = 7: 1762.577, n = 8: 1794.063, n = 9: 1825.382, n = 10: 1856.701, n = 11: 1888.021; found: $[Pd_{12}(exTTF\text{-}TEG)_6 + (KOTf)_{n=9\text{-}12} - 7OTf]^{7+}$ n = 9: 1543.329, n = 10: 1570.183, n = 11: 1597.027, n = 12: 1624.037; $[Pd_{12}(exTTF\text{-}TEG)_6 + (KOTf)_{n=7\text{-}11} - 6OTf]^{6+}$ n = 7: 1762.583, n = 8: 1794.065, n = 9: 1825.379, n = 10: 1856.701, n = 11: 1888.042.
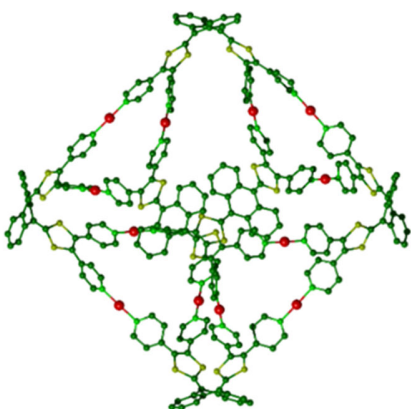
Self-assembly AA15

The ligand **exTTF-TEG** (100 mg, 0.075 mmol) and $AgBF_4$ (30.6 mg, 0.157 mmol, 2.1 equiv.) were stirred in $CHCl_3/CH_3NO_2$ (15 mL) for 1 h. Then, Et_2O was added, the resulting precipitate was centrifuged and washed 3 times with Et_2O, and dried under vacuum to give **AA15** (99 mg, 76%) as a dark brown solid.

^1H NMR (300 MHz, $CDCl_3/CD_3NO_2$) δ 8.35 (s(br), 48H), 7.20 (48H, d, J = 5.9 Hz), 7.03 (s, 48H), 4.13 (s(br), 48H, overlapped with residual solvent signal), (3.73 (s(br), 48H), 3.56 - 3.42 (m, 192H), 3.14 (s, 72H); ^{13}C NMR (300 MHz, $CDCl_3/CD_3NO_2$) δ 207.42, 152.50, 146.82, 142.19, 128.36, 127.96, 126.78, 125.37, 125.14, 124.29, 111.96, 71.64, 70.48, 70.17, 69.40, 69.08, 68.19, 58.49. ESI-FTICR (CH_2Cl_2/CH_3CN) m/z calculated: $[[Ag_{12}(exTTF\text{-}TEG)_6]^{12+} + (AgBF_4)_{9\text{-}15} - 6BF_4]^{6+}$ n = 9: 1932.123, n = 10: 1964.607, n = 11: 1997.092, n = 12: 2029.577, n = 13: 2061.895, n = 14: 2094.380, n = 15: 2126.865; $[[Ag_{12}(exTTF\text{-}TEG)_6]^{12+} + (AgBF_4)_{8\text{-}12} - 5BF_4]^{5+}$ n = 8: 2296.967, n = 9: 2335.948, n = 10: 2374.930, n = 11: 2416.912, n = 12: 2452.693; found: $[[Ag_{12}(exTTF\text{-}TEG)_6]^{12+} + (AgBF_4)_{9\text{-}15} - 6BF_4]^{6+}$ n = 9: 1932.138, n = 10: 1964.612, n = 11: 1997.084, n = 12: 2029.564, n = 13: 2061.880, n = 14: 2094.382, n = 15: 2126.867; $[[Ag_{12}(exTTF\text{-}TEG)_6]^{12+} + (AgBF_4)_{8\text{-}12} - 5BF_4]^{5+}$ n = 8: 2296.980, n = 9: 2335.956, n = 10: 2374.919, n = 11: 2416.888, n = 12: 2452.659.

Polymer $[(Ag_2(exTTF\text{-}TEG^{2+}))^{2+}]_x$

A mixture of ligand **exTTF-TEG** (7.1 mg, 0.005 mmol) and **$AgBF_4$** (4.1 mg, 0.021 mmol, 4.1 equiv.) in argon degassed $CHCl_3/CH3NO_2$ (0.5 mL) was left in dark for 5 days in an NMR tube. The resulting dark precipitate was centrifuged, washed with $CHCl_3$, Et_2O and dried under vacuum to afford **AA16** (6.2 mg, 66.2 %) as dark greenish crystals.
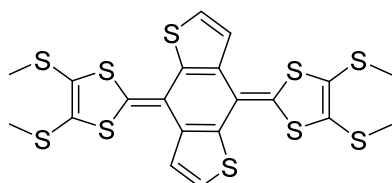
6.1. DithienoTTF family
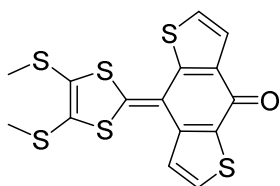
8-(4,5-bis(methylthio)-1,3-dithiol-2-ylidene)benzo[1,2-b:4,5-b']dithiophen-4(8H)-one 29

To a solution of dimethyl (4,5-bis(methylthio)-1,3-dithiol-2-yl)phosphonate **18** (276 mg, 0.90 mmol) in anhydrous tetrahydrofuran (10 mL) at -78°C, was added slowly *n*-butyl lithium (570 µL, 0.90 mmol, 1.6 M). The solution was stirred at -78°C for 1 h 30 and a suspension of benzo[1,2-b:4,5-b']dithiophene-4,8-dione (100 mg, 0.45 mmol) in anhydrous tetrahydrofuran at -78°C was added *via* cannula. The mixture was stirred 1 h at -78°C and overnight at room temperature. The solvent was removed under vacuum. The residue was treated with water and extracted with dichloromethane. The organic extracts were washed with water, and dried over magnesium sulfate. The solvent was removed under vacuum. A chromatography column on silica gel was performed using a gradient of eluent: from dichloromethane to dichloromethane/methanol (99/1). The compound **29** was isolated as a red powder (180 mg, 99 %).

^{1}H NMR (300 MHz, CDCl$_3$) δ 7.95 (d, J = 5.4 Hz, 1H), 7.87 (d, J = 5.4 Hz, 1H), 7.78 (d, J = 5.4 Hz, 1H), 7.43 (d, J = 5.4 Hz, 1H), 2.62 (s, 3H), 2.60 (s, 3H). ^{13}C NMR (76 MHz, CDCl$_3$) δ 173.21, 149.06, 144.71, 140.23, 137.06, 133.99, 131.85, 131.45, 130.98, 126.06, 125.05, 123.76, 113.23, 19.55. EI-HRMS: found: 397.9045, calculated: 397.9056.

4,8-bis(4,5-bis(methylthio)-1,3-dithiol-2-ylidene)-4,8-dihydrobenzo[1,2-b:4,5-b']dithiophene 30

To a solution of dimethyl (4,5-bis(methylthio)-1,3-dithiol-2-yl)phosphonate **18** (145,72 mg, 3.75 mmol) in anhydrous tetrahydrofuran (10 mL) at -78°C, was added slowly *n*-butyl lithium (2.35 mL, 3.75 mmol, 1.6 M). The solution was stirred at -78°C for 1 h and a suspension of benzo[1,2-b:4,5-b']dithiophene-4,8-dione **29** (300 mg, 0.75 mmol) in anhydrous tetrahydrofuran at -78°C was added *via* cannula. The mixture was stirred 1 h at -78°C and overnight at room temperature. The solvent was removed under vacuum. The residue was treated with water and extracted with dichloromethane. The organic extracts were washed with water, and dried over magnesium sulphate. The solvent was removed under vacuum. A chromatography column on alumina was performed using mixture EP/dichloromethane 75/25 with constant 1% thiethylamine as eluent. The compound **30** or **S-exTTF** was isolated as a red powder (145 mg, 33 %).

^{1}H NMR (300 MHz, CDCl$_3$) δ 7.61 (d, *J* = 5.4 Hz, 2H), 7.39 (d, *J* = 5.4 Hz, 2H), 2.61 (s, 12H). ^{13}C NMR (76 MHz, CDCl$_3$) δ 136.16, 133.76, 127.74, 127.65, 124.99, 124.22, 116.43, 19.34. EI-HRMS: found: 575.8456, calculated 575.8459.
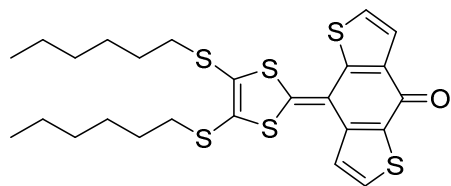
8-(4,5-bis(hexylthio)-1,3-dithiol-2-ylidene)benzo[1,2-b:4,5-b']dithiophen-4(8H)-one 31

To a solution of dimethyl (4,5-bis(hexylthio)-1,3-dithiol-2-yl)phosphonate **16** (970 mg, 2.18 mmol) in anhydrous tetrahydrofuran (10 mL) at -78°C, was added slowly *n*-butyl lithium (1.4 mL, 2.18 mmol, 1.6 M). The solution was stirred at -78°C for 1 h 30 and a suspension of benzo[1,2-b:4,5-b']dithiophene-4,8-dione (400 mg, 1.81 mmol) in anhydrous tetrahydrofuran at -78°C was added *via* cannula. The mixture was stirred 1 h at -78°C and overnight at room temperature. The solvent was removed under vacuum. The residue was treated with water and extracted with dichloromethane. The organic extracts were washed with water, and dried over magnesium sulfate. The solvent was removed under vacuum. A chromatography column on silica gel was performed using a gradient of eluent: from dichloromethane to dichloromethane/methanol (99/1). The compound **31** was isolated as a red powder (240 mg, 25 %).

^{1}H NMR (300 MHz, CDCl$_3$) δ 8.00 (d, *J* = 5.4 Hz, 1H), 7.93 (d, *J* = 5.4 Hz, 1H), 7.81 (d, *J* = 5.4 Hz, 1H), 7.45 (d, *J* = 5.3 Hz, 1H), 3.01 (t, *J* = 7.3 Hz, 4H), 1.72 (p, *J* = 7.3 Hz, 4H), 1.48 (d, *J* = 7.6 Hz, 4H), 1.38 – 1.27 (m, 8H), 0.97 – 0.83 (t, *J* = 6.4 Hz,6H). ^{13}C NMR (76 MHz, CDCl$_3$) δ 173.31, 149.24, 144.84, 140.43, 137.17, 134.12, 131.91, 131.70, 131.48, 126.10, 125.16, 123.74, 113.24, 37.05, 31.32, 29.75, 29.71, 28.24, 22.55, 14.04. EI-HRMS: found: 538.8510, calculated 538.8740.

7. Conclusions and perspectives

This work deals with the synthesis of new redox-active ligands, enriched in sulfur atoms, and with the building of the corresponding metalloreceptors using a coordination-driven self-assembly approach. The latter is promoted by combining complementary partners, *i.e.* polytopic ligands and various metal complexes, chosen to drive specific geometries for the corresponding self-assembled host structure. These new families of electroactive receptors are in particular of interest from a fundamental point of view for: *i)* studying the extensively developed metal-driven self-assembly process, through monitoring of the related redox properties, and *ii)* for exploring host-guest properties towards electron-poor species.
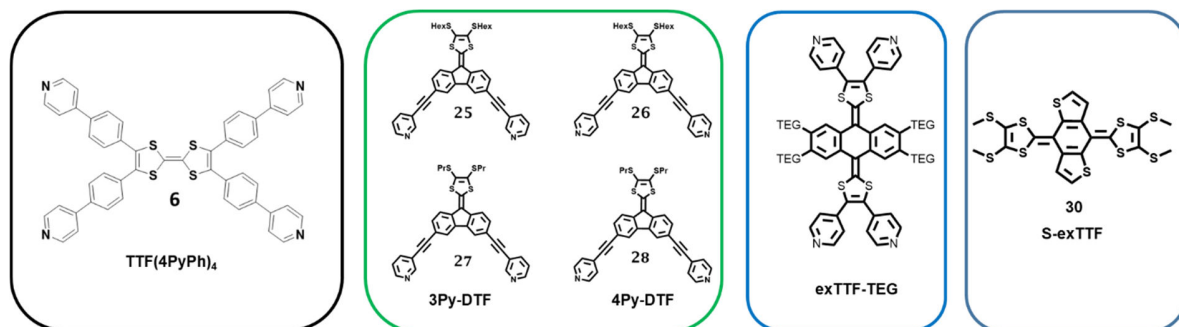
Three types of self-assembled electroactive architectures have been studied, *i.e.* 1) M_8L_2 metallacages involving a tetrathiafulvalene-based ligand, 2) metalla-assemblies M_xL_y (cages, clips) involving a new dithiol-fluorene-based unit (DTF), and 3) $M_{12}L_6$ metallacages involving an extended tetrathiafulvalene derivative, as well as a new electroactive π-conjugated scaffold (S-exTTF). Beyond their synthesis and their characterizations through usual spectroscopic methods, the electrochemical properties of the resulting assemblies have been studied and, in some cases, their solid-state analysis performed through DRX.

<u>**M_8L_2 metallacages based on TTF**</u>:
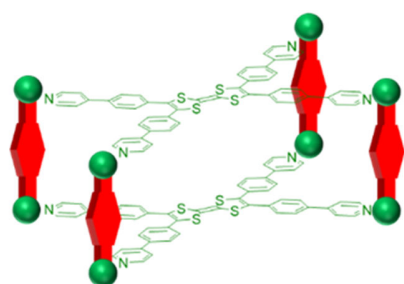
A new family of M_8L_2 cage was designed, featuring two facing electron-rich panels (TTF units). The four pillars correspond to *bis*-Ruthenium complexes, with a controlled Ru-Ru length. Two self-assemblies **AA1** and **AA2** involving different *bis*-Ruthenium complexes were synthesized and fully characterized, including in the solid state (XRD). A severe bending of the facing ligands is observed in the solid state, with a collapse towards the centre of the cavity, preventing any host-guest binding ability. The unique geometry of those M_8L_2 assemblies, for which two TTF units are forced to stack, offers a unique opportunity to promote close inter-TTF interactions upon oxidation. This is remarkably observed through
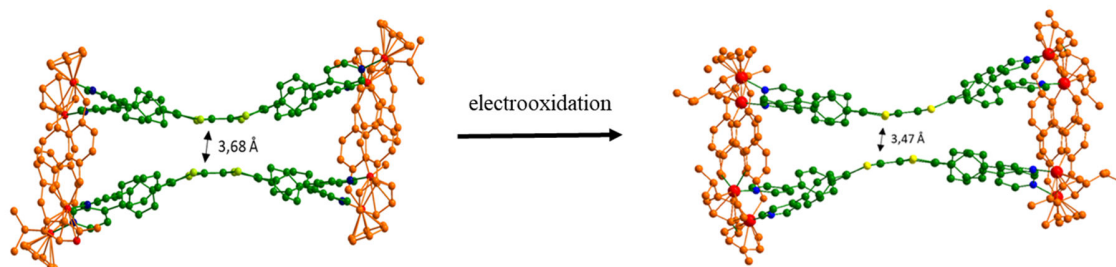
electrochemical studies as well as from single-crystal DRX from an electrocrystallized oxidized salt. The resulting cage clearly shows that facing TTF units strongly interact upon oxidation to the cation-radical state. Spectroelectrochemical analyses are in due course.

M_xL_y assemblies based on DTF:

Several new discrete assemblies were prepared from four electro-active ligands based on the 9-(1,3-dithiol-2-ylidene)fluorene (DTF) unit.

The "banana-shaped" ligand **3Py-DTF** (**25**), featuring two 3-pyridyl units, self-assembles with a naked palladium complex to form a M_2L_4 coordination cage (**AA3**). The latter exhibits an internal 600 Å^3 cavity decorated by four electro-active DTF units that can be reversibly oxidized to their radical-cation state at a moderate potential.

AA4 R - Hex
AA5 R - Pr

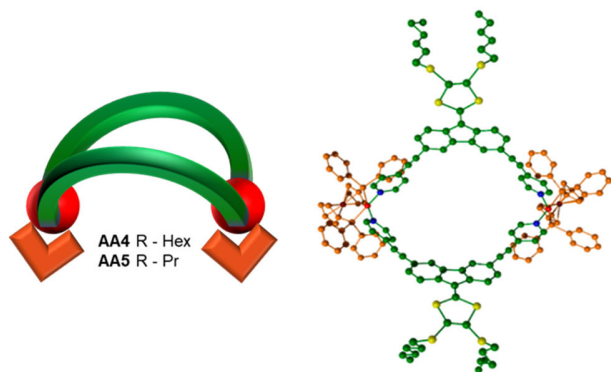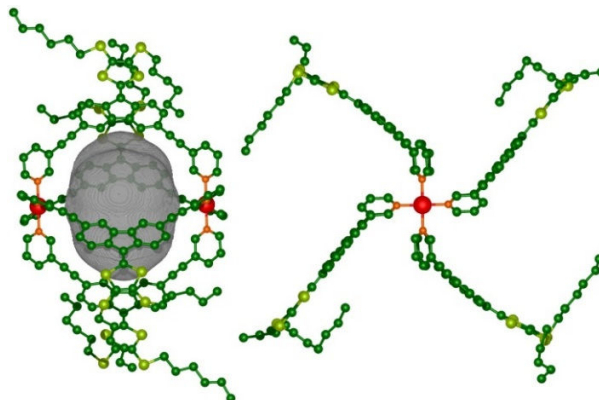Ligands **3Py-DTF** (**25** or **27**) and **4Py-DTF** (**26** or **28**) react with the square planar cis-blocked Pd(dppf)OTf$_2$ salt to form a series of M_2L_2 self-assembled metalla-macrocycles. Interestingly, while the metalla-cycles (**AA4-AA5**) constructed from the **4Py-DTF** ligands show a single redox wave for the DTF units (no interaction between DTF units), a mixed-valence species is observed for the **3Py-DTF** based discrete assemblies (**AA6-AA7**), illustrating a close proximity between both electro-active species.

Based on this result, the binding properties of **AA5** and **AA7** with DCTNF were evaluated by UV-Vis and NMR titration. A Job's plot analysis revealed that metalla-macrocycle **AA7** forms a 1:1 host-guest complex with DCTNF, while two DCTNF units interact with metalla-cycle **AA5**.
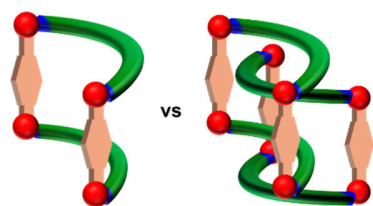
Finally, we demonstrated that ligands **4Py-DTF** (**26** or **28**) react with *bis*-Ruthenium complexes to quantitatively form M_4L_2 metalla-tweezers **AA9-AA13**. The close distance between DTF fragments in **AA9** and **AA11** leads to occurence of a mixed-valence species as for **AA6-AA7**. Interestingly, because of the internuclear distance in the *bis*-ruthenium complex and thanks to π-π interactions, **AA11** forms a stable dimeric structure in the solid phase (confirmed by XRD analysis) and in solution. The later can be transformed to its monomeric counterpart upon dilution, or inclusion of the electro-deficient DCTNF unit. Remarkably, expulsion of the later in the resulting host-guest complex could be achieved through a redox stimulus, as confirmed by cyclic voltammetry measurements.

M$_{12}$L$_6$ assemblies based on exTTF and redox-triggered transformation into a supramolecular 3D polymer:

The **exTTF-TEG** ligand was combined with *trans* palladium and silver complexes, affording two new electro-active large M$_{12}$L$_6$ metallocages **AA14** and **AA15** respectively (*ca.* 4000 Å^3). Despite similar structures, cage **AA14** (M = Pd) remains stable during the electrochemical oxidation, while the cyclic voltammetry of cage **AA15** (M = Ag) demonstrates its disassembling. The chemical oxidation of **AA15** using silver cations leads to an unprecedented transformation of a discrete cage into an infinite polycationic 3D polymer **[(Ag$_2$exTTF-TEG^{2+})$^{2+}$]$_x$**, providing a first example of a three dimensional coordination network involving an exTTF derivative.
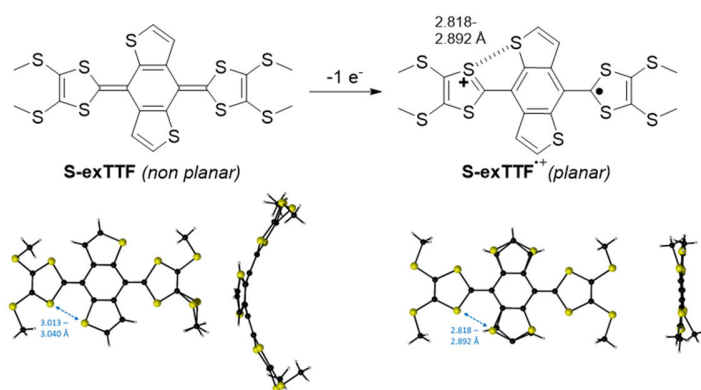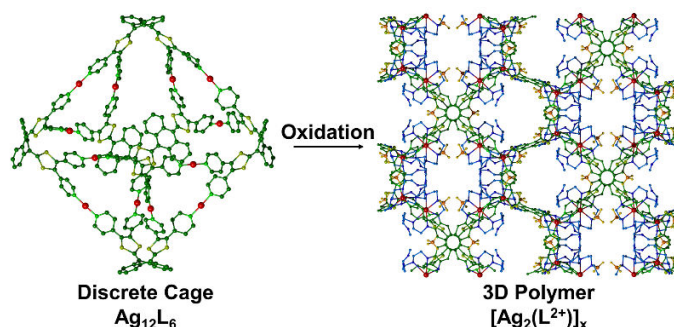
Finally, **a new aromatic scaffold S-exTTF** (benzo[1,2-b:4,5-b'] dithiophene) is explored as an alternative system to the well-established π-extended tetrathiafulvalene (exTTF). A combined experimental and theoretical study is proposed to characterize the specific structural and electronic properties of this new compound. Introduction of additional 1,5 S···S non-covalent interactions allowed to assert further control over the conformation and planarity of the molecule in both neutral and oxidized states. The single crystal X-Ray diffraction analysis of the oxidized [**S-exTTF**][PF$_6$]·THF salt, grown by electrocrystallization, shows a fully planarized molecule with remarkably short S···S distance of 2.82-2.89 Å. Theoretical calculations on the B3LYP-D3/6-31G** level assign this conformation to the contraction of S sp^2 lone pair of the dithiole rings in the oxidized state. This further causes lower Pauli repulsion, leading to shorter S···S contacts. Accordingly, it is worth noting that push-pull intermediates **29** and **31** show similar very short S···S distances, which suggests a high contribution of the charged mesomeric form.

8. Literature

1.   Chakrabarty, R.; Mukherjee, P. S.; Stang, P. J., Supramolecular Coordination: Self-Assembly of Finite Two- and Three-Dimensional Ensembles. *Chem. Rev.* **2011,** *111* (11), 6810-6918.

2.   Mateos-Timoneda, M. A.; Kerckhoffs JeEnrico, B., M. C. A.; Crego-Calama, M.; Reinhoudt, D. N., Ditopic Complexation and Release of Neutral Guest Molecules by a Hydrogen-Bonded "Endo–Exo" Receptor. *Angew. Chem. Int. Ed.* **2005,** *44* (21), 3248-3253.

3.   Huerta, E.; Serapian, S. A.; Santos, E.; Cequier, E.; Bo, C.; de Mendoza, J., Molecular Basis for the Recognition of Higher Fullerenes into Ureidopyrimidinone–Cyclotriveratrylene Self-Assembled Capsules. *Chem. Eur. J.* **2016,** *22* (38), 13496-13505.

4.   Appavoo, D.; Carnevale, D.; Deschenaux, R.; Therrien, B., Combining coordination and hydrogen-bonds to form arene ruthenium metalla-assemblies. *J. Organomet. Chem.* **2016,** *824*, 80-87.

5.   Hasell, T.; Cooper, A. I., Porous organic cages: soluble, modular and molecular pores. *Nature Reviews Materials* **2016,** *1*, 16053.

6.   Tozawa, T.; Jones, J. T. A.; Swamy, S. I.; Jiang, S.; Adams, D. J.; Shakespeare, S.; Clowes, R.; Bradshaw, D.; Hasell, T.; Chong, S. Y.; Tang, C.; Thompson, S.; Parker, J.; Trewin, A.; Bacsa, J.; Slawin, A. M. Z.; Steiner, A.; Cooper, A. I., Porous organic cages. *Nature Materials* **2009,** *8*, 973.

7.   Zhang, G.; Presly, O.; White, F.; Oppel, I. M.; Mastalerz, M., A Permanent Mesoporous Organic Cage with an Exceptionally High Surface Area. *Angew. Chem.* **2014,** *126* (6), 1542-1546.

8.   Collins, M. S.; Phan, N.-M.; Zakharov, L. N.; Johnson, D. W., Coupling Metaloid-Directed Self-Assembly and Dynamic Covalent Systems as a Route to Large Organic Cages and Cyclophanes. *Inorg. Chem.* **2018,** *57* (7), 3486-3496.

9.   Saha, S.; Regeni, I.; Clever, G. H., Structure relationships between bis-monodentate ligands and coordination driven self-assemblies. *Coord. Chem. Rev.* **2018,** *374*, 1-14.

10.   Kim, T. Y.; Vasdev, R. A. S.; Preston, D.; Crowley, J. D., Strategies for reversible guest uptake and release from metallosupramolecular architectures. *Chem. Eur. J.* **2018,** *24* (56), 14878-14890.

11.   Zhang, Y.-Y.; Gao, W.-X.; Lin, L.; Jin, G.-X., Recent advances in the construction and applications of heterometallic macrocycles and cages. *Coord. Chem. Rev.* **2017,** *344*, 323-344.

12.   Yoshizawa, M.; Yamashina, M., Coordination-driven Nanostructures with Polyaromatic Shells. *Chem. Lett.* **2017,** *46* (2), 163-171.

13.   Pan, M.; Wu, K.; Zhang, J.-H.; Su, C.-Y., Chiral metal–organic cages/containers (MOCs): From structural and stereochemical design to applications. *Coord. Chem. Rev.* **2017**.

14.   Huang, S.-L.; Hor, T. S. A.; Jin, G.-X., Metallacyclic assembly of interlocked superstructures. *Coord. Chem. Rev.* **2017,** *333*, 1-26.

15.   Bloch, W. M.; Clever, G. H., Integrative self-sorting of coordination cages based on 'naked' metal ions. *Chem. Commun.* **2017,** *53* (61), 8506-8516.

16.   Young, N. J.; Hay, B. P., Structural design principles for self-assembled coordination polygons and polyhedra. *Chem. Commun.* **2013,** *49* (14), 1354-1379.

17.   Fujita, M.; Yazaki, J.; Ogura, K., Preparation of a macrocyclic polynuclear complex, [(en)Pd(4,4'-bpy)]4(NO3)8 (en = ethylenediamine, bpy = bipyridine), which recognizes an organic molecule in aqueous media. *JACS* **1990,** *112* (14), 5645-5647.

18.   Stang, P. J.; Cao, D. H., Transition Metal Based Cationic Molecular Boxes. Self-Assembly of Macrocyclic Platinum(II) and Palladium(II) Tetranuclear Complexes. *JACS* **1994,** *116* (11), 4981-4982.

19.   L. Caulder, D.; N. Raymond, K., The rational design of high symmetry coordination clusters *J. Chem. Soc., Dalton Trans.* **1999,** (8), 1185-1200.

20.   Caulder, D. L.; Brückner, C.; Powers, R. E.; König, S.; Parac, T. N.; Leary, J. A.; Raymond, K. N., Design, Formation and Properties of Tetrahedral M4L4 and M4L6 Supramolecular Clusters. *JACS* **2001,** *123* (37), 8923-8938.

21. Hardy, M.; Struch, N.; Topić, F.; Schnakenburg, G.; Rissanen, K.; Lützen, A., Stepwise Construction of Heterobimetallic Cages by an Extended Molecular Library Approach. *Inorg. Chem.* **2018,** *57* (7), 3507-3515.

22. Fujita, M., Metal-directed self-assembly of two- and three-dimensional synthetic receptors. *Chem. Soc. Rev.* **1998,** *27* (6), 417-425.

23. Fujita, M.; Tominaga, M.; Hori, A.; Therrien, B., Coordination Assemblies from a Pd(II)-Cornered Square Complex. *Acc. Chem. Res.* **2005,** *38* (4), 369-378.

24. Norifumi, F.; Kumar, B.; Makoto, F.; Shigeru, S.; Kentaro, Y., A Porphyrin Prism: Structural Switching Triggered by Guest Inclusion. *Angew. Chem. Int. Ed.* **2001,** *40* (9), 1718-1721.

25. Kumar, B. A.; Rajesh, C.; Golam, M.; Sarathi, M. P., Self-Assembly of a Nanoscopic Pt12Fe12 Heterometallic Open Molecular Box Containing Six Porphyrin Walls. *Angew. Chem. Int. Ed.* **2008,** *47* (44), 8455-8459.

26. Holliday, B. J.; Mirkin, C. A., Strategies for the Construction of Supramolecular Compounds through Coordination Chemistry. *Angew. Chem. Int. Ed.* **2001,** *40* (11), 2022-2043.

27. Gianneschi, N. C.; Masar, M. S.; Mirkin, C. A., Development of a Coordination Chemistry-Based Approach for Functional Supramolecular Structures. *Acc. Chem. Res.* **2005,** *38* (11), 825-837.

28. Oliveri, C. G.; Ulmann, P. A.; Wiester, M. J.; Mirkin, C. A., Heteroligated Supramolecular Coordination Complexes Formed via the Halide-Induced Ligand Rearrangement Reaction. *Acc. Chem. Res.* **2008,** *41* (12), 1618-1629.

29. Zuideveld, M. A.; Swennenhuis, B. H. G.; Boele, M. D. K.; Guari, Y.; van Strijdonck, G. P. F.; Reek, J. N. H.; Kamer, P. C. J.; Goubitz, K.; Fraanje, J.; Lutz, M.; Spek, A. L.; van Leeuwen, P. W. N. M., The coordination behaviour of large natural bite angle diphosphine ligands towards methyl and 4-cyanophenylpalladium(ii) complexes. *J. Chem. Soc., Dalton Trans.* **2002,** (11), 2308-2317.

30. Hashiguchi, R.; Otsubo, K.; Ohtsu, H.; Kitagawa, H., A Novel Triangular Macrocyclic Compound, [(tmeda)Pt(azpy)]3(PF6)6·13H2O (tmeda: Tetramethylethylenediamine, azpy: 4,4′-Azopyridine). *Chem. Lett.* **2013,** *42* (4), 374-376.

31. Subhashis, P.; Rohith, J. P., Self-assembled Pd6L4 cage and Pd4L4 square using hydrazide based ligands: synthesis, characterization and catalytic activity in Suzuki-Miyaura coupling reactions. *RSC Advances* **2016,** *6* (15), 12453-12460.

32. Shanmugaraju, S.; Vajpayee, V.; Lee, S.; Chi, K.-W.; Stang, P. J.; Mukherjee, P. S., Coordination-Driven Self-Assembly of 2D-Metallamacrocycles Using a New Carbazole-Based Dipyridyl Donor: Synthesis, Characterization, and C60 Binding Study. *Inorg. Chem.* **2012,** *51* (8), 4817-4823.

33. Ferrer, M.; Pedrosa, A.; Rodríguez, L.; Rossell, O.; Vilaseca, M., New Insights into the Factors That Govern the Square/Triangle Equilibria of Pd(II) and Pt(II) Supramolecules. Unexpected Participation of a Mononuclear Species in the Equilibrium. *Inorg. Chem.* **2010,** *49* (20), 9438-9449.

34. Fujita, M.; Sasaki, O.; Mitsuhashi, T.; Fujita, T.; Yazaki, J.; Yamaguchi, K.; Ogura, K., On the structure of transition-metal-linked molecular squares. *Chem. Commun.* **1996,** (13), 1535-1536.

35. Uehara, K.; Kasai, K.; Mizuno, N., Synthetic and Computational Studies on Factors Controlling Structures of Molecular Triangles and Squares and Their Equilibrium in Solutions. *Inorg. Chem.* **2010,** *49* (4), 2008-2015.

36. Fang, Y.; Murase, T.; Fujita, M., Cavity-promoted Diels–Alder Reactions of Unsubstituted Naphthalene: Fine Reactivity Tuning by Cavity Shrinkage. *Chem. Lett.* **2015,** *44* (8), 1095-1097.

37. Yoshizawa, M.; Kumazawa, K.; Fujita, M., Room-Temperature and Solution-State Observation of the Mixed-Valence Cation Radical Dimer of Tetrathiafulvalene, [(TTF)2]+•, within a Self-Assembled Cage. *JACS* **2005,** *127* (39), 13456-13457.

38. Kiriyama, N.; Ebihara, M.; Udagawa, T.; Miyaji, H., Self-organization of dipyridylcalix[4]pyrrole into a supramolecular cage for dicarboxylates. *RSC Advances* **2016,** *6* (24), 19794-19796.

39.   Ghosh, S.; Mukherjee, P. S., Self-assembly of metal-organic hybrid nanoscopic rectangles. *Dalton Transactions* **2007,** (24), 2542-2546.

40.   Kim, J.; Ryu, D.; Sei, Y.; Yamaguchi, K.; Ahn, K. H., Tripodal oxazoline-based homochiral coordination cages with internal binding sites. *Chem. Commun.* **2006,** (10), 1136-1138.

41.   Ikeda, A.; Udzu, H.; Zhong, Z.; Shinkai, S.; Sakamoto, S.; Yamaguchi, K., A Self-Assembled Homooxacalix[3]arene-based Dimeric Capsule Constructed by a PdII−Pyridine Interaction Which Shows a Novel Chiral Twisting Motion in Response to Guest Inclusion. *JACS* **2001,** *123* (17), 3872-3877.

42.   Clever, G. H.; Punt, P., Cation–Anion Arrangement Patterns in Self-Assembled Pd2L4 and Pd4L8 Coordination Cages. *Acc. Chem. Res.* **2017,** *50* (9), 2233-2243.

43.   Schmidt, A.; Hollering, M.; Drees, M.; Casini, A.; Kuhn, F. E., Supramolecular exo-functionalized palladium cages: fluorescent properties and biological activity. *Dalton Transactions* **2016,** *45* (20), 8556-8565.

44.   Tomoki, T.; Wenchao, Z.; Hayato, F. T. L.; Tatsuo, K.; Kazuho, O.; Shuichi, H., Self-Assembly of a Pd4L8 Double-Walled Square Partly Takes Place Through the Formation of Kinetically Trapped Species. *Eur. J. Inorg. Chem.* **2018,** *2018* (10), 1192-1197.

45.   Zhang, T.; Zhou, L.-P.; Guo, X.-Q.; Cai, L.-X.; Sun, Q.-F., Adaptive self-assembly and induced-fit transformations of anion-binding metal-organic macrocycles. *Nature Communications* **2017,** *8*, 15898.

46.   Yazaki, K.; Akita, M.; Prusty, S.; Chand, D. K.; Kikuchi, T.; Sato, H.; Yoshizawa, M., Polyaromatic molecular peanuts. *Nature Communications* **2017,** *8*, 15914.

47.   Fujita, D.; Ueda, Y.; Sato, S.; Yokoyama, H.; Mizuno, N.; Kumasaka, T.; Fujita, M., Self-Assembly of M30L60 Icosidodecahedron. *Chem* **2016,** *1* (1), 91-101.

48.   Kim, T. Y.; Digal, L.; Gardiner, M. G.; Lucas, N. T.; Crowley, J. D., Octahedral [Pd6L8]12+ Metallosupramolecular Cages: Synthesis, Structures and Guest-Encapsulation Studies. *Chem. Eur. J.* **2017,** *23* (60), 15089-15097.

49.   Harris, K.; Fujita, D.; Fujita, M., Giant hollow MnL2n spherical complexes: structure, functionalisation and applications. *Chem. Commun.* **2013,** *49* (60), 6703-6712.

50.   Cotton, F. A.; Lin, C.; Murillo, C. A., The use of dimetal building blocks in convergent syntheses of large arrays. *Proceedings of the National Academy of Sciences* **2002,** *99* (8), 4810-4813.

51.   Cui, Y.; Chen, Z.-M.; Jiang, X.-F.; Tong, J.; Yu, S.-Y., Self-assembly and anion sensing of metal-organic [M6L2] cages from fluorescent triphenylamine tri-pyrazoles with dipalladium(ii,ii) corners. *Dalton Transactions* **2017**.

52.   Deng, Y.-X.; Zhang, H.-N.; Lin, Y.-J.; Jin, G.-X., Construction of half-sandwich rhodium- and iridium-based metallamacrocycles with different space conformations via isomeric pyridyl-substituted ligands. *J. Coord. Chem.* **2018**, 1-12.

53.   Bruno, T., Arene Ruthenium Cages: Boxes Full of Surprises. *Eur. J. Inorg. Chem.* **2009,** *2009* (17), 2445-2453.

54.   Mukherjee, P. S.; Adeyemo, A. A.; Shettar, A.; Bhat, I. A.; Kondaiah, P., Coordination-driven self-assembly of ruthenium(II) architectures: Synthesis, characterization and cytotoxicity studies. *Dalton Transactions* **2018,** *47*, 8466-8475.

55.   Ye, Y.; Cook, T. R.; Wang, S.-P.; Wu, J.; Li, S.; Stang, P. J., Self-Assembly of Chiral Metallacycles and Metallacages from a Directionally Adaptable BINOL-Derived Donor. *JACS* **2015,** *137* (37), 11896-11899.

56.   Cao, L.; Wang, P.; Miao, X.; Dong, Y.; Wang, H.; Duan, H.; Yu, Y.; Li, X.; Stang, P. J., Diamondoid Supramolecular Coordination Frameworks from Discrete Adamantanoid Platinum(II) Cages. *JACS* **2018,** *140* (22), 7005-7011.

57.   Zhang, M.; Xu, H.; Wang, M.; Saha, M. L.; Zhou, Z.; Yan, X.; Wang, H.; Li, X.; Huang, F.; She, N.; Stang, P. J., Platinum(II)-Based Convex Trigonal-Prismatic Cages via Coordination-Driven Self-Assembly and C60 Encapsulation. *Inorg. Chem.* **2017,** *56* (20), 12498-12504.

58.   Beuerle, F.; Gole, B., Covalent Organic Frameworks and Cage Compounds: Design and Applications of Polymeric and Discrete Organic Scaffolds. *Angew. Chem. Int. Ed.* **2018,** *57* (18), 4850-4878.

59.   Bloch, W. M.; Holstein, J. J.; Hiller, W.; Clever, G. H., Morphological Control of Heteroleptic cis- and trans-Pd2L2L′2 Cages. *Angew. Chem. Int. Ed.* **2017,** *56* (28), 8285-8289.

60.   Zhu, R.; Bloch, W. M.; Holstein, J. J.; Mandal, S.; Schäfer, L. V.; Clever Guido, H., Donor-site-directed Rational Assembly of Heteroleptic cis-[Pd2L2L′2] Coordination Cages from Picolyl Ligands. *Chem. Eur. J.* **2018,** *24* (49), 12976-12982.

61.   Bruns, C. J.; Stoddart, J. F., The nature of the mechanical bond : from molecules to machines. **2017**.

62.   Pease, A. R.; Jeppesen, J. O.; Stoddart, J. F.; Luo, Y.; Collier, C. P.; Heath, J. R., Switching Devices Based on Interlocked Molecules. *Acc. Chem. Res.* **2001,** *34* (6), 433-444.

63.   Balzani, V.; Credi, A.; Venturi, M., Light powered molecular machines. *Chem. Soc. Rev.* **2009,** *38* (6), 1542-1550.

64.   van Dongen, S. F. M.; Cantekin, S.; Elemans, J. A. A. W.; Rowan, A. E.; Nolte, R. J. M., Functional interlocked systems. *Chem. Soc. Rev.* **2014,** *43* (1), 99-122.

65.   Dietrich-Buchecker, C. O.; Sauvage, J. P., Interlocking of molecular threads: from the statistical approach to the templated synthesis of catenands. *Chem. Rev.* **1987,** *87* (4), 795-810.

66.   Crowley, J. D.; Goldup, S. M.; Lee, A.-L.; Leigh, D. A.; McBurney, R. T., Active metal template synthesis of rotaxanes, catenanes and molecular shuttles. *Chem. Soc. Rev.* **2009,** *38* (6), 1530-1541.

67.   Chambron, J.-C.; Sauvage, J.-P., Topologically complex molecules obtained by transition metal templation: it is the presentation that determines the synthesis strategy. *New J. Chem.* **2013,** *37* (1), 49-57.

68.   Hubin, T. J.; Busch, D. H., Template routes to interlocked molecular structures and orderly molecular entanglements. *Coord. Chem. Rev.* **2000,** *200-202*, 5-52.

69.   Fukuda, M.; Sekiya, R.; Kuroda, R., A Quadruply Stranded Metallohelicate and Its Spontaneous Dimerization into an Interlocked Metallohelicate. *Angew. Chem. Int. Ed.* **2008,** *47* (4), 706-710.

70.   Sekiya, R.; Fukuda, M.; Kuroda, R., Anion-Directed Formation and Degradation of an Interlocked Metallohelicate. *JACS* **2012,** *134* (26), 10987-10997.

71.   Rongmei, Z.; Jens, L.; Birger, D.; H., C. G., Stepwise Halide-Triggered Double and Triple Catenation of Self-Assembled Coordination Cages. *Angew. Chem. Int. Ed.* **2015,** *54* (9), 2796-2800.

72.   Jo, J.-H.; Singh, N.; Kim, D.; Cho, S. M.; Mishra, A.; Kim, H.; Kang, S. C.; Chi, K.-W., Coordination-Driven Self-Assembly Using Ditopic Pyridyl–Pyrazolyl Donor and p-Cymene Ru(II) Acceptors: [2]Catenane Synthesis and Anticancer Activities. *Inorg. Chem.* **2017,** *56* (14), 8430-8438.

73.   Song, Y. H.; Singh, N.; Jung, J.; Kim, H.; Kim, E. H.; Cheong, H. K.; Kim, Y.; Chi, K. W., Template-Free Synthesis of a Molecular Solomon Link by Two-Component Self-Assembly. *Angew. Chem. Int. Ed.* **2016,** *55* (6), 2007-2011.

74.   Kim, T. Y.; Digal, L.; Gardiner, M. G.; Lucas, N. T.; Crowley, J. D., Octahedral [Pd6L8]12+ Metallosupramolecular Cages: Synthesis, Structures and Guest-Encapsulation Studies. *Chem. Eur. J.* **2017,** *23* (60), 15089-15097.

75.   Yamashina, M.; Sartin, M. M.; Sei, Y.; Akita, M.; Takeuchi, S.; Tahara, T.; Yoshizawa, M., Preparation of Highly Fluorescent Host–Guest Complexes with Tunable Color upon Encapsulation. *JACS* **2015,** *137* (29), 9266-9269.

76.   Leenders, S. H. A. M.; Becker, R.; Kumpulainen, T.; de Bruin, B.; Sawada, T.; Kato, T.; Fujita, M.; Reek, J. N. H., Selective Co-Encapsulation Inside an M6L4 Cage. *Chem. Eur. J.* **2016,** *22* (43), 15468-15474.

77.   Wright, J. S.; Metherell, A. J.; Cullen, W. M.; Piper, J. R.; Dawson, R.; Ward, M. D., Highly selective CO2vs. N2 adsorption in the cavity of a molecular coordination cage. *Chem. Commun.* **2017,** *53* (31), 4398-4401.

78.   Barry, N. P. E.; Zava, O.; Dyson, P. J.; Therrien, B., Excellent Correlation between Drug Release and Portal Size in Metalla-Cage Drug-Delivery Systems. *Chem. Eur. J.* **2011,** *17* (35), 9669-9677.

79.   Pluth, M. D.; Raymond, K. N., Reversible guest exchange mechanisms in supramolecular host-guest assemblies. *Chem. Soc. Rev.* **2007,** *36* (2), 161-171.

80.   Chan, A. K.-W.; Lam, W. H.; Tanaka, Y.; Wong, K. M.-C.; Yam, V. W.-W., Multiaddressable molecular rectangles with reversible host–guest interactions: Modulation of pH-controlled guest release and capture. *Proceedings of the National Academy of Sciences* **2015,** *112* (3), 690-695.

81.   Clever, G. H.; Tashiro, S.; Shionoya, M., Light-Triggered Crystallization of a Molecular Host−Guest Complex. *JACS* **2010,** *132* (29), 9973-9975.

82.   Muxin, H.; Yuansu, L.; Bernd, D.; Laura, G.; Xavi, R.; Anex, J.; Patrick, P.; Michael, S.; H., C. G., Light-Controlled Interconversion between a Self-Assembled Triangle and a Rhombicuboctahedral Sphere. *Angew. Chem. Int. Ed.* **2016,** *55* (1), 445-449.

83.   Muxin, H.; Reent, M.; Bice, H.; Yu-Sheng, C.; Dietmar, S.; Michael, J.; H., C. G., Light-Triggered Guest Uptake and Release by a Photochromic Coordination Cage. *Angew. Chem. Int. Ed.* **2013,** *52* (4), 1319-1323.

84.   Li, K.; Zhang, L.-Y.; Yan, C.; Wei, S.-C.; Pan, M.; Zhang, L.; Su, C.-Y., Stepwise Assembly of Pd6(RuL3)8 Nanoscale Rhombododecahedral Metal–Organic Cages via Metalloligand Strategy for Guest Trapping and Protection. *JACS* **2014,** *136* (12), 4456-4459.

85.   Yoshizawa, M.; Miyagi, S.; Kawano, M.; Ishiguro, K.; Fujita, M., Alkane Oxidation via Photochemical Excitation of a Self-Assembled Molecular Cage. *JACS* **2004,** *126* (30), 9172-9173.

86.   Casini, A.; Woods, B.; Wenzel, M., The Promise of Self-Assembled 3D Supramolecular Coordination Complexes for Biomedical Applications. *Inorg. Chem.* **2017,** *56* (24), 14715-14729.

87.   Therrien, B.; Süss-Fink, G.; Govindaswamy, P.; Renfrew, A. K.; Dyson, P. J., The "Complex-in-a-Complex" Cations [(acac)2M⊂Ru6(p-iPrC6H4Me)6(tpt)2(dhbq)3]6+: A Trojan Horse for Cancer Cells. *Angew. Chem. Int. Ed.* **2008,** *47* (20), 3773-3776.

88.   Lewis, J. E. M.; Gavey, E. L.; Cameron, S. A.; Crowley, J. D., Stimuli-responsive Pd2L4 metallosupramolecular cages: towards targeted cisplatin drug delivery. *Chemical Science* **2012,** *3* (3), 778-784.

89.   Han, J.; Schmidt, A.; Zhang, T.; Permentier, H.; Groothuis, G. M. M.; Bischoff, R.; Kuhn, F. E.; Horvatovich, P.; Casini, A., Bioconjugation strategies to couple supramolecular exo-functionalized palladium cages to peptides for biomedical applications. *Chem. Commun.* **2017,** *53* (8), 1405-1408.

90.   Tabrizi, L.; Chiniforoshan, H., Ruthenium(II) p-cymene complexes of naphthoquinone derivatives as antitumor agents: A structure−activity relationship study. *J. Organomet. Chem.* **2016,** *822*, 211-220.

91.   Orhan, E.; Garci, A.; Riedel, T.; Soudani, M.; Dyson, P. J.; Therrien, B., Cytotoxic double arene ruthenium metalla-cycles that overcome cisplatin resistance. *J. Organomet. Chem.* **2016,** *803*, 39-44.

92.   Dubey, A.; Jeong, Y. J.; Jo, J. H.; Woo, S.; Kim, D. H.; Kim, H.; Kang, S. C.; Stang, P. J.; Chi, K.-W., Anticancer Activity and Autophagy Involvement of Self-Assembled Arene–Ruthenium Metallacycles. *Organometallics* **2015,** *34* (18), 4507-4514.

93.   Vajpayee, V.; Lee, S.; Kim, S.-H.; Kang, S. C.; Cook, T. R.; Kim, H.; Kim, D. W.; Verma, S.; Lah, M. S.; Kim, I. S.; Wang, M.; Stang, P. J.; Chi, K.-W., Self-assembled metalla-rectangles bearing azodipyridyl ligands: synthesis, characterization and antitumor activity. *Dalton Transactions* **2013,** *42* (2), 466-475.

94.   Cook, T. R.; Vajpayee, V.; Lee, M. H.; Stang, P. J.; Chi, K.-W., Biomedical and Biochemical Applications of Self-Assembled Metallacycles and Metallacages. *Acc. Chem. Res.* **2013,** *46* (11), 2464-2474.

95.   Bhowmick, S.; Jana, A.; Singh, K.; Gupta, P.; Gangrade, A.; Mandal, B. B.; Das, N., Coordination-Driven Self-Assembly of Ionic Irregular Hexagonal Metallamacrocycles via an Organometallic Clip and Their Cytotoxicity Potency. *Inorg. Chem.* **2018,** *57* (7), 3615-3625.

96.   McNeill, S. M.; Preston, D.; Lewis, J. E. M.; Robert, A.; Knerr-Rupp, K.; Graham, D. O.; Wright, J. R.; Giles, G. I.; Crowley, J. D., Biologically active [Pd2L4]4+ quadruply-stranded helicates: stability and cytotoxicity. *Dalton Transactions* **2015,** *44* (24), 11129-11136.

97.   Singh, K.; Gangrade, A.; Bhowmick, S.; Jana, A.; Mandal, B. B.; Das, N., Self-Assembly of a [1 + 1] Ionic Hexagonal Macrocycle and Its Antiproliferative Activity. *Frontiers in Chemistry* **2018,** *6*, 87.

98.   Lorenzo, C.; Qi, Z.; Konrad, T., Advantages of Catalysis in Self-Assembled Molecular Capsules. *Chem. Eur. J.* **2016,** *22* (27), 9060-9066.

99.   Zhang, D.; Ronson, T. K.; Nitschke, J. R., Functional Capsules via Subcomponent Self-Assembly. *Acc. Chem. Res.* **2018,** *51* (10), 2423-2436.

100.   Zhao, C.; Toste, F. D.; Raymond, K. N.; Bergman, R. G., Nucleophilic Substitution Catalyzed by a Supramolecular Cavity Proceeds with Retention of Absolute Stereochemistry. *JACS* **2014,** *136* (41), 14409-14412.

101.   Slagt, V. F.; Reek, J. N. H.; Kamer, P. C. J.; van Leeuwen, P. W. N. M., Assembly of Encapsulated Transition Metal Catalysts. *Angew. Chem. Int. Ed.* **2001,** *40* (22), 4271-4274.

102.   Zhang, Q.; Tiefenbacher, K., Terpene cyclization catalysed inside a self-assembled cavity. *Nature Chemistry* **2015,** *7*, 197.

103.   Pluth, M. D.; Bergman, R. G.; Raymond, K. N., Acid Catalysis in Basic Solution: A Supramolecular Host Promotes Orthoformate Hydrolysis. *Science* **2007,** *316* (5821), 85-88.

104.   Kang, J.; Santamaría, J.; Hilmersson, G.; Rebek, J., Self-Assembled Molecular Capsule Catalyzes a Diels−Alder Reaction. *JACS* **1998,** *120* (29), 7389-7390.

105.   Salles, A. G.; Zarra, S.; Turner, R. M.; Nitschke, J. R., A Self-Organizing Chemical Assembly Line. *JACS* **2013,** *135* (51), 19143-19146.

106.   Wang, Z. J.; Clary, K. N.; Bergman, R. G.; Raymond, K. N.; Toste, F. D., A supramolecular approach to combining enzymatic and transition metal catalysis. *Nature Chemistry* **2013,** *5*, 100.

107.   Croue, V.; Goeb, S.; Salle, M., Metal-driven self-assembly: the case of redox-active discrete architectures. *Chem. Commun.* **2015,** *51* (34), 7275-7289.

108.   Furutani, Y.; Kandori, H.; Kawano, M.; Nakabayashi, K.; Yoshizawa, M.; Fujita, M., In Situ Spectroscopic, Electrochemical, and Theoretical Studies of the Photoinduced Host−Guest Electron Transfer that Precedes Unusual Host-Mediated Alkane Photooxidation. *JACS* **2009,** *131* (13), 4764-4768.

109.   Zheng, Y.-R.; Suntharalingam, K.; Johnstone, T. C.; Lippard, S. J., Encapsulation of Pt(iv) prodrugs within a Pt(ii) cage for drug delivery. *Chemical Science* **2015,** *6* (2), 1189-1193.

110.   Yuan, M.; Weisser, F.; Sarkar, B.; Garci, A.; Braunstein, P.; Routaboul, L.; Therrien, B., Synthesis and Electrochemical Behavior of a Zwitterion-Bridged Metalla-Cage. *Organometallics* **2014,** *33* (18), 5043-5045.

111.   Szumna, A.; Jurczak, J., A New Macrocyclic Polylactam-Type Neutral Receptor for Anions − Structural Aspects of Anion Recognition. *Eur. J. Org. Chem.* **2001,** *2001* (21), 4031-4039.

112.   You, C.-C.; Würthner, F., Self-Assembly of Ferrocene-Functionalized Perylene Bisimide Bridging Ligands with Pt(II) Corner to Electrochemically Active Molecular Squares. *JACS* **2003,** *125* (32), 9716-9725.

113.   Frank, W.; Armin, S.; Dietmar, S.; A., W. P. J., Fluorescent and Electroactive Cyclic Assemblies from Perylene Tetracarboxylic Acid Bisimide Ligands and Metal Phosphane Triflates. *Chem. Eur. J.* **2001,** *7* (4), 894-902.

114.   Mahata, K.; Frischmann, P. D.; Würthner, F., Giant Electroactive M4L6 Tetrahedral Host Self-Assembled with Fe(II) Vertices and Perylene Bisimide Dye Edges. *JACS* **2013,** *135* (41), 15656-15661.

115.   van Staveren, D. R.; Metzler-Nolte, N., Bioorganometallic Chemistry of Ferrocene. *Chem. Rev.* **2004,** *104* (12), 5931-5986.

116.	Xu, L.; Wang, Y.-X.; Chen, L.-J.; Yang, H.-B., Construction of multiferrocenyl metallacycles and metallacages via coordination-driven self-assembly: from structure to functions. *Chem. Soc. Rev.* **2015,** *44* (8), 2148-2167.

117.	Ghosh, K.; Zhao, Y.; Yang, H.-B.; Northrop, B. H.; White, H. S.; Stang, P. J., Synthesis of a New Family of Hexakisferrocenyl Hexagons and Their Electrochemical Behavior. *The Journal of Organic Chemistry* **2008,** *73* (21), 8553-8557.

118.	Yang, H.-B.; Ghosh, K.; Zhao, Y.; Northrop, B. H.; Lyndon, M. M.; Muddiman, D. C.; White, H. S.; Stang, P. J., A New Family of Multiferrocene Complexes with Enhanced Control of Structure and Stoichiometry via Coordination-Driven Self-Assembly and Their Electrochemistry. *JACS* **2008,** *130* (3), 839-841.

119.	Zhao, G.-Z.; Li, Q.-J.; Chen, L.-J.; Tan, H.; Wang, C.-H.; Lehman, D. A.; Muddiman, D. C.; Yang, H.-B., Facile Self-Assembly of Supramolecular Hexakisferrocenyl Triangles via Coordination-Driven Self-Assembly and Their Electrochemical Behavior. *Organometallics* **2011,** *30* (13), 3637-3642.

120.	Ghosh, K.; Hu, J.; White, H. S.; Stang, P. J., Construction of Multifunctional Cuboctahedra via Coordination-Driven Self-Assembly. *JACS* **2009,** *131* (19), 6695-6697.

121.	Chen, L.-J.; Li, Q.-J.; He, J.; Tan, H.; Abliz, Z.; Yang, H.-B., Design and Construction of Endo-Functionalized Multiferrocenyl Hexagons via Coordination-Driven Self-Assembly and Their Electrochemistry. *The Journal of Organic Chemistry* **2012,** *77* (2), 1148-1153.

122.	Yao, L.-Y.; Yu, Z.-S.; Qin, L.; Li, Y.-Z.; Qin, Y.; Yu, S.-Y., Self-assembly of metallomacrocycles with dipyrazole ligands and anion sensing of [Pd4Fe2] macrocycle with ferrocene-based dipyrazole ligand. *Dalton Transactions* **2013,** *42* (10), 3447-3454.

123.	Das, N.; Arif, A. M.; Stang, P. J.; Sieger, M.; Sarkar, B.; Kaim, W.; Fiedler, J., Self-Assembly of Heterobimetallic Neutral Macrocycles Incorporating Ferrocene Spacer Groups: Spectroelectrochemical Analysis of the Double Two-Electron Oxidation of a Molecular Rectangle. *Inorg. Chem.* **2005,** *44* (16), 5798-5804.

124.	Yao, L.-Y.; Qin, L.; Xie, T.-Z.; Li, Y.-Z.; Yu, S.-Y., Synthesis and Anion Sensing of Water-Soluble Metallomacrocycles. *Inorg. Chem.* **2011,** *50* (13), 6055-6062.

125.	Stang, P. J.; Olenyuk, B.; Fan, J.; Arif, A. M., Combining Ferrocenes and Molecular Squares: Self-Assembly of Heterobimetallic Macrocyclic Squares Incorporating Mixed Transition Metal Systems and a Main Group Element. Single-Crystal X-ray Structure of [Pt(dppf)(H2O)2][OTf]2. *Organometallics* **1996,** *15* (3), 904-908.

126.	Vajpayee, V.; Kim, H.; Mishra, A.; Mukherjee, P. S.; Stang, P. J.; Lee, M. H.; Kim, H. K.; Chi, K.-W., Self-assembled molecular squares containing metal-based donor: synthesis and application in the sensing of nitro-aromatics. *Dalton Transactions* **2011,** *40* (13), 3112-3115.

127.	Jiang, F.; Wang, J.; Li, J.; Wang, N.; Bao, X.; Wang, T.; Yang, Y.; Lan, Z.; Yang, R., Supramolecular Assemblies with Symmetrical Octahedral Structures – Synthesis, Characterization, and Electrochemical Properties. *Eur. J. Inorg. Chem.* **2013,** *2013* (3), 375-380.

128.	Yazaki, K.; Noda, S.; Tanaka, Y.; Sei, Y.; Akita, M.; Yoshizawa, M., An M2L4 Molecular Capsule with a Redox Switchable Polyradical Shell. *Angew. Chem. Int. Ed.* **2016,** *55* (48), 15031-15034.

129.	Rizzuto, F. J.; Wood, D. M.; Ronson, T. K.; Nitschke, J. R., Tuning the Redox Properties of Fullerene Clusters within a Metal–Organic Capsule. *JACS* **2017,** *139* (32), 11008-11011.

130.	Hünig, S.; Schlaf, H.; Kießlich, G.; Scheutzow, D., Zweistufige, reversible redoxsysteme mit stabilem radikalkation. *Tetrahedron Lett.* **1969,** *10* (27), 2271-2274.

131.	Coffen, D. L., Condensation of carbon disulfide with dimethyl acetylenedicarboxylate. *Tetrahedron Lett.* **1970,** *11* (30), 2633-2636.

132.	Wudl, F.; Smith, G. M.; Hufnagel, E. J., Bis-1,3-dithiolium chloride: an unusually stable organic radical cation. *Journal of the Chemical Society D: Chemical Communications* **1970,** (21), 1453-1454.

133.	Wudl, F.; Wobschall, D.; Hufnagel, E. J., Electrical conductivity by the bis(1,3-dithiole)-bis(1,3-dithiolium) system. *JACS* **1972,** *94* (2), 670-672.

134.   Ferraris, J.; Cowan, D. O.; Walatka, V.; Perlstein, J. H., Electron transfer in a new highly conducting donor-acceptor complex. *JACS* **1973,** *95* (3), 948-949.

135.   Martín, N., Tetrathiafulvalene: the advent of organic metals. *Chem. Commun.* **2013,** *49* (63), 7025-7027.

136.   Jørgensen, T.; Hansen, T. K.; Becher, J., Tetrathiafulvalenes as building-blocks in supramolecular chemistry. *Chem. Soc. Rev.* **1994,** *23* (1), 41-51.

137.   Bryce, M. R., Functionalised tetrathiafulvalenes: new applications as versatile π-electron systems in materials chemistry. *J. Mater. Chem.* **2000,** *10* (3), 589-598.

138.   Segura, J. L.; Martín, N., New Concepts in Tetrathiafulvalene Chemistry. *Angew. Chem. Int. Ed.* **2001,** *40* (8), 1372-1409.

139.   Coronado, E.; Day, P., Magnetic Molecular Conductors. *Chem. Rev.* **2004,** *104* (11), 5419-5448.

140.   Canevet, D.; Salle, M.; Zhang, G.; Zhang, D.; Zhu, D., Tetrathiafulvalene (TTF) derivatives: key building-blocks for switchable processes. *Chem. Commun.* **2009,** (17), 2245-2269.

141.   Roncali, J., Linearly extended π-donors: when tetrathiafulvalene meets conjugated oligomers and polymers. *J. Mater. Chem.* **1997,** *7* (12), 2307-2321.

142.   Frère, P.; Skabara, P. J., Salts of extended tetrathiafulvalene analogues: relationships between molecular structure, electrochemical properties and solid state organisation. *Chem. Soc. Rev.* **2005,** *34* (1), 69-98.

143.   Brunetti, F. G.; López, J. L.; Atienza, C.; Martín, N., π-Extended TTF: a versatile molecule for organic electronics. *J. Mater. Chem.* **2012,** *22* (10), 4188-4205.

144.   Pérez, E. M.; Illescas, B. M.; Herranz, M. Á.; Martín, N., Supramolecular chemistry of π-extended analogues of TTF and carbon nanostructures. *New J. Chem.* **2009,** *33* (2), 228-234.

145.   Goeb, S.; Bivaud, S.; Dron, P. I.; Balandier, J.-Y.; Chas, M.; Salle, M., A BPTTF-based self-assembled electron-donating triangle capable of C60 binding. *Chem. Commun.* **2012,** *48* (25), 3106-3108.

146.   Balandier, J.-Y.; Chas, M.; Goeb, S.; Dron, P. I.; Rondeau, D.; Belyasmine, A.; Gallego, N.; Salle, M., A self-assembled bis(pyrrolo)tetrathiafulvalene-based redox active square. *New J. Chem.* **2011,** *35* (1), 165-168.

147.   Bivaud, S.; Balandier, J.-Y.; Chas, M.; Allain, M.; Goeb, S.; Sallé, M., A Metal-Directed Self-Assembled Electroactive Cage with Bis(pyrrolo)tetrathiafulvalene (BPTTF) Side Walls. *JACS* **2012,** *134* (29), 11968-11970.

148.   Bivaud, S.; Goeb, S.; Balandier, J.-Y.; Chas, M.; Allain, M.; Sallé, M., Self-Assembled Cages from the Electroactive Bis(pyrrolo)tetrathiafulvalene (BPTTF) Building Block. *Eur. J. Inorg. Chem.* **2014,** *2014* (14), 2440-2448.

149.   Bivaud, S.; Goeb, S.; Croué, V.; Dron, P. I.; Allain, M.; Sallé, M., Self-Assembled Containers Based on Extended Tetrathiafulvalene. *JACS* **2013,** *135* (27), 10018-10021.

150.   Croué, V.; Goeb, S.; Szalóki, G.; Allain, M.; Sallé, M., Reversible Guest Uptake/Release by Redox-Controlled Assembly/Disassembly of a Coordination Cage. *Angew. Chem. Int. Ed.* **2016,** *55* (5), 1746-1750.

151.   Szaloki, G.; Croue, V.; Allain, M.; Goeb, S.; Salle, M., Neutral versus polycationic coordination cages: a comparison regarding neutral guest inclusion. *Chem. Commun.* **2016,** *52* (65), 10012-10015.

152.   Szalóki, G.; Croué, V.; Carré, V.; Aubriet, F.; Alévêque, O.; Levillain, E.; Allain, M.; Aragó, J.; Ortí, E.; Goeb, S.; Sallé, M., Controlling the Host–Guest Interaction Mode through a Redox Stimulus. *Angew. Chem. Int. Ed.* **2017,** *56* (51), 16272-16276.

153.   Mitamura, Y.; Yorimitsu, H.; Oshima, K.; Osuka, A., Straightforward access to aryl-substituted tetrathiafulvalenes by palladium-catalysed direct C–H arylation and their photophysical and electrochemical properties. *Chemical Science* **2011,** *2* (10), 2017-2021.

154. Vajpayee, V.; Bivaud, S.; Goeb, S.; Croué, V.; Allain, M.; Popp, B. V.; Garci, A.; Therrien, B.; Sallé, M., Electron-Rich Arene–Ruthenium Metalla-architectures Incorporating Tetrapyridyl–Tetrathiafulvene Donor Moieties. *Organometallics* **2014,** *33* (7), 1651-1658.

155. Nielsen, K.; Jeppesen, J. O.; Thorup, N.; Becher, J., A Pyrrolo-Tetrathiafulvalene Belt and Its TCNQ Complex: Syntheses and X-ray Crystal Structures. *Org. Lett.* **2002,** *4* (8), 1327-1330.

156. Cotelle, Y.; Hardouin-Lerouge, M.; Legoupy, S.; Alévêque, O.; Levillain, E.; Hudhomme, P., Glycoluril–tetrathiafulvalene molecular clips: on the influence of electronic and spatial properties for binding neutral accepting guests. *Beilstein Journal of Organic Chemistry* **2015,** *11*, 1023-1036.

157. Andrieux, A.; Duroure, C.; Jérome, D.; Bechgaard, K., The metallic state of the organic conductor TMTSF-DMTCNQ at low temperature under pressure. *Journal de Physique Lettres* **1979,** *40* (15), 381-383.

158. Spruell Jason, M., Molecular recognition and switching via radical dimerization. In *Pure Appl. Chem.*, 2010; Vol. 82, p 2281.

159. Zhang, D.-W.; Tian, J.; Chen, L.; Zhang, L.; Li, Z.-T., Dimerization of Conjugated Radical Cations: An Emerging Non-Covalent Interaction for Self-Assembly. *Chemistry – An Asian Journal* **2015,** *10* (1), 56-68.

160. Huchet, L.; Akoudad, S.; Levillain, E.; Roncali, J.; Emge, A.; Bäuerle, P., Spectroelectrochemistry of Electrogenerated Tetrathiafulvalene-Derivatized Poly(thiophenes): Toward a Rational Design of Organic Conductors with Mixed Conduction. *The Journal of Physical Chemistry B* **1998,** *102* (40), 7776-7781.

161. Khodorkovsky, V.; Shapiro, L.; Krief, P.; Shames, A.; Mabon, G.; Gorgues, A.; Giffard, M., Do π-dimers of tetrathiafulvalene cation radicals really exist at room temperature? *Chem. Commun.* **2001,** (24), 2736-2737.

162. Rosokha, S. V.; Kochi, J. K., Molecular and Electronic Structures of the Long-Bonded π-Dimers of Tetrathiafulvalene Cation-Radical in Intermolecular Electron Transfer and in (Solid-State) Conductivity. *JACS* **2007,** *129* (4), 828-838.

163. Ziganshina, A. Y.; Ko, Y. H.; Jeon, W. S.; Kim, K., Stable π-dimer of a tetrathiafulvalene cation radical encapsulated in the cavity of cucurbit[8]uril. *Chem. Commun.* **2004,** (7), 806-807.

164. A. Christensen, C.; Becher, J.; A. Christensen, C.; M. Goldenberg, L.; R. Bryce, M., Synthesis and electrochemistry of a tetrathiafulvalene (TTF)21–glycol dendrimer: intradendrimer aggregation of TTF cation radicals. *Chem. Commun.* **1998,** (4), 509-510.

165. Lyskawa, J.; Salle, M.; Balandier, J.-Y.; Le Derf, F.; Levillain, E.; Allain, M.; Viel, P.; Palacin, S., Monitoring the formation of TTF dimers by Na+ complexation. *Chem. Commun.* **2006,** (21), 2233-2235.

166. Bejger, C.; Davis, C. M.; Park, J. S.; M. Lynch, V.; Love, J. B.; Sessler, J. L., Palladium Induced Macrocyclic Preorganization for Stabilization of a Tetrathiafulvalene Mixed-Valence Dimer. *Org. Lett.* **2011,** *13* (18), 4902-4905.

167. Hasegawa, M.; Daigoku, K.; Hashimoto, K.; Nishikawa, H.; Iyoda, M., Face-to-Face Dimeric Tetrathiafulvalenes and Their Cation Radical and Dication Species as Models of Mixed Valence and π-Dimer States. *Bull. Chem. Soc. Jpn.* **2012,** *85* (1), 51-60.

168. Spruell, J. M.; Coskun, A.; Friedman, D. C.; Forgan, R. S.; Sarjeant, A. A.; Trabolsi, A.; Fahrenbach, A. C.; Barin, G.; Paxton, W. F.; Dey, S. K.; Olson, M. A.; Benítez, D.; Tkatchouk, E.; Colvin, M. T.; Carmielli, R.; Caldwell, S. T.; Rosair, G. M.; Hewage, S. G.; Duclairoir, F.; Seymour, J. L.; Slawin, A. M. Z.; Goddard Iii, W. A.; Wasielewski, M. R.; Cooke, G.; Stoddart, J. F., Highly stable tetrathiafulvalene radical dimers in [3]catenanes. *Nature Chemistry* **2010,** *2*, 870.

169. Wang, Y.; Frattarelli, D. L.; Facchetti, A.; Cariati, E.; Tordin, E.; Ugo, R.; Zuccaccia, C.; Macchioni, A.; Wegener, S. L.; Stern, C. L.; Ratner, M. A.; Marks, T. J., Twisted π-Electron System Electrooptic Chromophores. Structural and Electronic Consequences of Relaxing Twist-Inducing Nonbonded Repulsions. *The Journal of Physical Chemistry C* **2008,** *112* (21), 8005-8015.

170. Cohen, Y.; Avram, L.; Frish, L., Diffusion NMR Spectroscopy in Supramolecular and Combinatorial Chemistry: An Old Parameter—New Insights. *Angew. Chem. Int. Ed.* **2005,** *44* (4), 520-554.

171. Spanggaard, H.; Prehn, J.; Nielsen, M. B.; Levillain, E.; Allain, M.; Becher, J., Multiple-Bridged Bis-Tetrathiafulvalenes: New Synthetic Protocols and Spectroelectrochemical Investigations. *JACS* **2000,** *122* (39), 9486-9494.

172. Michail I. Knyazhanskii; Yakov R. Tymyanskii; Vladimir M. Feigelman; Katritzky, A. R., Pyridinium Salts: Luminescent Spectroscopy and Photochemistry. *Heterocycles* **1987,** *26* (11), 2963 - 2982.

173. Jung, H.; Dubey, A.; Koo, H. J.; Vajpayee, V.; Cook, T. R.; Kim, H.; Kang, S. C.; Stang, P. J.; Chi, K. W., Self-Assembly of Ambidentate Pyridyl-Carboxylate Ligands with Octahedral Ruthenium Metal Centers: Self-Selection for a Single-Linkage Isomer and Anticancer-Potency Studies. *Chem. Eur. J.* **2013,** *19* (21), 6709-6717.

174. Orhan, E.; Garci, A.; Therrien, B., Flexible arene ruthenium metalla-prisms. *Inorg. Chim. Acta* **2015,** *438*, 5-9.

175. Suzuki, K.; Tominaga, M.; Kawano, M.; Fujita, M., Self-assembly of an M6L12 coordination cube. *Chem. Commun.* **2009,** (13), 1638-1640.

176. Wang, H.; Mei, J.; Liu, P.; Schmidt, K.; Jiménez-Osés, G.; Osuna, S.; Fang, L.; Tassone, C. J.; Zoombelt, A. P.; Sokolov, A. N.; Houk, K. N.; Toney, M. F.; Bao, Z., Scalable and Selective Dispersion of Semiconducting Arc-Discharged Carbon Nanotubes by Dithiafulvalene/Thiophene Copolymers for Thin Film Transistors. *ACS Nano* **2013,** *7* (3), 2659-2668.

177. Amriou, S.; Wang, C.; Batsanov, A. S.; Bryce, M. R.; Perepichka, D. F.; Ortí, E.; Viruela, R.; Vidal-Gancedo, J.; Rovira, C., The Interplay of Inverted Redox Potentials and Aromaticity in the Oxidized States of New π-Electron Donors: 9-(1,3-Dithiol-2-ylidene)fluorene and 9-(1,3-Dithiol-2-ylidene)thioxanthene Derivatives. *Chem. Eur. J.* **2006,** *12* (12), 3389-3400.

178. Croue, V.; Krykun, S.; Allain, M.; Morille, Y.; Aubriet, F.; Carre, V.; Voitenko, Z.; Goeb, S.; Salle, M., A Self-Assembled M2L4 Cage incorporating Electron-rich 9-(1,3-dithiol-2-ylidene)Fluorene Units. *New J. Chem.* **2017,** *41* (9), 3238-3241.

179. The cavity volume has been estimated based on voidoo algorithm with ABSiCC (Automating Boring Stuff in Computational Chemistry), a homemade POVRAY-interfaced program designed by Thomas Cauchy and written by Yohann Morille, Angers University.

180. Perepichka, D. F.; Perepichka, I. F.; Ivasenko, O.; Moore, A. J.; Bryce, M. R.; Kuz'mina, L. G.; Batsanov, A. S.; Sokolov, N. I., Combining High Electron Affinity and Intramolecular Charge Transfer in 1,3-Dithiole–Nitrofluorene Push–Pull Diads. *Chem. - Eur. J.* **2008,** *14* (9), 2757-2770.

181. Krykun, S.; Allain, M.; Carré, V.; Aubriet, F.; Voitenko, Z.; Goeb, S.; Sallé, M., A M2L2 Redox-Active Metalla-Macrocycle Based on Electron-Rich 9-(1,3-Dithiol-2-ylidene)Fluorene. *Inorganics* **2018,** *6* (2), 44.

182. Ferrer, M.; Gutiérrez, A.; Rodríguez, L.; Rossell, O.; Ruiz, E.; Engeser, M.; Lorenz, Y.; Schilling, R.; Gómez-Sal, P.; Martín, A., Self-Assembly of Heterometallic Metallomacrocycles via Ditopic Fluoroaryl Gold(I) Organometallic Metalloligands. *Organometallics* **2012,** *31* (4), 1533-1545.

183. Samanta, D.; Shanmugaraju, S.; Joshi, S. A.; Patil, Y. P.; Nethaji, M.; Mukherjee, P. S., Pillar height dependent formation of unprecedented Pd8 molecular swing and Pd6 molecular boat via multicomponent self-assembly. *Chem. Commun.* **2012,** *48* (17), 2298-2300.

184. Niu, Z.; Li, D.; Liu, D.; Xia, D.; Zou, Y.; Sun, W.; Li, G., Syntheses, electrochemical behaviors, spectral properties and DFT calculations of two 1,3-dithiole derivatives. *Chem Res Chinese U* **2014,** *30* (3), 425-430.

185. Ganesamoorthy, R.; Sathiyan, G.; Sakthivel, P., Review: Fullerene based acceptors for efficient bulk heterojunction organic solar cell applications. *Sol. Energy Mater. Sol. Cells* **2017,** *161*, 102-148.

186.   Szalóki, G.; Krykun, S.; Croué, V.; Allain, M.; Morille, Y.; Aubriet, F.; Carré, V.; Voitenko, Z.; Goeb, S.; Sallé, M., Redox-Driven Transformation of a Discrete Molecular Cage into an Infinite 3D Coordination Polymer. *Chem. Eur. J.* **2018,** *24* (44), 11273-11277.

187.   S. Bivaud, Thèse de doctorat, Université d'Angers, 2012

188.   Gruhn, N. E.; Macías-Ruvalcaba, N. A.; Evans, D. H., Studies of Potential Inversion in an Extended Tetrathiafulvalene. *Langmuir* **2006,** *22* (25), 10683-10688.

189.   Amriou, S.; Wang, C.; Batsanov, A. S.; Bryce, M. R.; Perepichka, D. F.; Ortí, E.; Viruela, R.; Vidal-Gancedo, J.; Rovira, C., The Interplay of Inverted Redox Potentials and Aromaticity in the Oxidized States of New π-Electron Donors: 9-(1,3-Dithiol-2-ylidene)fluorene and 9-(1,3-Dithiol-2-ylidene)thioxanthene Derivatives. *Chem. Eur. J.* **2006,** *12* (12), 3389-3400.

190.   Sun, Q. F.; Iwasa, J.; Ogawa, D.; Ishido, Y.; Sato, S.; Ozeki, T.; Sei, Y.; Yamaguchi, K.; Fujita, M., Self-assembled M24L48 polyhedra and their sharp structural switch upon subtle ligand variation. *Science* **2010,** *328* (5982), 1144-7.

191.   The cavity volume has been estimated based on voidoo algorithm with ABSiCC (Automating Boring Stuff in Computational Chemistry), a homemade POVRAY-interfaced program designed by Thomas Cauchy and written by Yohann Morille, Angers University.

192.   Szalóki, G.; Croué, V.; Carré, V.; Aubriet, F.; Aleveque, O.; Levillain, E.; Allain, M.; Arago, J.; Orti, E.; Goeb, S.; Sallé, M., Controlling the Host-Guest Interaction Mode through a Redox Stimulus. *Angew. Chem. Int. Ed.* **2017,** *56* (51), 16272-16276.

193.   Wang, H.-Y.; Cui, L.; Xie, J.-Z.; Leong, C. F.; D'Alessandro, D. M.; Zuo, J.-L., Functional coordination polymers based on redox-active tetrathiafulvalene and its derivatives. *Coord. Chem. Rev.* **2017,** *345* (Supplement C), 342-361.

194.   Krykun, S.; Croué, V.; Allain, M.; Voitenko, Z.; Aragó, J.; Ortí, E.; Goeb, S.; Sallé, M., Tuning the electronic properties and the planarity degree in the π-extended TTF series: the prominent role of heteroatoms. *Journal of Materials Chemistry C* **2018,** *6* (48), 13190-13196.

195.   Moore, A. J.; Bryce, M. R., Highly conjugated [π]-electron donors for organic metals: synthesis and redox chemistry of new 1,3-dithiole and 1,3-selenathiole derivatives. *J. Chem. Soc., Perkin Trans. 1* **1991,** *0* (1), 157-168.

196.   Bryce, M. R.; Moore, A. J.; Hasan, M.; Ashwell, G. J.; Fraser, A. T.; Clegg, W.; Hursthouse, M. B.; Karaulov, A. I., Electrical and Magnetic Properties and X-Ray Structure of a Highly Conductive 4:1 Complex of Tetracyanoquinodimethane and a Tetrathiafulvalene Derivative. *Angew. Chem. Int. Ed* **1990,** *29* (12), 1450-1452.

197.   Yamashita, Y.; Kobayashi, Y.; Miyashi, T., p-Quinodimethane Analogues of Tetrathiafulvalene. *Angew. Chem. Int. Ed.* **1989,** *28* (8), 1052-1053.

198.   Bryce, M. R.; Moore, A. J., A new highly-conjugated TTF analogue: Synthesis, electrochemistry and a conducting TCNQ complex of 9,10-anthracenediylidene-2,2′-bis(4,5-dimethyl-1,3-dithiole). *Synth. Met.* **1988,** *25* (2), 203-205.

199.   Brunetti, F. G.; Lopez, J. L.; Atienza, C.; Martin, N., pi-Extended TTF: a versatile molecule for organic electronics. *J. Mater. Chem.* **2012,** *22* (10), 4188-4205.

200.   Ogi, D.; Fujita, Y.; Mori, S.; Shirahata, T.; Misaki, Y., Bis- and Tris-fused Tetrathiafulvalenes Extended with Anthracene-9,10-diylidene. *Org. Lett.* **2016,** *18* (22), 5868-5871.

201.   Younes, E. A.; Zhao, Y., Highly [small pi]-extended tetrathiafulvalene analogues derived from pentacene-5,7,12,14-tetraone. *RSC Adv.* **2015,** *5* (108), 88821-88825.

202.   Christensen, M. A.; Parker, C. R.; Sorensen, T. J.; de Graaf, S.; Morsing, T. J.; Brock-Nannestad, T.; Bendix, J.; Haley, M. M.; Rapta, P.; Danilov, A.; Kubatkin, S.; Hammerich, O.; Nielsen, M. B., Mixed valence radical cations and intermolecular complexes derived from indenofluorene-extended tetrathiafulvalenes. *J. Mater. Chem. C* **2014,** *2* (48), 10428-10438.

203.	Christensen, M. A.; Rudebusch, G. E.; Parker, C. R.; Andersen, C. L.; Kadziola, A.; Haley, M. M.; Hammerich, O.; Nielsen, M. B., Diindenothienoacene-tetrathiafulvalene redox systems. *RSC Adv.* **2015,** *5* (61), 49748-49751.

204.	Petersen, J. F.; Frederickson, C. K.; Marshall, J. L.; Rudebusch, G. E.; Zakharov, L. N.; Hammerich, O.; Haley, M. M.; Nielsen, M. B., Expanded Indacene–Tetrathiafulvalene Scaffolds: Structural Implications for Redox Properties and Association Behavior. *Chem. Eur. J.* **2017,** *23* (53), 13120-13130.

205.	Broman, S. L.; Andersen, C. L.; Jousselin-Oba, T.; Manso, M.; Hammerich, O.; Frigoli, M.; Nielsen, M. B., Tetraceno[2,1,12,11-opqra]tetracene-extended tetrathiafulvalene - redox-controlled generation of a large PAH core. *Org. Biomol. Chem.* **2017,** *15* (4), 807-811.

206.	Giguère, J.-B.; Morin, J.-F., Superextended Tetrathiafulvalene: Synthesis, Optoelectronic Properties, Fullerenes Complexation, and Photooxidation Study. *J. Org. Chem.* **2015,** *80* (13), 6767-6775.

207.	Conboy, G.; Spencer, H. J.; Angioni, E.; Kanibolotsky, A. L.; Findlay, N. J.; Coles, S. J.; Wilson, C.; Pitak, M. B.; Risko, C.; Coropceanu, V.; Bredas, J.-L.; Skabara, P. J., To bend or not to bend - are heteroatom interactions within conjugated molecules effective in dictating conformation and planarity? *Mater. Horiz.* **2016,** *3* (4), 333-339.

208.	Moore, A. J.; Bryce, M. R., New vinylogous tetrathiafulvalene (TTF) π-electron donors. *Tetrahedron Lett.* **1992,** *33* (10), 1373-1376.

209.	Ren, Y.; Lee, S.; Bertke, J. A.; Moore, J. S., Crystal structure of 9,10-bis(1,3-dithiol-2-ylidene)-9,10-dihydroanthracene. *Act. Cryst. E* **2015,** *71* (12), 1475-1479.

210.	Batsanov, A. S.; Bryce, M. R.; Coffin, M. A.; Green, A.; Hester, R. E.; Howard, J. A. K.; Lednev, I. K.; Martín, N.; Moore, A. J.; Moore, J. N.; Ortí, E.; Sánchez, L.; Savirón, M.; Viruela, P. M.; Viruela, R.; Ye, T.-Q., Donor–π-Acceptor Species Derived from Functionalised 1,3-Dithiol-2-ylidene Anthracene Donor Units Exhibiting Photoinduced Electron Transfer Properties: Spectroscopic, Electrochemical, X-Ray Crystallographic and Theoretical Studies. *Chem. Eur. J.* **1998,** *4* (12), 2580-2592.

211.	Liu, S.-G.; Pérez, I.; Martín, N.; Echegoyen, L., Intramolecular Electronic Interactions in Conjugated Ferrocene−π-Extended-Tetrathiafulvalene Donor-π-Donor Molecular Hybrids. *J. Org. Chem.* **2000,** *65* (26), 9092-9102.

212.	Yamashita, Y.; Ono, K.; Tanaka, S.; Imaeda, K.; Inokuchi, H., Nonplanar bis(1,3-dithiole) donors affording novel cation radical salts. *Adv. Mater.* **1994,** *6* (4), 295-298.

213.	Carlier, R.; Frère, P.; Sallé, M.; Roncali, J.; Jubault, M.; Tallec, A.; Gorgues, A., Prediction of the stoichiometry of cation radical salts of organic metals by thin layer cyclic voltammetry. *Adv. Mater.* **1993,** *5* (6), 445-447.

214.	Szaloki, G.; Krykun, S.; Croué, V.; Allain, M.; Morille, Y.; Aubriet, F.; Carré, V.; Voitenko, Z.; Goeb, S.; Sallé, M., Redox-Driven Transformation of a Discrete Molecular Cage into an Infinite 3D Coordination Polymer. *Chem. Eur. J.* **2018,** *24* (44), 11273-11277.

215.	Jones, A. E.; Christensen, C. A.; Perepichka, D. F.; Batsanov, A. S.; Beeby, A.; Low, P. J.; Bryce, M. R.; Parker, A. W., Photochemistry of the π-Extended 9,10-Bis(1,3-dithiol-2-ylidene)- 9,10-dihydroanthracene System: Generation and Characterisation of the Radical Cation, Dication, and Derived Products. *Chem. Eur. J.* **2001,** *7* (5), 973-978.

216.	Masaru, K.-n.; John, M.; Nagao, K.; Masahiko, S.; Kenji, Y.; Teruo, S., Synthesis, Optical Properties, and Electronic Structures of Fully Core-Modified Porphyrin Dications and Isophlorins. *Chem. Eur. J.* **2012,** *18* (42), 13361-13371.

217.	Ozturk, T.; Povey, D. C.; Wallis, J. D., HETEROCYCLIC CATIONS WITH DELOCALISED PI-SYSTEMS AND SHORT INTRAMOLECULAR SULFUR… SULFUR CONTACTS: THE STRUCTURES OF TWO DERIVATIVES OF THE 2-(1,3-DITHIOL-2-YLIDENEMETHYL)-1,3-DITHIOLIUM CATION. *Phosphorus, Sulfur, and Silicon and the Related Elements* **1997,** *122* (1), 313-324.

218.   Emanuel, V.; Michael, P.; Adalbert, H.; Torsten, W.; Christoph, K.; Johann, L.; Maurice, G.; Paul, G. J., Porphyrinoid Macrocycles Based on Thiophene—The Octaethyltetrathiaporphyrin Dication. *Angew. Chem. Int. Ed.* **1996,** *35* (13-14), 1520-1524.

219.   Suzuki, T.; Sakimura, T.; Tanaka, S.; Yamashita, Y.; Shiohara, H.; Miyashi, T., 2-(Thiopyran-4[prime or minute]-yliden)-1,3-dithioles fused with thiophene units: intramolecular S [three dots, centered] S interaction affecting the redox properties and molecular geometries. *J. Chem. Soc., Chem. Commun.* **1994,** (12), 1431-1432.

220.   Yan, H.; Suss-Fink, G.; Neels, A.; Stoeckli-Evans, H., Mono-, di- and tetra-nuclear p-cymeneruthenium complexes containing oxalato ligands. *J. Chem. Soc., Dalton Trans.* **1997,** (22), 4345-4350.

221.   Barry Nicolas, P. E.; Furrer, J.; Freudenreich, J.; Süss-Fink, G.; Therrien, B., Designing the Host-Guest Properties of Tetranuclear Arene Ruthenium Metalla-Rectangles to Accommodate a Pyrene Molecule. *Eur. J. Inorg. Chem.* **2010,** *2010* (5), 725-728.

222.   Kobin, B.; Grubert, L.; Blumstengel, S.; Henneberger, F.; Hecht, S., Vacuum-processable ladder-type oligophenylenes for organic–inorganic hybrid structures: synthesis, optical and electrochemical properties upon increasing planarization as well as thin film growth. *J. Mater. Chem.* **2012,** *22* (10), 4383-4390.

9. Annexes

Annex 1. Spectroelectrochemistry

Spectroelectrochemistry allows to combine electrochemical experiment with spectroscopic observation, thus serving as an additional tool to the classic electrochemistry. As a result, usually an absorption or a fluorescent spectrum is obtained, couples with a cyclic voltammetry data. This allows to identify characteristic spectroscopic signatures of compounds, which are formed during the oxidation or reduction of the sample. Therefore, this method allows to gain additional information about structural and electronic properties of the compound.
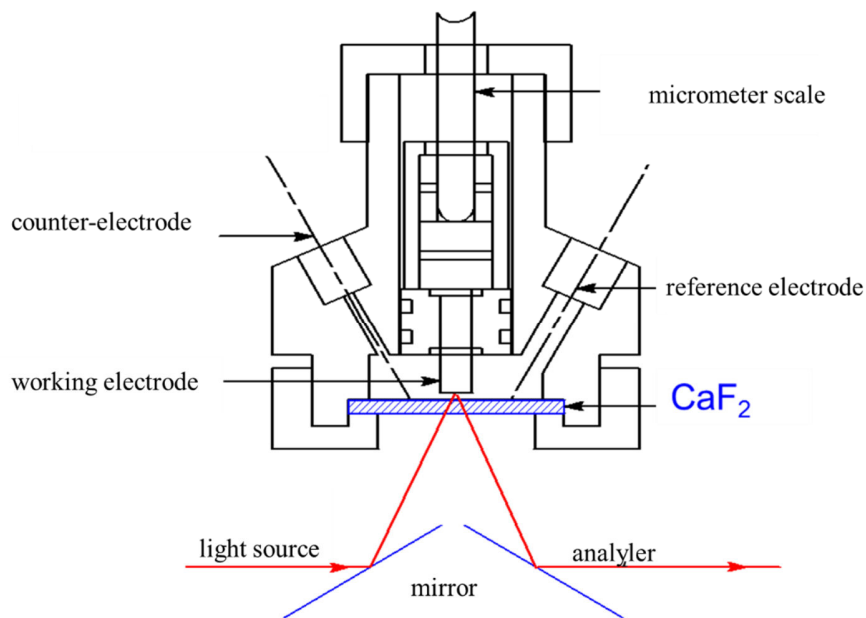
In our case, Teflon cell (picture above) is used, which is resistant to most organic solvents. Electrochemical measurements are conducted using the standard system of three electrodes. More importantly, working electrode could be adjusted to work within the semi-infinite diffusion mode similarly to the thin layer cyclic voltammetry. Light source is provided via optical fibers. The light is reflected by the working electrode which is glassy carbon or platinum. The signal is then recovered by the optical fiber is transmitted to the analyzer.

Annex 1.1.   Spectroelectrochemistry for Ru3
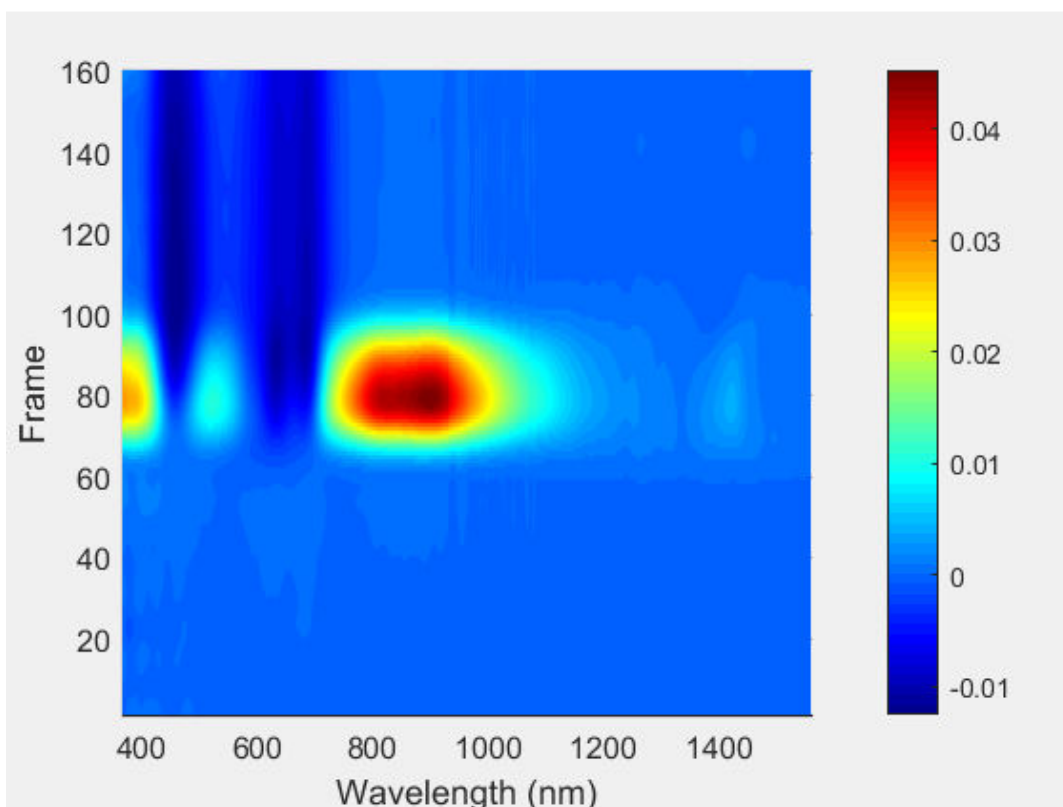
Annex 1.2.   Spectroelectrochemistry for compound 7
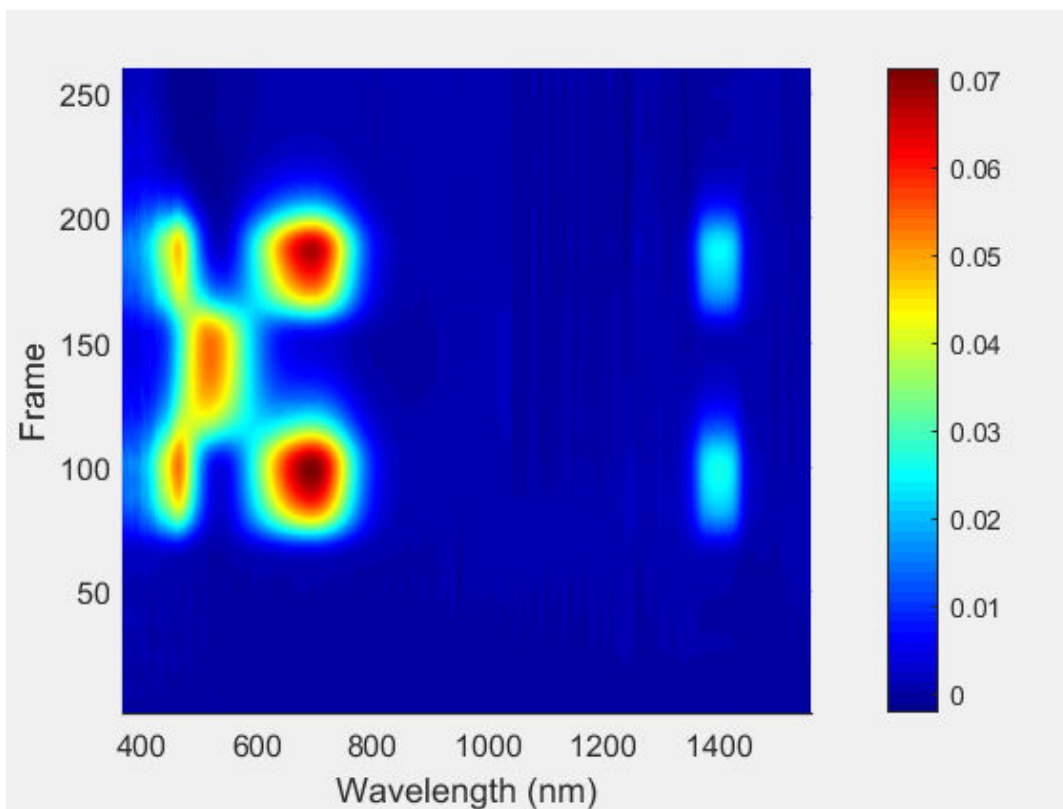
Annex 1.3. **Spectroelectrochemistry for self-assembly AA1**
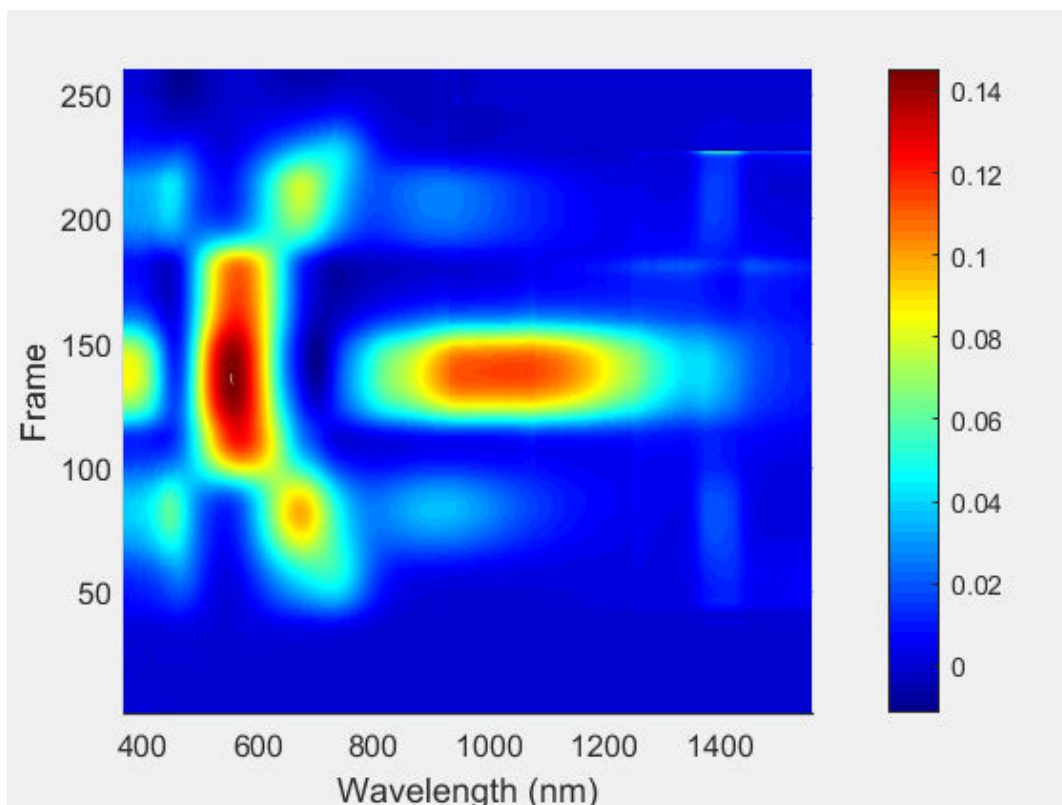
Annex 2. Electrocrystallization

Electrocrystallization allows to obtain single crystals of the oxidized compound for further applications, in our case – for x-ray diffraction analysis. Main principle is based on the slow oxidation or reduction of the electro-active molecule and generation of corresponding charge particle. The later than crystalize with counter-ions, present in solution in order to maintain conductivity.

Experiment is conducted using the standard U-shaped electrochemical cell, with compartments separated with a glass filter in order to prevent mixing and contamination while maintaining conductivity. On order to prevent impurities, cell is washed with a H_2SO_4/H_2O_2 mixture, followed by methanol, water, acetone and drying in the oven.

Pt wire with 1mm diameter and approximately ~2 cm length is used, which is also cleaned by an electrolysis in 1M H_2SO_4 and then washed with water and acetone. In order to obtain crystals of sufficient quality such parameters as concentration of the compound and supporting electrolyte, solvent, temperature and current density can be adjusted.

Table 1. Experimental conditions for **AA1** and for **S-exTTF**

| Solvent	Anion	Temperature	Current	Result
AA1				
CH_2Cl_2/MeOH	nBu$_4$NPF$_6$	20 ^{0}C	0,5 μA	dark powder precipitate
CH_2Cl_2/MeOH	nBu$_4$NClO$_4$	20 ^{0}C	0,5 μA	dark powder precipitate
CH_2Cl_2/MeOH	nBu$_4$NOf	20 ^{0}C	0,5 μA	clear solution
CH_2Cl_2/acetonitrile	nBu$_4$NPF$_6$	20 ^{0}C	0,5 μA	dark powder precipitate
CH_2Cl_2/MeOH	nBu$_4$NPF$_6$	5 ^{0}C	0,5 μA	dark powder precipitate
$C_2H_4Cl_2$/MeOH	nBu$_4$NPF$_6$	20 ^{0}C	0,5 μA	dark powder precipitate
$C_2H_4Cl_2$/MeOH	nBu$_4$NClO$_4$	5 ^{0}C	0,5 μA	dark powder precipitate
CH_2Cl_2/MeOH	nBu$_4$NPF$_6$	20 ^{0}C	0,1 μA	dark powder precipitate
$C_2H_4Cl_2$/MeOH	nBu$_4$NPF$_6$	20 ^{0}C	0,1 μA	dark powder precipitate
MeOH	nBu$_4$NPF$_6$	20 ^{0}C	0,5 μA	dark crystals
acetone	nBu$_4$NPF$_6$	20 ^{0}C	0,5 μA	clear solution
S-exTTF				
CH_2Cl_2	nBu$_4$NPF$_6$	20 ^{0}C	0,5 μA	Some crystals, structure could not be obtained
CH_2Cl_2	nBu$_4$NPF$_6$	20 ^{0}C	0,5 μA	Purple precipitate
CH_2Cl_2	nBu$_4$NClO$_4$	20 ^{0}C	0,5 μA	Purple precipitate
CH_2Cl_2	nBu$_4$NPF$_6$	10 ^{0}C	0,5 μA	Purple precipitate
THF	nBu$_4$NPF$_6$	10 ^{0}C	0,5 μA	Dark needle crystals

Annex 3. NMR spectra

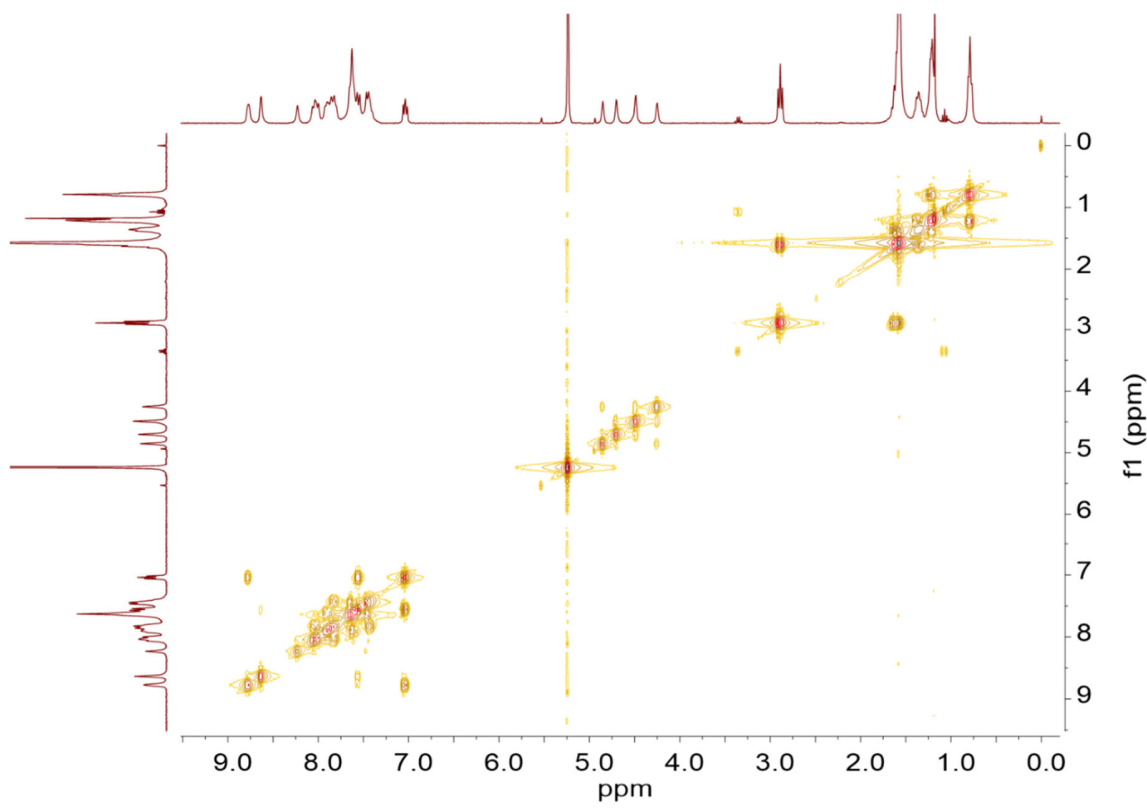### Annex 3.1. ¹H NMR for self-assembly AA2 in acetone-d₆
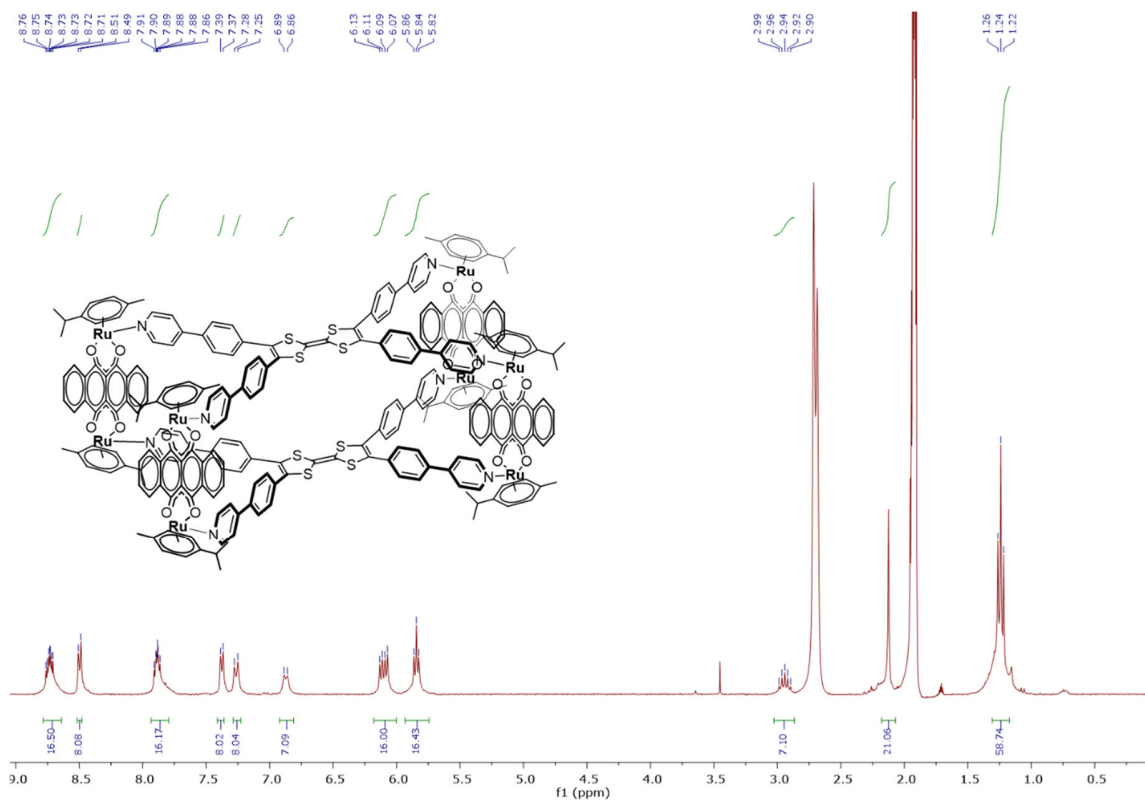
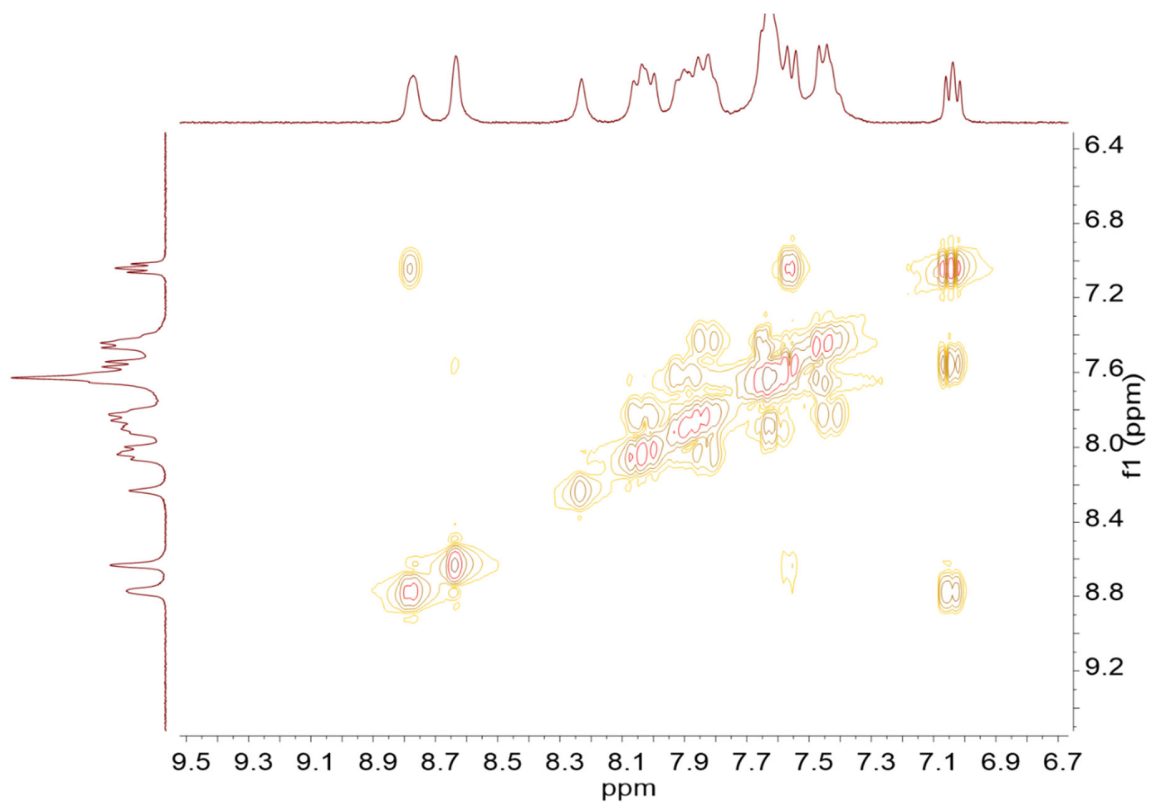### Annex 3.2. ¹H NMR for self-assembly AA3 in DMSO-d₆
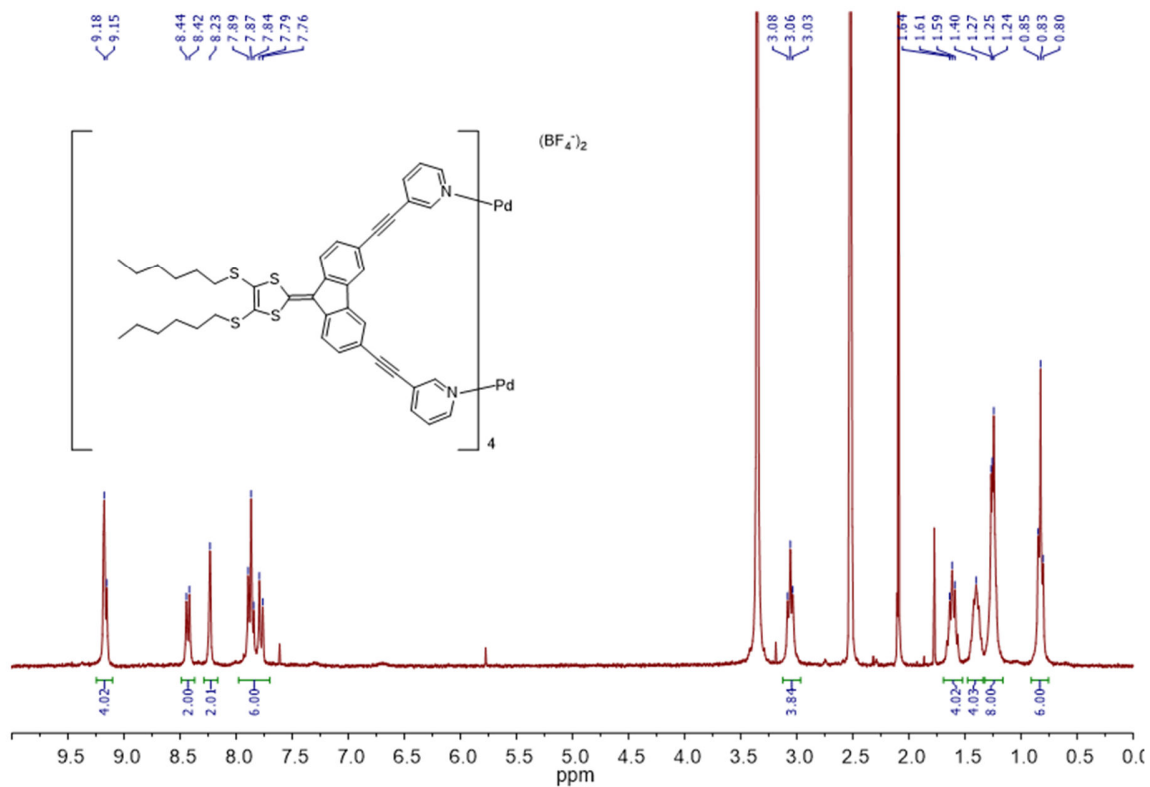
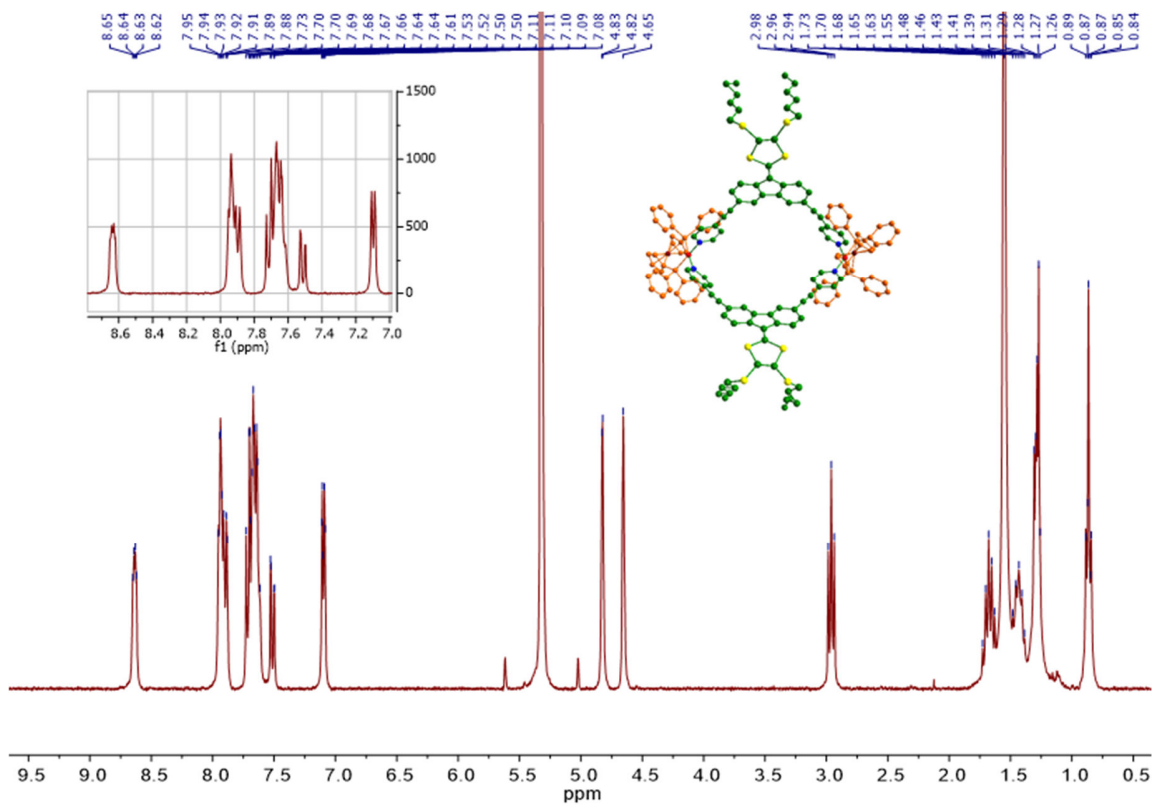**Annex 3.3.** **¹H NMR for self-assembly AA6 in CD₂Cl₂**
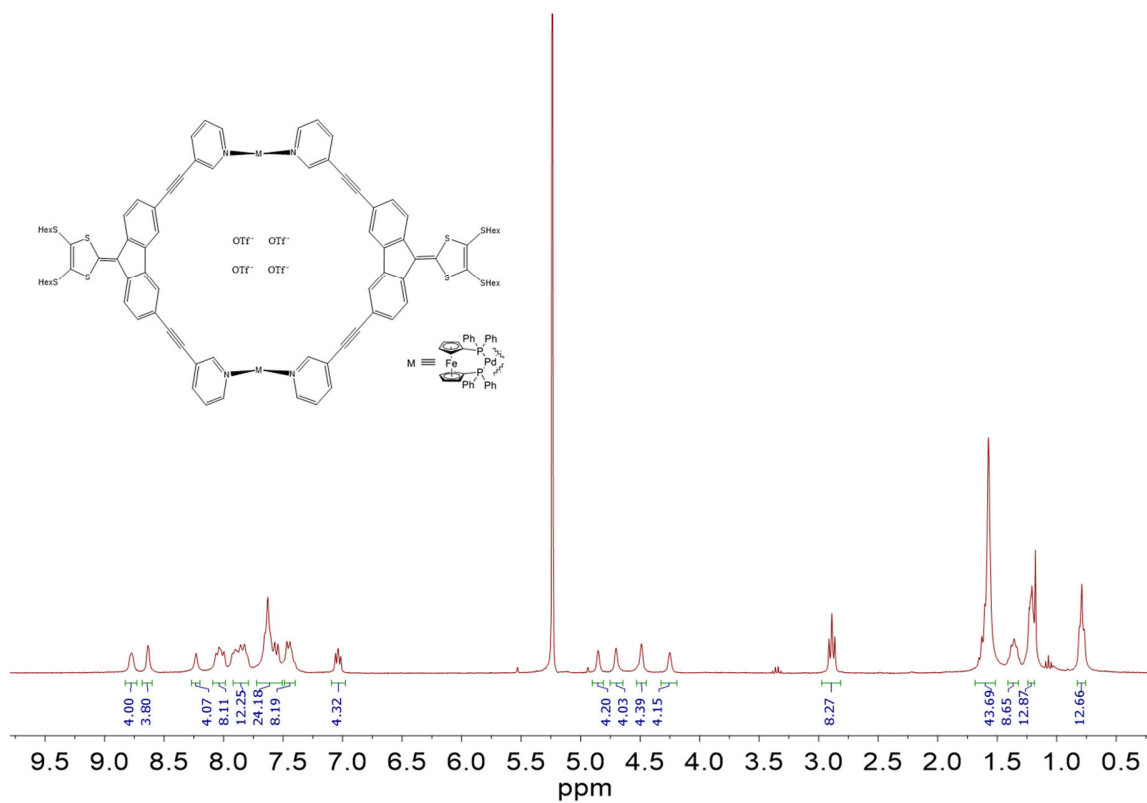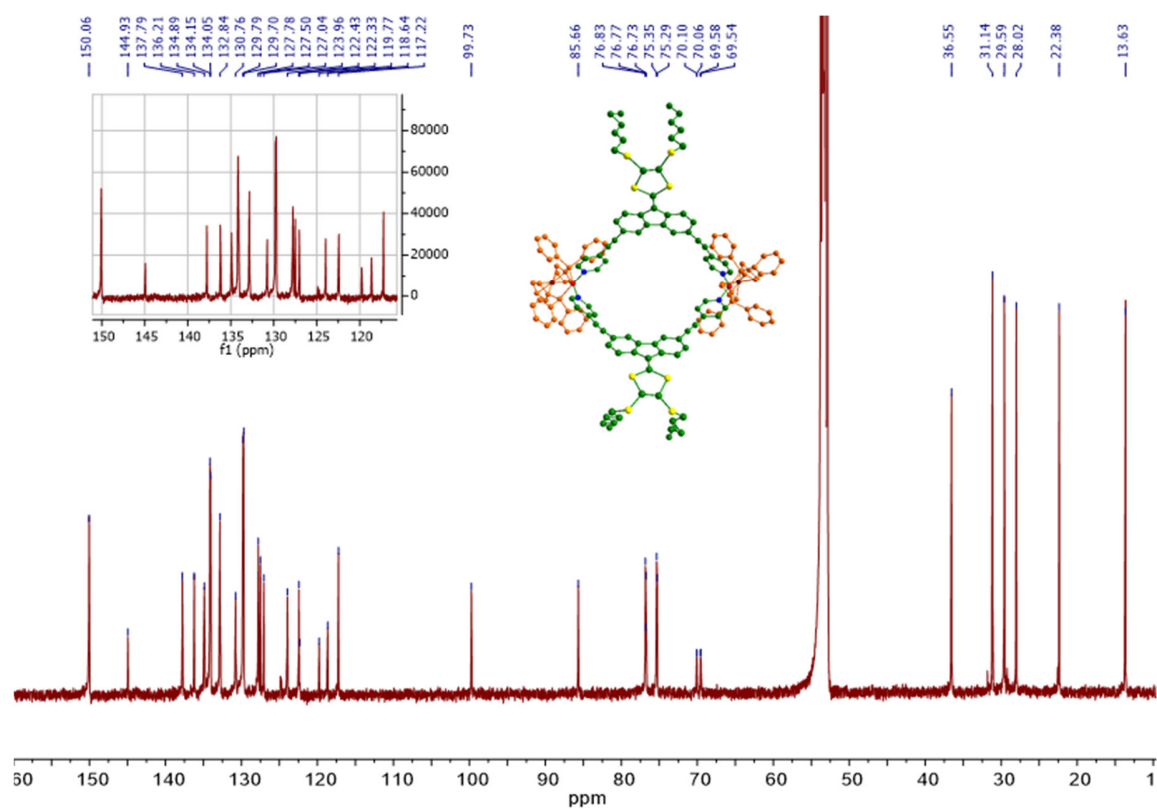

Annex 3.4. **COSY NMR for self-assembly AA6**

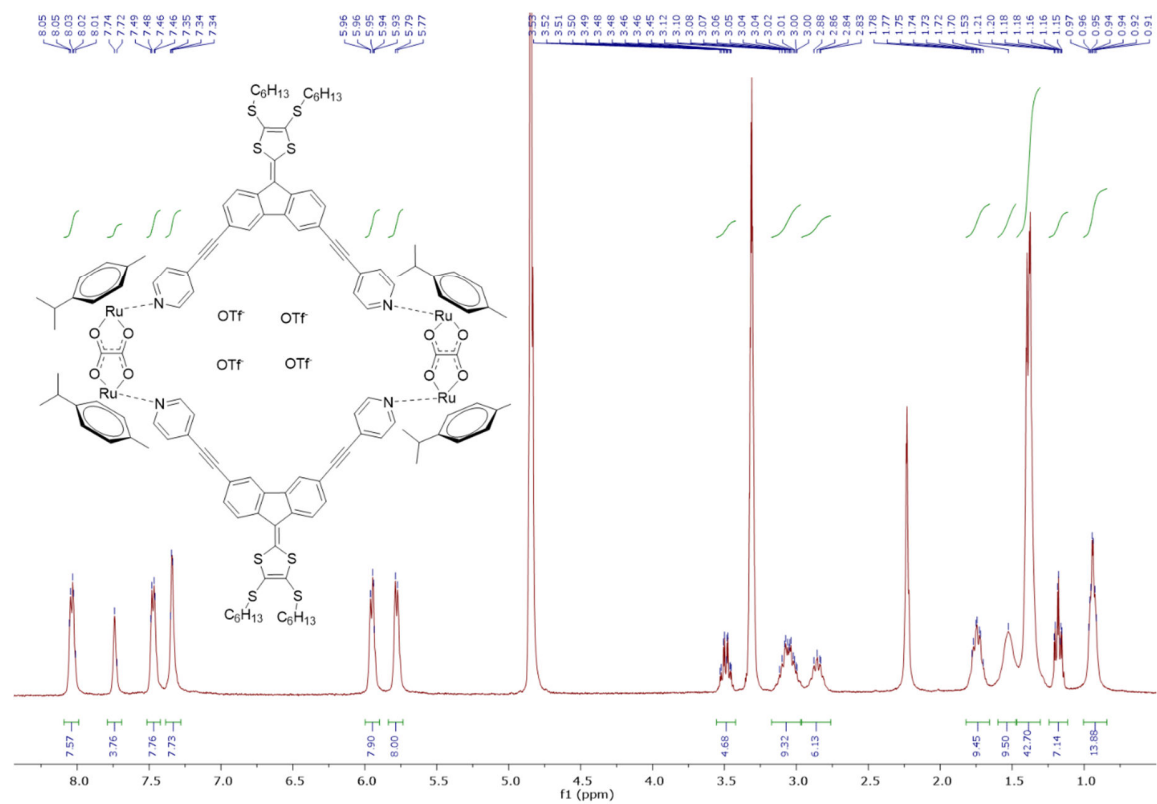**Annex 3.5.**　　　　**COSY NMR for self-assembly AA6 – aromatic region**

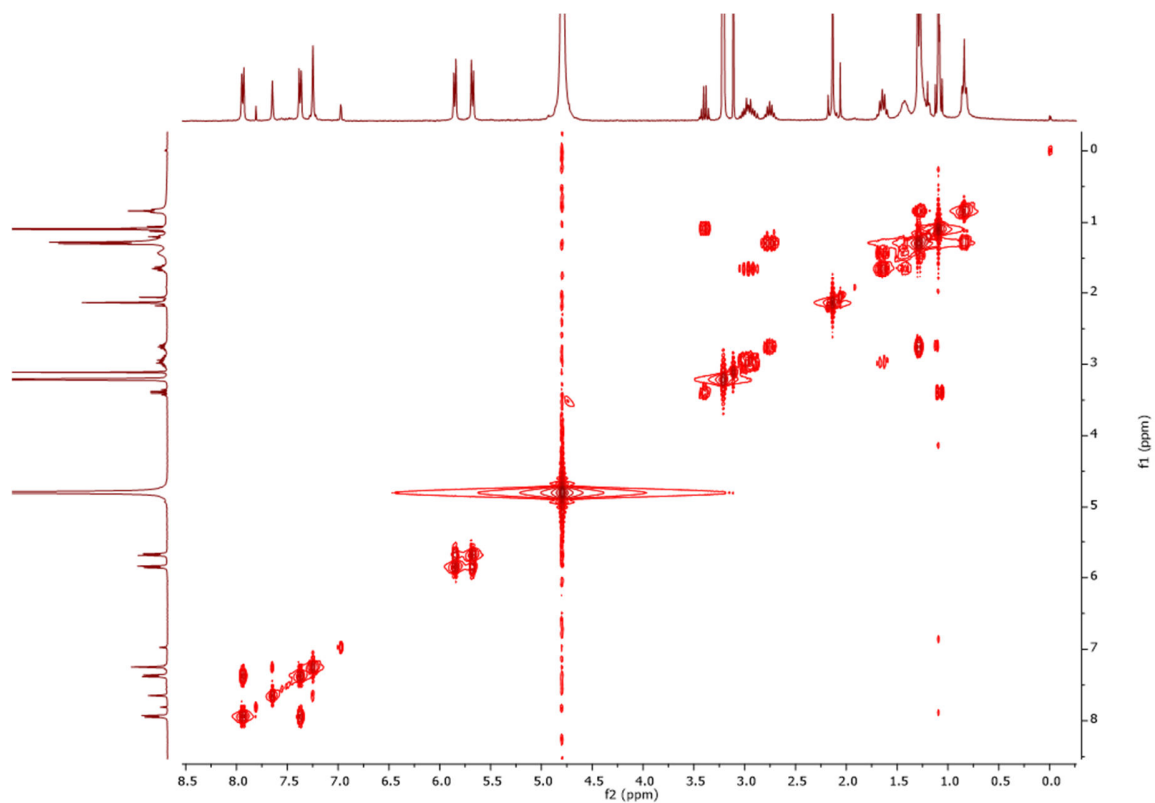**Annex 3.6.**　　　　**^{1}H NMR for self-assembly AA4 in CD$_2$Cl$_2$**

Annex 3.7. ^{13}C NMR for self-assembly AA4 in CD$_2$Cl$_2$

Annex 3.8. ^{1}H NMR for self-assembly AA8 in CD$_3$OD

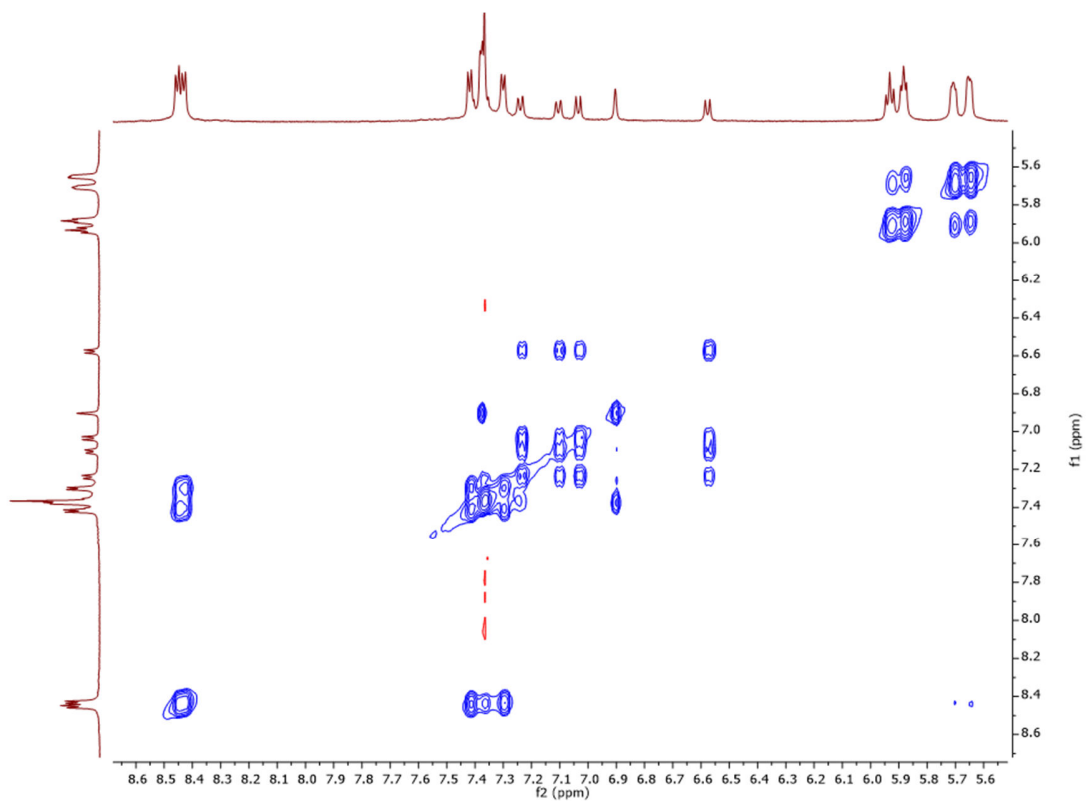**Annex 3.9.**   **COSY NMR for self-assembly AA8 in CD₃OD**

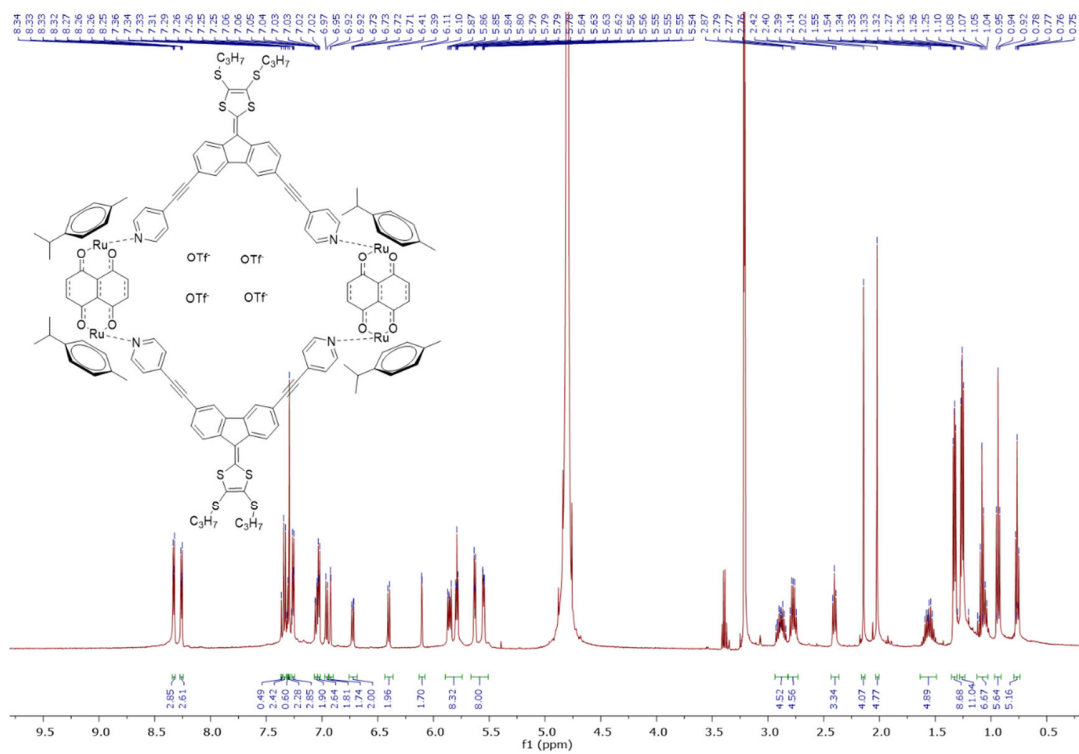**Annex 3.10.**   **¹H NMR for self-assembly AA10 in CD₃OD**
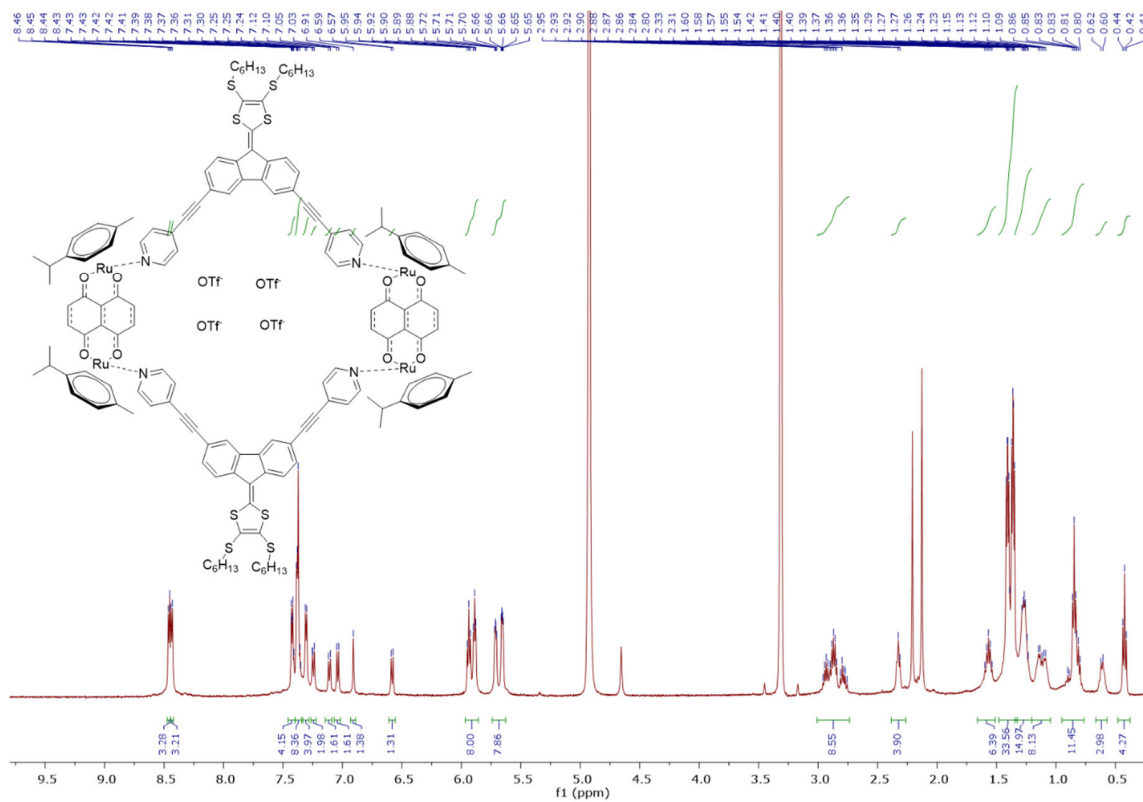
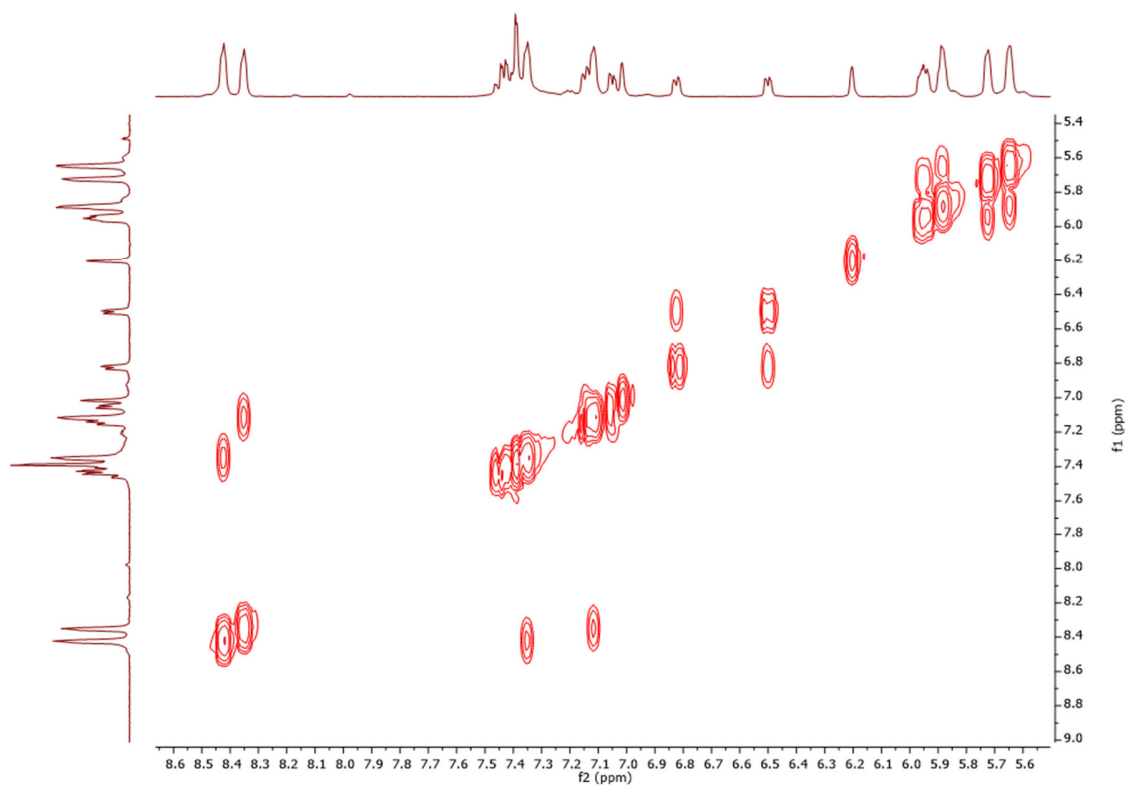**Annex 3.11.**   **COSY NMR for self-assembly AA10 in CD₃OD**
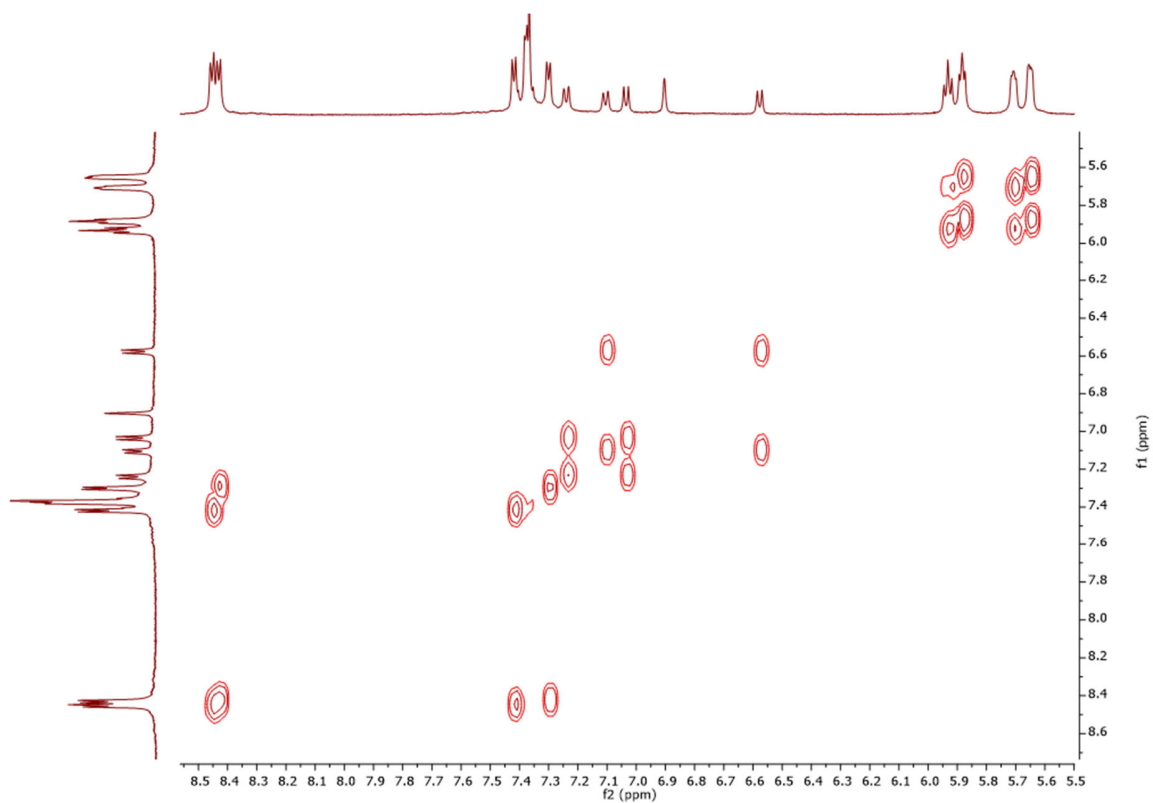
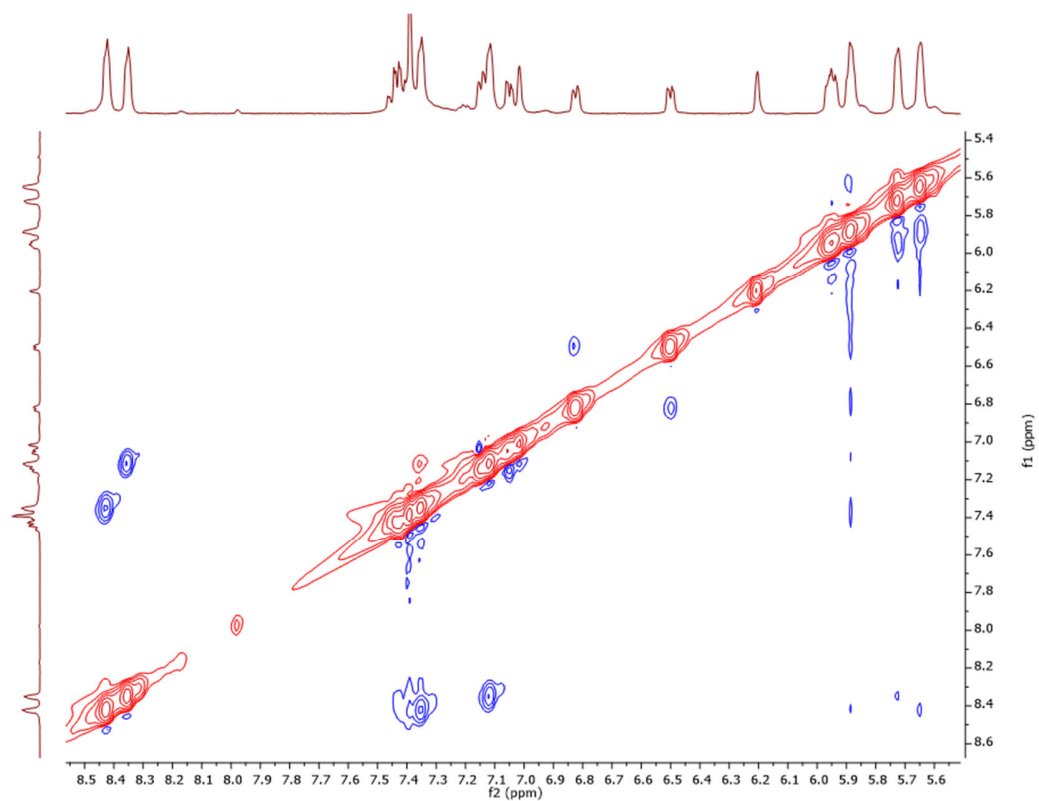**Annex 3.12.**   **ROESY NMR for self-assembly AA10 in CD₃OD**

Annex 3.13.   **^{1}H NMR for self-assembly AA11 in CD₃OD**
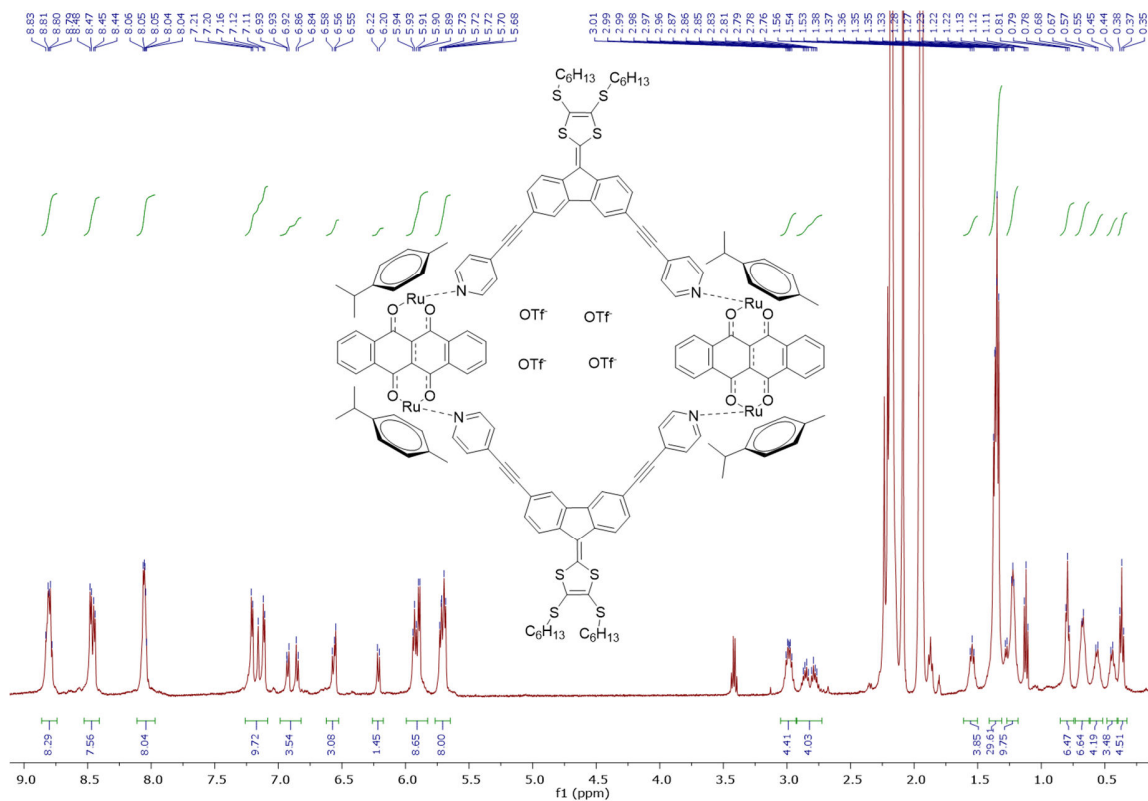
Annex 3.14.   **COSY NMR for self-assembly AA11 in CD₃OD**
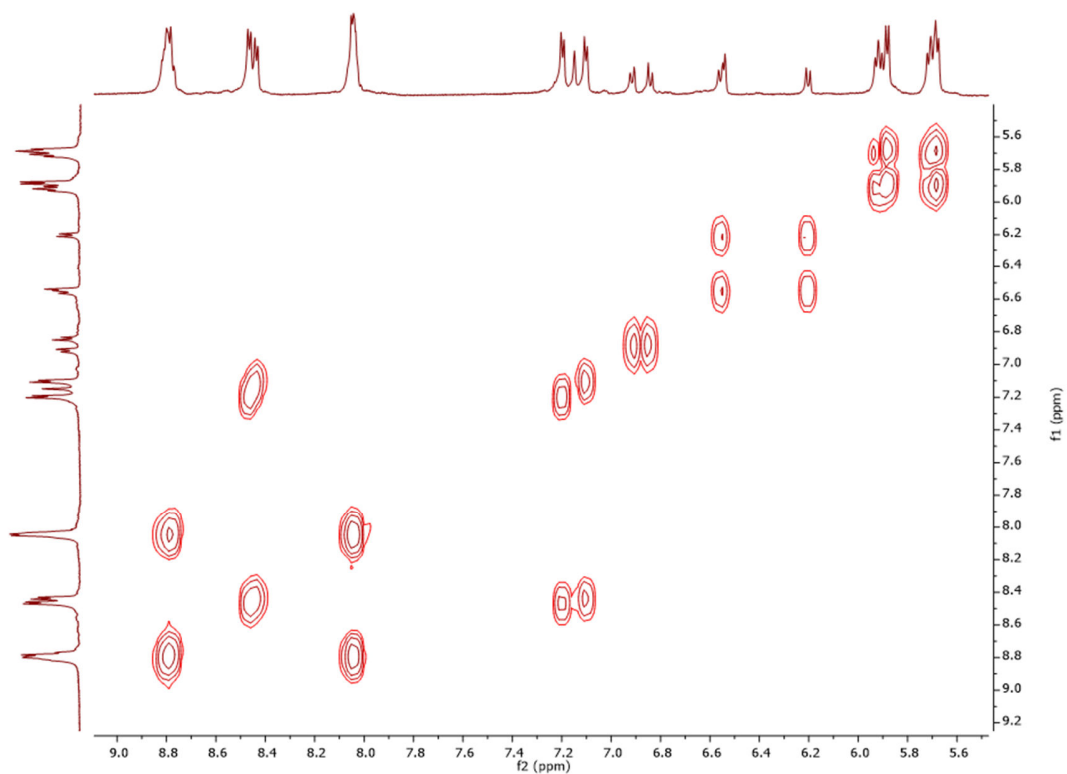

Annex 3.15.   **ROESY NMR for self-assembly AA11 in CD₃OD**
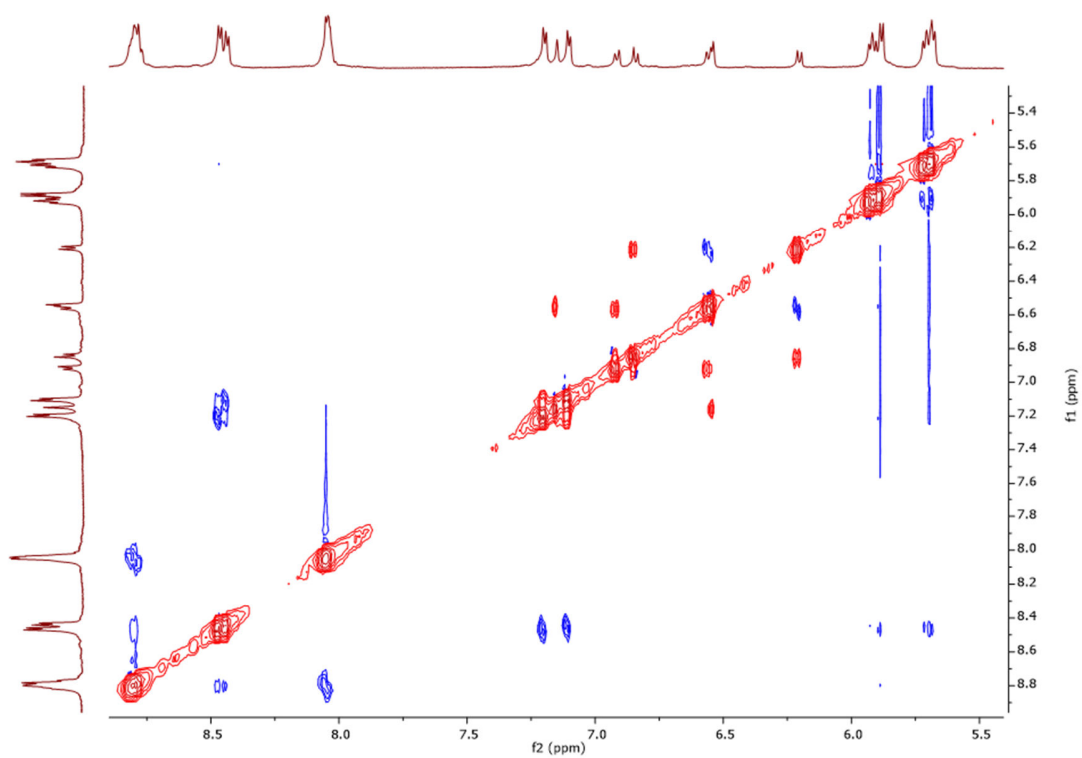
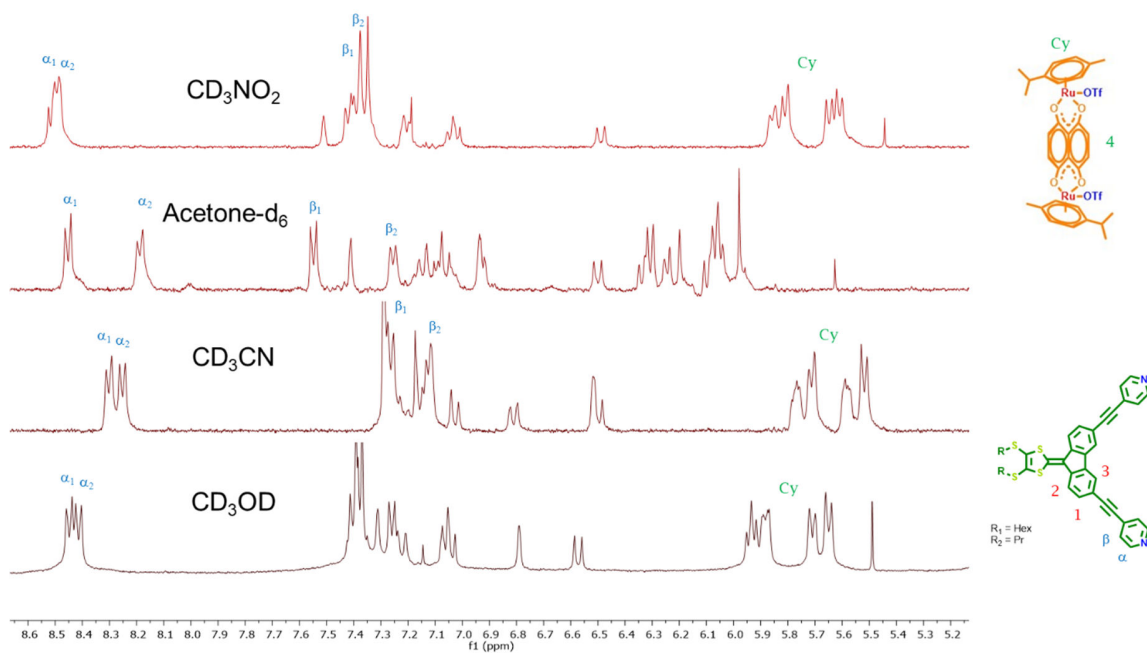**Annex 3.16.** ^{1}H NMR for self-assembly AA12 in CD$_3$CN

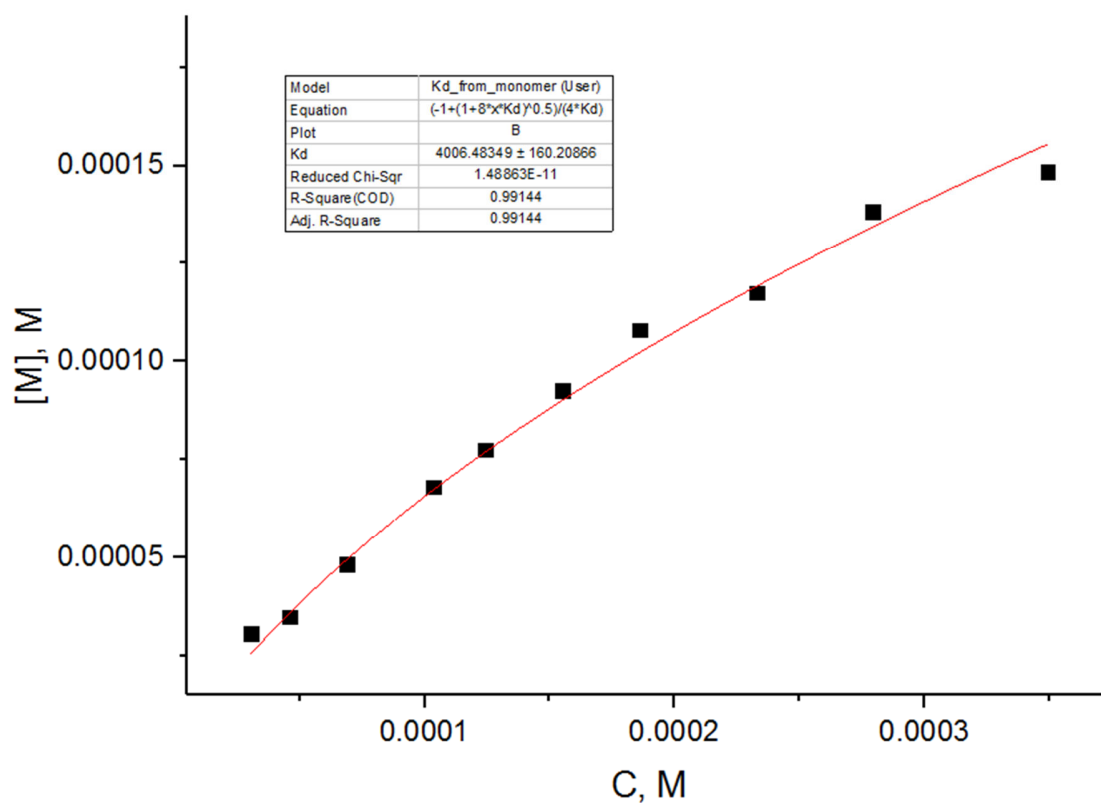**Annex 3.17.** COSY NMR for self-assembly AA12 in CD$_3$CN

Annex 3.18. **ROESY NMR for self-assembly AA12 in CD₃CN**

Annex 3.19. **¹H NMR for self-assembly AA10 in different solvents**

Annex 3.20.   **Fit for association constant using NMR data for self-assembly AA11**

Model	Kd_from_monomer (User)
Equation	(-1+(1+8*x*Kd)^0.5)/(4*Kd)
Plot	B
Kd	4006.48349 ± 160.20866
Reduced Chi-Sqr	1.48863E-11
R-Square (COD)	0.99144
Adj. R-Square	0.99144

Annex 3.21.   **^{1}H NMR for self-assembly AA14 in CDCl$_3$**

Annex 3.22. **COSY NMR for self-assembly AA14 in CDCl₃**

*

Annex 3.23. **NOESY NMR for self-assembly AA14 in CDCl₃**

159

Annex 3.24. ¹H NMR for self-assembly AA15 in CDCl₃
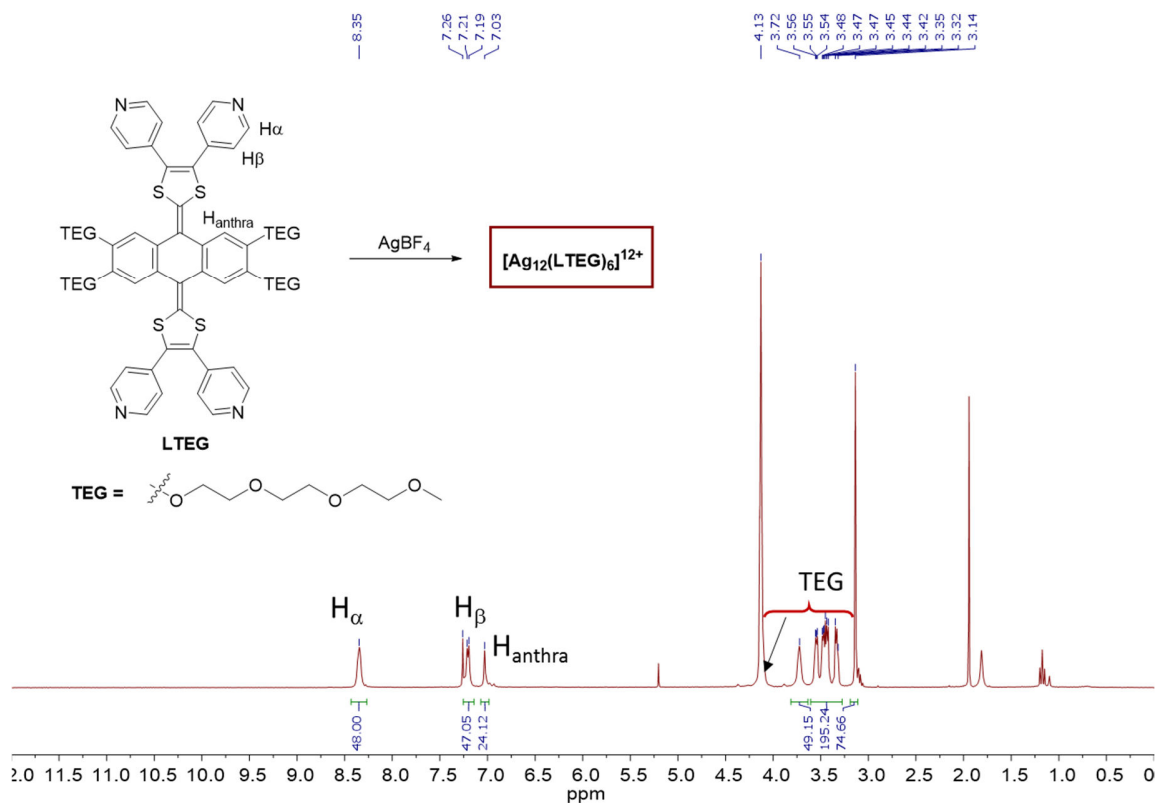
Annex 3.25. COSY NMR for self-assembly AA15 in CDCl₃

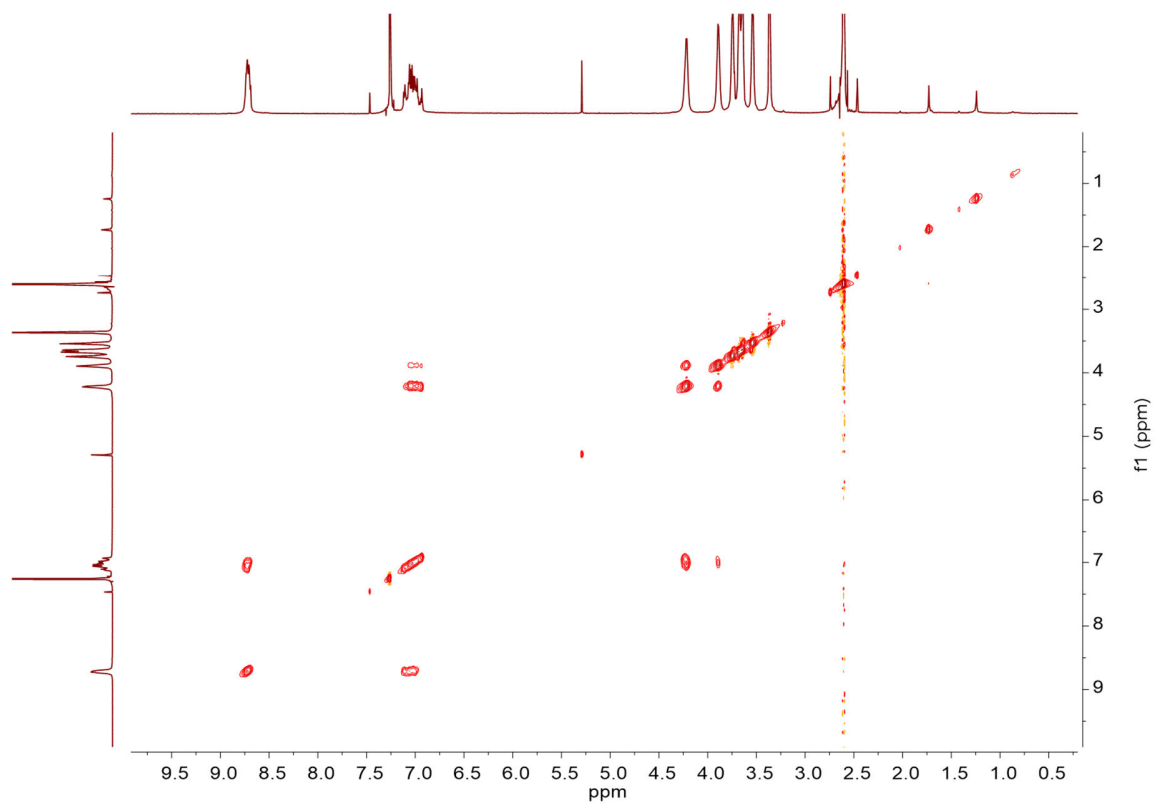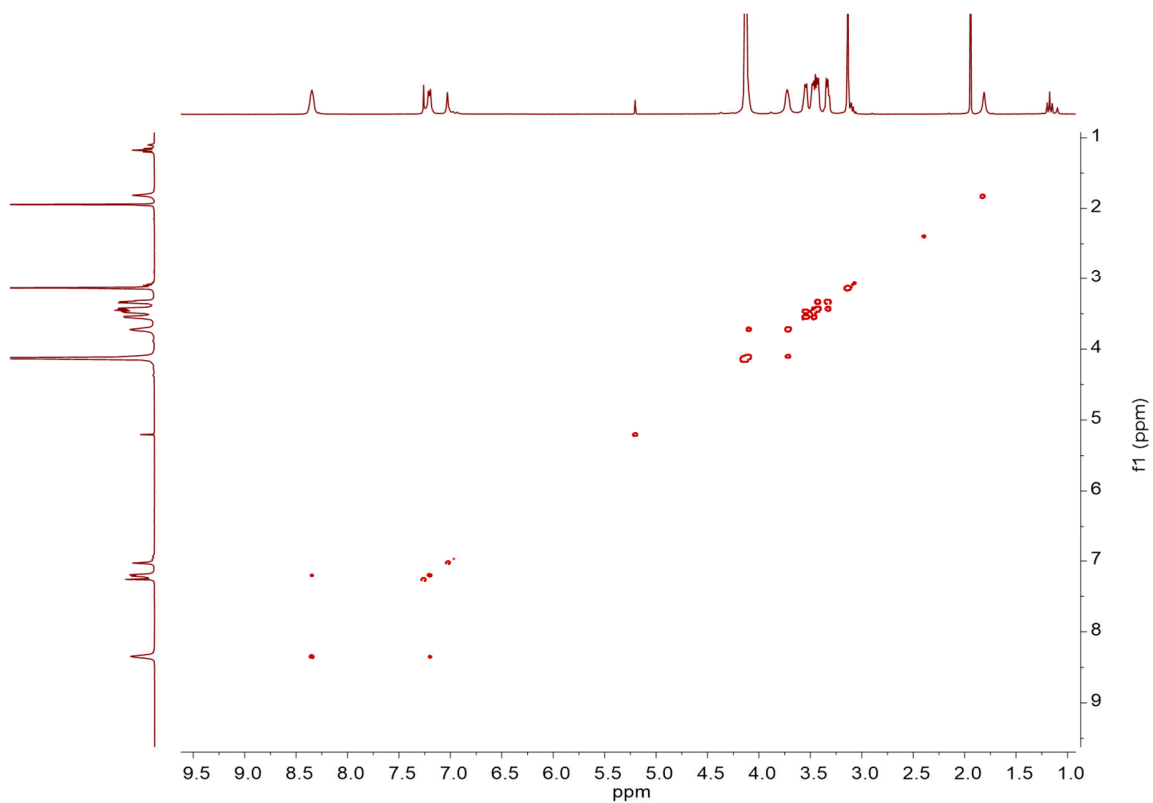**Annex 3.26.**   **NOESY NMR for self-assembly AA15 in CDCl₃**
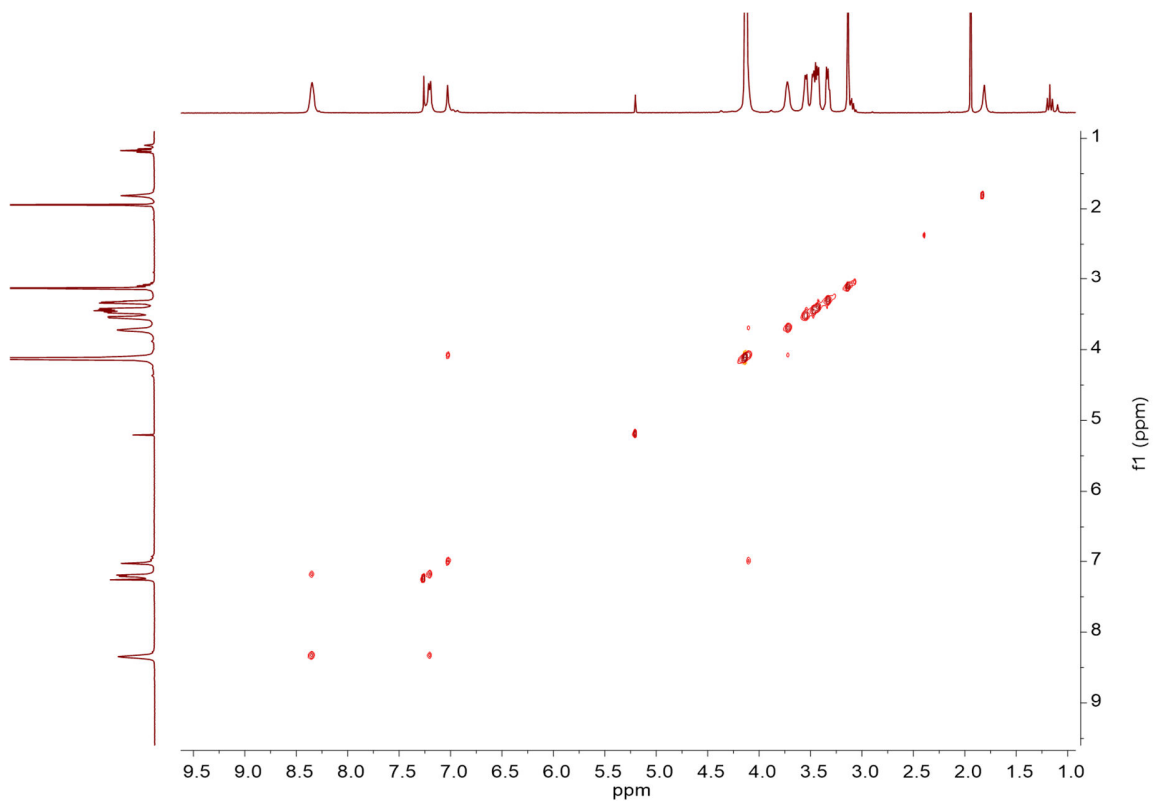
Annex 3.27.   **¹H NMR for ligand exTTF-TEG with 4 eq. of AgBF₄ in CD₃CN**
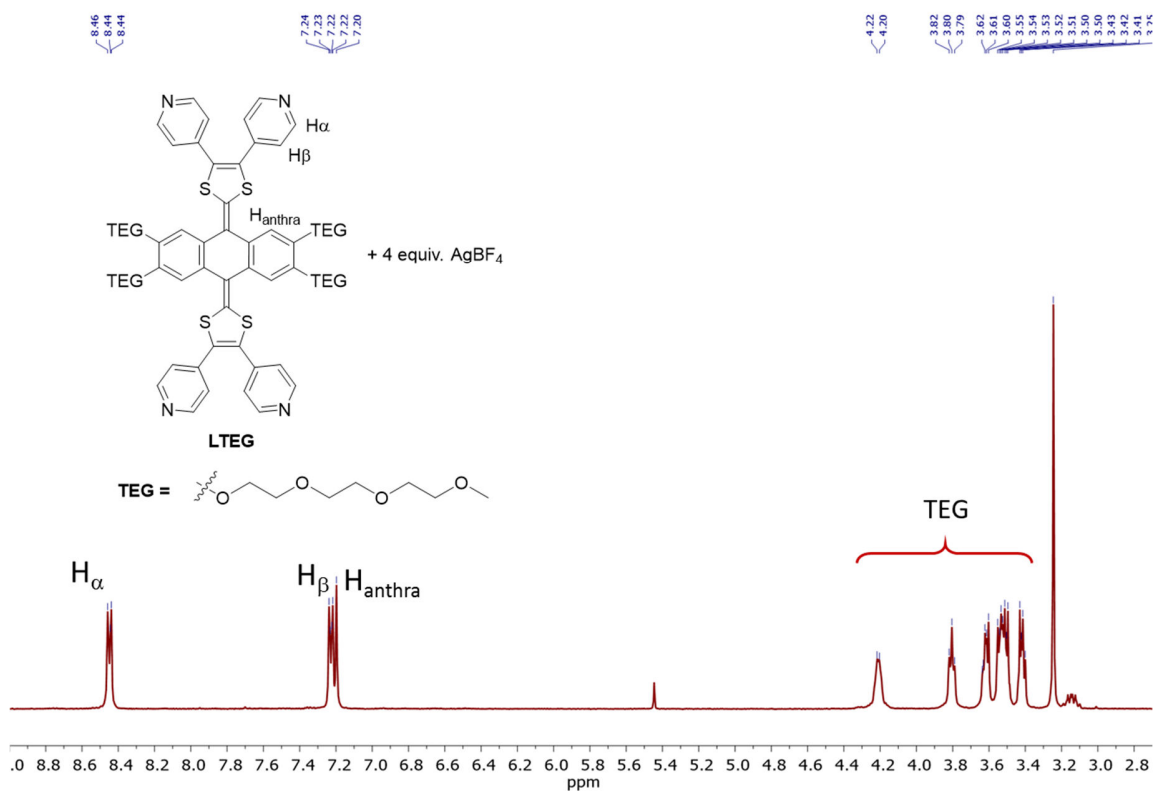
Annex 3.28. **DOSY NMR for ligand exTTF-TEG with 4 eq. of AgBF₄ in CD₃CN**
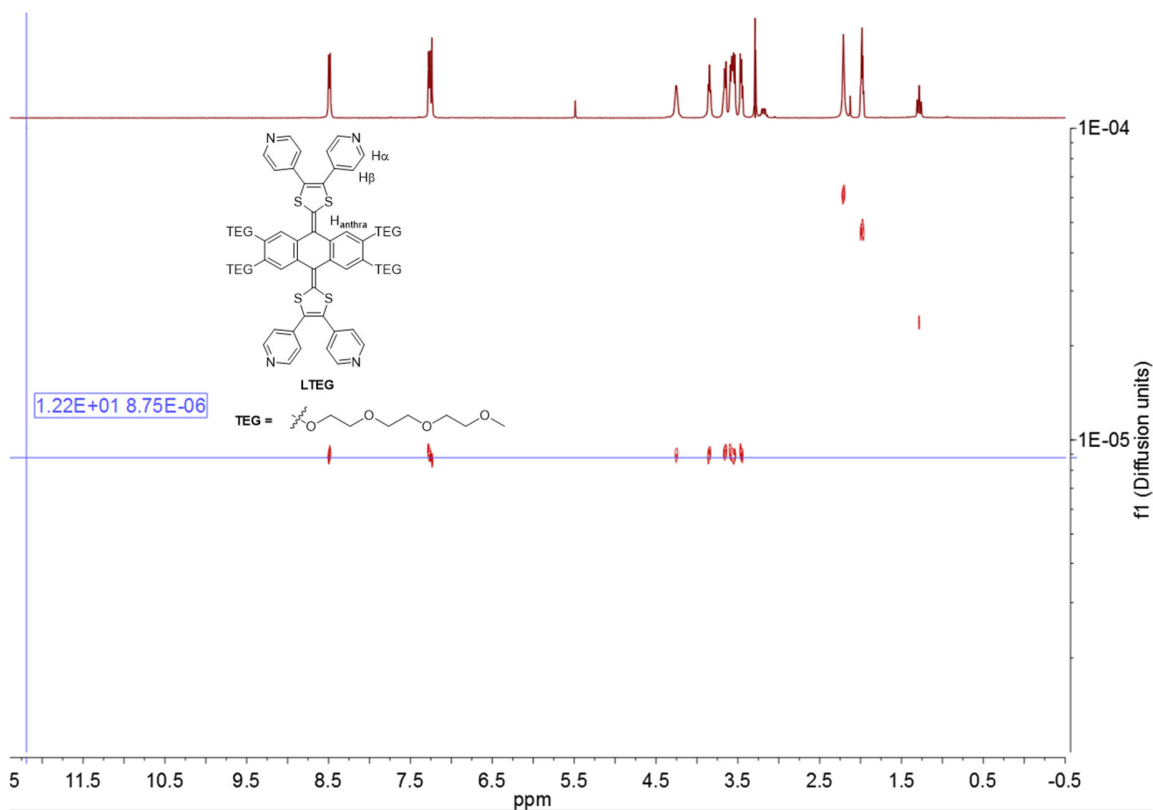
Annex 3.29. **¹H NMR for compound 30 (S-exTTF) in CD₂Cl₂**

Annex 3.30. ¹³C NMR for compound 30 (S-exTTF) in CD₂Cl₂

Annex 4.   IR spectra

Annex 4.1.   IR spectra for ligand TTF (4PyPh)₄
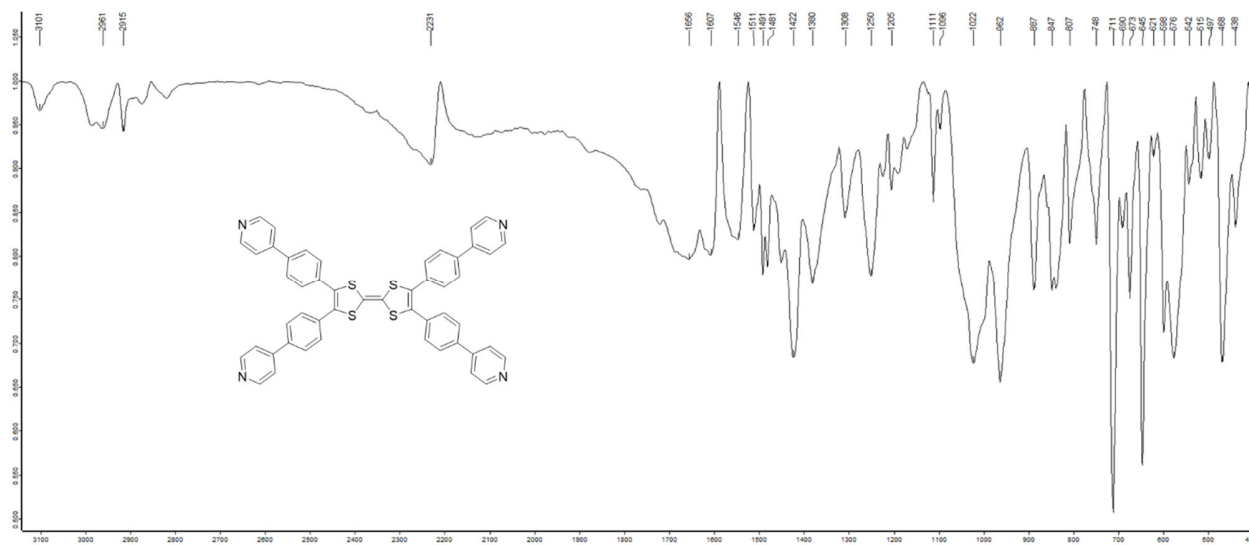
Annex 4.2.   IR spectra for ligand 25

164
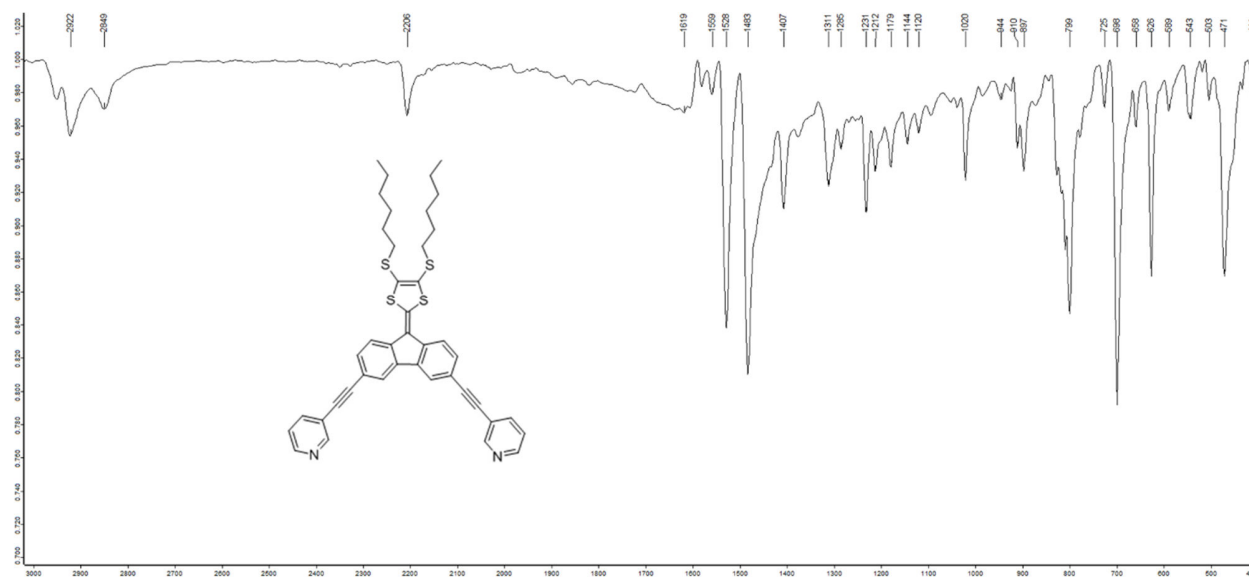
Annex 4.3.   IR spectra for $[(Ag_2exTTF\text{-}TEG^{2+})^{2+}]_x$
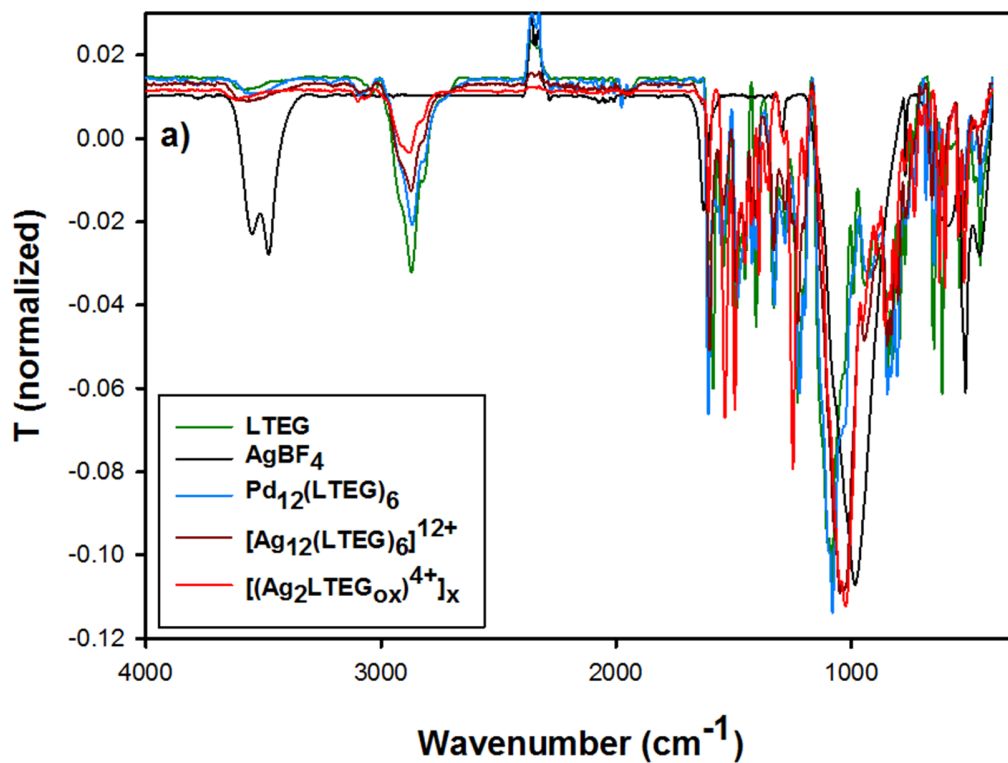
Annex 4.4.   IR spectra for $[(Ag_2exTTF\text{-}TEG^{2+})^{2+}]_x$
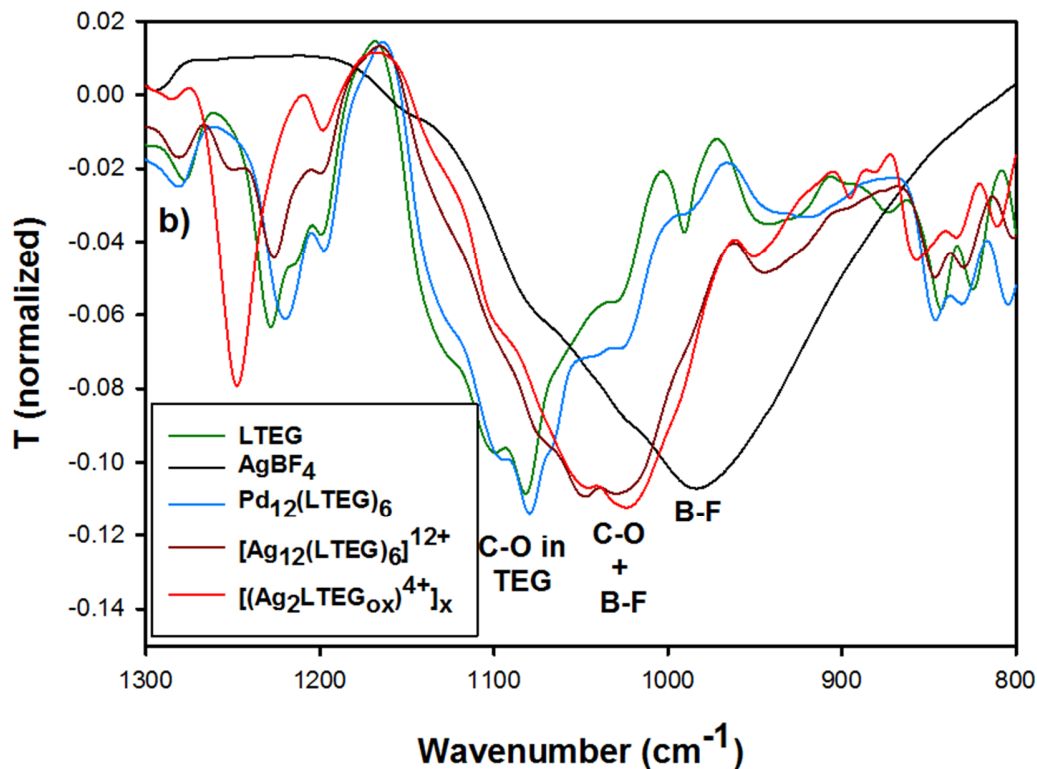
Annex 5.   HRMS

Annex 5.1.   ESI-FTCIR for self-assembly AA7 in CH₂Cl₂.
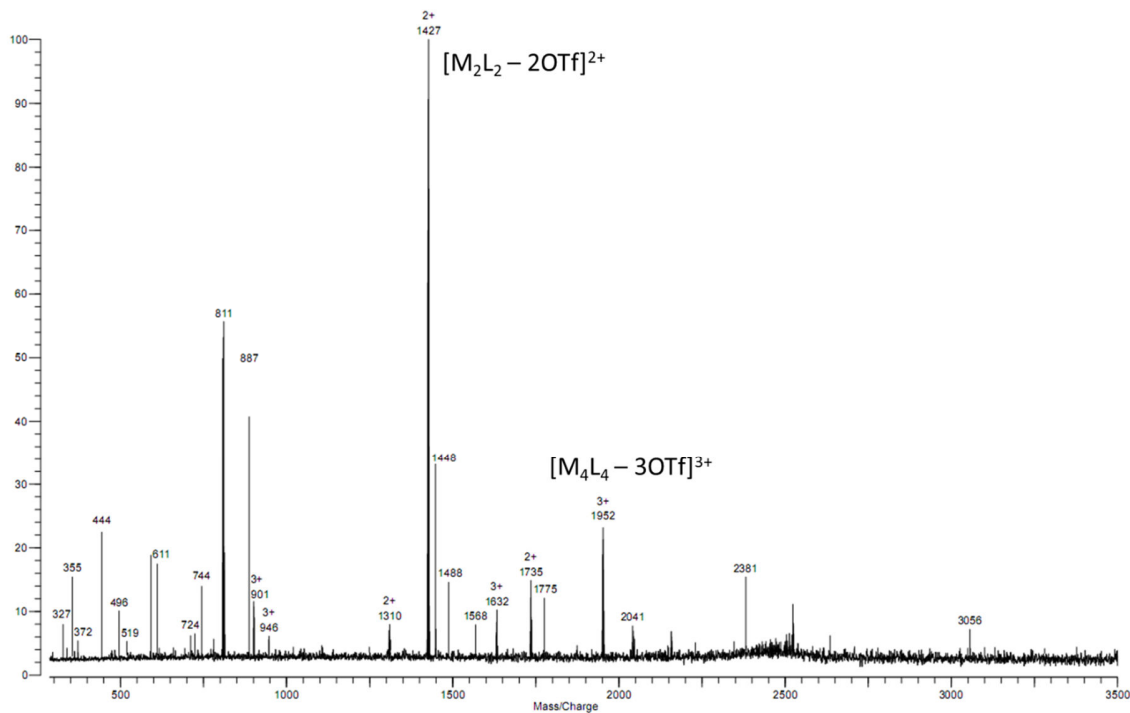
Annex 5.2.   ESI-FTCIR for self-assembly AA8 in methanol.
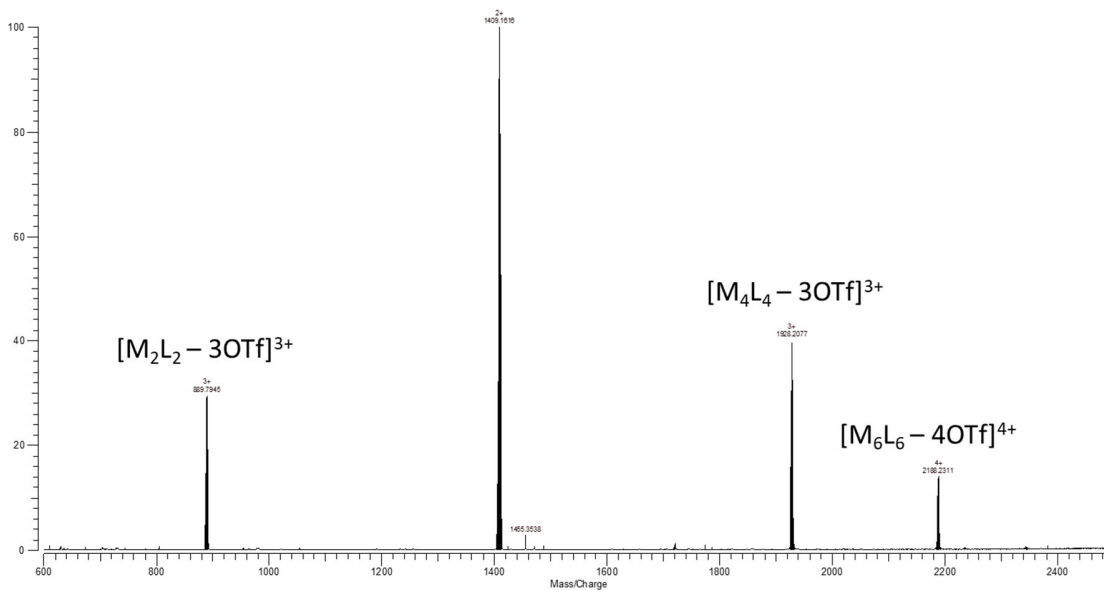
Annex 5.3. **ESI-FTCIR for self-assembly AA10 in methanol.**
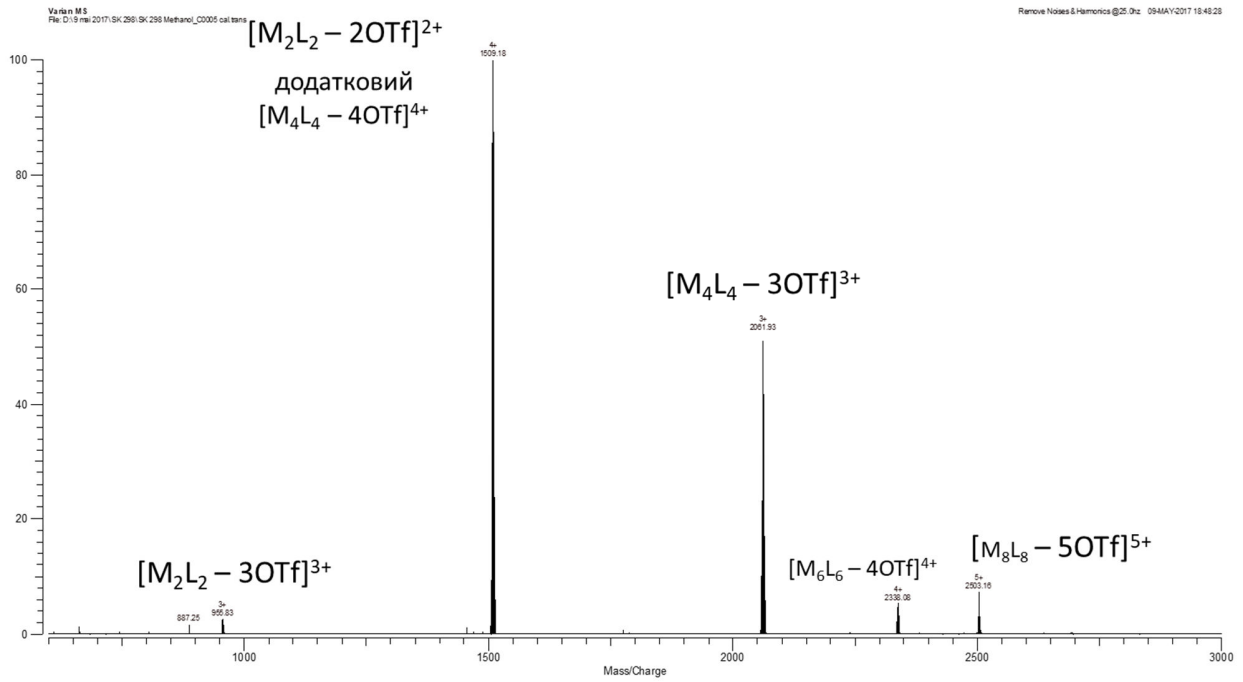
Annex 5.4. **ESI-FTCIR for self-assembly AA12 in methanol.**
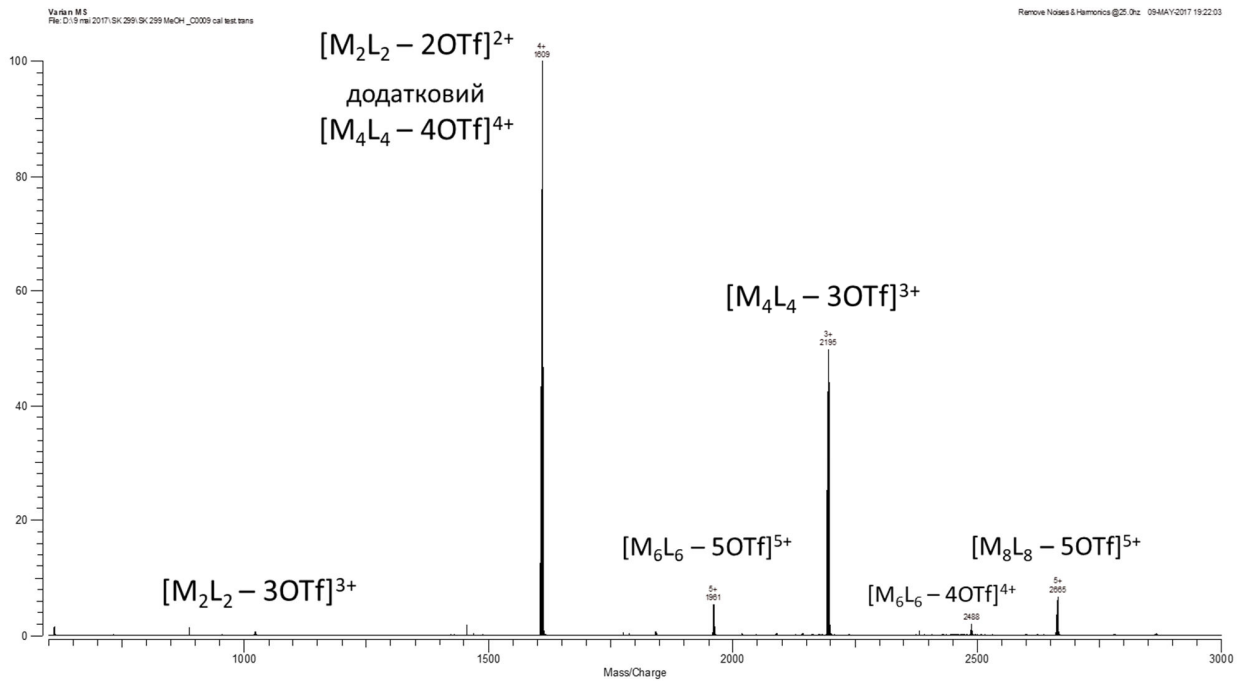
Annex 6. X-ray data

Annex 6.1. X-ray data for self-assembly TTF(PhPy)$_4$

Empirical formula	$C_{105}H_{84}N_8O_5S_8$, 2 ($C_{50}H_{32}N_4S_4$), 5 (CH_4O)
Formula weight, mr	1794.28
Temperature	250(2) K
Wavelength	0.71073 Å
Crystal system, space group	Monoclinic, P 21/c
Unit cell dimensions	a = 20.340(5) Å α = 90^0 b = 5.3607(6) Å β = 113.09(2)^0 c = 21.704(4) Å γ = 90^0
Volume, V	2176.9(7) Å^3
Number of molecules, z	1
Calculated density, ρ	1.369 mg/m^3
Absorption coefficient	0.268 mm^{-1}
F(000)	938
Crystal size	0.3 x 0.25 x 0.13 mm
Θ range for data collection	2.18 to 26.61^0
Limiting indices	- 25<=h<=22, - 6<=k<=6, - 24<=l<=26
Reflections collected / unique	29430 / 4364 [R(int) = 0.0577]
Completeness to θ = 25.00	98.4 %
Absorption correction	Semi-empirical from equivalents
Max. and min. transmission	0.966 and 0.660
Refinement method	Full-matrix least-squares on F^2
Data / restraints / parameters	4364 / 0 / 336
Goodness-of-fit on, F2	1.079
Final R indices [I>2σ(I)]	R1 = 0.0732, wR2 = 0.2072 [2593 Fo]
R indices (all data)	R1 = 0.1143, wR2 = 0.2389
Largest diff. peak and hole	0.460 and -0.301 e.Å^{-3}

Taux d'occupation des atomes:

τ C6A, H6A, C7A, H7A, C9A, H9A, C10A, H10A = 0.68

τ C6B, H6B, C7B, H7B, C9B, H9B, C10B, H10B = 0.32

τ C17A, H17A, C18A, H18A, C20A, H20A, C21A, H21A = 0.53

τ C17B, H17B, C18B, H18B, C20B, H20B, C21B, H21B = 0.47
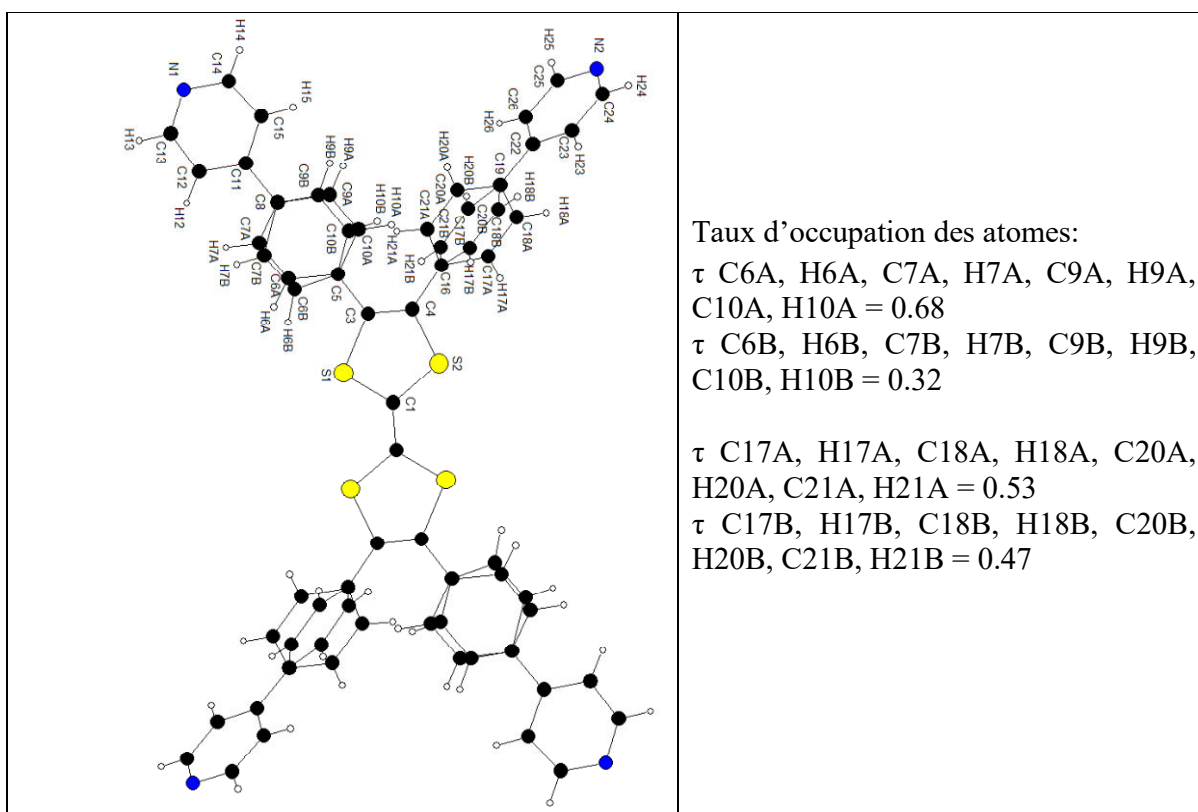
Annex 6.2. **X-ray data for self-assembly AA1**

Empirical formula	$C_{234}H_{216}F_{24}N_8O_{46}Ru_8S_{16}$
Formula weight, *mr*	5653.66
Temperature	150.0(1) K
Wavelength	1.54184 Å
Crystal system, space group	Triclinic, P -1
Unit cell dimensions	a = 20.4033(18) Å α= 77.017(5)^0 b = 25.5763(15) Å β= 69.854(7)^0 c = 26.2645(15) Å γ= 77.969(6)^0
Volume, *V*	12409.1(16) Å^3
Number of molecules, *z*	2
Calculated density, ρ	1.513 mg/m^3
Absorption coefficient	5.867 mm^{-1}
F(000)	5736
Crystal size	0.352 x 0.094 x 0.044 mm
Θ range for data collection	2.729 to 74.887^0
Limiting indices	-25<=h<=24, -31<=k<=31, -32<=l<=27

Reflections collected / unique	90746 / 46952 [R(int) = 0.1461]
Completeness to θ = 67.684	98.5 %
Absorption correction	Semi-empirical from equivalents
Max. and min. transmission	1.00000 and 0.62323
Refinement method	Full-matrix least-squares on F^2
Data / restraints / parameters	46952 / 139 / 1963
Goodness-of-fit on, F2	0.967
Final R indices [$I>2\sigma(I)$]	R1 = 0.1562, wR2 = 0.3888 [12655 Fo]
R indices (all data)	R1 = 0.2618, wR2 = 0.4467
Largest diff. peak and hole	2.803 and -1.229 e.Å^{-3}
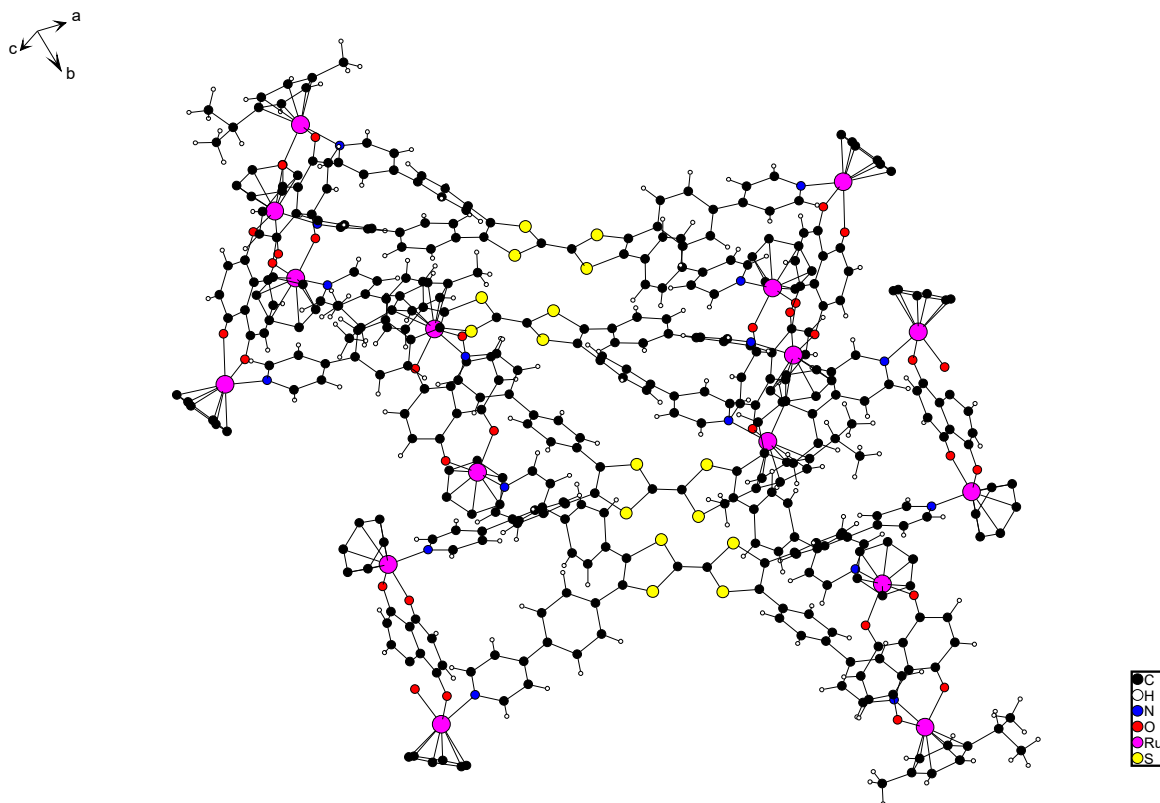
Annex 6.3.   X-ray data for ligand 25 (3Py-DTF-SHex)

Empirical formula	$C_{42}H_{40}N_2S_4$
Formula weight, mr	701.00
Temperature	293.0(1) K
Wavelength	1.54184 Å
Crystal system, space group	Tetragonal, P 4/n

Unit cell dimensions	a = 37.5699(7) Å α = 90 °
	b = 37.5699(7) Å β = 90 °
	c = 5.3064(1) Å γ = 90 °
Volume, V	7490.0(2) Å^3
Number of molecules, z	8
Calculated density, ρ	1.243 mg/m^3
Absorption coefficient	2.566 м$^{-1}$
F(000)	2960
Crystal size	0.3043 x 0.0726 x 0.0565 mm
Θ range for data collection	3.33 to 75.35 °
Limiting indices	-27<=h<=36, -46<=k<=44, -4<=l<=6
Reflections collected / unique	15624 / 7536 [R(int) = 0.0293]
Completeness to θ = 73.00	98.5 %
Absorption correction	Semi-empirical from equivalents
Max. and min. transmission	1.00000 and 0.65930
Refinement method	Full-matrix least-squares on F²
Data / restraints / parameters	7536 / 13 / 435
Goodness-of-fit on, F2	1.057
Final R indices [$I>2\sigma(I)$]	R1 = 0.0727, wR2 = 0.2050 [5562 Fo]
R indices (all data)	R1 = 0.0944, wR2 = 0.2286
Largest diff. peak and hole	0.517 and -0.471 e. Å^{-3}
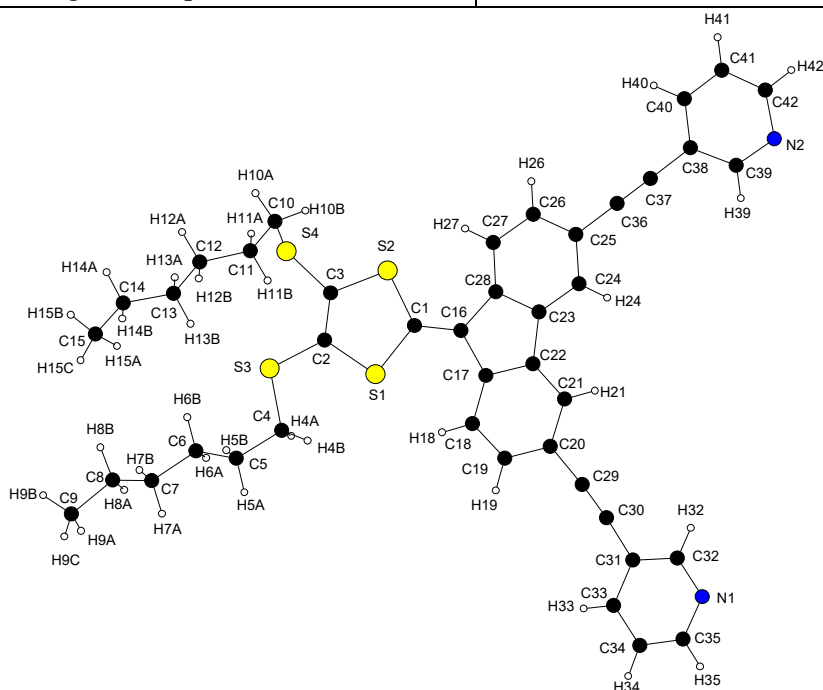
Annex 6.4.   **X-ray data for ligand 27 (3Py-DTF-SPr)**

Empirical formula	$C_{145}H_{114}Cl_2N_8S_{16}$ or 4 ($C_{36}H_{28}N_2S_4$), CH_2Cl_2
Formula weight, mr	2552.30
Temperature	149.3(4) K
Wavelength	1.54184 Å
Crystal system, space group	Monoclinic, I 2/a
Unit cell dimensions	a = 27.9519(10) Å α = 90^0 b = 5.3827(2) Å β = $105.354(4)^0$ c = 44.054(2) Å γ = 90^0
Volume, V	6391.7(5) Å^3
Number of molecules, z	2
Calculated density, ρ	1.326 mg/m^3
Absorption coefficient	3.332 mm^{-1}
F(000)	2660
Crystal size	0.434 x 0.214 x 0.052 mm
Θ range for data collection	3.279 to 73.147^0
Limiting indices	-31<=h<=34, -6<=k<=6, -54<=l<=54
Reflections collected / unique	23074 / 6302 [R(int) = 0.0367]
Completeness to θ = 73.147	98.3 %
Absorption correction	Semi-empirical from equivalents
Max. and min. transmission	1.00000 and 0.55620
Refinement method	Full-matrix least-squares on F²
Data / restraints / parameters	6302 / 0 / 403
Goodness-of-fit on, F2	1.052
Final R indices [$I>2\sigma(I)$]	R1 = 0.0445, wR2 = 0.1242 [5807 Fo]
R indices (all data)	R1 = 0.0475, wR2 = 0.1281
Largest diff. peak and hole	0.423 and -0.391 e.Å^{-3}
	Taux d'occupation des atomes: -τ C33A,H33A, H33B, H33C, H32A, H32B =0.52 -τ C33B, H33D, H33E, H33F, H32C, H32D = 0.48 -τ C36A, H36A, H36B, H36C, H35A, H35B = 0.69 -τ C36B, H36D, H36E, H36F, H35C, H35D = 0.31
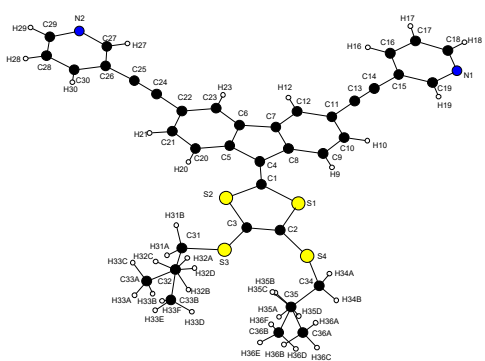
Annex 6.5. **X-ray data for self-assembly AA3**

Empirical formula	$C_{100}H_{128}B_2F_8N_4O_8PdS_{16}$ or $C_{84}H_{80}N_4PdS_8$, $2(BF_4)$, $8(C_2H_6SO)$
Formula weight, mr	2307.04
Temperature	120(1) K
Wavelength	0.67221 Å
Crystal system, space group	Triclinic, P -1
Unit cell dimensions	a = 17.4676(7) Å α = 74.016(4)^0 b = 17.8158(6) Å β = 67.644(4)^0 c = 20.0640(10) Å γ = 89.049(3)^0
Volume, V	5524.0(4) Å^3
Number of molecules, z	2
Calculated density, ρ	1.387 mg/m^3
Absorption coefficient	0.412 mm^{-1}
F(000)	2408
Crystal size	0.12 x 0.10 x 0.06 mm
Θ range for data collection	1.558 to 32.304^0
Limiting indices	-27<=h<=27, -27<=k<=26, -31<=l<=31
Reflections collected / unique	68110 / 68110 [R(int) = 0.0000]
Completeness to θ = 23.786	96.1 %
Absorption correction	Semi-empirical from equivalents
Max. and min. transmission	1.00000 and 0.96692
Refinement method	Full-matrix least-squares on F²
Data / restraints / parameters	68110 / 25 / 969
Goodness-of-fit on, F2	0.708
Final R indices [I>2σ(I)]	R1 = 0.0908, wR2 = 0.2262 [12796 Fo]
R indices (all data)	R1 = 0.2912, wR2 = 0.2725
Largest diff. peak and hole	1.100 and -1.052 e.Å^{-3}
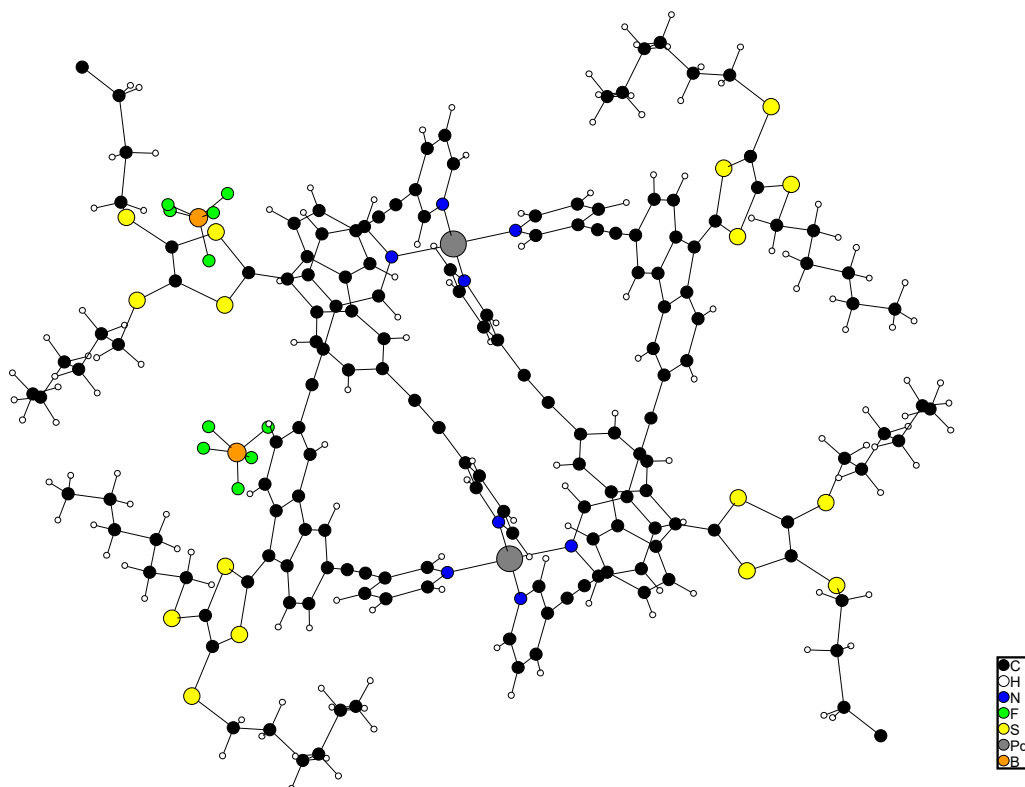
Annex 6.6.   **X-ray data for self-assemblyAA4**

Empirical formula	$C_{352}H_{368}F_{24}Fe_4N_8O_{32}P_8Pd_4S_{24}$ or $2(C_{152}H_{136}Fe_2N_4P_4Pd_2S_8)$, $8(CF_3O_3S)$, $8(C_5H_{12}O)$
Formula weight, *mr*	7344.72
Temperature	150.0(1) K
Wavelength	1.54184 Å
Crystal system, space group	Triclinic, P -1
Unit cell dimensions	$a = 20.4323(8)$ Å $\alpha = 74.192(3)^0$ $b = 27.8575(11)$ Å $\beta = 88.216(3)^0$ $c = 32.2485(11)$ Å $\gamma = 87.829(3)^0$
Volume, *V*	17644.6(12) Å^3
Number of molecules, *z*	2
Calculated density, *ρ*	1.382 mg/m^3
Absorption coefficient	5.192 mm^{-1}
F(000)	7600
Crystal size	0.226 x 0.139 x 0.076 mm
Θ range for data collection	2.454 to 72.990^0
Limiting indices	-24<=h<=21, -25<=k<=33, -39<=l<=39

Reflections collected / unique	123021 / 66698 [R(int) = 0.1446]
Completeness to θ = 67.684	98.6 %
Absorption correction	Semi-empirical from equivalents
Max. and min. transmission	1.00000 and 0.61562
Refinement method	Full-matrix least-squares on F^2
Data / restraints / parameters	66698 / 97 / 3061
Goodness-of-fit on, F2	0.914
Final R indices [$I>2\sigma(I)$]	R1 = 0.1257, wR2 = 0.3112 [22013 Fo]
R indices (all data)	R1 = 0.2092, wR2 = 0.3734
Largest diff. peak and hole	2.867 and -1.988 e.Å^{-3}
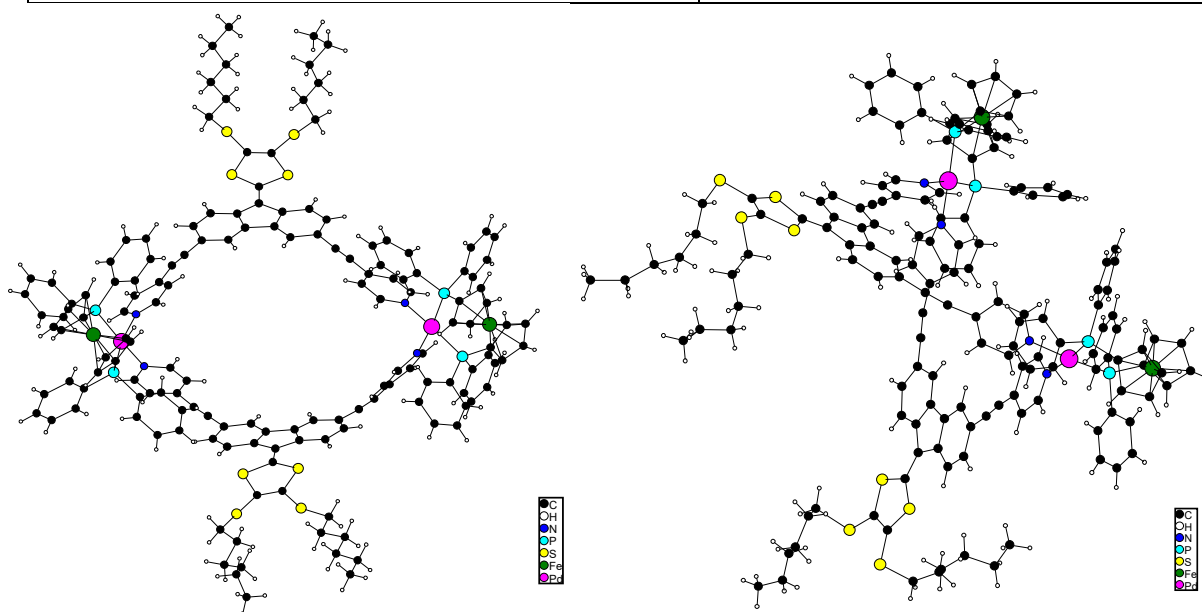
Annex 6.7.   X-ray data for self-assemblyAA9

Empirical formula	$C_{255}H_{260}F_{24}N_8O_{43}Ru_8S_{24}$ or 4($C_{36}H_{28}N_2S_4$), 4($C_{22}H_{28}O_4 Ru_2$), 8(CF_3O_3S), 3($C_5H_{12}O$)
Formula weight, mr	6158.69
Temperature	150.0(5) K
Wavelength	1.54184 Å
Crystal system, space group	Triclinic, P -1
Unit cell dimensions	a = 13.7219(7) Å α = 84.292(3)^0 b = 24.6967(11) Å β = 83.089(4)^0 c = 43.7717(15) Å γ = 86.483(4)^0
Volume, V	14634.5(11) Å^3

Number of molecules, z	2
Calculated density, ρ	1.398 mg/m^3
Absorption coefficient	5.532 mm^{-1}
F(000)	6284
Crystal size	0.238 x 0.061 x 0.034 mm
Θ range for data collection	2.594 to 63.346^0
Limiting indices	-15<=h<=15, -27<=k<=28, -35<=l<=48
Reflections collected / unique	71642 / 45102 [R(int) = 0.0542]
Completeness to θ = 63.346	94.4 %
Absorption correction	Semi-empirical from equivalents
Max. and min. transmission	1.00000 and 0.52267
Refinement method	Full-matrix least-squares on F²
Data / restraints / parameters	45102 / 196 / 2461
Goodness-of-fit on, F2	1.114
Final R indices [$I>2\sigma(I)$]	R1 = 0.1336, wR2 = 0.3497 [19740 Fo]
R indices (all data)	R1 = 0.1995, wR2 = 0.4124
Largest diff. peak and hole	2.388 and -1.037 e.Å^{-3}
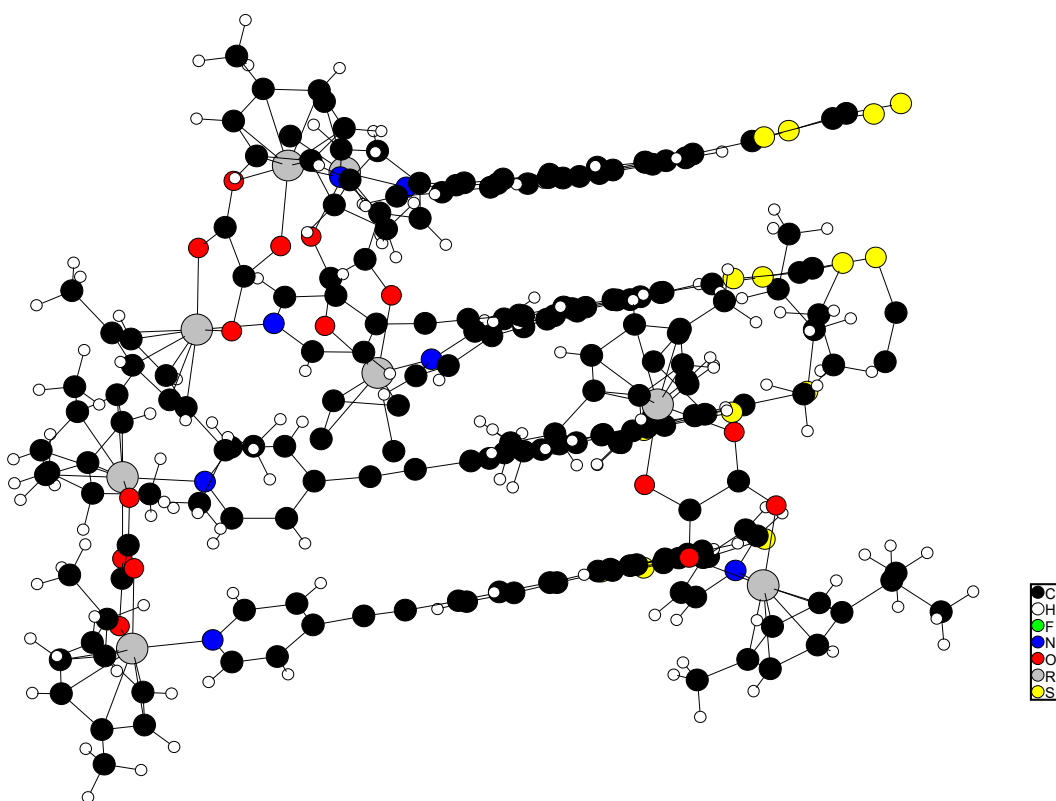
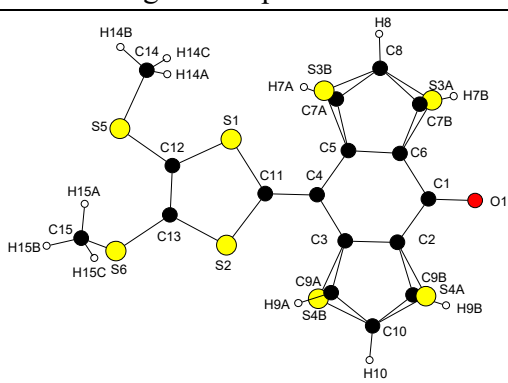**Annex 6.8.**   **X-ray data for self-assembly AA11**

Empirical formula	$C_{142}H_{132}F_{12}N_4O_{22}Ru_4S_{12}$ or 2 ($C_{66}H_{60}N_2O_4Ru_2S_4$), 4($CF_3SO_3$), 2($C_3H_6O$)
Formula weight, *mr*	3263.51
Temperature	130.0(1) K
Wavelength	1.54184 Å
Crystal system, space group	Triclinic, P -1
Unit cell dimensions	a = 15.7252(5) Å α = 85.029(4)^0 b = 18.9126(7) Å β = 74.925(4)^0 c = 25.2381(13) Å γ = 68.488(3)^0
Volume, *V*	6742.4(5) Å^3
Number of molecules, *z*	2
Calculated density, *ρ*	1.607 mg/m^3
Absorption coefficient	6.047 mm^{-1}
F(000)	3328
Crystal size	0.210 x 0.133 x 0.050 mm
Θ range for data collection	2.511 to 73.919^0
Limiting indices	-19<=h<=18, -23<=k<=22, -25<=l<=31
Reflections collected / unique	49174 / 25663 [R(int) = 0.0832]
Completeness to θ = 73.00	98.2 %
Absorption correction	Semi-empirical from equivalents
Max. and min. transmission	1.00000 and 0.59078
Refinement method	Full-matrix least-squares on F²
Data / restraints / parameters	25663 / 185 / 1682
Goodness-of-fit on, F2	1.423
Final R indices [$I>2\sigma(I)$]	R1 = 0.1517, wR2 = 0.3939 [16811 Fo]
R indices (all data)	R1 = 0.1855, wR2 = 0.4344
Largest diff. peak and hole	2.855 and -2.585 e.Å^{-3}
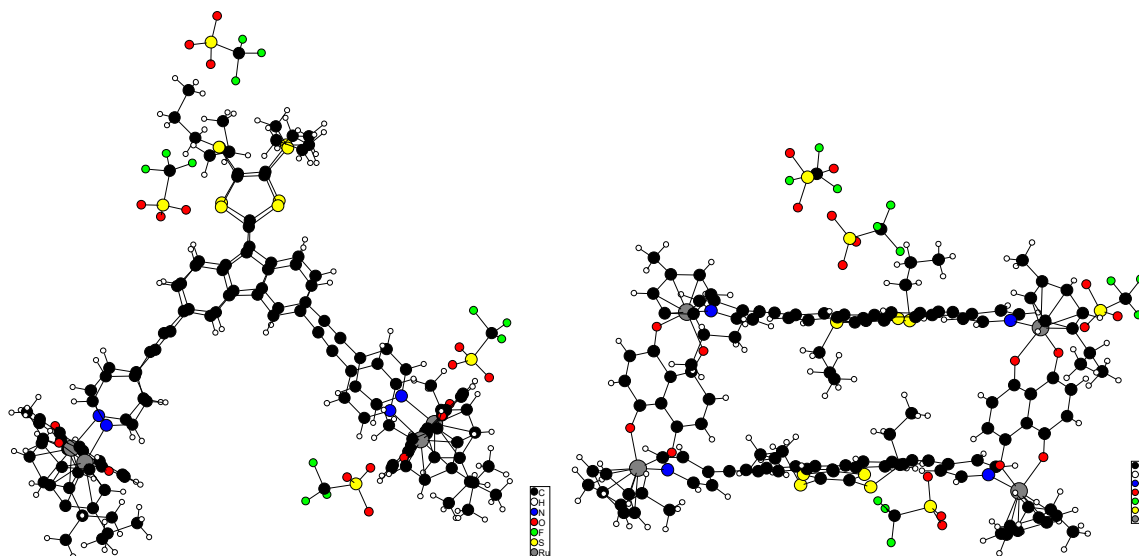
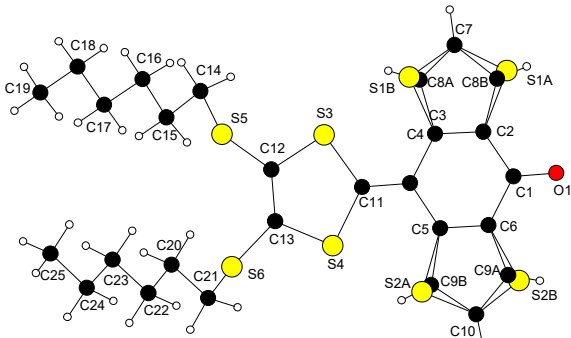**Annex 6.9.** X-ray data for [(Ag₂exTTF-TEG²⁺)²⁺]ₓ

Empirical formula	$C_{297}H_{345}Ag_8B_{16}Cl_{75}F_{64}N_{16}O_{64}S_{16}$
Formula weight, *mr*	10586.5
Temperature	130.00 K
Wavelength	1.506 Å
Crystal system, space group	Tetragonal, I 4₁/a
Unit cell dimensions	a = b = 21.416(1) Å, c = 50.908(6) Å
Volume, *V*	23349(4) Å³
Number of molecules, *z*	2
Calculated density, *ρ*	1.506 mg/m³
Absorption coefficient	8.007 mm⁻¹
F(000)	10628
Crystal size	0.158 x 0.141 x 0.081 mm
Θ range for data collection	2.238° and 72.564⁰
Limiting indices	-25<=h<=26, -26<=k<=21, -62<=l<=58
Reflections collected / unique	37450 / 11243 [R(int) = 0.050]
Completeness to θ = 72.561	0.969
Absorption correction	Semi-empirical from equivalents
Refinement method	Full-matrix least-squares on F²
Goodness-of-fit on, F2	0.975
Final R indices [*I*>2σ(*I*)]	R1 = 0.1229, wR2 = 0.3570 [3516 Fo]
R indices (all data)	R1 = 0.1926, wR2 = 0.4123
Largest diff. peak and hole	-0.676 < Δρ < 0.515 e.Å⁻³

Annex 6.10. X-ray data for compound 29

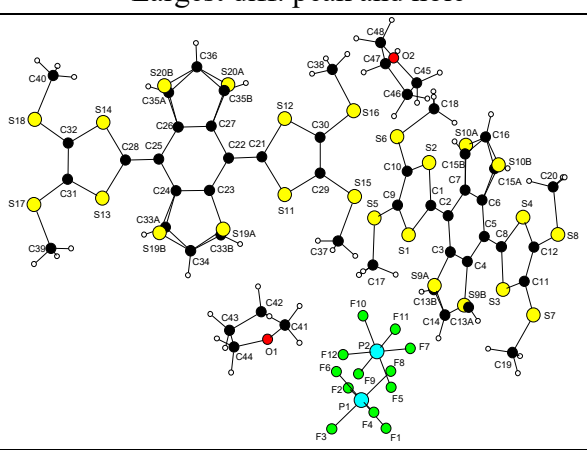|	
Empirical formula	$C_{15}H_{10}OS_6$
Formula weight, *mr*	398.59
Temperature	150.0(1) K
Wavelength	1.54184 Å
Crystal system, space group	orthorhombic, , P b c a
Unit cell dimensions	a = 7.4384(3) Å α = 90^0 b = 17.5671(6) Å β = 90^0 c = 24.0601(8) Å γ = 90^0
Volume, *V*	3144.0(2) Å^3
Number of molecules, *z*	8
Calculated density, *ρ*	1.684 mg/m^3
Absorption coefficient	8.010 mm^{-1}
F(000)	1632
Crystal size	0.266 x 0.049 x 0.023 mm
Θ range for data collection	3.67 to 76.29^0
Limiting indices	-7<=h<=9, -21<=k<=20, -26<=l<=29
Reflections collected / unique	7920 / 3216 [R(int) = 0.0299]
Completeness to θ = 75.00	98.4 %
Absorption correction	Semi-empirical from equivalents
Max. and min. transmission	1.00000 and 0.64906
Refinement method	Full-matrix least-squares on F²
Data / restraints / parameters	3216 / 24 / 239
Goodness-of-fit on, F2	1.137
Final R indices [$I>2\sigma(I)$]	R1 = 0.0686, wR2 = 0.1823 [2938 Fo]
R indices (all data)	R1 = 0.0749, wR2 = 0.1880
Largest diff. peak and hole	1.634 and -0.601 e.Å^{-3}
	Taux d'occupation des atomes: τ C7A, H7A, S3A = 0.576 τ C7B, H7B, S3B = 0.424 τ C9A, H9A, S4A = 0.433 τ C9B, H9B, S4B = 0.567

Annex 6.11.   X-ray data for compound 31

Empirical formula	$C_{25}H_{30}OS_6$
Formula weight, *mr*	538.85

Temperature	150.0(1) K
Wavelength	1.54184 Å
Crystal system, space group	Monoclinic, P 21/c
Unit cell dimensions	$a = 18.9180(4)$ Å $\alpha = 90^0$ $b = 7.3987(2)$ Å $\beta = 95.334(2)^0$ $c = 18.6770(4)$ Å $\gamma = 90^0$
Volume, V	2602.87(11) Å^3
Number of molecules, z	4
Calculated density, ρ	1.375 mg/m^3
Absorption coefficient	4.978 mm^{-1}
F(000)	1136
Crystal size	0.321 x 0.127 x 0.078 mm
Θ range for data collection	4.70 to 72.68^0
Limiting indices	-23<=h<=22, -9<=k<=6, -22<=l<=21
Reflections collected / unique	10077 / 4987 [R(int) = 0.0303]
Completeness to θ = 71.00	98.2 %
Absorption correction	Semi-empirical from equivalents
Max. and min. transmission	1.00000 and 0.28614
Refinement method	Full-matrix least-squares on F²
Data / restraints / parameters	4987 / 12 / 328
Goodness-of-fit on, F2	1.051
Final R indices [$I>2\sigma(I)$]	R1 = 0.0343, wR2 = 0.0871 [4535 Fo]
R indices (all data)	R1 = 0.0400, wR2 = 0.0905
Largest diff. peak and hole	0.285 and -0.314 e.Å^{-3}
	Taux d'occupation des atomes: τ C8A, H8A, S1A, C9A, H9A, S2A = 0.776 τ C8B, H8B, S1B, C9B, H9B, S2B = 0.224

Annex 6.12. **X-ray data for compound 30**[*+]

Empirical formula	$C_{48}H_{48}F_{12}O_2P_2S_{20}$ or $2(C_{20}H_{16}S_{10})$, $2(PF_6)$, $2(C_4H_8O)$
Formula weight, mr	1588.00

Temperature	200.0(1)
Wavelength	1.54184 Å
Crystal system, space group	Triclinic, P -1
Unit cell dimensions	a = 10.1850(6) Å α = 104.200(4)^0 b = 13.7241(6) Å β = 90.154(4)^0 c = 24.2742(11) Å γ = 111.727(5)^0
Volume, V	3039.2(3) Å^3
Number of molecules, z	2
Calculated density, ρ	1.735 mg/m^3
Absorption coefficient	7.771 mm^{-1}
F(000)	1620
Crystal size	0.359 x 0.041 x 0.030 mm
Θ range for data collection	3.60 to 72.81^0
Limiting indices	-11<=h<=12, -15<=k<=16, -26<=l<=29
Reflections collected / unique	22499 / 11585 [R(int) = 0.0573]
Completeness to θ = 70.00	98.1 %
Absorption correction	Semi-empirical from equivalents
Max. and min. transmission	1.00000 and 0.62684
Refinement method	Full-matrix least-squares on F^2
Data / restraints / parameters	11585 / 48 / 842
Goodness-of-fit on, F2	1.006
Final R indices [$I>2\sigma(I)$]	R1 = 0.0554, wR2 = 0.1207 [8320 Fo]
R indices (all data)	R1 = 0.0802, wR2 = 0.1383
Largest diff. peak and hole	0.763 and -0.428 e.Å^{-3}
	Taux d'occupation des atomes: τ C13A,H13A,S9A = 0.441 τ C13B,H13B,S9B = 0.559 τ C15A,H15A,S10A = 0.571 τ C15B,H15B,S10B = 0.429 τ C33A,H33A,S19A = 0.479 τ C33B,H33B,S19B = 0.521 τ C35A,H35A,S20A = 0.532 τ C35B,H35B,S20B = 0.468